National Library of Canada
Acquisitions and Bibliographic Services Branch
395 Wellington Street
Ottawa, Ontario
K1A 0N4

Bibliothèque nationale du Canada
Direction des acquisitions et des services bibliographiques
395, rue Wellington
Ottawa (Ontario)
K1A 0N4

Your file Votre référence

Our file Notre référence

NOTICE

The quality of this microform is heavily dependent upon the quality of the original thesis submitted for microfilming. Every effort has been made to ensure the highest quality of reproduction possible.

If pages are missing, contact the university which granted the degree.

Some pages may have indistinct print especially if the original pages were typed with a poor typewriter ribbon or if the university sent us an inferior photocopy.

AVIS

La qualité de cette microforme dépend grandement de la qualité de la thèse soumise au microfilmage. Nous avons tout fait pour assurer une qualité supérieure de reproduction.

S'il manque des pages, veuillez communiquer avec l'université qui a conféré le grade.

La qualité d'impression de certaines pages peut laisser à désirer, surtout si les pages originales ont été dactylographiées à l'aide d'un ruban usé ou si l'université nous a fait parvenir une photocopie de qualité inférieure.

Canada

Nonlinear Effects in Chemical Dynamics and Chemical Kinetics: Chaos in Physical Chemistry

by

Delmar N. S. Permann, B.Sc., M.Sc.

A thesis submitted to the

School of Graduate Studies and Research

in partial fulfilment of the requirements

for the degree of

Doctor of Philosophy

Department of Chemistry

University of Ottawa

Ottawa, Ontario

Canada

September 1993

Ph. D. Candidate	Co-Supervisor	Co-Supervisor
Delmar N. S. Permann	Heshel Teitelbaum	Ian Hamilton

ISBN 0-315-95966-5

UNIVERSITÉ D'OTTAWA
UNIVERSITY OF OTTAWA

Acknowledgements

I would like to thank Drs. Bill Waltz and Ron Verrall for having faith in my ability to do Ph.D. level work.

My time at the University of Ottawa has been split between two projects. One investigating nonlinear effects in chemical dynamics and one investigating nonlinear effects in chemical kinetics. I gratefully acknowledge the help and direction that Ian Hamilton has given me on nonlinear chemical dynamics. Heshel Teitelbaum has been a wonderful source of help and inspiration about science in general and nonlinear kinetics, specifically. I am grateful to Heshel Teitelbaum for his generous support throughout all of the time I was at the University of Ottawa.

I thank the Faculty of Graduates Studies and Research for a partial scholarship which allowed me to complete the last year at the University of Ottawa.

Zhikai Cheng has been a friend and we have shared long discussions on science, society and the interactions of the two. I thank him for his help and support. I also thank Zhichung Su for his help in getting the program for post shock conditions to work correctly.

I am grateful to François Allard for his help in taking my design for the schlieren detectors and building a first rate, up-to-date system. I also thank François for supplying me with several drawings having to do with the schlieren detection system.

I thank my family for their support, my sister Sherry, my brother-in-law Gerry, my mother Ida and especially my wife, Maria.

Abstract

This work shows that nonlinear dynamic systems are quite different from linear dynamic systems. The usual phase plots of linear and nonlinear dynamical systems are also distinctly different, even before damping or forcing terms are added. It is also shown that the usual phase plot allows for the visualization of unobservable information that is present in the times series. The higher-order phase plots give yet additional information that is not present in the existing methods of plotting the data. Higher-order phase plots were originated and applied for the first time to a dynamical system (Morse oscillator) for the purpose of earlier detection of nonlinear effects.

The dynamics of a weakly forced and weakly damped Morse oscillator is examined. The novel tool of higher-order phase plots is used to visualize the importance of the higher harmonics in the phase which are essential for the dynamics to be complicated and dissociative. Expansions of the higher-order phase plots in regions about $x^{(n-1)} = 0$, $x^{(n)} = 0$ are considered and it is shown that there is a topological change that occurs sequentially for each higher-order phase plot. After the topological change, which occurs at a critical value of initial total energy E(0) for a particular value of forcing F, the higher-order phase space structure has a circular loop. As F or E(0) is further increased the phase space trajectory loops an increasing number of times in the higher-order phase plot. It is shown that for $F = 1.0\times 10^{-3}$ the topological change occurs around E(0) = 0.96 for the fifth-order phase plot and around E(0) = 0.94 for the eleventh-order phase plot. This is also illustrated with a series of higher-order phase plots ($2^{nd} - 10^{th}$) for $F= 1 \times 10^{-3}$, and E(0) = 0.97. These plots indicate that although the 5^{th} order phase plot forms loops the 4^{th} forms only half-loops. Thus the higher-order phase plots are increasingly sensitive probes of the phase space dynamics as the order increases. Qualitatively this is because, as the

order increases, part of each higher-order phase space structure is increasingly close to the point $(x^{(n)},x^{(n-1)}) = (0,0)$. For larger values of F the topological change occurs at a smaller value of E(0) for each higher-order phase plot, as the radius of the loop centered on $x^{(n-1)} = 0$, $x^{(n)} = 0$ is larger. While the phase space trajectory loops the energy is approximately constant with small oscillations. The circular loop in the higher-order phase plot is the higher-order space structure that is expected for the weakly forced and weakly damped free particle. The significance of the circular loop is that the lower the order of the higher-order phase plot in which the phase space trajectory loops, the closer the Morse oscillator is to dissociation. From this viewpoint, the Morse oscillator dissociates when the value of F or E(0) becomes sufficiently large that the topological change occurs in the usual phase plot. That is, the Morse oscillator dissociates when the phase space structure becomes open for the usual phase plot.

The circular loop in the higher-order phase plots is the higher-order phase space structure that is expected for free H and F atoms in a laser field. For a time interval in which the trajectory loops in the higher-order phase plots, HF behaves as though it has dissociated and this is why the compensated energy, $E_c(t)$, is constant for the time interval. The energy jumps either up or down in a "random" fashion (the dynamics is chaotic) in the pre- and postloop switching regions, and HF may dissociate at a later time. To directly observe energy stepping for HF in a moderate laser field one could promote the $v = 0$ state (which is close to a minimum uncertainty wavepacket) to the $v = 21$ level (or another very high-lying level) and then measure the energy of the evolving wavepacket within a few optical cycles *i.e.* before wavepacket spreading could destroy this effect.

Wavelet analysis is applied to dynamical systems, for the first time, for the purpose of extracting a weak forcing term. A wavelet analysis of the coordinate of a

weakly forced and weakly damped Morse oscillator near dissociation is presented. The coordinate is highly aperiodic in this highly anharmonic regime and, in fact, chaotic under some of the conditions presented. It is shown that the forcing amplitude can be qualitatively extracted while the forcing frequency can be quantitatively extracted, even for short total times. When the coordinate is highly aperiodic it is not possible to determine these quantities by subtracting off the coordinate of the unforced and undamped Morse oscillator since the unforced undamped coordinate has a completely different period that the forced and damped case. Therefore subtraction of the two cases is not possible. The FFT of the Morse has too many large amplitude frequencies present from the Morse potential, and the frequencies of the forcing term are effectively buried.

"Details" of the coordinate at several stages are compared and a weak forcing term is detected in certain "details" when the corresponding wavelet basis functions have the appropriate localization in both frequency and time. The combination of a wavelet transform followed by an FFT of the "details" shows, for the first time, that several frequencies can be detected at the same time. In fact, these frequencies can be detected even when their amplitudes are much smaller than the amplitude of the frequencies that make up the Morse potential.

Two aspects of wavelet analysis are addressed. First, unlike a Fourier transform, a wavelet transform is not unique. The present work shows that, for the Morse oscillator system, effective results may be obtained using several of the basic sets of mother functions devised by Daubechies. Second, this work shows that weak forcing frequencies can be determined only when the rate of change of the coordinate is relatively slow (small).

In analogy to the nonlinear dynamics system, a nonlinear kinetic system is examined both experimentally and theoretically. For the first time, simulations and

experiments were performed to determine the effect of dilution of CCl_3F with Ar on oscillating laser schlieren signals.

In the experiments CCl_3F gas (pure and in mixtures with Ar) is shock compressed, inducing a redistribution of clusters. A quasi-periodic and/or chaotic approach to equilibrium, associated with an exothermic process, is observed using the laser-schlieren method. Similar behaviour is observed for SF_6 and CCl_3H. Dilution with argon seems to switch off thermal feedback, and therefore quietens down the observed signals, as well as changes the form of the signal.

A new data collection system is developed for observing the process at three stations in the apparatus, each with slightly different experimental conditions within 2% (sometimes less than 1%), thus allowing, for the first time, a probe of the sensitivity of the kinetics to initial conditions. The new system allows each one of the three photodiode preamplifiers to be disabled in sequence on the microsecond time scale which makes sure that the signals do not interfere with each other. The system also increases the number of data points collected, and therefore the final waveform can be sampled at a much higher rate.

A wavelet analysis of a laser schlieren millivolt signal, with real noise, is able to pick out the high frequency noise present in the HeNe laser system used, but is not useful in doing an analysis of the lower frequencies present in the signal. However, it is shown that under certain circumstances the wavelet analysis technique can be used to greatly reduce the amount of noise present in the schlieren millivolt signal. Thus denoising of a signal from a single-shot experiment is now possible.

The model proposed in this work describes what occurs when a room temperature distribution of clusters (dimer to pentamer) is heated and compressed suddenly and a new Boltzmann distribution of clusters results. Oscillatory behaviour is observed. Argon seems to switch off the thermal feedback.

The simulations basically prove that a model of cluster formation via excited monomer addition to an existing n-mer is realistic. The calculated observable shows the negative-going peak expected from a system with heat release. The oscillations are shown to have a large dependence upon nonlinear effects with the dilution parameter being able to turn off and on the thermal feedback.

This work has shown that nonlinear effects are important in understanding the processes involved in the kinetics of the formation of CCl_3F clusters.

Table of Contents

List of Tables

List of Figures

1 Introduction and Theory of Nonlinear Systems

1.1 Introduction

1.1.1 Introduction

This chapter is concerned with the presentation and explanation of how simple systems (dynamic or kinetic) when forced, can respond in a manner that is not expected[1–3]. The system must be a nonlinear system, usually far from equilibrium, and then be pushed into a part of parameter space that results in the system exhibiting chaos. This introductory section will explain terms and processes such as, what is and what is not chaos, what is a nonlinear system, how parameter space is defined and how chaotic a system is, since a chaotic system does not respond in a completely random manner.

The units here are Hartree's[4] and they are presented in Appendix A. The nonlinear dynamic system, that has been used here, is the Morse[5] oscillator. The Morse oscillator is first discussed in a general sense, as Morse himself and other authors have done, and then more specific details are examined. Thus, the reader will be able to see the strengths and weakness of this useful model.

This work outlines the use of two new techniques for analyzing nonlinear systems. The first of these techniques is higher-order phase plots and has been used to detect a weak forcing term. The second technique, wavelet analysis, has been used in geophysics[6], etc. and this is the first use of this technique in chemistry. It is also used to detect a very weak forcing term whether the system is chaotic or not. Neither of these new techniques have their resolution tied to the total amount of time of the signal that is being analyzed, as is the case for the Fourier transform. The Fourier transform data point size, Δf, is related to the inverse of the total time of

the signal. Thus, the longer the total time of the signal the "better" the resolution of the transform.

The nonlinear kinetics section of this work, Chapter four, deals with oscillatory experimental signals from shock compression of CCl_3F, CCl_3H, and SF_6. The apparatus was improved by changing the type of amplification for the detection system and the data collection system was replaced with a modern data collection system. The resulting experiments allow discussion of the oscillations with larger data sets. The oscillations are related to the formation and dissociation of small size clusters in the gas phase.

1.1.2 Overview of the Morse Oscillator

Shirts[7] describes the Morse oscillator with the total energy of the form

$$H = I\omega_0(1 - I\omega_0/4D) \qquad [1.1]$$

where the action-angle variable

$$I = \hbar(n + \frac{1}{2}) \qquad [1.2]$$

is used to give exact quantum eigenvalues, ω_0 is the classical harmonic frequency and D is the dissociation energy. In the previous section it was noted that for atomic units $\hbar = 1.0$. It is also known that[5,7]

$$\omega_0 = a(2D/m)^{1/2} \qquad [1.3]$$

where m is the reduced mass of the diatomic and a is the spectroscopic constant specific to the diatomic. Expansion of Shirts's[7] action-angle equation, above, gives

$$H = I\omega_0 - I^2\omega_0^2/4D. \qquad [1.4]$$

Then, substitution of I with

$$(n + \frac{1}{2}) \qquad [1.5]$$

results in

$$H(n) = \omega_0(n + \frac{1}{2}) - \omega_0^2/(4D)(n + \frac{1}{2})^2. \qquad [1.6]$$

If Morse's[5] assumption is used namely,

$$D = \omega_0^2/(4\omega_0 x_0), \qquad [1.7]$$

then

$$\omega_0^2/(4D) = \omega_0 x_0 \qquad [1.8]$$

and the total energy becomes

$$H(n) = \omega_0(n + \frac{1}{2}) - \omega_0 x_0(n + \frac{1}{2})^2, \qquad [1.9]$$

where $\omega_0 x_0$ is the anharmonicity of the diatomic. This is the same equation that is generally used in spectroscopic calculations of the energy of the vibrational levels[11,13]. This is well known to be a first order approximation. For diatomics containing hydrogen atoms there needs to be a further correction of $+\omega_0 y_0(n + \frac{1}{2})^3$ added to the above equation. So the spectroscopic equation for vibrational energy[12,13] is

$$\epsilon_v = \omega_0(v + \frac{1}{2}) - \omega_0 x_0(v + \frac{1}{2})^2 + \omega_0 y_0(v + \frac{1}{2})^3. \qquad [1.10]$$

To further understand how this limiting of the energy equation came about, investigation of Morse's[5] original work is needed. Morse had four requirements that energy, E, needed to have.

"1) It should come asymptotically to a finite value as $r \longrightarrow \infty$;

2) It should have its only minimum point at $r = r_e$;

3) It should become infinity at $r = 0$ (this need not be exactly true, however, the results are practically the same if E becomes very large at $r = 0$);

4) It should exactly give the allowed energy levels as the finite polynomial $W(n) = -D + h\omega_0[(n + \frac{1}{2}) - x(n + \frac{1}{2})^2]$."

Morse then proposed his now famous potential energy function (see below) and went on to prove that it fit his above stated criteria.

Walker and Preston[8] stated that the Morse oscillator had "$\cdots$ energy levels,

$$\epsilon_n^0 = DB(n + \frac{1}{2})[2 - B(n + \frac{1}{2})], \qquad [1.11]$$

where

$$B^2 = (\hbar^2 a^2/2mD)." \qquad [1.12]$$

From substituting equation [1.3] into equation [1.8] it can be seen that,

$$\omega_0 x_0 = a^2/(2m). \qquad [1.13]$$

Then from substituting equation [1.13] into equation [1.12], and from the previous discussion for the conversion of equation [1.6] into [1.9], equation [1.11] can be seen to have the same form as the first order spectroscopic equation, [1.9], mentioned above. Walker and Preston[8] refer to ter Haar[9] for the equation for vibrational energies, and ter Haar makes a very strong point of stating that the equation that gives rise to the vibrational energy levels having the above form "is only an approximation, although in every practical case of the diatomic molecules, a very good approximation $\cdots$". Walker and Preston[8] go on, in the appendix of their paper, to use this B value to determine the number of bound levels in a diatomic,

$$N_{max} = [1/B + \frac{1}{2}], \qquad [1.14]$$

where the square bracket function [ ] denotes the greatest integer function. They proceed to further use B to talk about the anharmonicity of the Morse oscillator. If

the original constants defined by Morse[5] are used then a simplification can be realized. Rearranging [1.3] it can be shown that the reduced mass is,

$$m = a^2 2D/\omega_0^2. \qquad [1.15]$$

Since Hartree's atomic units are being used, $\hbar = 1.0$ therefore

$$B^2 = a^2/(2Dm). \qquad [1.16]$$

Replacing m with the new formula, [1.15] above, results in

$$B^2 = \omega_0^2/(4D^2). \qquad [1.17]$$

Next, using Morse's statement relating dissociation to the classical harmonic frequency and the anharmonicity, equation [1.7], (and thus by going back to the original concepts outlined by Morse) it can be seen that

$$B = 2\omega_0 x_0/\omega_0. \qquad [1.18]$$

Therefore the number of bound levels is really related to the harmonic frequency and the anharmonicity of the diatomic in question, that is

$$N_{max} = [\frac{\omega_0}{2\omega_0 x_0} + \frac{1}{2}]. \qquad [1.19]$$

In fact, as can be seen by the above ratio, the number of bound levels is really only determined by $1/(2x_0)$, thus

$$N_{max} = [\frac{1}{2x_0} + \frac{1}{2}]. \qquad [1.20]$$

Therefore, if the anharmonicity constant (x_0) is reported it can be used directly. Usually the anharmonicity and the harmonic frequency are reported and therefore the first formula provides an easier method.

For HF, from Herzberg[10], $\omega_0 = 4138.52\ cm^{-1}$, and $\omega_0 x_0 = 90.069\ cm^{-1}$ and therefore $N_{max} = [23.5]$. If this is rounded up, the number of bound levels of HF is the same number as Walker and Preston[8] reported; however this is not necessarily correct. To show this, an evaluation of equation [1.6] is done. Equation [1.6] is the same as that outlined by Shirts[7] which is also the same as stated by Walker and Preston[8]. Using the parameters for HF, $\omega_0 = 1.486\ 037 \times 10^{-2}$ and $D = 0.225\ 089\ 5$ atomic units, the energy of the n^{th} level is calculated and compared to the dissociation energy. The essential usage is as a functional method for expressing the oscillators total energy as a percentage of the dissociation energy. The results of this procedure are tabulated in Table 1.1. Notice that $H(24)$ is less than either $H(23.5)$ or $H(23)$. Since only integer values are allowed there are only 23 bound levels in HF. At least that is what is determined by the equations outlined by Shirts[7] and set up originally by Morse[5].

Table 1.1 Vibrational energy (a.u.) levels of HF.

Level #	Energy(a.u.)	$\%D$
24.0	0.224 932 3	99.930 11
23.5	0.225 082 7	99.996 98
23.0	0.225 035 7	99.976 09
22.0	0.224 349 0	99.671 01
21.0	0.222 872 2	99.014 92

The energy is in atomic units (a.u.) and for HF the dissociation energy is $D = 0.225\ 089\ 5$ a.u.

It is well known[11,12,13] that as the vibrational ladder is climbed, for an anharmonic oscillator, the energy spacing between the vibrational levels decreases until a continuum is reached. This work ignores the effects of rotation, which are that the rotational constant decreases as the vibrational level increases and the centrifugal

force causes the bond length to increase as the rotational level increases. The rotational energy difference usually increases as the energy is increased but this will be dependent upon the individual molecule. The number of vibrational levels is usually calculated using numerical methods and the known potential function of the molecule of interest. The results presented here are used as a way of giving a general overview of the Morse oscillator and are not presented as a way of replacing more sophisticated methods of calculating the number of vibrational levels in a molecule.

It is worth noting here that when $\omega_0 = a(2D/m)^{\frac{1}{2}}$ is used to calculate the harmonic frequency for HF, the result is $1.486\ 037 \times 10^{-2}$ atomic units. If the values for the Rydberg constant (for infinite mass, R_∞) in cm^{-1}, Hz, J, and eV, as tabulated in Table 1.2 (from the work of Cohen and Taylor[14]) are used, the harmonic frequency can be converted from atomic units to cm^{-1}, and the value is 4139.4 cm^{-1}. This is very close to the value report by Herzberg[10] of 4138.52 cm^{-1}. Furthermore, $\omega_0 x_0 = a^2/(2m) = 3.950\ 793 \times 10^{-4}$ atomic units. This converts to 86.710 cm^{-1}, and Herzberg[10] reports the anharmonicity to be 90.069 cm^{-1}. The difference between these two values can be attributed to the tunnelling of hydrogen. To prove this, the same calculations are repeated for DF. The harmonic frequency calculated from the basic equation is 2998.069 cm^{-1} and the reported[10] value is 2998.25 cm−1. The calculated anharmonicity is 45.486 cm^{-1} and the reported[10] value is 45.71 cm^{-1}. Thus the equation is good at predicting mechanical anharmonicity.

Therefore, even though the Morse potential is known to be incorrect near dissociation[15] there are still several reasons it is used. On the expansion of the coordinate it is well known that the Morse oscillator model does not increase fast enough but it still can be used as a model. It is a simple model and is still used in classical (Miller[16]) and quantum mechanical studies. Here it is used as a simple way of introducing new techniques for analysis. By using a simple model, reasonable computational times can

Table 1.2 Rydberg constant (R_∞).

R_∞	Hartree $= 2R_\infty$	Units
$1.097\ 373\ 153\ 4 \times 10^5$	$2.194\ 746\ 306\ 8 \times 10^5$	cm^{-1}
$3.289\ 841\ 949\ 9 \times 10^{15}$	$6.579\ 683\ 899\ 8 \times 10^{15}$	Hz
$2.179\ 874\ 1 \quad \times 10^{-18}$	$4.359\ 748\ 2 \quad \times 10^{-18}$	J
13.605 698 1	27.211 396 2	eV

atomic unit of time, t(a.u.), is based on $\hbar$ set to unity in atomic units.
t(a.u.) $= \hbar/\text{Hartree} = \frac{6.626\ 075\ 5\times10^{-34}\text{Js}}{2\pi\cdot4.359\ 748\ 2\times10^{-18}\text{J}} = 2.418\ 884\ 4 \times 10^{-17}$ s.
This is about 0.024 189 femto (10^{-15}) seconds (fs) or approximately 24.189 atto (10^{-18}) seconds (as).
The atomic unit of length is the bohr radius ($0.529\ 177\ 249 \times 10^{-8}$ cm).

be used to explore areas of interest. The Morse model exhibits chaos when it has been forced in the right parameter regime, and since the chaos of dynamical systems is not completely understood simple models (small computational time) allow exploration with available computers.

1.1.3 Chaotic Response of a System

Chaos is sometimes mistakenly considered to mean completely random and encompassing all and every possible solution or result. That is, if a system is chaotic it will respond in a unpredictable way to any and all input parameter choices. In fact it has been shown[3] that a system may behave in a chaotic manner where the choices of solution to the response are infinite but have an upper and lower bound. An example of this is the logistic map (presented below) in which the solution has a value between 0 and 1 but under certain conditions an infinite choice of solutions is possible. Thus, even though a system may exhibit chaos it does not follow that the solutions will cover an infinite space (phase space or parameter space). In fact even in the bounded space of choices there will be some solutions that are periodic with

varying periods and others that are not periodic but chaotic (see the logistic map). This leads to a definition for chaos that is different than a completely random choice and a set of rules defining how a system becomes chaotic can be outlined. In other words, the "route" to chaos can be determined for a system.

Why do we want to study chaos? Since the time of Newton scientists have used ordinary differential equations to model physical systems. Newton modeled the motion of planetary systems using differential equations. Although the planets of our star system, overall, fit this deterministic approach there is at least one body in our solar system that does not. One moon of Saturn, Hyperion, has a regular orbit about Saturn but instead of spinning on its axis it tumbles in a chaotic manner[17]. Another physical process, lasing[18], is expected to behave in a well known manner but under certain sets of conditions lasers will behave chaotically. Even chemical systems have been known to exhibit chaotic behaviour. In fact oscillatory behaviour has been known to exist for the long known process of $H_2 + \frac{1}{2}O_2 \rightleftharpoons H_2O$. (This reaction has over 100 elementary constituent chemical reactions producing this overall result.) This was reported to exhibit oscillatory behaviour in 1936 and has recently shown chaotic behaviour[19]. When an experiment gave results that did not fit a linear model, the results were ignored or deleted. Some chaotic behaviour only exists for a small parameter regime and it is not until precise measurements are done on the system that the chaotic behaviour was detected as noted by Gray[19]. Chaos exists not only in the realm of theory but has been and is still being pursued by experimentalists[18].

1.1.4 Justification of Work

As will be discussed further in Chapter 3, wavelets have been used to analyse signals for some time[6]. Signal capture is, simply expressed, the process of taking a continuous data stream, digitizing it, and saving this data. The data can then be

analysed by a process that will determine the frequency components or oscillatory behaviour. Since physical chemistry experiments involve data capture, as outlined above, any signal processing method used by other scientists should be of interest to physical chemists. Wavelet analysis is one such technique and although there are others, this work will only be concerned with the wavelet transform. This has already been applied to the Duffing oscillator[64] and the work here focuses on the Morse oscillator and expands the usefulness of the wavelet transform.

This work also introduces physical chemists to higher-order phase plots which have been presented initially in three papers[52,38,65]. These higher-order phase plots allow well-buried information that is present in the usual phase plot to become observed. The usual phase plot is made because it presents information that exists in the time plots of the phase and velocity but not all of the information is observable in the time plots alone. This is exactly what the higher-ordered phase plots allow as well. There is no new information, merely a magnification of the existing information and a new tool with which to present it. This allows researchers to study the model that they are using and gives them a tool that is sensitive to the forcing of the system. Thus the onset of chaos may be determined where, previously the tool used allowed only a broad guess as to when the system became chaotic.

Experimentalists such as Lienau, Williamson and Zewail[37] are probing the photodissociation process. An oscillator close to the dissociation limit in the presence of a perturbing photon can be modelled by equations described in this work. Higher-order phase plots and wavelet analysis *i.e.* the new tools described here for analyzing chemical dynamics and kinetics may be useful for further understanding the photodissociation process.

As will be pointed out in the various sections on nonlinear kinetics, just because

chaos has been reported in only some chemical systems does not mean it is nonexistent in other chemical systems. Both the dynamics and kinetics of a chemical system can exhibit chaotic behaviour. This is because both the dynamics and kinetics are nonlinear systems and when nonlinear systems are driven in certain parameter regimes they may become chaotic. This is a basic fact of nonlinear systems. It is well known to chemists that a chemical reaction may be well-behaved when carried out in a small test tube in solution but when the chemical reaction is scaled up the system may no longer work as it did under the restricted circumstances. In a larger vessel nonlinearity may be more important than in the small reaction vessel. (The opposite situation may also be encountered.) The mixing of the reactants may occur in a completely different manner and on a different time scale when the reaction is scaled up. If a system is in a chaotic parameter regime, a small change in one parameter may cause the system to react very differently. Also, if a system is in a chaotic parameter regime and is in a stable window of periodicity it may have a choice of 2, 3, 5, or 7 stable states rather than just one. Again a small change of one parameter may allow the system to change stable states and thus result in different products. Noid *et al*[20] have calculated the reaction dynamics of He + I_2 collisions and found a regime where the reaction dynamics is smooth and another regime where it chatters. The chattering region has a fractal dimension of ≈ 2 and after the chattering region is passed the reaction dynamics is once again smooth. Thus, there is a parameter regime in which chaos is present in between two well-behaved regions. Laidler[21] has also pointed out that when a reaction path is followed the system may oscillate several times from the product to reactant side of the reaction coordinate. The final state of the system may be in either the reactants or the products side after undergoing this type of oscillation. Chemists are trying to understand the basic reasons for chemical reactions taking place, and the understanding of chaos has a place in the path to understanding chemical reactions.

1.2 Theory of Nonlinear Systems

1.2.1 Introduction

Dynamics deals with the study of forces involving equations of motion. Only differential equations of motion will be discussed in this work. Thompson and Stewart[2] give a good overview of dynamical systems, some of which will be presented later in the next section. The usual way to simplify a physical or chemical problem has been to use a linearized version of the nonlinear equations if they are difficult to solve. The difference between a linear and nonlinear system of equations will be presented in the next section. One of the important reasons for considering nonlinear systems is that a forced nonlinear system of dimension 2 can exhibit chaos. Scientists used to believed that in order to model a chaotic system a large number of equations were needed. Lorenz[22], with three differential equations (in three unknowns), was able to produce a system that exhibited chaotic behavior in a dissipative system. He did have difficulty in getting his work published, but the idea that a simple system of nonlinear equations, using certain parameters, can exhibit chaos is now widely accepted by scientists. It has been shown to be true for predator-prey models, heartbeat models, and nonlinear oscillators[2]. Oscillating (and chaotic) chemical systems have been modeled[19,23–28] using a large set of differential equations which were then reduced in number with the loss of some information, but with the retention of essential behaviour. In this reduced set of equations a parameter regime was found that modeled experimental data which followed a bifurcation route to chaos. When the parameter was further increased the system became well-behaved again. This region of chaotic response may cover only a small region of the parameter space and this gives a plausible explanation as to why it is difficult to measure this behavior in some chemical systems. In other words, precise measurements of chemical concentrations or vibrational energy, or of whatever parameter is affecting the sensitivity to initial conditions, must be made.

Since there is the possibility of windows of one kind of behaviour embedded in a region with another kind of behaviour, it might be difficult to detect the change and there is a risk that the data will be considered to be unimportant and discarded.

1.2.2 Ordinary Differential Equations

A simple first order differential equation is $\frac{dy}{dt} = f(y)$; the derivative is with respect to time. Differential equations have been used to model many physical and chemical systems. A simple differential equation can be used to model the concentration change of a reacting species. For example, A + B $\longrightarrow$ C is represented by $\frac{d[A]}{dt} = -k[A][B]$, where k is the rate constant. Differential equations are also used to model motions governed by the forces acting on bodies such as the planets of our solar system. Another simple system expressed by differential equations is the motion of a rigid pendulum. The simple rigid pendulum will be presented in a latter section as an example of an unforced system. If $f(y)$ is a linear function of y, then the differential equation is termed linear.

An equation that has had the derivative taken twice with respect to time is a second order equation. The equations of motion for the simple pendulum and the Morse oscillator (presented later) are examples of such systems.

Solving systems of differential equations has been pursued since the time of Newton and Leibniz[29]. Linear differential equations usually have analytic solutions and so the results can be calculated exactly[29]. This is one of the reasons that nonlinear systems of equations were and sometimes still are linearized. The resulting approximation is then used to probe the real systems. The alternative is to leave the nonlinearity in place and integrate the equations using a numerical method.

The stability of differential equations is an extremely important consideration.

Differential equations display various kinds of behaviour, and these different behaviours are defined in phase space or a phase plot[29]. A phase plot is the plot of the velocity of a system *versus* the phase (position) of the system. (This plot is sometimes referred to as the phase plane.) The phase of a system is the displacement from an equilibrium position or the actual position itself. The velocity of the system is the derivative of the phase (position) with respect to time. In other words, velocity is the first derivative of the phase of the system and acceleration is the second derivative of the phase of the system, with respect to time. The trajectory of a system is the path that a set of points will traverse in phase space. If the trajectory is spiraling in either a clockwise or counter-clockwise direction into the center of the phase plot the fixed point is considered to be stable. This point, which actually need not be in the center of the plot, is called an attractor. If, on the other hand, the trajectory is spiraling in an outward direction, counter-clockwise or clockwise, the fixed point is said to be unstable and the point is called a repeller. A saddle point, in two dimensions, combines both features mentioned above. It separates one solution that is unstable from one solution that is stable. It is a special unstable point since if the system starts at this point and is allowed to evolve it will likely go somewhere else in the phase plot rather than stay in the region of the saddle point.

When the system of equations is second order a variable substitution is used to convert it into a system of first order equations. For example, if the equation is $\ddot{z}(t) = ay(t) + c$, it can be replaced with a set of equations such as; $\dot{w}(t) = u(t)$ and $\dot{u}(t) = ay(t) + c$, since $\dot{u}(t) = \ddot{z}(t)$. Thus by substituting a variable for the first derivative of another variable the resulting set of equations are all first order, and most existing numerical methods can be used to integrate the system.

1.2.3 Numerical Integration

Burden and Faires[30] explain the general concepts of numerical integration by starting with the basic method called numerical quadrature. Here $\int_a^b f(x)dx$ is replaced by a sum,

$$\sum_{i=0}^{n} a_i f(x_i), \qquad [1.21]$$

where the coefficients a_i are chosen to weight the function $f(x_i)$ such that the result produces a correct approximation of the integral. Burden and Faires[30] mention two examples of numerical quadrature with equally spaced nodes, sample points or evaluation points. These are the well known Trapezoidal rule and Simpson's rule.

1.2.3.1 Types

The formula for the Trapezoidal rule is,

$$\int_a^b f(x)dx = \frac{h}{2}[f(x_0) + f(x_1)] - \frac{h^3}{12}f^{(2)}(\xi). \qquad [1.22]$$

Where $h = x_1 - x_0$, the two points chosen on the x interval and $x_0 < \xi < x_1$. The overall result is a shape that looks like a trapezoid and thus the reason for the name.

Simpson's rule has better error correction, uses three points on the x interval and is given by

$$\int_{x_0}^{x_2} f(x)dx = \frac{h}{3}[f(x_0) + 4f(x_1) + f(x_2)] - \frac{h^5}{90}f^{(4)}(\xi). \qquad [1.23]$$

Where $h = x_2 - x_1 = x_1 - x_0$, the equally spaced points on the x interval, $(x_2 - x_1)^5 - (x_0 - x_1)^5 = 2h^5$ and $x_0 < \xi < x_2$. Since the error term is the fourth derivative Simpson's rule gives exact results for any polynomial of degree three or less.

By definition the Trapezoidal rule has a degree of precision of one while Simpson's rule has a degree of precision of three. Neither of these two methods are considered

to be good methods for large intervals, especially the Trapezoidal rule. Polynomials of large degree oscillate and thus large intervals are a problem. The precision can be improved by using subintervals. The large intervals are divided into subintervals, and this procedure is called Composite Integration. The Composite Simpson's rule for $n = 2m$ subintervals of $[a, b]$ is,

$$\int_a^b f(x)dx = \frac{h}{3}[f(a) + 2\sum_{j=1}^{m-1} f(x_{2j}) + 4\sum_{j=1}^{m} f(x_{2j-1}) + f(b)] - \frac{(b-a)}{180}h^4 f^{(4)}(\mu). \qquad [1.24]$$

Where $a = x_0, x_1, \ldots < x_n = b$, $h = (b-a)/n$ and $x_j = x_0 + jh$ for each $j = 0, 1, \ldots, n$ and $\mu \in [a, b]$.

Burden and Faires[30] state that where 20 subintervals give an acceptable result for Simpson's rule, even 360 subintervals do not give an acceptable result for the Trapezoidal rule. There are other changes that can be made to the Trapezoidal rule to improve its results, but Simpson's rule is generally faster and more efficient than the Trapezoidal rule.

This leads to the obvious idea that the interval should be changed to fit the requirements of the function being integrated. Since the process has to adapt to the conditions of the function, it is called Adaptive Quadrature. Burden and Faires[30] base their discussion on the Composite Simpson's rule. The most important part of this procedure is to decide when the result is close enough to stop integration. This is done by a procedure for error analysis, outlined by Burden and Faires[30]. Therefore the error tolerance is set and the error is calculated for a subinterval. If the error is less than the allowed tolerance the routine goes to the next subinterval and integrates. If the error is greater than the allowed tolerance the subinterval is divided into a smaller subinterval (in fact it is halved) and integration is tried again. This is is continued

until the procedure passes the tolerance test or fails a minimum step size requirement.

The next improvement is to choose the approximating functions precisely and choose the coefficients for the approximating functions correctly. One such method is Gaussian quadrature, where orthogonal functions are used to approximate the sample function. The integral of the convolution of two orthogonal functions is zero, $\int_{-\infty}^{+\infty} \phi_1 \phi_2 = 0$. Various polynomials fitting these requirements have been tabulated, such as the Legendre polynomials, and thus by using a basis set of such functions another function can be approximated in an efficient manner.

Initial-value problems, choosing a starting value for velocity, position or concentration for example, are common in physics and chemistry. There are various methods to solve these problems, and the Runge-Kutta fourth order method is explored here. The algorithm is usually expressed as a set of difference equations,

$$\begin{aligned} w_0 &\equiv \alpha, \\ k_1 &\equiv h f(t_i, w_i), \\ k_2 &\equiv h f(t_i + \frac{h}{2}, w_i + \frac{1}{2}k_1), \\ k_3 &\equiv h f(t_i + \frac{h}{2}, w_i + \frac{1}{2}k_2), \\ k_4 &\equiv h f(t_{i+1}, w_i + k_3), \\ \text{where } \quad w_{i+1} &\equiv w_i + \frac{1}{6}(k_1 + 2k_2 + 2k_3 + k_4), \end{aligned} \qquad [1.25]$$

for each $i = 0, 1, \ldots, N-1$. Therefore with $i = 0$ $w_1 = w_0 + 1/6(k_1 + 2k_2 + 2k_3 + k_4)$ and each w_i is calculated recursively.

The final methods to be discussed are both used to solve initial-value problems, and are special methods called predictor-corrector. This means that a solution is predicted (by one method) and compared to the calculated, if these differ by more that a set amount, the step size is decreased. It is then corrected by another method.

Also the first step is usually to calculate the starting values of the integration. In some cases the initial step is done using a fourth-order one step Runge-Kutta method and the subsequent steps, calculating the approximation, could be done using the Adams-Bashforth method to get

$$w_4^{(0)} = w_3 + \frac{h}{24}[55f(t_3, w_3) - 59f(t_2, w_2) + 37f(t_1, w_1) - 9f(t_0, w_0)]. \qquad [1.26]$$

This is then corrected with a three step Adams-Moulton method,

$$w_4^{(1)} = w_3 + \frac{h}{24}[9f(t_4, w_4^{(0)}) + 19f(t_3, w_3) - 5f(t_2, w_2) + f(t_1, w_1)]. \qquad [1.27]$$

This result is then used as predictor and the process is repeated until the approximation gives a result within the chosen error tolerance. The last method is the Gear predictor-corrector method which is described in the section on stiff equations.

1.2.3.2 Stability

There are two concerns with the stability of a solution to a set of differential equations. It is expected that the integration will be consistent and convergent. The solution is consistent if the sum of the local errors approaches zero. The solution is said to be convergent if the sum of the absolute value of the difference of the exact and calculated values of the integral approach zero. Thus the solution is expected to be convergent if the solution approaches the exact value as the step size goes to zero. Since there are errors caused by round-off errors of the computer's significant digits there is no ideal convergence. The solution is stated to be stable if the initial conditions are varied slightly and the results vary slightly. Ultimately, consistency and convergence in a multistep method are dependent upon the round-off stability.

1.2.3.3 Stiff Equations

One of the first systems to be evaluated was a set of differential equations modeling the motion of a spring and a mass. The springs were stiff and therefore had large

spring constants, and the differential equations were difficult to solve. Thus, Stiff equations are hard to integrate and chemical kinetics and dynamics problems usually fall under this heading, especially nonlinear systems. Gear has developed a predictor-corrector method for dealing with such equations. The reader is referred to Gear's book[31] for a complete discussion of the method. Gear has stated that stability is still the main concern when integrating a set of stiff equations especially in a chaotic regime. In fact, Shampine and Gear[32] wrote a paper discussing how to identify and solve stiff equations. They state that it is not the solutions that are stiff but rather the equations themselves. Under some circumstances it might be better to find some manner in which to make the equations nonstiff and then use nonstiff methods to solve them. As expected from a spring with a large spring constant stiff systems are expected to be very stable[33] and this is why their solution is difficult.

Shampine and Gear[32] also point out that accuracy and stability are related. Accuracy deals with local errors, and these are kept as small as possible by decreasing the step size. Stability has to do with stopping the growth of errors as iteration process of integration takes place. This is sometimes best accomplished by increasing the step size. Thus a trade-off between the two must be made through error analysis.

Gear[33] has stated that there are still some very difficult problems to be solved to ensure that integration is done correctly. The end-user must check solutions by using several integrators.

1.2.4 Chaos

1.2.4.1 Determination of Chaos

A system of equations is considered to be chaotic when the response of the system is extremely sensitive to initial conditions. Bergé, Pomeau, and Vidal[1] have discussed

this for dynamical systems but their discussion is valid for kinetic systems as well since both can be expressed using systems of nonlinear differential equations. The Lyapunov exponent (λ), named for the mathematician that developed it, is a measure of how fast neighboring trajectories are diverging. In fact when the neighboring trajectories are diverging in an exponential manner the system is considered to be chaotic and if the Lyapunov exponent is positive than the system is considered to be chaotic. The Lyapunov exponent, as calculated in this work, is coordinate dependent and is the slope of the log of the algebraic equation for determining the distance between two points in a plane given by,

$$\lambda = \text{slope of } \left[\log_{10}\left(\sqrt{(x_1 - x_2)^2 + (y_1 - y_2)^2}\right) \textit{ versus } \text{time}\right]. \qquad [1.28]$$

The plane in this case is the phase plot of the system. Since $\log_{10}(dist)$, in this work, is coordinate dependent it will vary in a cyclic manner with time and when the slope is positive the system is chaotic.

1.2.4.2 Routes to Chaos

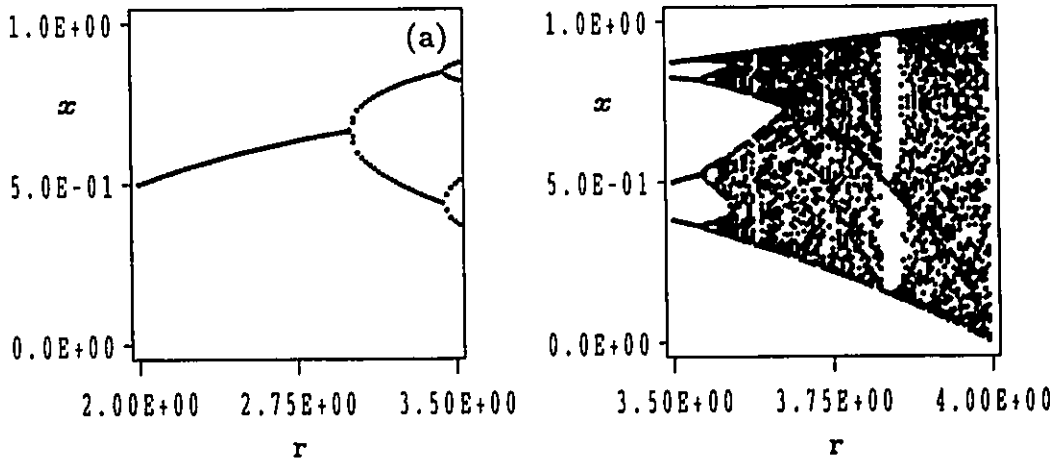

Figure 1.1 Plot of the logistic map for r from 2.0 to 4.0, $\Delta r = 0.02$ for r from 2.00 to 3.5, and $\Delta r = 0.005$ for r from 3.5 to 4.0. The last four iterations are plotted for (a) and the last 50 iterations are plotted for (b).

As discussed by Thompson and Stewart[2] there are many routes to chaos, but for the work outlined in this manuscript the period-doubling route to chaos is as useful an example as any. The simple logistic equation ($x_{n+1} = rx_n(1 - x_n)$) is used here to explore this idea, where x_n is the nth crossing of the trajectory through a section.

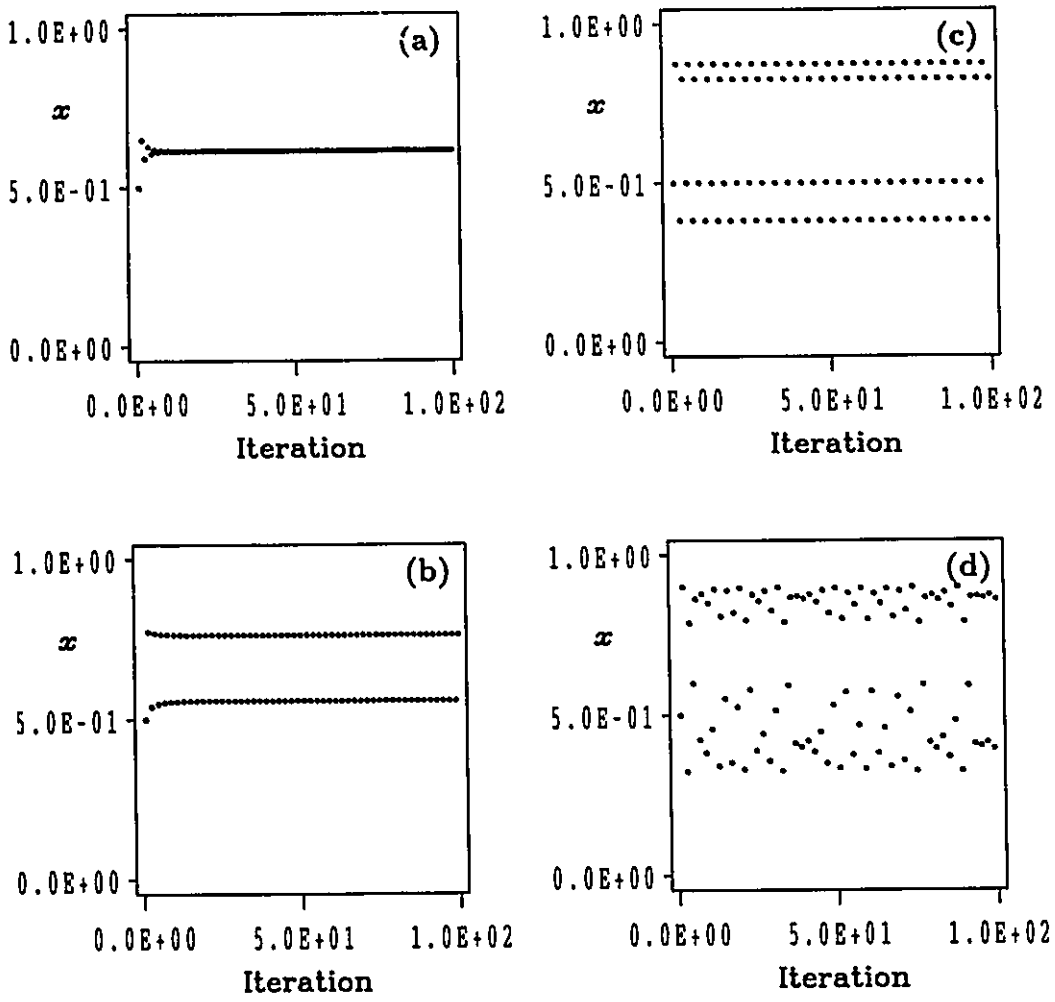

Figure 1.2 Plots of the nth trajectory crossing for 0 to 100 iterations of the equation. r = 2.6 to 3.6. (a) is for r = 2.6, one state; (b) is for r = 3.1, two states; (c) is for r = 3.5, 4 states; and (d) is for r = 3.6, and a chaotic response.

The logistic map is a simple mapping of the value of x to the r value. For Figures 1.2 to 1.5 the calculation was done for 1100 iterations and only the first 100 iterations

are usually shown to illustrate the fact that the iterative equation approaches its final number after several iterations. However, for the general case of Figure 1.1(a), only 4 data points are plotted of the 100 calculated (iterations), while r is only changed (hereafter referred to by using Δr) by 0.02. For Figure 1.1(b) the last 50 points of the calculated 100 points were plotted with a smaller step size of $\Delta r = 0.005$. Thus, Figure 1.1 is a picture of the bifurcation, or doubling, route to chaos. Figure 1.1 shows how the choice for x bifurcates as r is increased until there are a large number of choices. Notice, however, that there are windows of periodic behaviour in the chaotic regime, as discussed later.

Figure 1.2 is of a range of r values from 2.6 (period one) to 3.6 (chaotic). Figure 1.2(a) is period one and when r is changed to slightly greater than 3.0 a doubling occurs and x has two states it can occupy, such as shown in Figure 1.2(b) for $r = 3.1$ (these states are referred to as period two). If r is increased further another bifurcation occurs at $r > 3.4$ which is illustrated in Figure 1.2(c) where $r = 3.5$, and there are four states for x. When $r > 3.596$ the actual values that x can assume become numerous, as shown in Figure 1.2(d).

Although Figure 1.2(d) was for a case of $r = 3.6$, Figure 1.3 is for a smaller value of r, $r = 3.550$, but the plot has 8 states. Figure 1.3(a) is a fullscale plot and it is not easy to identify all of the eight distinct states. Figures 1.(b), (c), and (d) are each expansions of the vertical axis with $\Delta x = 0.1$, but it is easy to identify that there are eight separate states. Overall in Figures 1.2 and 1.3 it is possible to observe that for values of r from 2.6 to 3.6 x goes from period 1, 2, 4, 8, to chaotic, thus showing a doubling route to chaos.

Although the value of x is in general chaotic for $r > 3.6$ there are "windows" of periodic behaviour. This is illustrated in Figure 1.4 with r values increasing from

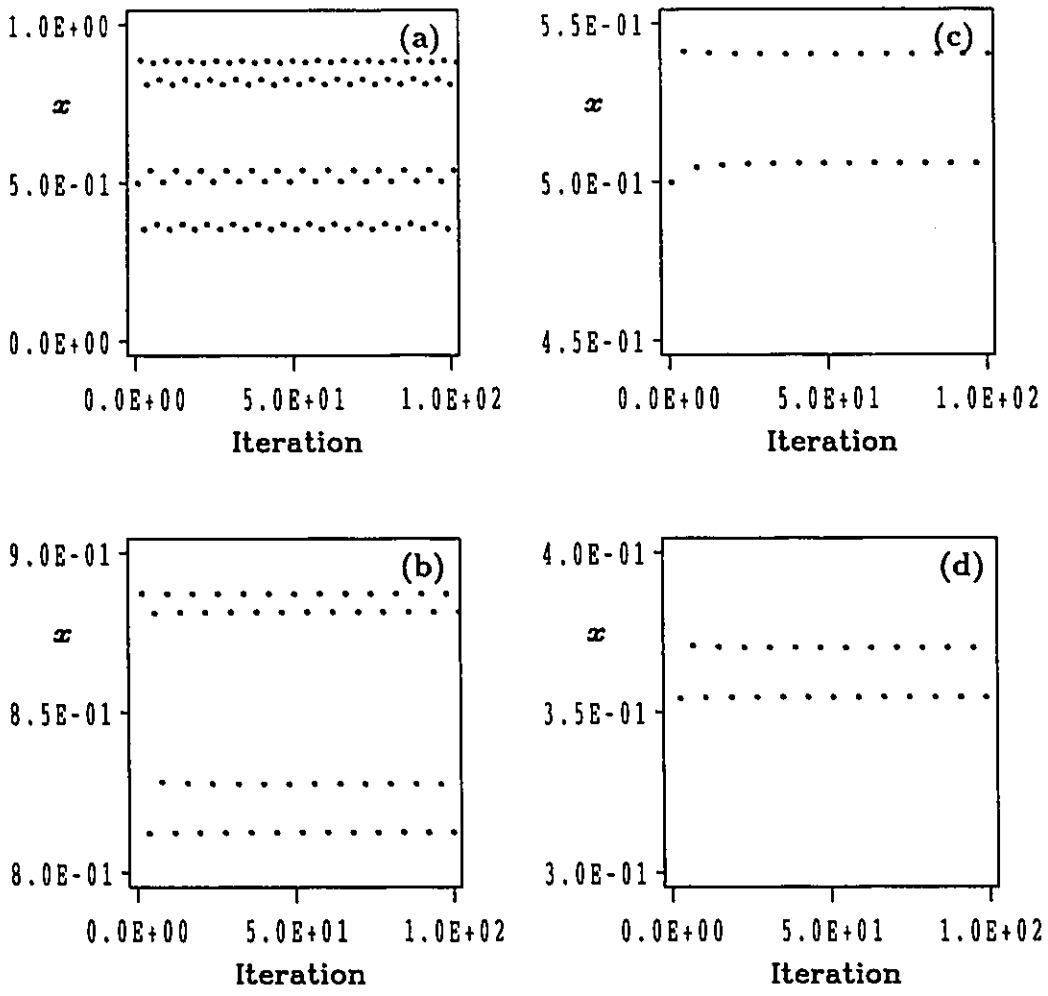

Figure 1.3 Plots of the n^{th} trajectory crossing for 0 to 100 iterations of the equation. $r = 3.550$. (a) is the fullscale plot with 8 states (which is not obvious), (b) is an expansion of the top part of the fullscale plot and shows 4 states, (c) is an expansion of middle section of (a) showing 2 states, and (d) is an expansion of the bottom section of (a) showing 2 states. The total for the expansions is eight states.

3.633 to 3.801. In Figure 1.4(a) $r = 3.633$, and the window has 6 states, while in Figure 1.4(b) with $r = 3.702$ there are 7 states. In Figure 1.4(c) $r = 3.739$ with 5 states, and Figure 1.4(d) $r = 3.801$, with 8 states. Note that even though Figures 1.4(d) and 1.3(a) are both 8 states, the individual state values are not the same. Thus the multiplicity of the states may be the same but this does not guarantee that the actual state values will be identical or even similar.

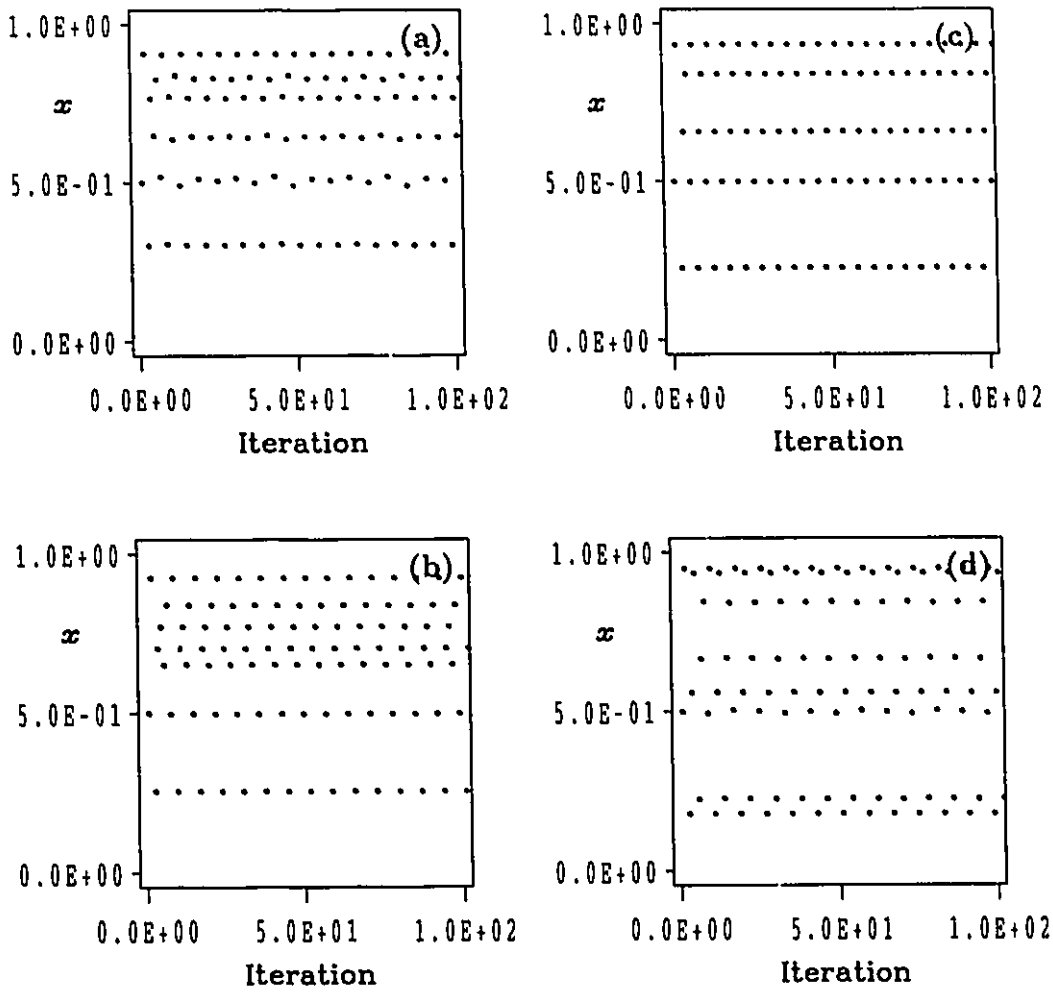

Figure 1.4 Plots of the n^{th} trajectory crossing for 0 to 100 iterations of the equation. $r = 3.633$ to 3.801 resulting in periodic windows in an otherwise chaotic response. (a) is for $r = 3.633$, 6 states; (b) is for $r = 3.702$, 7 states; (c) is for $r = 3.739$, 5 states; and (d) is for $r = 3.801$, with 8 states.

Figure 1.5 is for the case of $r = 3.830$, which results in a period 3 "window". As was stated at the beginning of this subsection, x was calculated for 1100 iterations of the logistic equation. Figure 1.5(a) is for the first 100 iterations while (b) is for the last 100 iterations. Notice that the values of x for each state have remained the same. However, notice that in Figure 1.2(a) it took several iterations of the logistic equation, with $r = 2.6$, for x to stabilise on the single state. In Figure 1.2(b) it also took several iterations for the system to stabilise on two states. The case of $r = 3.961$

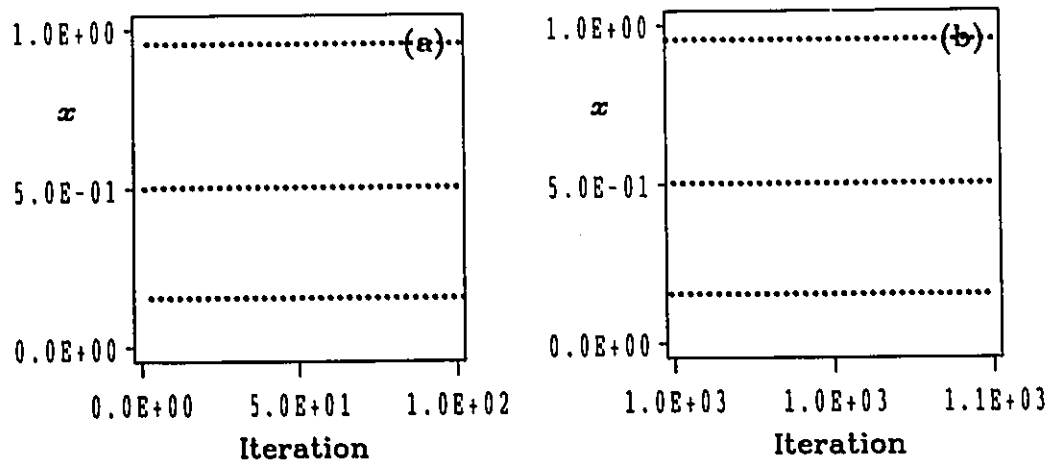

Figure 1.5 Plots of the n^{th} trajectory crossing for $r = 3.830$ which results in a period 3 window in the chaotic response area. (a) is for 0 to 100 iterations of the equation, (b) is for 1000 to 1100 iterations of the equation.

is not shown but it is period 4 with different state values than the previous case of $r = 3.500$.

If different parts of the logistic map for r between 3.0 and 4.0 are expanded and observed in detail the overall initial shape of the mapping can still be seen. In other words, the logistic map displays self-similarity if expanded[2]. What has been realized through this exercise is that although the system maybe become chaotic via a doubling route it does not mean that the system is completely random. There is a range of values that the system will have. Thus chaos is bounded within a determinable set of values. Also note that when the system is in a chaotic regime there can be windows of periodicity and the system may be bumped from these well-behaved "windows" into a chaotic response with a very small change of r. This is where the "butterfly" effect can be seen. In other words, if a weather system is chaotic, the beating of the wings of a butterfly in the Amazon jungle may cause a hurricane to occur several months later in the northern hemisphere. This is an illustration of how sensitive a chaotic system is to initial conditions.

1.2.5 Nonlinear Dynamic Systems

1.2.5.1 The Pendulum

A linearized equation is usually used to discuss basic harmonic oscillators. That is an equation of motion of the type

$$\ddot{x} = -C\dot{x} - kx. \qquad [1.29]$$

This is a general equation where C is the damping coefficient, k is related to the natural frequency of the system, the force constant, no forcing term has been included and the derivative is, of course, with respect to time. The nonlinear (pendulum) system with forcing is modeled[2,38] using

$$\ddot{x} = -C\dot{x} - k\sin(x) + F\sin(t). \qquad [1.30]$$

The examples in this section are for the unforced (F= 0) and undamped (C= 0) case. The calculations were done using a step size of 2.00×10^{-2} for 2000 steps which is 40 dimensionless time units.

Figure 1.6 illustrates the phase (x) *versus* t for a short period of time as well as the usual phase plot of $\dot{x}$ *versus* x. The linear case is shown in Figures 1.6(a) and (b) while the nonlinear case is shown in Figures 1.6(c) and (d) for no forcing and no damping. Notice that although both of the phase plots are distinctly different for a linear and nonlinear system the plots of phase *versus* time are similar. The phase *versus* time plots are sinusoidal but the nonlinear system has a longer period than does the linear system even though the conditions are the same. Notice that Figure 1.6(a) has a waveform with seven negative peaks while Figure 1.6(c) has a waveform with six negative peaks for 40 time units. In Figure 1.6(b) the waveform is circular while the waveform in Figure 1.6(d) is definitely elliptical.

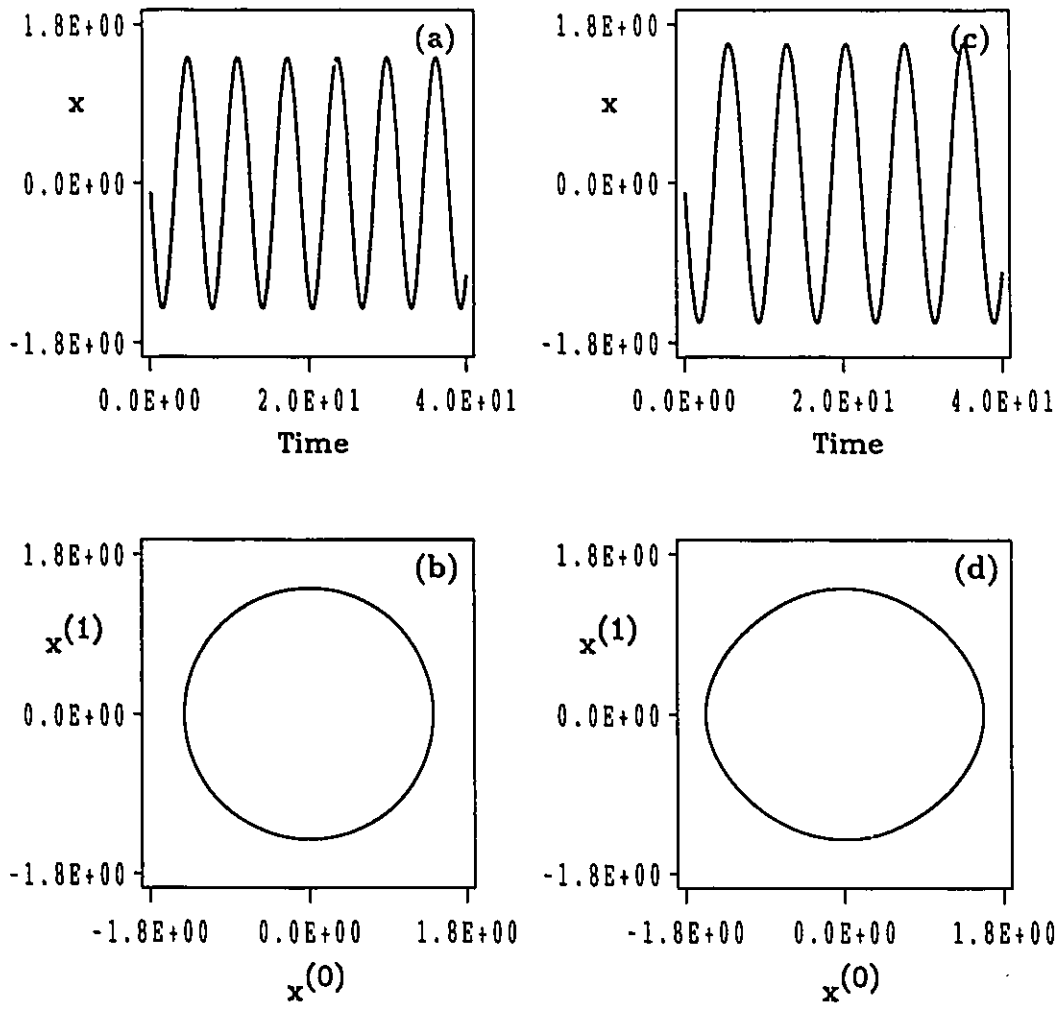

Figure 1.6 Plot of unforced undamped linear pendulum (left column) and nonlinear pendulum (right column). Figures (a) and (c) are plots of the phase with respect to time while (b) and (d) are phase plots (as defined in 1.2.2).

Figure 1.7 is the case of the above nonlinear system with a damping coefficient, C= 10^{-1}, and therefore the signal decays very fast (see Figure 1.7(a)) over time and comes to rest eventually at zero. This is further illustrated in the phase diagram of Figure 1.7(b), with the trajectory spiraling in towards (0,0). Thus the time plots and the phase plots give complementary information but the phase plot gives information that can not be realized in the time plot alone.

In Figure 1.8 the nonlinear pendulum is presented for a case having x(0)=3.72,

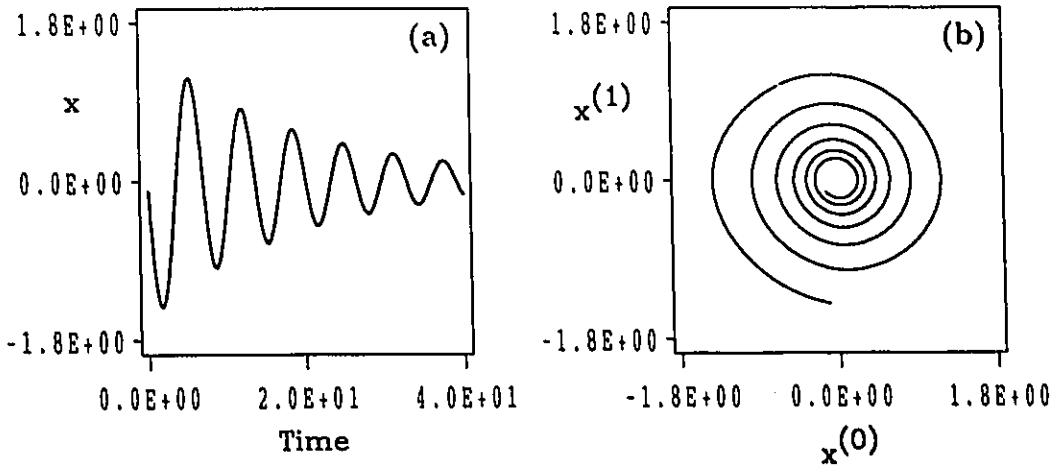

Figure 1.7 Nonlinear unforced pendulum system with damping. Figure (a) is a plot of the phase *versus* time while (b) is the usual phase plot.

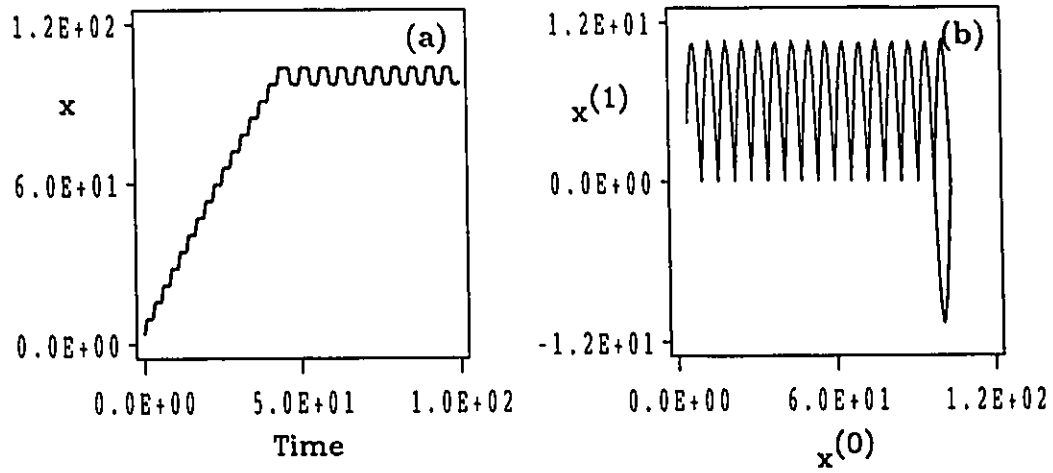

Figure 1.8 Nonlinear pendulum started with a non-zero velocity and non-zero phase. Figure (a) is the phase *versus* time plot while (b) is the phase plot, $x^{(1)}$–x.

$x^{(1)}(0) = 3.00$, k=27.66, $C=10^{-6}$ with a step size of 2.00×10^{-2} for 5000 steps (total of 100 time units). The pendulum is started with some kinetic energy. The damped pendulum is started at a non-zero position and with non-zero velocity and is then allowed to evolve. In Figure 1.8(a) the plot of x(t) steps up (rotation is taking place), and when enough energy has been lost the system begins to librate. (The pendulum swings from the top left position down through the x=0 position and up to an almost

vertical position, on the right, never actually rotating). In other words, the stepping motion in the x(t) plot stops and x(t) plateaus. This is further illustrated in the phase plot, Figure 1.8(b), where semiellipses are drawn until the plateauing occurs in the x(t) plot, then the system trajectory forms a completed ellipse. This is then where the trajectory spends its time. If the pendulum is left long enough the spiraling in effect of the damping will become noticeable.

1.2.5.2 The Morse Oscillator

The Morse oscillator has been used to model diatomics and diatomic fragments of polyatomics. Although the Morse potential is known to be deficient for energies close to the dissociation energy[15], it is often used in studies of reaction dynamics because of its simplicity. The effect of external forces (such as a laser field) on the Morse oscillator may be modeled by the addition of forcing and damping terms[8]. In this manuscript aspects of the classical mechanics of the weakly forced and weakly damped Morse oscillator are considered.

For a Morse oscillator the potential[5] energy is

$$V = D(1 - e^{-ax})^2 \qquad [1.31]$$

For the unforced and undamped Morse oscillator, the total energy, which is the sum of the kinetic and potential energies, is constant. The equation of motion of the forced and damped Morse oscillator used here is

$$\ddot{x} = -2aD\ (e^{-ax} - (e^{-ax})^2) - C\dot{x} + (1 - \alpha x)e^{-\alpha x}F\sin(t) \qquad [1.32]$$

Here x is the phase of the Morse oscillator, which corresponds to the bond displacement of the diatomic or diatomic fragment, and the derivative is with respect to time, for which the units are arbitrary (note that the forcing frequency is unity). For simplicity, the Morse spectroscopic term a and the dissociation energy D are chosen to be 1.0. The parameters C (the damping coefficient), F (the forcing coefficient) and α (a realistic scaling factor for the forcing term) must also be specified and these choices are discussed in the appropriate section. The term $(1 - \alpha x)e^{-\alpha x}$ allows for a realistic application of the forcing term including the dipole moment. As x increases there is less interaction of the forcing (monochromatic light such as a laser) with the diatomic. For F = 0, this dynamical system is a point attractor[1], and the asymptotic

dynamics is uninteresting as the total energy, E(t), tends to zero. Time plots of E(t) and higher-order phase plots for different values of F and E(0) are presented in the next chapter. The initial total energy, E(0), is specified as a decimal value, or %, of the dissociation energy, *i.e.* 0.99 or 99%.

Equation [1.32] is treated as two coupled nonlinear differential equations[1,2] for x and $\dot{x}$. Once x(0) and $\dot{x}(0)$ are specified, it is straightforward to obtain x(t), $\dot{x}(t)$ and $x^{(n)}(t)$ at any future time. For simplicity x(0) = 0.0 is chosen and, having specified E(0), $x^{(1)}(0)$ is solved for, choosing the negative root. Here $^{(n)}$ denotes the nth derivative of x with respect to time and this notation is used for all derivatives of x in this work. Note that all of the equations for the higher derivatives ($n > 2$) are analytic equations. In other words, they are derived from the equation of motion, one derivative at a time up to the n^{th} derivative. Thus, only the errors of the integration from $x^{(2)}$ to $x^{(1)}$ and for $x^{(1)}$ to $x^{(0)}$ (x) are involved in this process. The derivatives are *not* done numerically.

The nonforced Morse oscillator exhibits well-behaved motion. In other words, the trajectory (as seen in Figure 1.9) repeats in a cyclic manner (period one). In Figure 1.9(a) a Morse potential has been drawn with the energy levels corresponding to an initial total energy of 10%, 90%, and 99% emphasized by horizontal lines. The total displacement noted in Figure 1.9(a) is the same as the distance that corresponds to the maximum displacement of the trajectories plotted in Figure 1.9(b). Note that as the total initial energy increases the trajectory plotted in the usual phase plot becomes more distorted. Thus, the closer to dissociation the system gets the less it behaves like a harmonic oscillator. A harmonic system (cosine or sine function for example) would result in a symmetric trajectory and a circular phase plot (this is discussed further in Appendix B). Figure 1.10 is plotted in such a manner.

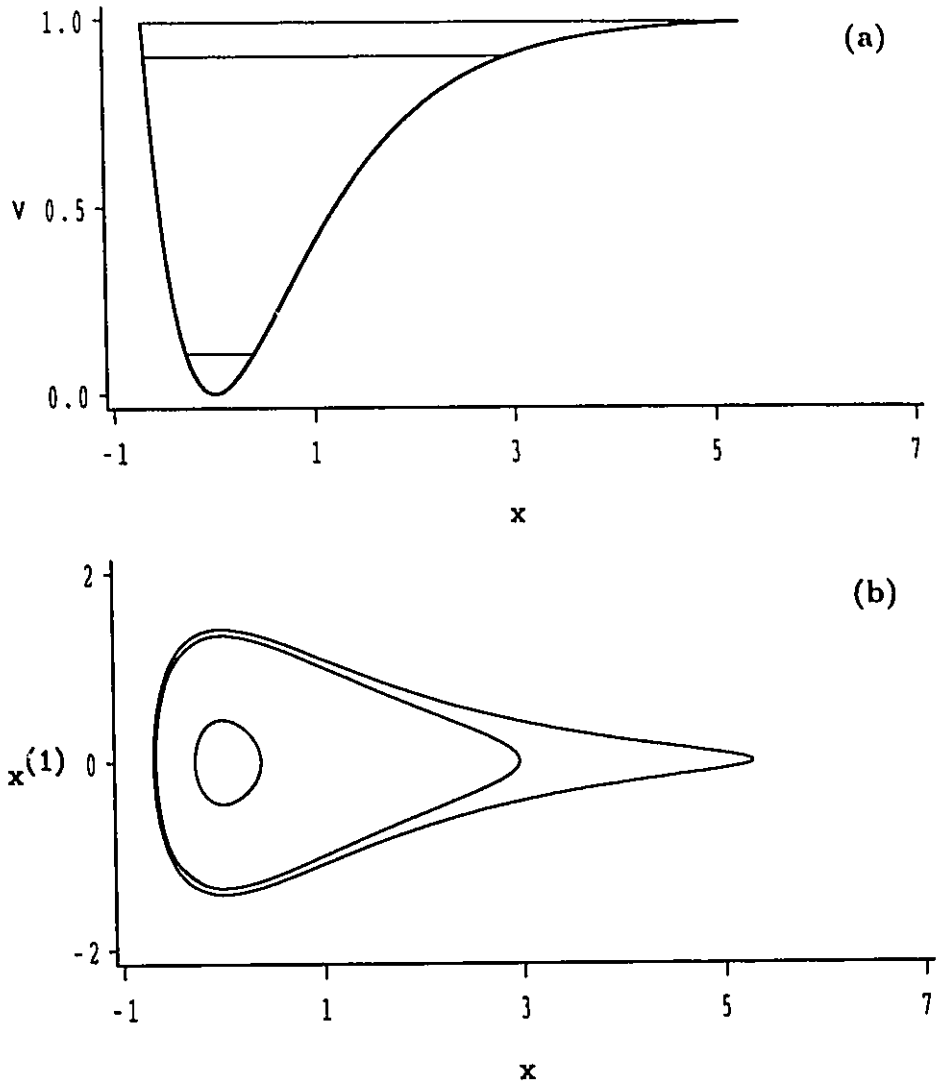

Figure 1.9 Morse potential and phase plot. Energy levels are drawn in for an initial total energy of 10%, 90%, and 99% of dissociation. Notice that the x axes for both (a) and (b) are the same and thus the extent of the level in (a) is the same as the maximum extent of the trajectory.

In Figure 1.10(a) the trajectory that is the smallest is for an initial total energy of 0.1%. The next largest is for 1.0% while the largest is for 10%. In Figure 1.10(b) the 0.1% data is repeated with an expansion of the x and y axes scale. Even at an initial total energy of only 0.1% the plot is not circular and visibly deviates from the phase plot of a harmonic function.

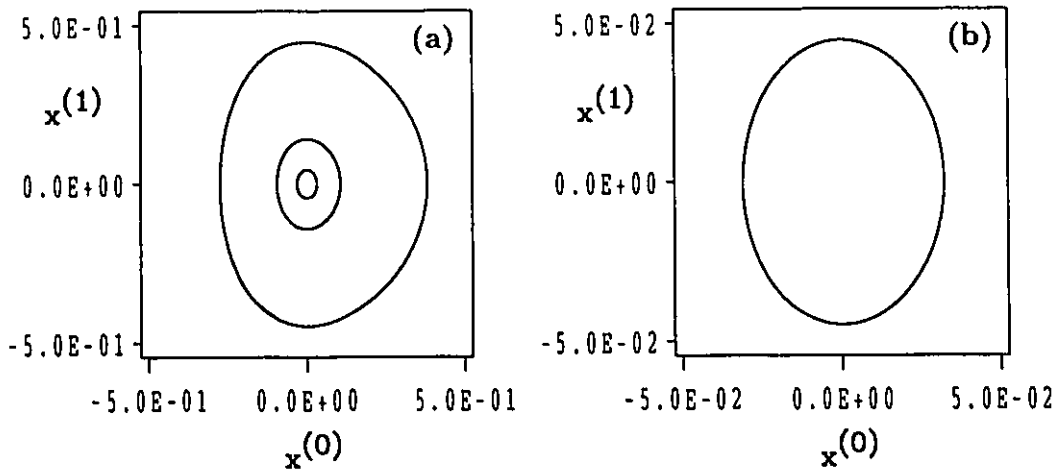

Figure 1.10 Phase plots for an initial total energy of 10%, 1.0%, and 0.1% of dissociation.Figure (a) has an initial total energy of 10% (the largest trajectory), 1.0%, and 0.1% (the smallest). Figure (b) is an expanded plot of only the 0.1% data, notice that the axes are an order of magnitude smaller than in (a).

The Morse potential is used because there exist analytic functions to determine bound energy levels, even though it is generally known that the function is not correct when it approaches dissociation. (The function fails to go towards dissociation fast enough.) These bound levels are discussed elsewhere in this work, in the section that deals with the general ideas of the Morse oscillator in the introduction section of this chapter.

1.2.5.3 Summary

It has been shown in the previous plots that nonlinear dynamic systems are quite different from linear dynamic systems. The usual phase plots of linear and nonlinear dynamical systems are also distinctly different, even before damping or forcing terms are added. It has also been shown that the usual phase plot allows the visualization of unobservable information that is present in the times series. It will be shown in later sections that the higher-ordered phase plots also give additional information that is not present in the existing methods of plotting the data.

1.2.6 Nonlinear Kinetic Systems

Hunt, Hunt, and Ross[34] have outlined, in a very clear manner, the need for chemists to understand nonlinear behaviour of chemical systems. They discuss a variety of interesting behaviour of the system from the formation of multiple steady states, to relaxation oscillations, to quasi-periodic oscillations and even to complex oscillations consisting of large and small amplitude peaks with bursts of high frequency oscillations embedded in the regular signal. They describe how these processes are possible because the chemical systems are far from equilibrium. Hunt *et al*[34] go on to review the Belousov-Zhabotinskii (BZ) reaction and state that the "Brussels school" (Brusselator) of Prigogine, Glansdorff, Nicolis, and other collaborators showed that oscillating chemical reactions are consistent with the thermodynamics of closed systems.

Samardzija, Greller, and Wasserman[35] have described how nonlinear ordinary differential equations that are used to represent dynamic systems can be transformed to represent kinetic studies. Samardzija *et al*[35] has shown how the usual dynamic equations for the Duffing oscillator can be transformed to include kinetic information and mass balance equations (mass-action chemical schemes). They even take this to the extreme and show how it is possible to relate the usual RLC (resistance-inductance-capacitance) description of a forced damped harmonic oscillator to a kinetic scheme. They believe that systems of equations that are centered at zero of an X-Y plane can be shifted to be centered on positive values (negative concentrations are considered to be non-realistic) with little distortion of the concentrations. In fact the distortions may cause a misdirection of the investigation since it is often a small change, in concentration, that causes the effect that is being investigated. However, the study[35] is useful for pointing out that nonlinear equations can be and are used to present both the kinetics and dynamics of a chemical system.

Closer to the ideas used in this work are those presented by Gray *et al*[23] which discussed oscillatory ignition and cool flames of oxidation of acetaldehyde in a continuously stirred reactor. That work indicates that the experimental system could go from a well-behaved case to an oscillatory case depending upon the rate of flow of the reactants into the system and upon the initial temperature of the system. Cook, Gray, Knapp, and Scott[24] expanded on these ideas to discuss a set of equations for autocatalysis reactions. A reduced set of equations was used, and they exhibited bifurcations as well as oscillations. This was presented in an experimental way by Gray and Scott[25] for the stoichiometric ignition of $2H_2 + O_2$. The temperature of the system was monitored and went through a bifurcation process as the initial temperature of the system was increased. The apparatus was at a specific temperature but the measured temperature of the system had oscillatory behaviour and the frequency of this behaviour increased depending upon the initial temperature of the system. Gray and Kay[26] showed how such complex behaviour could be modeled with relatively simple equations, using a single species, A, a catalyst, B, and an equation for the temperature, T. Thermal feedback is the main feature of the theories presented, and the basic equations are outlined below. It is a nonisothermal scheme for a closed system, that is T varies and p decays, but $p + a + b + c =$ constant, where p, a, b, and c are concentrations. The scheme is

$$\mathrm{P} \xrightarrow{k_0} \mathrm{A} \qquad \text{responsive to temperature}$$

$$\mathrm{A} + 2\mathrm{B} \xrightarrow{k_1} 3\mathrm{B} \qquad \text{autocatalytic}$$

$$\mathrm{B} \xrightarrow{k_2} \mathrm{C} \qquad \text{exothermic decay with } (-\Delta H) = Q$$

$$\mathrm{A} \xrightarrow{k_3} \mathrm{B} \qquad \text{uncatalyzed}$$

The rate equations are

$$\frac{dp}{dt} = -k_0 p \qquad \text{with } k_0 \propto \exp(-E/RT)$$
$$\frac{da}{dt} = k_0 p - k_1 a b^2 - k_3 a$$
$$\frac{db}{dt} = k_1 a b^2 + k_3 a - k_2 b$$
$$\sigma c_v \frac{dT}{dt} = VQk_2 b - hS(T - T_a)$$

where V is the reactor volume,

σ is the molar density of the mixture,

c_v is the molar heat capacity of the mixture,

h is the surface heat transfer coefficient,

S is the surface area of the reactor, and

T_a is temperature of the surroundings.

The dimensionless form of the rate equations with three variables (α, β, and θ) and four parameters (μ, κ, ζ, and χ) are,

$$\dot{\alpha} = \frac{d\alpha}{d\tau} = \mu(1 + \theta) - \alpha\beta^2 - \kappa\alpha \qquad \text{species A}$$
$$\dot{\beta} = \frac{d\beta}{d\tau} = \alpha\beta^2 + \kappa\alpha - \beta \qquad \text{catalyst B}$$
$$\dot{\theta} = \frac{d\theta}{d\tau} = \zeta\beta - \chi\theta \qquad \text{temperature}$$

where $\alpha = a/a_{rf}$ and $\beta = b/a_{rf}$ are reduced concentration,

$\tau = k_1 a_{rf}^2 t = k_2 t$, the reduced time,

$a_{rf} = (k_2/k_1)^{1/2}$,

$\theta = (T - T_a)/(RT_a^2/E)$, the reduced temperature excess,

$\mu = (k_0/k_2)(p_0/a_{rf})$,

$\kappa = k_3/k_2$,

$\chi = (hS/V\sigma c_v k_2)$, the reduced heat-exchange coefficient, and

$\zeta = \frac{Qa_{rf}}{\sigma c_v (RT^2/E)}$, the intensity of thermal feedback.

Gray and Kay[26] show plots of β *versus* μ, and there are oscillations in the amplitude of the β variable (reduced concentration of species B). More importantly they show how a plot of β *versus* time can go from being periodic (period one limit cycle) to a chaotic time sequence and even a period three limit cycle. Gray and Kay have also plotted the reduced concentrations from the above mentioned cases and the chaotic times series produces a strange attractor in the plane of α *versus* β. Thus, in this kinetic scheme, with various pathways, there can be several different types of behaviour but all are dependent upon thermal feedback. By reducing the chemistry to a few steps a complex system has been modeled with some loss of information, but the general topology of the behaviour is relatively preserved, and important information on how temperature can affect the behaviour of a chemical system was gained.

Peng, Scott and Showalter[27] and especially Scott, Peng, Tomlin, and Showalter[28] show how the oscillatory behaviour can be pushed through a parameter regime where bifurcation takes place until the system is chaotic, and if the system is pushed further *i.e.* the parameter increased still more the reverse process takes place. In other words, the system goes from chaotic to well-behaved via a reverse bifurcation route. Thus a chemical system may start out well-behaved and then become chaotic, but on the other hand it may start off being chaotic and then become well-behaved. The system may have "islands" of chaotic behaviour in an otherwise well-behaved parameter regime but it may also have "islands" of non-chaotic behaviour in an otherwise chaotic parameter regime.

Therefore nonlinear kinetic studies can exhibit the same behaviour that nonlinear dynamic studies exhibit (*e.g.* "the logistic map" study presented earlier in this work). Once a system of nonlinear ordinary differential equations has been set up the integration and the solution follow the same rules whether the nonlinear ordinary differential equations are modeling nonlinear kinetics or nonlinear dynamics.

2 Higher-Order Phase Plots

2.1 Introduction

Extensive studies of dynamical systems have been done using the $x^{(1)}$ *versus* x phase plot[2,36]. The use of higher derivatives to form higher-order phase plots have been considered for the linearly damped simple pendulum[38]. Also, successive derivatives were calculated by Packard *et al*[39] using a "spline on spline method" but they and Kreul *et al*[40] found that numerical errors were too large after the fourth derivative using "the spline on spline method". This present work calculates the higher derivatives analytically, after the equation of motion is integrated to get x, and $x^{(1)}$. These higher derivatives are then used to form the higher-order phase plots. In this chapter, this is first done for a unforced and undamped situation, then a weakly forced and weakly damped situation and finally for the diatomic HF. There are limitations for these higher-order phase plots and they will be presented later in this work. From the higher derivatives of x higher-order phase plots of $x^{(n)}$ *versus* $x^{(n-1)}$ (in this work written as $x^{(n)}$–$x^{(n-1)}$) can be constructed. For a linear system the higher-order phase plots are essentially identical to the $x^{(1)}$–x phase plot and provide no new information. As shown in the appropriate section in the introduction chapter, the $x^{(1)}$–x phase plot trajectories form single ellipse-shaped structures and the trajectories in the higher-order phase plots, of a linear system, form identical structures.

For a nonlinear system the higher derivatives of x are increasingly sensitive probes of the dynamics as the order increases. For the $x^{(1)}$–x phase plot of the Morse oscillator, trajectories form ellipse-shaped structures that become distorted for energies close to the dissociation energy. It might be expected that for the higher-order phase plots these trajectories would form expanded and perhaps more distorted ellipse-shaped structures. However, a nonlinear system has higher harmonics in the Fourier

expansion of the phase. Consequently, for the higher-order phase plots, these trajectories form complicated structures that are not equivalent to an ellipse. Instead, each is equivalent to a set of overlapping and intersecting ellipse-like structures and the number of ellipse-like structures in each set increases as the order increases. Thus the higher-order phase plots are increasingly intricate as the order increases and some of this intricacy can only be seen if the horizontal and vertical axes are expanded, as discussed later in this work. For the simple pendulum[38] there is a hyperbolic fixed point at $x = \pm\pi$ (the period of rotation) while for the Morse oscillator there is a marginally stable fixed point at $x = \infty$. In both cases these fixed points correspond to the point $(x^{(n)},x^{(n-1)}) = (0,0)$ in each higher-order phase plot.

Higher-order phase plots are used, in this work, to visualize the higher harmonics of the phase, which are essential for complicated and dissociative dynamics. This work focuses on changes in the topology[42] of the higher-order phase space structures as F and E(0), the initial total energy, are varied. The higher-order phase plots will be shown to provide information regarding the dissociation process that is not easily obtained from the usual phase plot. Equation [1.32], of chapter one, is integrated using the well-tested predictor-corrector method of Gear[31] and usually the spline fit of the data is plotted but under certain circumstances the actual data points are plotted at a finite time interval.

2.2 The Unforced and Undamped Morse Oscillator

The use of the Morse function, or potential as it has become to be known, is a useful example to show how additional existing information can be realized using higher-order phase plots. To emphasize this a MacLaurin[41] series expansion of the exponential is used here. Where

$$e^{-x} = 1 - x + x^2/2! - x^3/3! + x^4/4! - x^5/5! + \cdots \sum(-1)^n(x)^n/n!. \qquad [2.1]$$

The Morse potential as stated in equation [1.31], of the chapter one, is modified by setting $a = D = 1$ resulting in $(1 - e^{(-x)})^2$ and for this example, no forcing nor damping is used. Note that the Morse potential stated in the previous line, when expanded has the form $(1 - 2e^{(-x)} + e^{(-2x)}$. The last term, is $e^{(-2x)}$ and the MacLaurin series truncated to x^3 would result in an equation truncated to x^6.

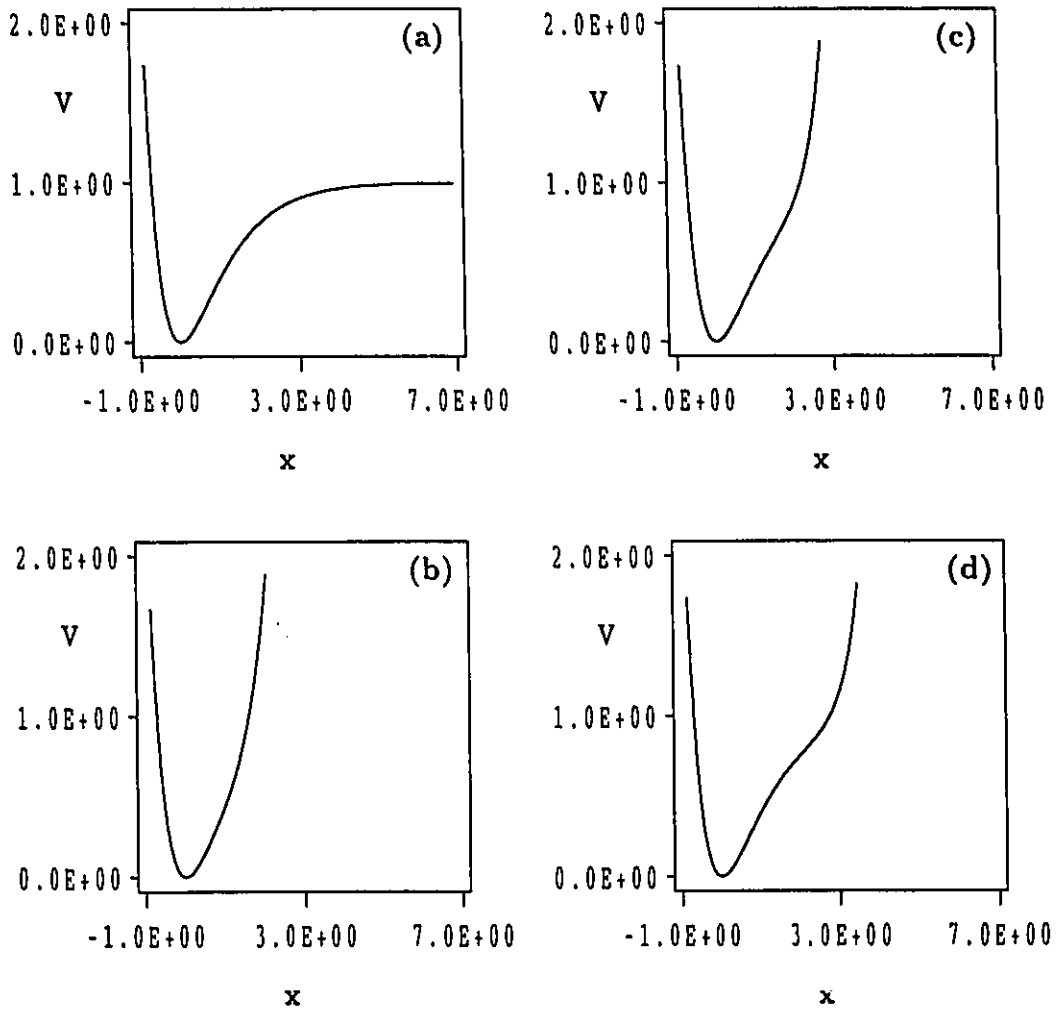

Figure 2.1 Comparison plots of the Morse potential and the MacLaurin series expansion truncated at different odd ordered terms, for the undamped and unforced case. (a) Plot of the Morse potential. The MacLaurin series truncated to x^3 (b), x^5 (c), and x^7 (d). Only the line resulting from a spline fit of the 100 calculated data points is plotted.

The form of the Morse potential is such that the part of the curve that represents

the expansion (x > 0) of the bond (x= $r - r_e$) is a different shape than the part of the curve that represents the compression of the bond (x < 0). In Figure 2.1(a) the left-hand side of the curve does not mimic the right-hand side of the curve. The Morse potential has a single minimum and thus only the odd ordered truncated formulas of the expansion need to be used since the even ordered truncations result in potentials that have two minima. The odd ordered functions truncated at degree 3, 5, and 7, are shown in Figures 2.1(b), (c), and (d), respectively, with the Morse potential shown in Figure 2.1(a).

Comparison of Figures 2.1(b), (c), and (d) with (a), shows the errors introduced by the use of truncated functions. Figure 2.1(b), as do the rest of the truncated functions, seemed to be a good approximation of the bond compression (x < 0) when compared to Figure 2.1(a). Also the lower part of the curve, which is close to the minimum, seems to approximate the Morse potential. The x^3 truncation, of course, fails when it approaches the dissociation energy of the Morse (set to 1.0). This is the case for all of the truncated equations shown here. Notice that in Figure 2.1(d) the curve at least starts to bend at the same place that the Morse curve bends over to approach dissociation. Thus, this collection of plots of the truncated functions allows the reader to see that the addition of terms (higher harmonics) in the series allows the system to model the Morse correctly only if all the terms are present.

The equation of motion used here is the same as that presented in [1.32] but the constants a and D are set to 1, there is no forcing nor damping and the exponentials have been replaced with the truncated MacLaurin series as defined earlier. Thus, without losing all of the information (in the exponentials), it is quite possible to take a $3rd$ derivative of the equation of motion, which is itself a 2^{nd} derivative with respect to time, resulting in the 5^{th} derivative of x with respect to time. In Figure 2.2(a) a fifth ordered phase plot is shown for the complete Morse potential and the fifth

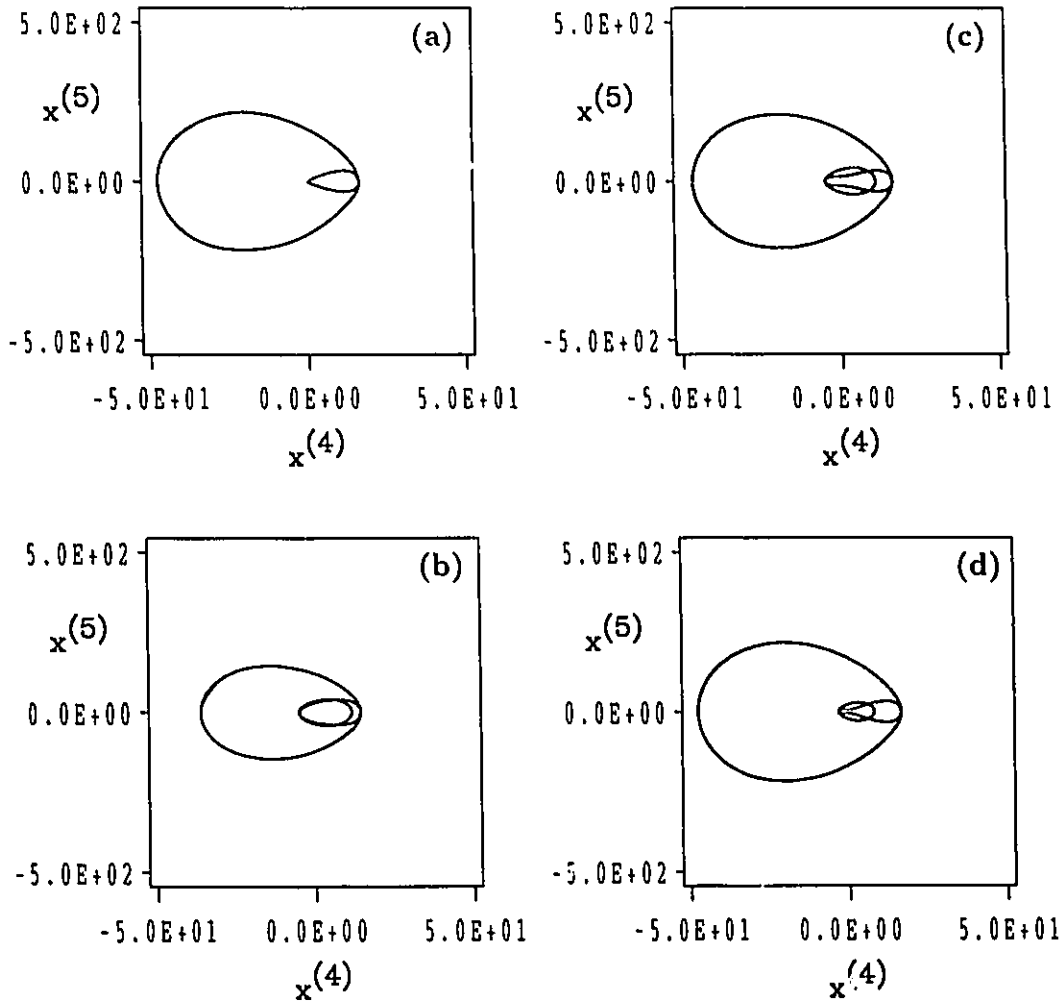

Figure 2.2 Comparison plots as in Figure 2.1 but for the fifth-order phase plot. (a) the Morse case. The MacLaurin series truncated to the order 3 (b), 5 (c), and 7 (d). Notice that all of these plots have the same vertical and horizontal scale.

ordered phase plots for the functions truncated to x^3, x^5, and x^7 terms are in (b), (c), and (d), respectively. It is quite evident that as the number of terms in the truncation is increased the fifth-order phase plot topology comes closer and closer to the topology of the fifth-order Morse phase plot. Notice that in the phase plot in Figure 2.2(a) the plot takes up most of the left half of the plot. In Figure 2.2(b) the vertical and horizontal sizes of the figure are undersized compared to Figure 2.2(a). In Figure 2.2(c) the vertical size is correct but the horizontal size is actually too large which is the same case for Figure 2.2(d).

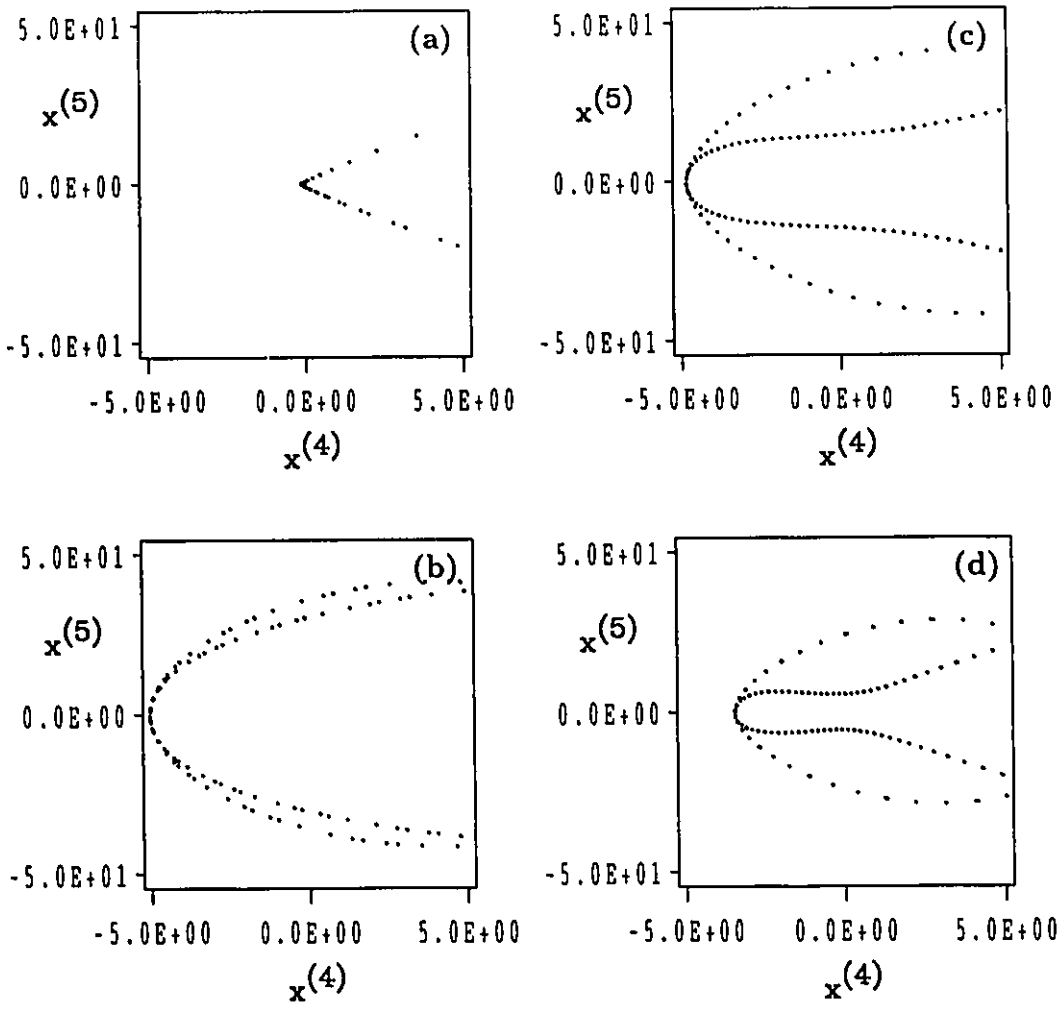

Figure 2.3 Expansion of the same plots as in previous figure. In this figure the actual data points are plotted.

There are two intersecting and overlapping ellipse-like structures in all of the plots but the third lobe is formed apparently only in Figures 2.2(b), (c), and (d). It actually exists in Figure 2.2(a) as well but can be only seen with further expansion(see Figure 2.4). Notice that the second lobe changes distinctly through Figures 2.2(b), (c) and (d). In Figure 2.2(b) it is oval, in (c) it has started to be pinched and in (d) the pinching is increased. This is illustrated further in the expansion plots in Figures 2.3(b), (c), and (d), and in Figure 2.3(d) it can be seen that if the pinching is taken to closure the curve would have the same shape as 2.3(a). That is if the higher

terms (harmonics) are included this closure would occur and a better approximation of the Morse potential would occur.

Figure 2.4 presents further expansions of the Morse fifth-order phase plot that was in Figure 2.3(a). In Figure 2.4(a) another lobe can be seen which could be the lobe that would occur once the waveform in (d) of the previous figure had been pinched and then folded over. These last two figures are therefore illustrations of the higher-order phase plots allowing the researcher to visualize the higher harmonics of the Morse potential which are not present in the truncated functions.

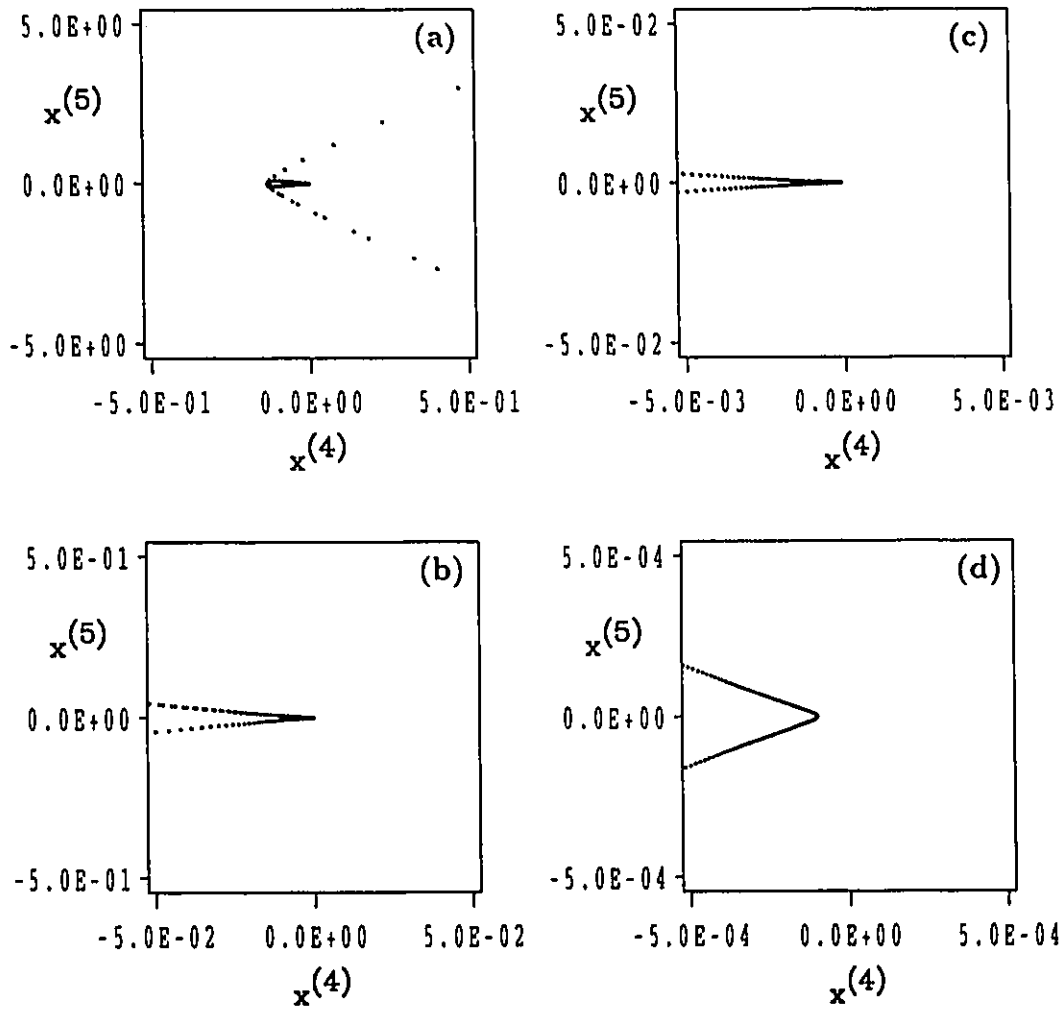

Figure 2.4 Further expansion of the Morse fifth-order phase plot.

2.3 The Weakly Forced and Damped Morse Oscillator

The usual $x^{(1)}$–x phase plot and also the fifth-order ($x^{(5)}$–$x^{(4)}$) and eleventh-order ($x^{(11)}$–$x^{(10)}$) phase plots for a spline fit of the calculated points are plotted, and considered here. Unless otherwise stated a time interval of 4.0×10^{-2} (total time 200) is used. Unless otherwise stated the parameters $\alpha = 0$ and C= 10^{-6}. Also, for comparison, higher-order phase plots are considered for which data points are calculated and plotted for a time interval of π (total time 1200π). This is therefore a stroboscopic picture which defines a map of the $x^{(n)}$–$x^{(n-1)}$ plane onto itself.

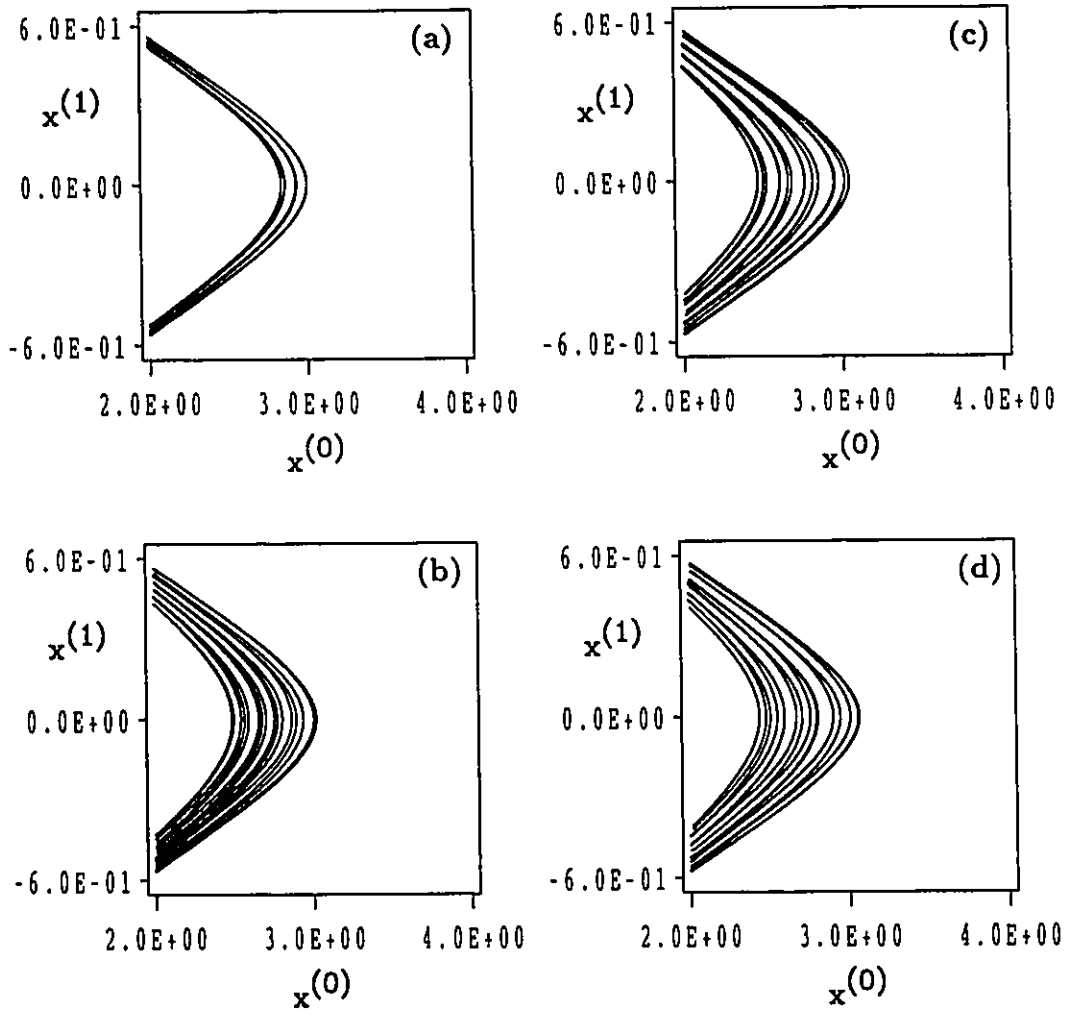

Figure 2.5 Expansions of the $x^{(1)}$—x phase plot for E(0) = 0.90. (a) F = 3.0×10^{-3}; (b) F = 5.0×10^{-3}; (c) F = 7.0×10^{-3}; (d) F = 9.0×10^{-3}.

Figures 2.5(a), (b), (c) and (d) show an expansion of the usual phase plot for E(0) = 0.90 and F = 3.0, 5.0, 7.0 and 9.0× 10^{-3} respectively. It may be seen that, as F increases, a broader range of $x^{(1)}$-x values is accessed but that there is nothing remarkable about the $x^{(1)}$-x phase plot. Figures 2.6(a), (b), (c) and (d) show an expansion of the fifth-order phase plot for the same E(0) and F values. In contrast to the usual phase plot, it may be seen that for the $x^{(5)}$–$x^{(4)}$ phase plot, there is complicated dynamics close to the point $(x^{(5)},x^{(4)})$ = (0,0) and, in this region the higher-order phase space structure is increasingly contorted as F increases.

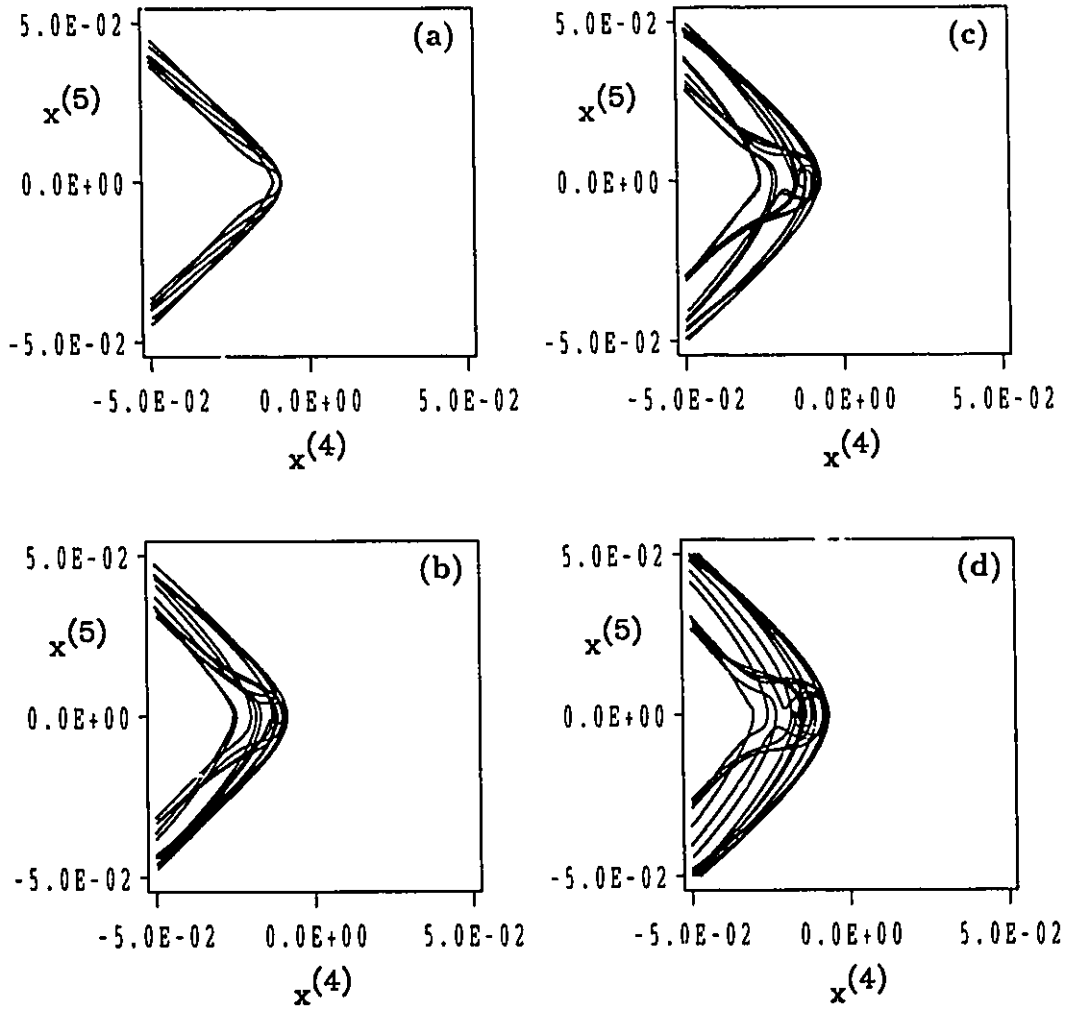

Figure 2.6 As for Figure 2.5 but for the $x^{(5)}$—$x^{(4)}$ phase plot.

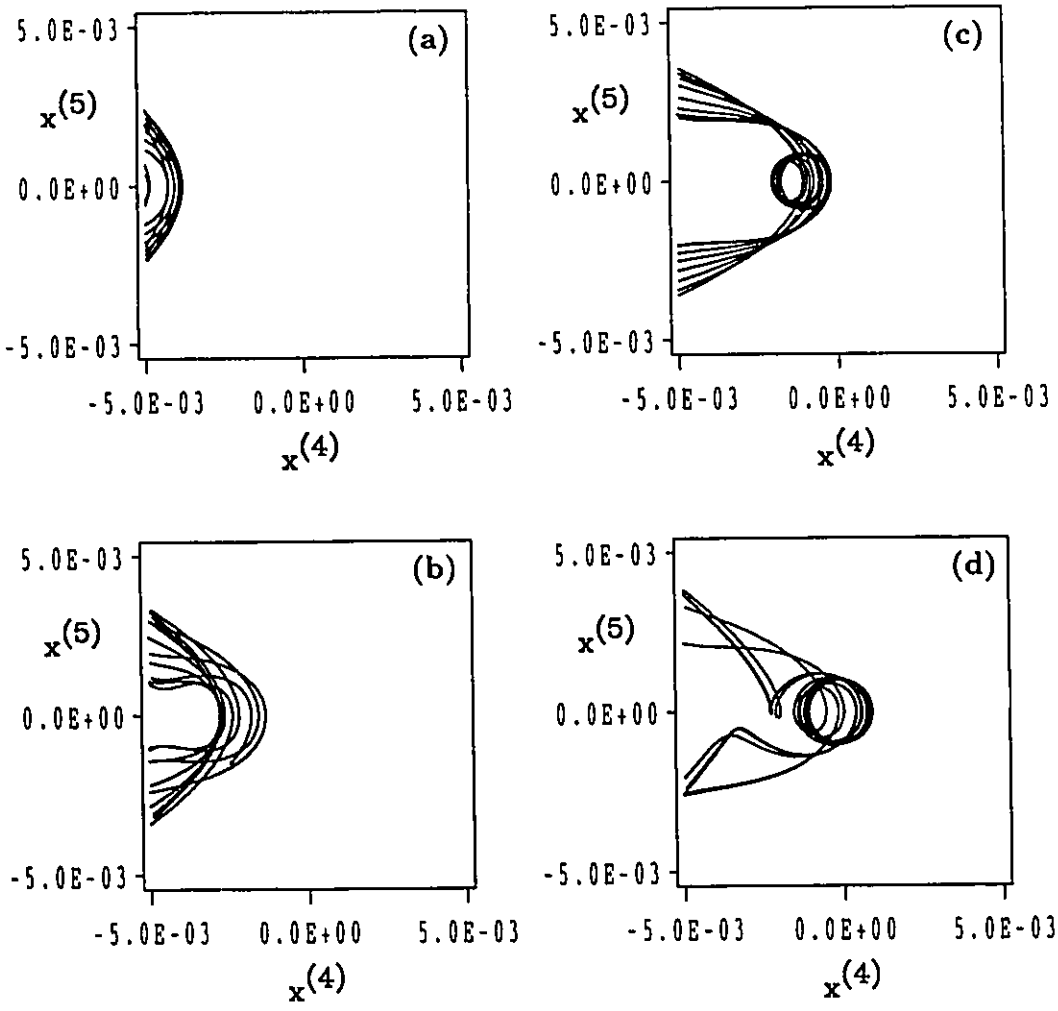

Figure 2.7 Expansions of the $x^{(5)}$—$x^{(4)}$ phase plot for $F = 1.0 \times 10^{-3}$. (a) $E(0) = 0.93$; (b) $E(0) = 0.95$; (c) $E(0) = 0.97$; (d) $E(0) = 0.99$.

Now results are considered for the fifth-order and eleventh-order phase plots for $F = 1.0\times 10^{-3}$ with varying E(0). Figures 2.7(a), (b), (c) and (d) show an expansion of the fifth-order phase plot for E(0) = 0.93, 0.95, 0.97 and 0.99 respectively. Notice that as E(0) is increased complicated dynamics is developed when the trajectories are close to the point $(x^{(5)},x^{(4)}) = (0,0)$ which was also true in Figure 2.6. For E(0) = 0.93 and 0.95 (Figures 2.7(a) and (b)) the higher-order phase space structure is contorted but no loops have formed. For E(0) = 0.97, Figure 2.7(c), there are circular loops but they are not centered on $x^{(4)} = 0$, $x^{(5)} = 0$ while for E(0) = 0.99, Figure 2.7(d), the loops are centered on this point. Figures 2.8(a), (b), (c) and (d)

show the same expansions as for Figure 2.7 but for the eleventh-order phase plot. It may be seen that, as E(0) increases, complicated dynamics is developing close to the point $(x^{(11)},x^{(10)}) = (0,0)$. For E(0) = 0.93, Figure 2.8(a), the higher-order phase space structure is contorted in this region but there no loops are formed. For E(0) = 0.95, Figure 2.8(b), there are circular loops but they are not centered on $x^{(10)} = 0$, $x^{(11)} = 0$ while for E(0) = 0.97 and 0.99, Figures 2.8(c) and 2.8(d), the loops are centered on (0,0). Comparison of Figures 2.7 and 2.8 shows that the radius of the loops are the same for the fifth-order and eleventh-order phase plots. The radius of the loops are the same for all higher-order phase plots and are directly proportional to the value of F. (See Appendix B for a more detailed discussion on how the forcing term affects the trajectory.) For each value of E(0) the higher-order phase space structures in Figures 2.7 and 2.8 are more developed for higher-ordered phase plots indicating that as the order increases the higher-order phase plots are an increasingly more sensitive probe of the phase space dynamics. Of relevance for the time plots of E(t) shown later in this chapter, note that for E(0) = 0.99, there are fewer passes of the trajectory through Figures 2.7(d) and 2.8(d) indicating that the phase space trajectory spends most of its time in the circular loop.

The next set of figures are also used to illustrate that the sensitivity of the probe increases as the order of the phase plot increases. These two figures (Figures 2.9 and 2.10) are for a forcing of $F = 1.0\times10^{-3}$ and an initial total energy of $E = 97\%$. Notice that as the order of the phase plot increases the trajectory goes from a condition of being contorted to forming loops. Figures 2.9(a), and (b), show contortion while (c) has half-loops being formed and in the fifth-order phase plot of Figure 2.7(c) complete loops formed but they were not centered on (0,0).

However, as can be seen in the sixth-order phase plot of Figure 2.9(d), loops have not only formed but are now centered on (0,0). Figure 2.10 has the 7^{th}, 8^{th}, 9^{th} and

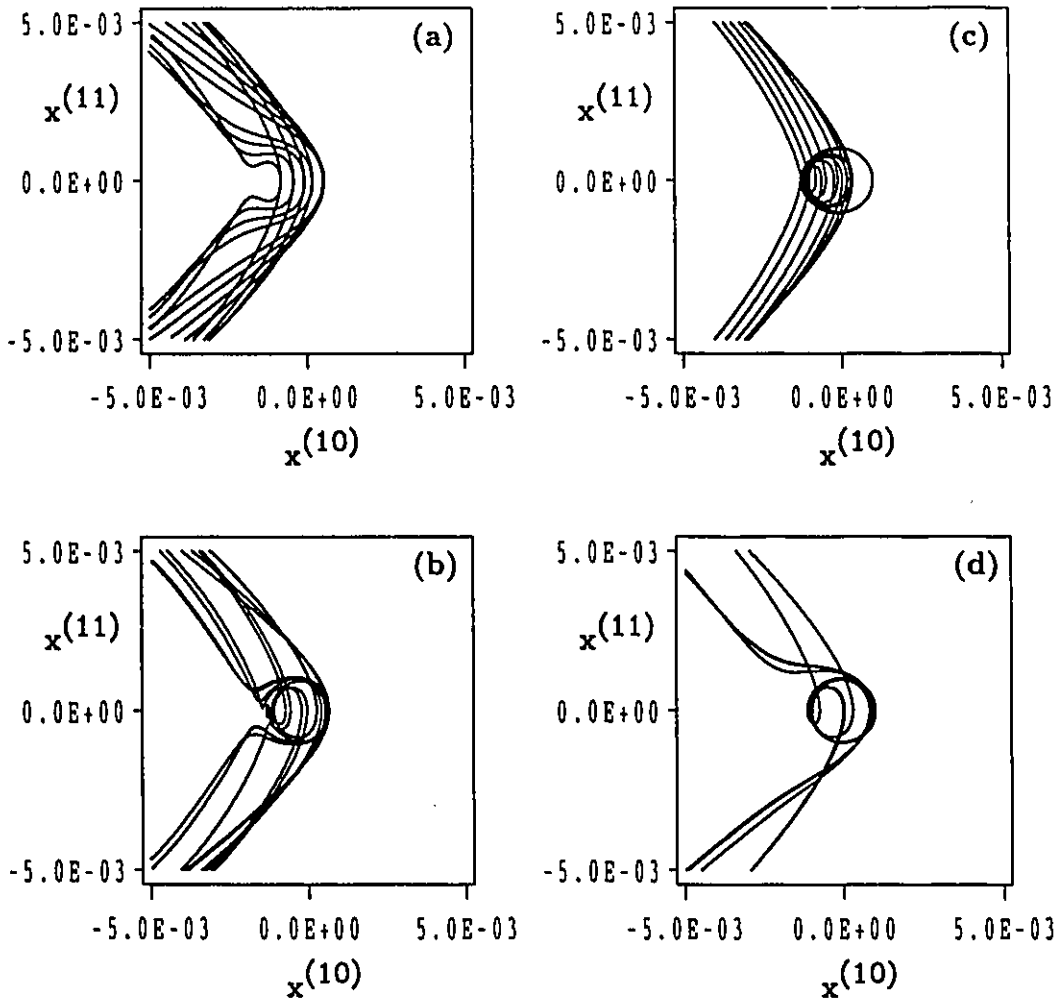

Figure 2.8 As for Figure 2.7 but for the $x^{(11)}$—$x^{(10)}$ phase plot.

10^{th} order phase plots. The 7^{th} order phase plot has a striking similarity to the 11^{th} order phase plot for the same parameters, but direct comparison of Figures 2.10(a) and 2.8(c), shows that these two plots are *not* identical.

Through the use of Figures 2.9 and 2.10, the difference between even ordered phase plots and odd order phase plots can be seen. In the above plots the trajectories in the even ordered phase plots, are drawn from bottom left to bottom right while the the trajectories in the odd ordered phase plots, are drawn from the top left to bottom left. The number of lines drawn in each plot decrease with the increased time spent in the circular loops.

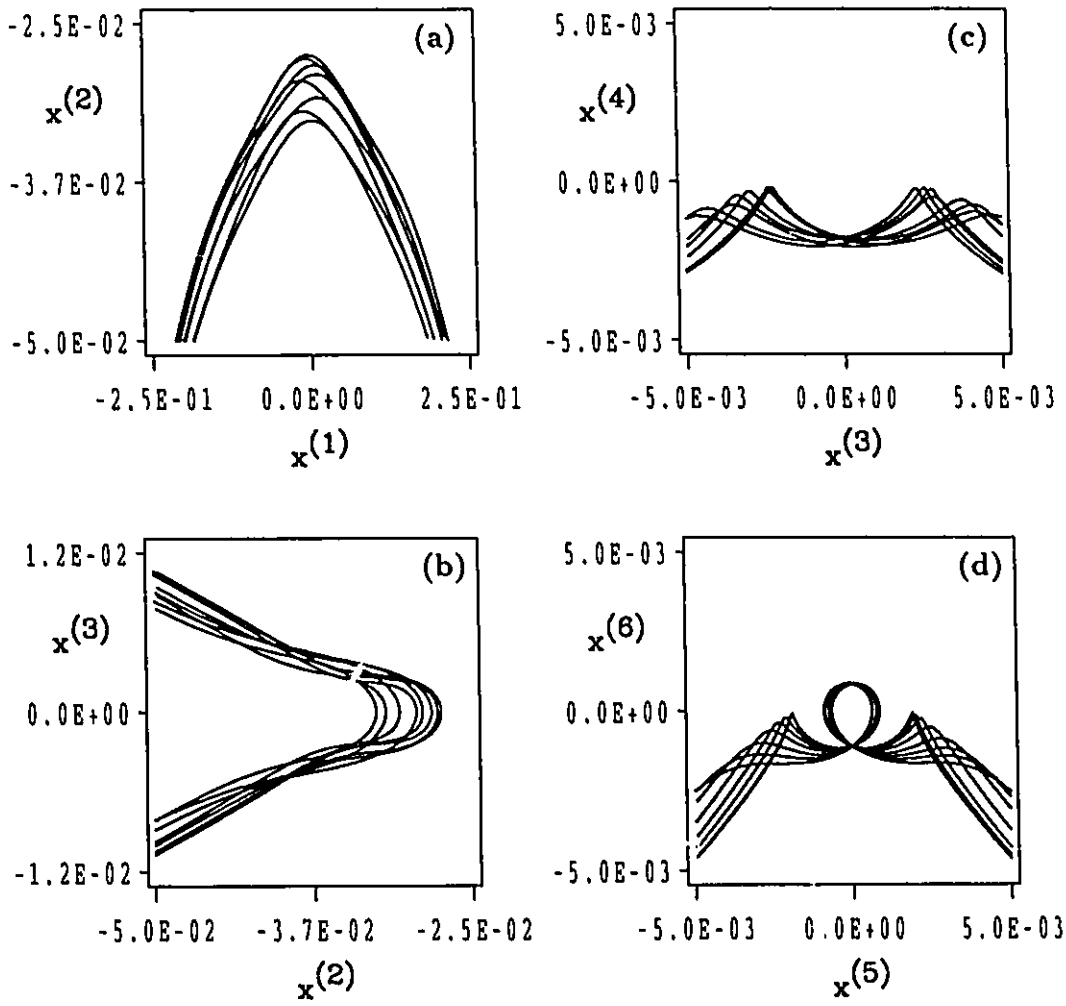

Figure 2.9 Expansions of phase plots for $F = 1.0 \times 10^{-3}$ and $E(0) = 97\%$. (a) is for $x^{(2)}$—$x^{(1)}$, (b) is for $x^{(3)}$—$x^{(2)}$, (c) is for $x^{(4)}$—$x^{(3)}$, and (d) is for $x^{(6)}$—$x^{(5)}$.

Stroboscopic mappings of higher-order phase plots are now presented. Data points were calculated using a time interval of π for a total time of 1200π. Figures 2.11(a) and (b) show an expansion (the same scales as for Figure 2.7) of the fifth-order phase plot for $E(0) = 0.93$ and 0.99 respectively while 2.11(c) and (d) are the eleventh-order phase plots for the same energies as 2.11(a) and (b) respectively. The resulting higher-order phase space structures are two overlapping curves which outline the corresponding higher-order phase space structures in Figures 2.7(a) and (d), the fifth-order, and 2.8(a) and (d), the eleventh-order. The upper and lower curves correspond

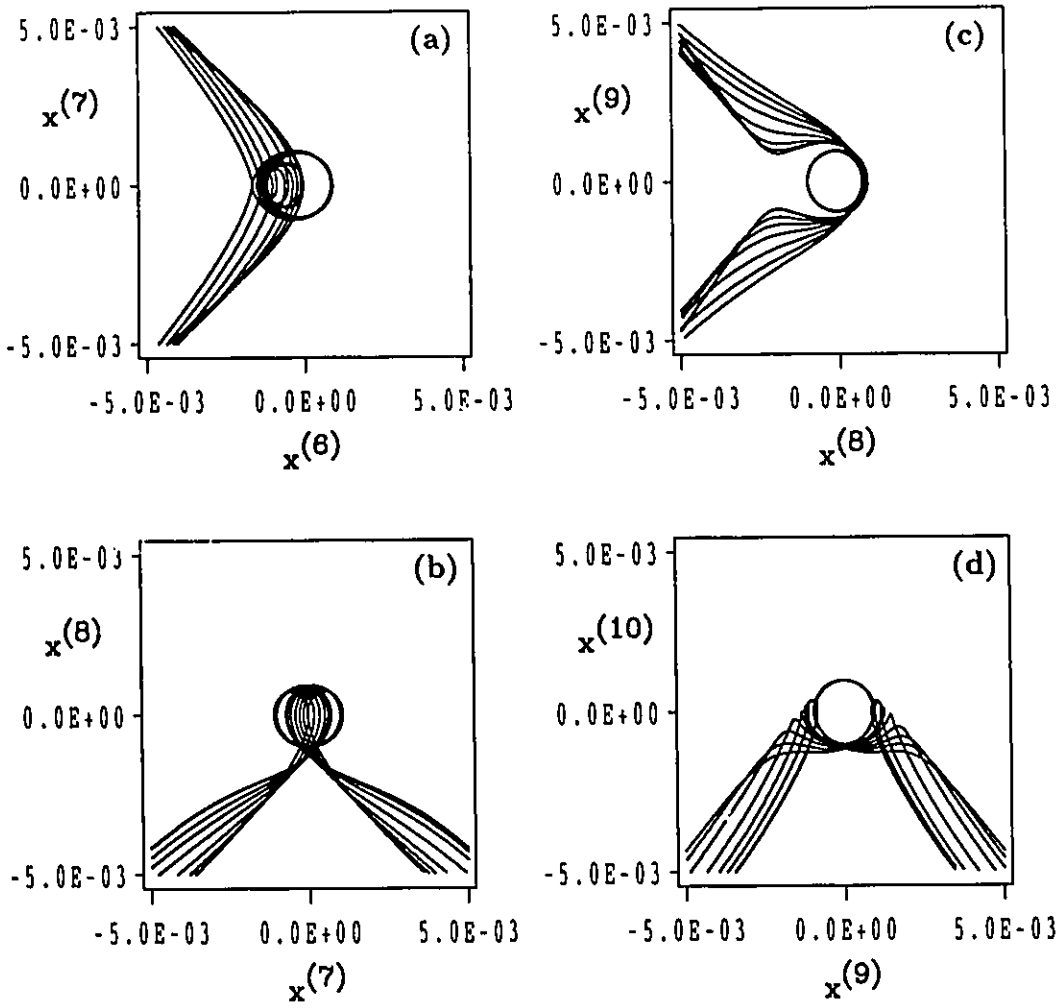

Figure 2.10 Expansions of phase plots for $F = 1.0 \times 10^{-3}$ and E(0) = 97%. (a) is for $x^{(7)}$—$x^{(6)}$, (b) is for $x^{(8)}$—$x^{(7)}$, (c) is for $x^{(9)}$—$x^{(8)}$, and (d) is for $x^{(10)}$—$x^{(9)}$.

to points plotted for odd and even values of π respectively. The slight width of these curves is an indication of chaotic dynamics that is confined to a small region of phase space.

Equation [1.32], of chapter one, had a term $(1 - \alpha x)e^{-\alpha x}$ which was part of the forcing term. Now choosing $\alpha > 0$, the effects of this realistic addition to the forcing can be observed in the higher-order phase plots. This term, because of $e^{-\alpha x}$, allows the affect of F sin(t) to be reduced as x increases. This is expected to be a more

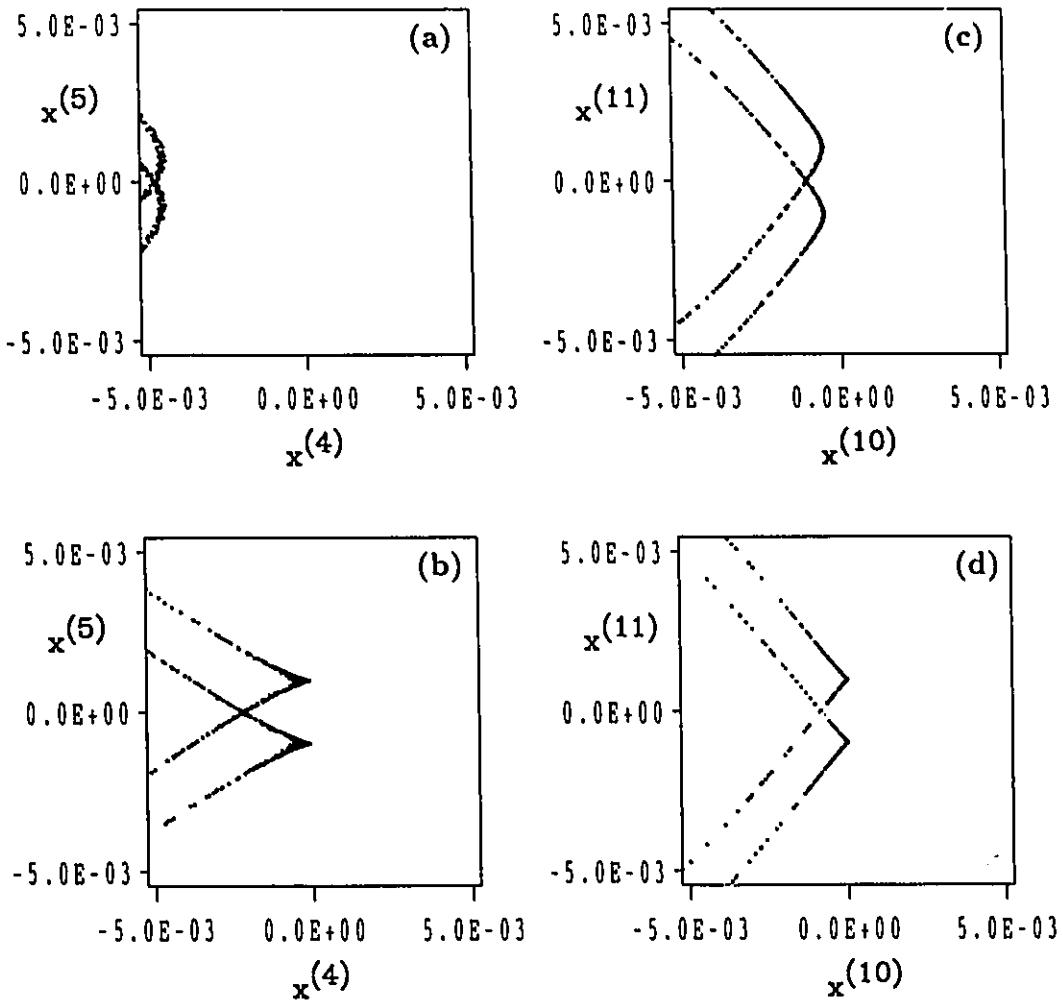

Figure 2.11 Expansions of the $x^{(5)}$—$x^{(4)}$ phase plot (time interval π) for F $= 1.0 \times 10^{-3}$. (a) E(0) = 0.93 and (b) E(0) = 0.99; (c) and (d) are as for (a) and (b) respectively but for the $x^{(11)}$—$x^{(10)}$ phase plot.

realistic representation of the laser interaction with the bond since the energy gap between vibrational levels of the system decreases dramatically with the lengthening of the bond while the energy of the photons from the laser is constant. Thus there will be a decrease in the interaction between the bond of the diatomic and the laser as the bond length changes. This can also be discussed in terms of how "good" is the overlap of the vibrational wavefunctions of the two vibrational levels. The vibrational wavefunctions of the ground and excited state levels will not overlap well for all values of the bond length. Figures 2.12(a), (b) and (c) show an expansion (the same as for

Figure 2.7) of the fifth-order phase plot for E = 0.99 and α = 0.001, 0.01 and 0.1 respectively while 2.12(d) shows a further expansion of 2.12(c). It may be seen that Figure 2.12(a) is almost identical to 2.7(d) but that as α increases the radius of the loop decreases. This is reasonable since as α increases the forcing term is attenuated. These results show that the existence of the circular loop is not dependent on the particular forcing term used, only the loop size is. Although for α = 0.1 the loop size is much smaller, the loops are structurally similar to those in Figures 2.12(a) and 2.7(d). This also indicates that the higher-order phase space structures are structurally stable.

Figure 2.13 shows time plots of x(t), $\log_{10}(dist(t))$, and E(t) for F = 1.0×10^{-3} with E(0) = 0.93 (column 1) and 0.99 (column 2). In Figures 2.13(a) and 2.13(d) x(t) is plotted for t = 0 to 200 and the approximate period of x(t) is longer for E(0) = 0.99 than for E(0) = 0.93, which is expected. Figures 2.13(b) and 2.13(e) show $\log_{10}(dist(t))$, with $dist(0) = 10^{-12}$, for t = 0 to 200. In this work $\log_{10}(dist(t))$ is used to represent the log (base 10) of the distance between identical equations of motion that have initial conditions that differ by only 10^{-12}, for which the $\log_{10} = -12$. Thus, λ(t)= slope of [$\log_{10}(dist(t))$ *versus* time] is a dynamic coordinate dependent Lyapunov exponent. A positive Lyapunov exponent is one measure of whether a system is chaotic or not, as described in the section of chapter one on chaos. It may be seen that the overall rate of increase of $\log_{10}(dist(t))$ appears to be linear for E = 0.99 but slower for E = 0.93. This is confirmed for longer times and indicates that there is chaotic dynamics[43] for E(0) = 0.99 but not for E(0) = 0.93. Figures 2.13(c) and 2.13(f) show E(t) for t = 0 to 200. In Figure 2.13(c) where E(0) = 0.93 the energy, E(t), is rapidly changing at all times although there appears to be a long overall period. In contrast, in Figure 2.13(f) where E(0) = 0.99, there are time intervals of variable length during which the energy, E(t), is approximately constant with small oscillations. Although, in Figure 2.13(f), there is an overall decrease in E(t) from t

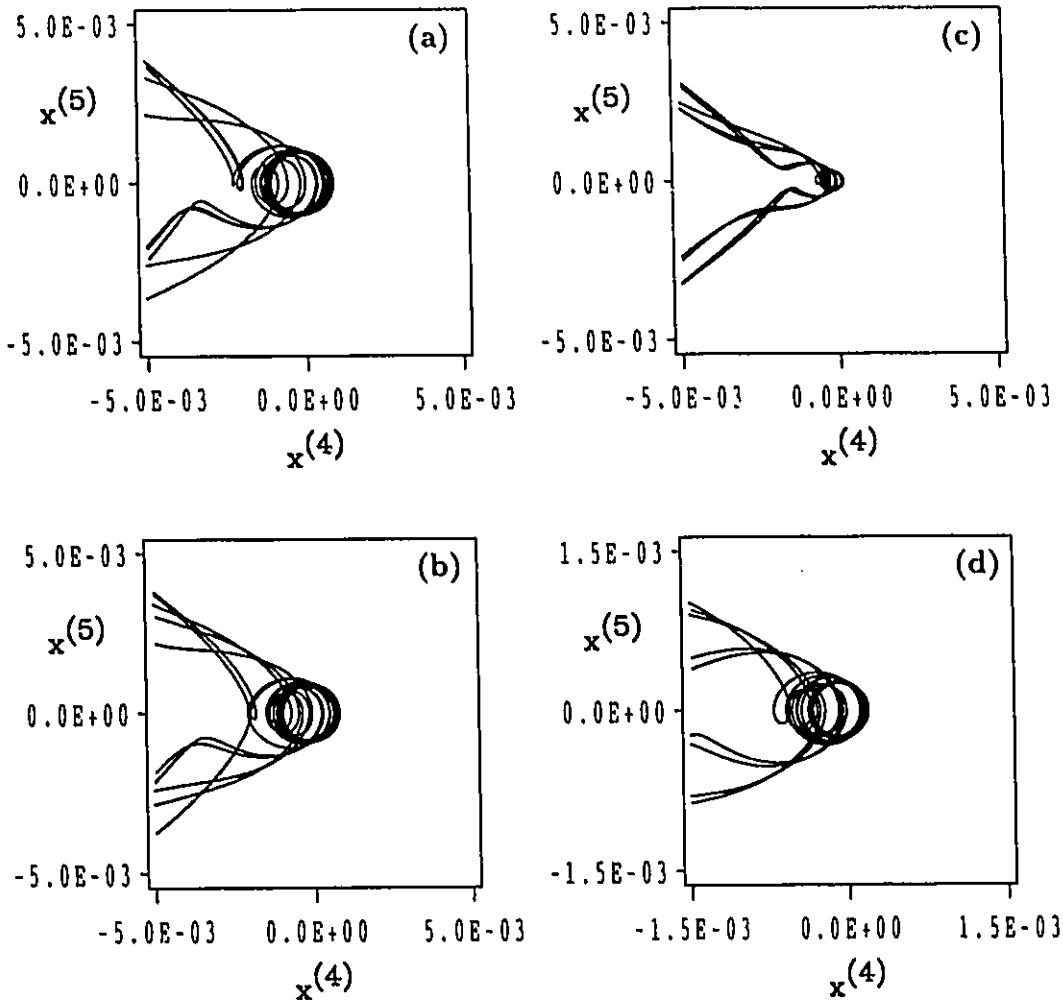

Figure 2.12 Expansions of the $x^{(5)}$—$x^{(4)}$ phase plot for $F = 1.0 \times 10^{-3}$, and $E(0) = 0.99$ (a) $\alpha = 0.001$; (b) $\alpha = 0.01$; (c) $\alpha = 0.1$; (d) Further expansion of (c).

= 0 to 200, for the same parameters there is an overall increase in E(t) from t = 200 to 400 and subsequently the energy decreases and increases in a "random" stepwise fashion. Once the energy has stepped the oscillations start to decrease. The time interval during which E(t) has the smallest amplitude oscillations corresponds to the time in which the trajectory in the higher-order phase plots is forming loops. While the phase space trajectory loops the dynamics is regular. The chaotic dynamics is primarily associated with the pre and post loop switching regions. After the Morse oscillator dissociates the energy is approximately constant with small oscillations (al-

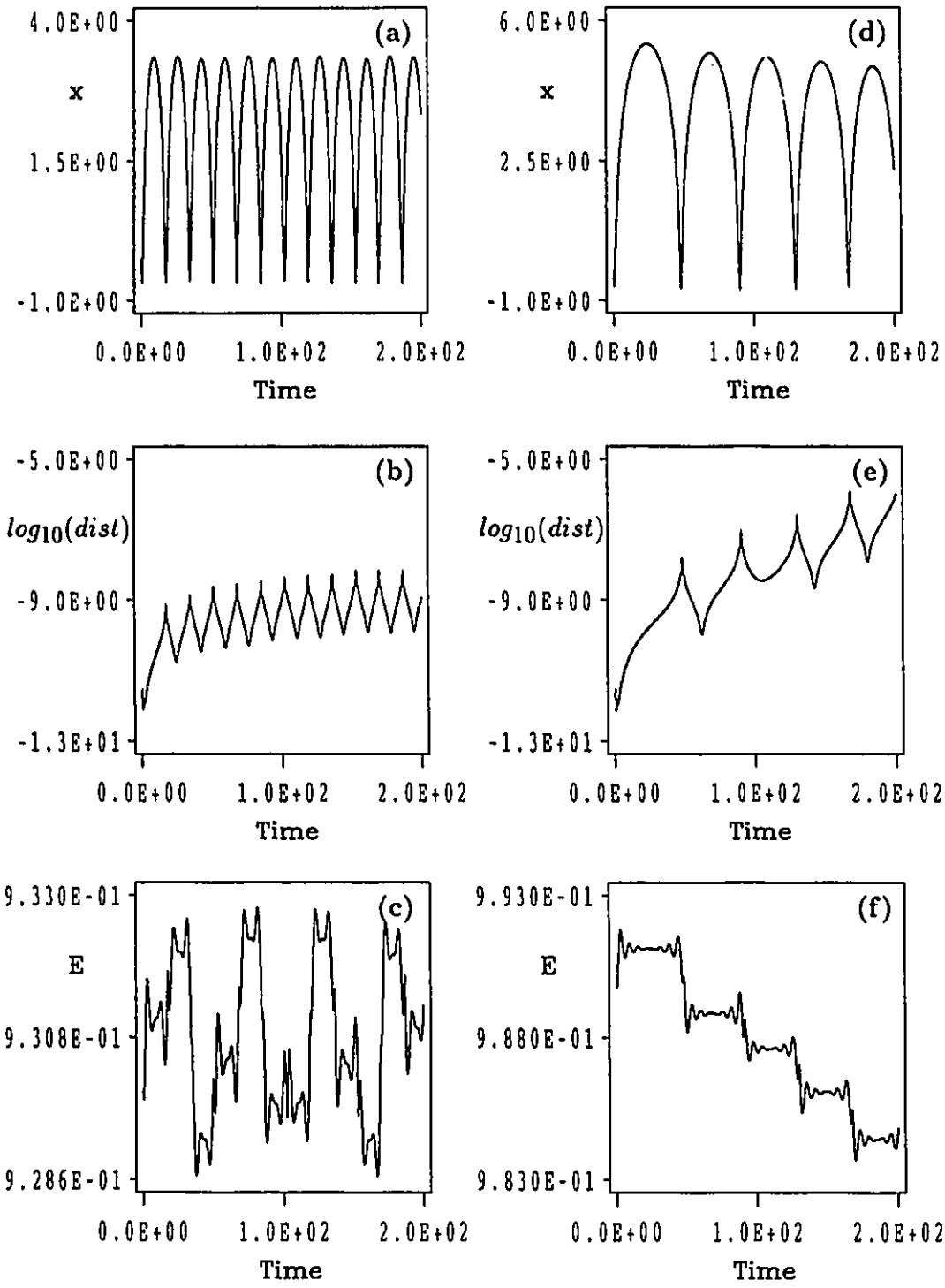

Figure 2.13 F = 1.0 × 10^{-3} and E(0) = 0.93. (a) The phase, x(t), *vs* t for t = 0 to 200; (b) $\log_{10}(dist(t))$ *vs* t for t = 0 to 200; (c) The energy, E(t), *vs* t for t = 0 to 200; (d),(e),(f), as for (a),(b),(c) respectively, but for E(0) = 0.99.

ways above 1.0) while the higher-order phase space structure is a circular loop, of the same size, in each higher-order phase plot.

2.4 The HF Case

Since the initial work of Walker and Preston[8] there have been numerous classical and quantum studies[44–51] of HF in a laser field. In these studies HF is modeled by a Morse oscillator[5] for which the energy is

$$\mathrm{E} = \mathrm{p}^2/(2m) + D(1 - e^{-\mathrm{ax}})^2 \qquad [2.2]$$

where x = r-r_e, m is the reduced mass, a and D as defined in chapter one and restated earlier in this chapter. In these studies the laser field is intense (43 Tw/cm^2 in reference 8) and the initial energy, E(0), is chosen using the well-known formula E_n = $(n+1/2)\omega_0[1-(n+1/2)\omega_0/(4D)]$ with $n = 0$, where ω_0 is the harmonic frequency. (See chapter one, Introduction for a more detailed discussion of the calculation of energy, number of bound levels and factors determining number of bound levels for the Morse potential.) General agreement was found between the classical and quantum studies although significant differences were noted[8,44–51]. In the present classical study the laser field is moderate (three orders of magnitude smaller than in reference 8) and the initial energy, E(0) is chosen using the above formula with $n = 21$ (99.01% of the dissociation energy). This work shows that, for these trajectories, the energy changes in a stepping fashion. A similar effect was observed by Leopold and Percival[53] in a classical study of highly excited electronic states for an atom in a laser field. The equation of motion for a Morse oscillator in a laser field used here is

$$\begin{aligned} \dot{\mathrm{x}} &= \mathrm{p}/m \\ \dot{\mathrm{p}} &= -2aD\ (e^{-\mathrm{ax}} - (e^{-\mathrm{ax}})^2) - C\mathrm{p} + E_0(d\mu/d\mathrm{x})\sin(\omega \mathrm{t}) \end{aligned} \qquad [2.3]$$

where C is the damping coefficient, E_0 is the laser amplitude, ω is the laser frequency and μ is the dipole function. Here $E_0(d\mu/d\mathrm{x})\sin(\omega \mathrm{t})$ takes the place of the realistic

forcing term used in the previous section when equation [2.3] with $m = 1, a = 1$, $D = 1$ and $\omega = 1$ was used in a classical study of the dynamics[52] of the forced and weakly damped Morse oscillator. Since this work follows Walker and Preston[8], the following parameters are chosen (in atomic units[4]) $m = 1744.6$, $a = 1.1741$, $D = 0.225\ 09$ and $\omega = 1.791\ 04 \times 10^{-2}$ (chosen to be $0.95\omega_0$). Also, μ is a linear dipole function[47], $d_0 + d_1 x$, with $d_1 = 0.297\ 69$ (similar results are obtained for a quadratic dipole function). $C = 10^{-10}$ is chosen to model weak damping. Results are shown for $E_0 = 1.0676 \times 10^{-3}$, corresponding to a laser power of 40 Gw/cm^2 (similar results are obtained for other E_0 values). For simplicity, x(0) = 0 and $p(0) = -(2mE(0))^{1/2}$ are used for initial conditions.

Figure 2.14(a) shows E(t)/D versus t for a total time t = 0 to 20 670 (0.5 picoseconds or approximately 59 optical cycles). As previously shown for E(t) there are superimposed oscillations, here the energy varies from 98.9% to 99.4% of the dissociation energy changing in a stepping fashion. Leopold and Percival[53] introduced a modified energy which is designed to compensate for oscillations in the energy due to the laser field. The compensated energy used in this work is

$$E_c = [p + \frac{E_0}{\omega}(d\mu/dx)\cos(\omega t)]^2/2m + D(1 - e^{-ax})^2. \qquad [2.4]$$

Figure 2.14(b) shows $E_c(t)/D$ versus t for the total time of Figure 2.14(a) and the superimposed oscillations of Figure 2.14(a) have been largely suppressed. It is even more clear that the energy (compensated or otherwise) changes in a stepping fashion and there are time intervals in which $E_c(t)$ is essentially constant. In Figures 2.14(a) and (b) the length of each time interval is approximately 10 optical cycles but, in general, these time intervals have variable length. As expected, the time interval is longer the closer the system is to dissociation. This effect may be qualitatively understood from the higher-order phase plots for the trajectory that generated Figure 2.14(a).

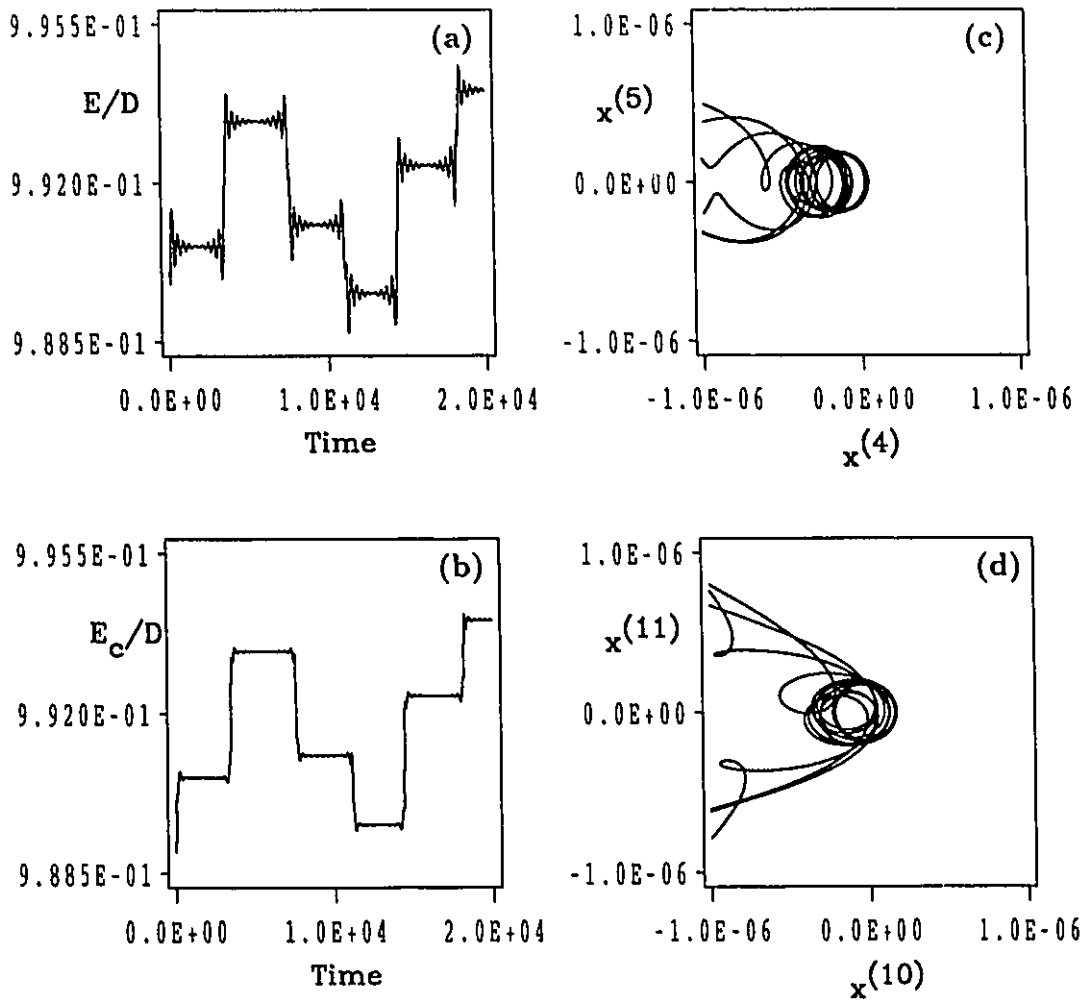

Figure 2.14 (a) E(t)/D versus t for t = 0 to 20 670; (b) As for (a) but for $E_c(t)/D$; (c) Expansion of the $x^{(5)}$–$x^{(4)}$ phase plot for $\tau = 0$ to 185.10; (d) As for (c) but for the $x^{(11)}$–$x^{(10)}$ phase plot.

In this section, to avoid complications arising from factors of ω^n, the higher-order phase plots are calculated for scaled time $\tau = \omega t$ (taking scaling into account the $E(\tau)$ versus τ plot is, of course, identical to that shown in Figure 2.14(a)). This is believed to have been a another complication that limited the confidence of Packard *et al* [39] and Kreul *et al*[40] in the use of higher derivatives. Figures 2.14(c) and (d) show expansions of the fifth- and eleventh-order phase plots respectively for a total scaled time $\tau = 0$ to 185.10 (half the unscaled time of Figure 2.14(a)). In Figures 2.14(c) and (d) the notable feature is the circular loop, which is centered on $x^{(10)} = 0$ and $x^{(11)} =$

0 for the eleventh-order phase plot. This feature, which is not present for $E_0 = 0$, is due to the laser field and, as E_0 increases, the radius of the circular loop increases[52] (see Appendix B). As pointed out in the previous section the loops in the higher-order phase plots correspond to the time intervals when the energy has stepped. That is in Figures 2.14(c) and (d) the loops form when then energy in Figures 2.14(a) and (b) is constant. This is more evident in Figure 2.14(b) for the compensated energy. Figure 2.15 is the kinetic and potential energy plotted on separate graphs for the case of Figure 2.14(a). The kinetic and potential energy of Figure 2.14 were plotted separately to point out that neither one separately can account for the stepping of the energy in 2.14(a).

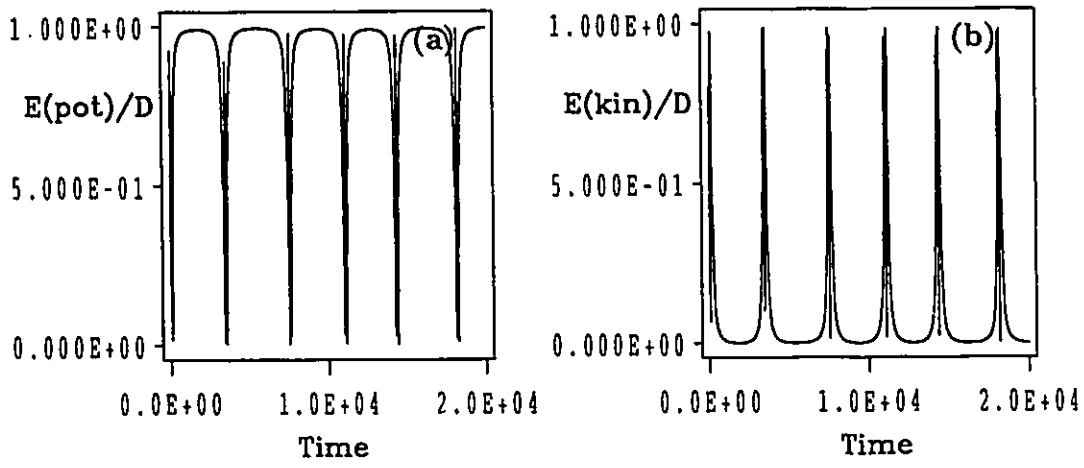

Figure 2.15 (a) E(pot)/D versus t for t = 0 to 20 670; (b) E(kin)/D versus t for t = 0 to 20 670.

2.5 Summary

2.5.1 The Weakly Forced and Damped Morse Oscillator

In the previous section the dynamics of a weakly forced and weakly damped Morse oscillator has been examined. The novel tool of higher-order phase plots has been used to visualize the importance of the higher harmonics in the phase which are essential for the dynamics to be complicated and dissociative. Expansions of the higher-order

phase plots in regions about $x^{(n-1)} = 0$, $x^{(n)} = 0$ have been considered and it has been shown that there is a topological change that occurs sequentially for each higher-order phase plot. After the topological change, which occurs at a critical E(0) value for a particular F value, the higher-order phase space structure has a circular loop. As F or E(0) is further increased the phase space trajectory loops an increasing number of times in the higher-order phase plot. It has been shown that for $F = 1.0\times 10^{-3}$ the topological change occurs around E(0) = 0.96 for the fifth-order phase plot and around E(0) = 0.94 for the eleventh-order phase plot. This was also illustrated with a series of higher-order phase plots ($2^{nd} - 10^{th}$) for $F= 1 \times 10^{-3}$, E(0) = 0.97. These plots indicated that although the 5^{th} order phase plot had formed loops the 4^{th} had only half-loops. Thus the higher-order phase plots are increasingly sensitive probes of the phase space dynamics as the order increases. Qualitatively this is because, as the order increases, part of each higher-order phase space structure is increasingly close to the point $(x^{(n)},x^{(n-1)}) = (0,0)$. For larger F values the topological change occurs at a smaller E(0) value for each higher-order phase plot, as the radius of the loop centered on $x^{(n-1)} = 0$, $x^{(n)} = 0$ is larger. While the phase space trajectory loops the energy is approximately constant with small oscillations. (These oscillations were compensated for in the next section.) The circular loop in the higher-order phase plot is the higher-order space structure that is expected for the weakly forced and weakly damped free particle. The significance of the circular loop is that the lower the order of the higher-order phase plot in which the phase space trajectory loops, the closer the Morse oscillator is to dissociation. From this viewpoint, the Morse oscillator dissociates when the value of F or E(0) becomes sufficiently large that the topological change occurs in the usual phase plot. That is, the Morse oscillator dissociates when the phase space structure becomes open for the usual phase plot.

2.5.2 The HF Case

Time intervals in which $E_c(t)$ is essentially constant were also observed by Leopold and Percival[53] in a classical study of highly excited electronic states for an atom in a laser field. These time intervals occur for trajectories which gain energy early but not enough energy to ionize as the electron moves away from the proton into an often highly eccentric elliptic orbit with superimposed oscillations due to the laser field. Typically, the closer to the ionization energy, the more stable the electron orbit. The circular loop in the higher-order phase plots is the higher-order phase space structure that is expected for free H and F atoms in a laser field. For a time interval in which the trajectory loops in the higher-order phase plots, HF behaves as though it has dissociated and this is why the compensated energy is constant for the time interval. The energy jumps either up or down in a "random" fashion (the dynamics is chaotic) in the pre- and postloop switching regions, and HF may dissociate at a later time. To directly observe energy stepping for HF in a moderate laser field one could promote the $n = 0$ state (which is close to a minimum uncertainty wavepacket) to the $n = 21$ level (or another very high-lying level) and then measure the energy of the evolving wavepacket. Unfortunately, the results of Walker and Preston[8] and others indicate that wavepacket spreading would destroy this effect in a few optical cycles. However, their results also indicate that phase coherence of the wavepacket may be preserved for many optical cycles suggesting that this effect might be observed indirectly.

2.6 Future Work on Higher-Order Phase Plots

The next stages of this work should mainly follow a path of adding a second Morse potential to the existing equation of motion. The derivatives could then be calculated using a mathematical manipulation program such as Maple. The equation of motion could then be integrated to get x, $x^{(1)}$, and $x^{(2)}$ which would be placed into the analytic derivative equations of $x^{(3)}$, $\cdots$, $x^{(n)}$ and the higher-order phase plots derived. This would allow the modeling of a co-linear triatomic or a 'T'-shaped triatomic depending on the form of the Morse potentials used and the equation of motion used. Definitions would need to be worked out to define the bond lengths for the diatomic sections and the relationship of one diatomic section to the other. The scope of this work was to define a general case for the novel technique of higher-order phase plots for diatomics which has been done. It is left to future users to develop the general case for triatomics and larger sections of polyatomics.

3 Wavelet Analysis as Applied to the Morse Potential

3.1 Introduction

The Fourier transform decomposes a function using sine and cosine basis functions and similarly the wavelet transform decomposes a function using wavelet basis functions. Although sine and cosine basis functions are completely localized in frequency they are completely unlocalised in time. That is, there is a single frequency but the function is expected to continue for all time ($+\infty$). Wavelet basis functions[54–59] are fairly well localised in both frequency and time depending, of course, upon the wavelet basis set used. The wavelet basis functions are a two parameter family of functions that are a basis for $L^2(\mathrm{R})$. They are obtained from a single function by shifts and dilations producing a time-frequency window of constant area. Since the time-frequency window is of constant area an increase in the delta time means a decrease in the delta frequency. Chui[62] has pointed out that this is exactly the requirement needed for "time-frequency" analysis. The dilations and translations are done by a factor of two for computational simplicity and efficiency. The wavelet basis functions and some of their mathematical properties are discussed in the next section. As outlined by Goupillaud *et al*[60] and restated by Daubechies[61], wavelets were initially developed for the analysis of seismic signals but have recently been used to analyse signals connected with speech and vision for which there are large variations in the frequency or time scales[6].

The wavelet transform used in this work employs a pyramidal algorithm developed by Mallat[58]. It is termed a multiresolution decomposition because each stage of the decomposition uses a different resolution. The difference between the approximation to the function at a given and a previous stage may be computed and this is termed the detail of the function at that stage. In this work, a wavelet transform of the coordinate of a weakly forced and weakly damped Morse oscillator is evaluated. Details of the

coordinate at several stages are obtained with the purpose being to detect the weak forcing term as was done for the Duffing oscillator [64].

There is a close analogy between the wavelet transform and the windowed Fourier transform[56,57,62] in that both perform a frequency analysis of the signal locally in time. Chui[62] has noted that the windowed Fourier transform time resolution is the same for all frequencies thus making it difficult to analyse low frequencies or resolve high frequencies. Whereas the wavelet transform zoom-in and zoom-out[62] ability of its time-frequency window allows the low frequencies to be thoroughly analysed and, as pointed out by Daubechies[56], it more easily detects high frequencies. Thus, a wavelet analysis can more easily resolve a small high frequency component of the signal. It has been shown, for the Duffing oscillator[64], that a wavelet transform can do so even when the system is in the highly anharmonic regime and the signal is highly aperiodic. This work will prove the case for the Morse oscillator and also show how the combination of a wavelet transform followed by a Fourier transform improves the selection process for a multiple frequency signal.

As discussed earlier in this work, the Morse[5] oscillator is commonly used as a model for an anharmonic oscillator. In this work x is called the coordinate of the Morse oscillator and it is sometimes referred to as the bond displacement. The derivative of x is with respect to time, for which the units are arbitrary. Equation [1.32] is a well studied[8,79] model for a diatomic in a laser field but the Morse oscillator parameters are not chosen to model a specific diatomic. That is μ (the reduced mass) a (spectroscopic parameter) and D are chosen to be 1.0 and then for the unforced and undamped Morse oscillator[7] the harmonic frequency is $2^{1/2}$. The parameters C (the damping coefficient), F (the forcing amplitude) and ω (the forcing frequency for each cosine function) must also be specified.

When a system is in the harmonic regime a Fourier analysis of the coordinate is straightforward for long time intervals since the Morse potential may be approximated

by a quadratic potential. However, when the system is close to dissociation and therefore in the highly anharmonic regime, the coordinate is highly aperiodic. In fact it is chaotic[65] and there are many large amplitude low and high frequency components in a Fourier expansion of the coordinate. As a result, in a practical sense, the usual Fourier analysis is problematic since it is assumed that the coordinate is stationary[66] for the time interval. The ramification of the assumption of stationarity is discussed briefly but clearly by Cartwright[66] in the context of economics and the analysis of stock prices as a function of time. Thus, to paraphrase Cartwright[66], 'no finite time interval has a sensible Fourier spectrum. There is an effective discontinuity at the end points and the components this generates are likely to swamp any 'real' cyclical features. '

Since D = 1.0 and the initial total energy, E(0) = 0.99, the Morse oscillator is therefore in the highly anharmonic regime. For simplicity x(0) = 0.0 is chosen and since E(0) is specified, the initial velocity is solved by $x^{(1)}(0) = -(2E(0))^{1/2}$. Then for the unforced (F=0) and undamped (C=0) Morse oscillator x(t) is periodic with period ten times the harmonic period[7]. Finally, the other Morse oscillator parameters were chosen such that C= 1.0×10^{-6} while F was varied. It has been shown, see the chapter on higher-order phase plots, that although the forcing term is weak it has a strong effect on the dynamics and x(t) is highly aperiodic. Therefore Gear's[31] accurate predictor-corrector numerical integrator is used here. In this work, it is assumed that the coordinate is known to six significant figures.

3.2 The Fourier Transform

The discrete Fourier transform is known to be only an approximation to the continuous Fourier transform and Brigham[67] has outlined some of the problems associated with the discrete Fourier transform:

$$G(\frac{n}{NT}) = \sum_{k=0}^{N-1} g(kT)e^{-j2\pi k/N}. \qquad [3.1]$$

To get a discrete Fourier transform the continuous function is convoluted (each point is multiplied by a function) with the sampling function. For correct sampling to take place the continuous function needs to be sampled 10 times per period, of the highest frequency component, to reduce aliasing effects. These are effects that cause low frequency components to be added into the high frequency part of the spectrum by a folding mechanism explained in detail by Brigham[67]. Also the function must be truncated at intervals equal to the period of the function. Therefore to get good results the period of the function should be known and the function should not be truncated at times other than multiples of the period, T. If it is truncated at other intervals "edge" effects will be observed. Brigham[67] states

> "The effect of truncation at other than multiples of the period is to create a periodic function with sharp *discontinuities* ···. Intuitively, we expect the introduction of these sharp changes in the time domain to result in additional frequency components in the frequency domain. Viewed in the frequency domain, time-domain truncation is equivalent to the convolution of a $[\sin(f)]/f$ function with the single impulse representing the original frequency function. Consequently, the frequency function is no longer a single impulse, but a continuous function of frequency with a local maximum centered at the original impulse and a series of other peaks that are termed *side lobes*."

A truncation function called the Hanning function is used as a best general function for waveforms of unknown period (T) and total time T_0.

$$\begin{aligned} w_H(t) &= \cos^2\left(\frac{\pi t}{T_0}\right) \\ &= \frac{1}{2}\left[1+\cos\left(\frac{2\pi t}{T_0}\right)\right] \qquad |t| \le \frac{T_0}{2} \\ &= 0 \qquad\qquad\qquad\qquad\quad |t| > \frac{T_0}{2} \end{aligned} \qquad [3.2]$$

It is used to minimize the starting and ending amplitude of the sample waveform (time domain) thus limiting the side lobes. Thus, the Hanning function is used to reduce "edge" effects. [The Hanning function is not used in this work since the wavelet details are well behaved with no large excursions at the beginning or end but it is mentioned for clarification purposes.]

The Fast Fourier Transform (abbreviated to FFT), as explained by Brigham[67] and Cartwright[66], is a formulation of the Fourier transform that allows faster computation of the transform. The Fourier transform of a sample signal of N data points requires N^2 multiplications and $N(N-1)$ additions. However the FFT of N sample points only requires $N \log_2 N$ multiplications and additions. Thus resulting in very significant computational time reduction.

Adding a constant to the data points is done to shift the waveform in such a manner so the area of the waveform above and below the new zero point will be easier for the cosine/sine functions to approximate. Remember that cosine and sine functions are symmetric with respect to the horizontal axis and they therefore have the same maximum negative value as positive value. Since $FFT(f(x)+c) = FFT(fx)+FFT(c)$ then if c is negative the result of this process is to decrease the amplitude of the zero frequency component in the Fourier transform. The FFT of any constant is added to the amplitude of the zero frequency component.

The data files, in this work, are usually 4096 points and therefore the wavelet transform detail files are 2048 or less points as discussed in the next section. The detail files were zero-filled (zeros are added to the file at the end of the file) to obtain 4096 data points before the FFT was done. This does not change the location of the frequencies. The zeros are added in multiples of the existing data points which results in adding a data point in between each data point that existed before.

The mainframe computer at the University of Ottawa has IMSL libraries that can be called from Fortran programs. The IMSL library FFTRC was used to do the FFT in this work. Actually what is plotted is the power spectrum which is the square of the amplitude from the FFT program.

The following are some notes on the relationship between frequency and time as they pertain to Fourier transforms. The total time (T_0) determines the frequency

step $\Delta f = 1/T_0$. So as long as the total time remains the same the frequency step is constant no matter what the time step size is for the data created. Also, if the input file to the FFT program has 4096 points the resulting power spectrum will have 2048 points. Thus the maximum frequency that can be displayed will be $\Delta f \times 2048$. Now if the total time is kept constant by using a large step size but less steps , Δf is the same but f_{max} will be less. For example, if the step size is doubled and the number of steps is halved (only 2048 instead of 4096) the total time is still the same but f_{max} is now half of what it was since there are only 1024 steps in the FFT file. This will be used to explain some of the results of the wavelet transform-FFT procedure.

The doubling of the step size also can cause problems with aliasing. Since the sampling step determines where the frequency function will be located, by increasing the step size the impulse locations, in the frequency domain, are closer together and therefore there is more likelihood of aliasing to occur with the larger step size.

3.3 The Wavelet Transform

Now some mathematical properties[54–59] of the wavelet basis functions and the corresponding subspaces of L^2(R) will be presented. The V_m are subspaces of L^2 such that their union is L^2 and the W_m are subspaces of L^2 such that their orthogonal sum is L^2, however W_m are also subsets of V_{m-1}. The W_m are subspaces of L^2 such that their union is L^2 and their intersection is null and the W_m are mutually orthogonal subspaces. Also note that each V_m is a subset of V_{m-1}, and its principal property is that if $f(t)$ is an element of V_m then $f(2t)$ is an element of V_{m-1}. Thus $V_{j-1} = V_j \oplus W_j$ where $\oplus$ means orthogonal sum. It is possible to define a set of two-parameter functions $\phi_{mn}(t) = 2^{-m/2}\phi(2^{-m}t - n)$ that are basis functions for V_m and a set of two-parameter functions $\psi_{mn}(t) = 2^{-m/2}\psi(2^{-m}t - n)$ that are basis functions for W_m. The set ($\phi_{mn}(t)$,$\psi_{mn}(t)$) is called a scaling function, wavelet set

with $\psi_{mn}(t)$ as an orthogonal basis for L^2 and these are the wavelet basis functions used in this work.

Wavelet analyses can be done using various mother functions to build the wavelet basis functions but, as discussed by Strang[59], the basic set of mother functions (each dilation by a factor of two) was devised by Daubechies[55]. In this work, these are denoted by ψ_M where M is the number of filter function coefficients as defined below. For all M values the filter function coefficients have been tabulated[55,62] and, for many M values, the mother functions have been plotted[55,59]. For $M = 2$, the mother function is Haar's box function which is not differentiable but which is of pedagogic value, as discussed by Strang[59] and Chui[62]. Daubechies[55] has shown that the smoothness of the mother function increases slowly as M increases and therefore the localization of the mother function decreases slowly as M increases. In this work results are for the relatively smooth and fairly localized mother function ψ_8 and results for $M = 4$, 6, and 10 are pointed out when they occur.

Wavelets have been used to decompose a time series by use of an orthonormal basis set such as that used in Mallat's pyramidal algorithm[55,58] which shows the correspondence between orthonormal wavelet basis sets and discrete multiresolution decomposition. Thus, a signal is built from coarser and coarser approximations (multiresolutions) of original signal. Each "detail" is of lower resolution, one data point is removed between two that are kept. Each detail could be considered to be a spatial frequency band and this is not a trivial concern. Vetterli[63] discusses the idea of filter banks and how a wavelet analysis can be used to do signal processing. Chui[62] and Mallat[58] also refer to this process as partitioning the frequencies into octaves or frequency bands. Mallat's[58] description was "Hence, the detail signal $D_{2^j}f$ describes $f(t)$ in the frequency bands $[-2^{-j+1}\pi, -2^{-j}\pi] \cup [2^{-j}\pi, 2^{-j+1}\pi]$." The decomposition is based on powers of 2 and the reader is referred to Daubechies[55] for the derivations

of the following equations although, this work follows the terminology of Mallat[58] and Strang [59]. Therefore, discrete signal approximations are identified with $A_{\#}$ while details are identified with $D_{\#}$ (where # is an integer). We start with a function f which is constructed from a data sequence c^0 such that,

$$f = \sum_n c_n^0 \phi_{0n} \qquad [3.3]$$

or

$$f(t) = \sum_n c_n^0 \phi(t-n). \qquad [3.4]$$

Thus f is a function of V_0 (as defined earlier). The decomposition can be viewed as taking a set of basis transformations and therefore the signal is projected onto the basis plane while keeping only the projection. The approximation ($A_j f$) that is left is fuzzier (coarser) resolution and also a "detail"($D_j f$) data set is kept at this resolution that corresponds to the difference in information between two adjacent signal approximations, $A_j f$ and $A_{j-1} f$. Since $V_0 = V_1 \oplus W_1$, f is decomposed into its components

$$f = A_1 f + D_1 f, \qquad [3.5]$$

where

$$A_1 f = \sum_k c_k^1 \phi_{1k} \qquad [3.6]$$

and

$$D_1 f = \sum_k d_k^1 \psi_{1k}. \qquad [3.7]$$

Since

$$c_k^1 = \sum_k c_n^0 < \phi_{1k}, \phi_{0n} >, \qquad [3.8]$$

and the inner product is

$$< \phi_{1k}, \phi_{0n} >= 2^{-\frac{1}{2}} \int dt \phi(\frac{1}{2}t) \phi(t-(n-2k)), \qquad [3.9]$$

therefore

$$c_k^1 = \sum_n h(n-2k)c_n^0 \qquad [3.10]$$

with the filter function being

$$h(n) = 2^{-\frac{1}{2}} \int dt \phi(\frac{1}{2}t)\phi(t-n). \qquad [3.11]$$

In a similar manner

$$d_k^1 = \sum_n g(n-2k)c_n^0 \qquad [3.12]$$

with its filter function being

$$g(n) = 2^{-\frac{1}{2}} \int dt \psi(\frac{1}{2}t)\psi(t-n). \qquad [3.13]$$

The shorthand for this is $c^1 = Hc^0$ and $d^1 = Gc^0$ and the next level of decomposition is

$$A_1 f = A_2 f + D_2 f \qquad [3.14]$$

where

$$A_2 f = \sum_k c_k^2 \phi_{2k} \qquad [3.15]$$

and

$$D_2 f = \sum_k d_k^2 \psi_{2k}. \qquad [3.16]$$

Therefore the iterative procedure is

$$\begin{aligned} A_{j-1} f &= A_j f + D_j f \\ &= \sum_k c_k^j \phi_{jk} + \sum_k d_k^j \psi_{jk} \end{aligned} \qquad [3.17]$$

where the shorthand would give $c^j = Hc^{j-1}$ and $d^j = Gc^{j-1}$. Each lower detail (higher number) has one-half of the data points of the previous detail. Each detail is peeling[62] off a layer of information from the approximated signal and storing it

into the detail at that resolution. Note that the ϕ, ψ are considered to be a scaling function, wavelet pair as noted by Chui[62]. To reconstruct, just reverse the process.

The wavelet transform of x(t) is calculated and then details of x(t) at several stages for a specific time interval are discussed. A_jx(t) is a fuzzy approximation of x(t) at stage j while A_{j-1}x(t) is a less fuzzy approximation of x(t) at stage $j-1$ which can be reconstructed from A_jx(t) and D_jx(t). D_jx(t) is termed the detail of x(t) at stage j, or simply detail j and is the difference between the approximations to x(t) at stages j and $j-1$. Thus, the amplitude of D_jx(t) is proportional to the different information present in A_jx(t) and A_{j-1}x(t) in a time interval, t. In this work the amplitude of D_jx(t) is plotted and, to guide the eye, the points are joined by straight line segments with no smoothing.

3.4 Results

The complete wavelet transform and reconstruction of x(t) is calculated but the attention of this work is on the intermediate stages. Therefore, several details of x(t) are investigated for various total time intervals but these details are shown only for a specific time interval. In this time interval D_jx has high amplitude when A_{j-1}x and A_jx are significantly different. Unless otherwise stated, results are for a forcing frequency of $\omega = 1.0$. Figures 3.1(a), (b), (c) and (d) show x(t) for a total time interval of 0 to 200 for F = 1.0, 2.0, 4.0 and 6.0×10^{-3}, respectively. For the unforced and undamped Morse oscillator x(t) is periodic with period $10(2^{1/2}\pi) = 44.4$, and for the smallest F value (Figure 3.1(a)) it may be seen that the period of x(t) is close to this expected value. Even though in Figures 3.1(b), (c) and (d) the F values of the forcing term are considered to be weak, they still have a strong effect on the dynamics, and x(t) is highly aperiodic . This was first discussed in the higher-ordered phase plots chapter of this work.

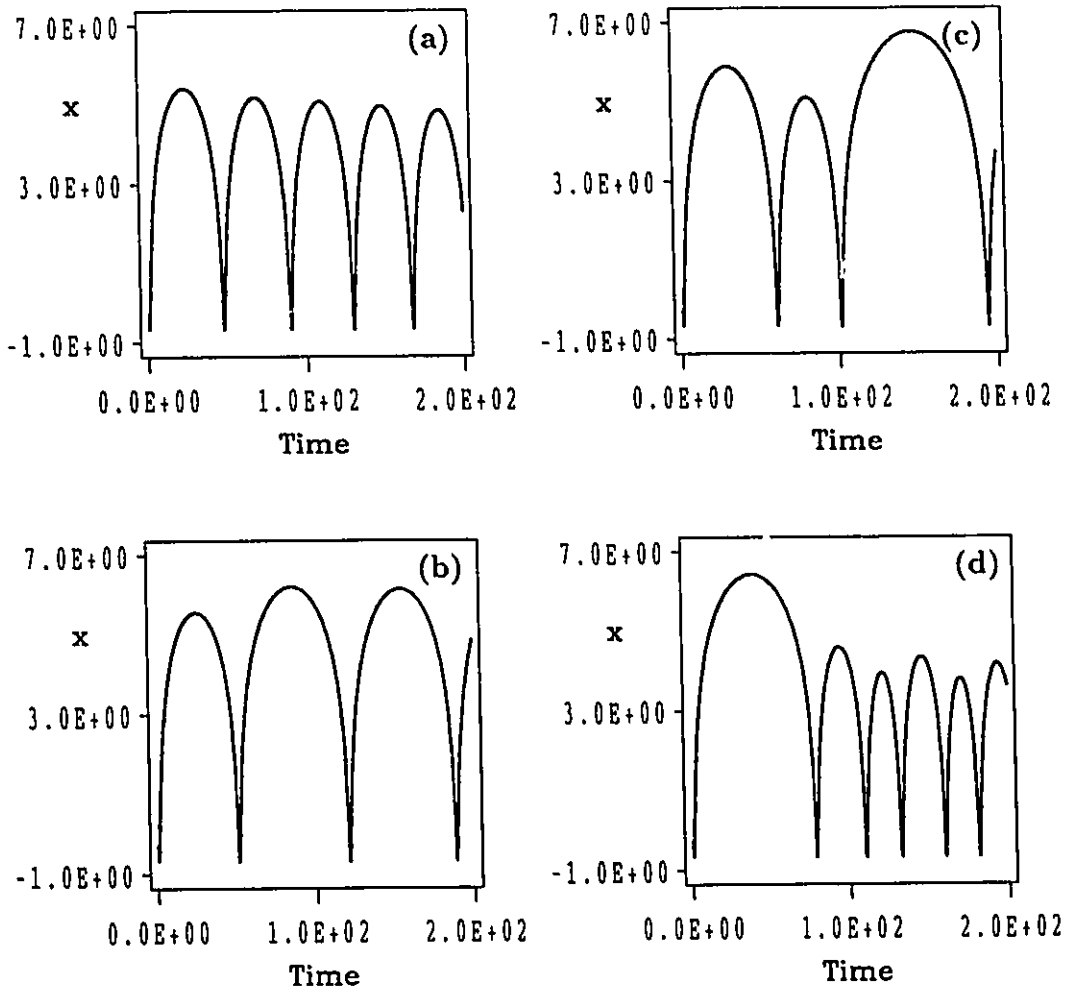

Figure 3.1 The coordinate, x(t), vs t for t = 0 to 200. (a) F = 1.0×10^{-3}; (b) F = 2.0×10^{-3}; (c) F = 4.0×10^{-3}; (d) F = 6.0×10^{-3}. A spline fit of the calculated data points was done and only the resulting line is plotted.

Unless otherwise stated, the signal x(t) was calculated using a step size of 5.00×10^{-2} for 4096 steps, which is a total time of 0 to 204.8 time units and the wavelet transform was also for this same total time. Since $4096 = 2^{12}$, there are 12 details of x(t), but only details 3, 4 and 5 for t = 10 to 40 are shown, in most cases. For this time interval, Figures 3.2(a), (b), (c) and (d) show an expanded vertical scale of x(t) for F = 1.0, 2.0, 4.0 and 6.0×10^{-3} and it may be seen that there is a relatively slow rate of change of the coordinate for this time interval. Figures 3.3(a), (b), (c) and (d) show detail 3 of the wavelet transform of x(t) (hereafter referred to simply

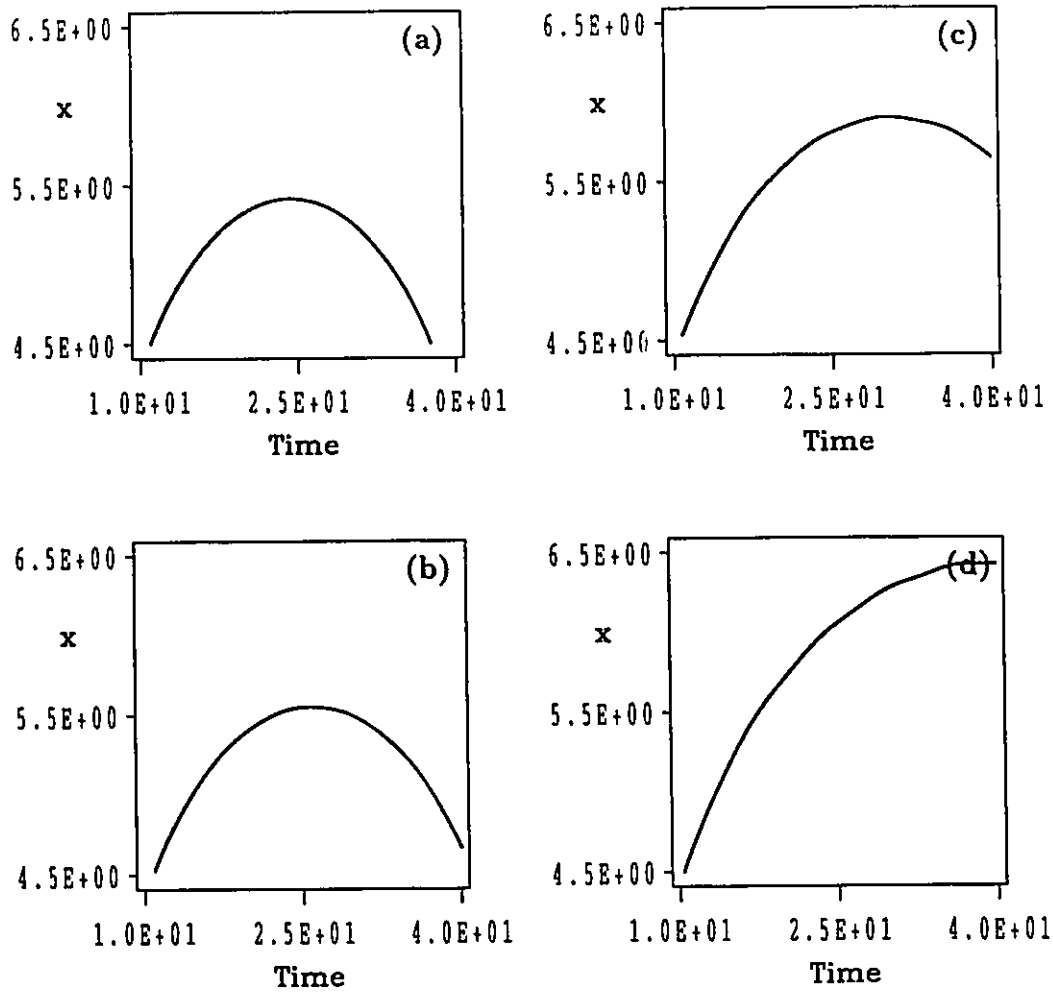

Figure 3.2 Same as for Figure 3.1 but for t = 10 to 40 with the vertical scale expanded.

as detail 3 or D_3) for F = 1.0, 2.0, 4.0 and 6.0×10^{-3} and since the plots are "noisy" no useful information can be extracted. Details 1 and 2 are not shown since even less information is present in them. Figures 3.4(a), (b), (c) and (d) show detail 4 of x(t) for F = 1.0, 2.0, 4.0 and 6.0×10^{-3} with the same vertical scale for all F values. In Figure 3.4 the plots have structure that is predominantly periodic which is not present for the unforced and undamped Morse oscillator and therefore is due to the weak forcing term. Notice that the vertical axis scale of Figure 3.4 is an order of magnitude larger than that of Figure 3.3. In Figure 3.4 as the F value increases the

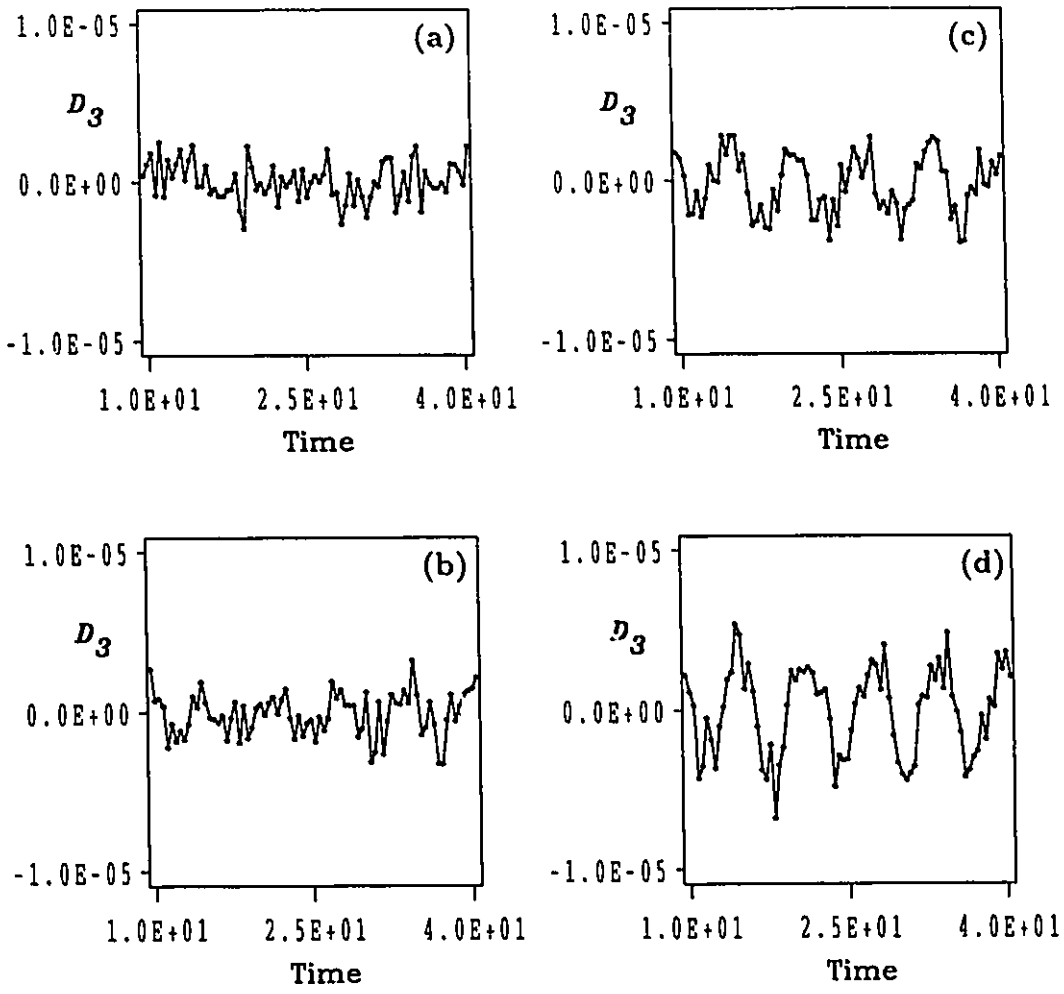

Figure 3.3 Detail 3 of x(t) for t = 10 to 40. (a) F = 1.0×10^{-3}; (b) F = 2.0×10^{-3}; (c) F = 4.0×10^{-3}; (d) F = 6.0×10^{-3}. Notice that the axes are scaled the same for all plots.

amplitude of the oscillations ((a)-(d)) increases and therefore the amplitude of the forcing term is qualitatively determined. It is clear that the period of the waveform in each detail is approximately 2π, as expected for $\omega = 1.0$ indicating that the frequency of the forcing term has been quantitatively determined from the detail. Figures 3.5(a), (b), (c) and (d) show detail 5 of x(t) for F = 1.0, 2.0, 4.0 and 6.0×10^{-3}, respectively. Note that although the vertical scale is the same for all F values, it is an order of magnitude greater than the vertical scale used in Figure 3.4. Comparison of Figures 3.4 and 3.5 indicate that detail 5 is similar to detail 4, although in Figure 3.5 the

jaggedness of each detail is more pronounced as there are half as many points and the waveform is not sampled correctly. Detail 6 and higher are more jagged still for this time interval and are therefore not shown. From these figures it is obvious that the higher details are more sensitive in that the amplitude of the oscillations is greater but it may be more difficult to pick out the weak forcing term due to an improper sampling rate of the waveform. It would be expected that an increase in either the number of data points or a change in step size, or both, could be used to overcome this problem. The wavelet transform is not that straightforward and these suggestions will be discussed later in this section.

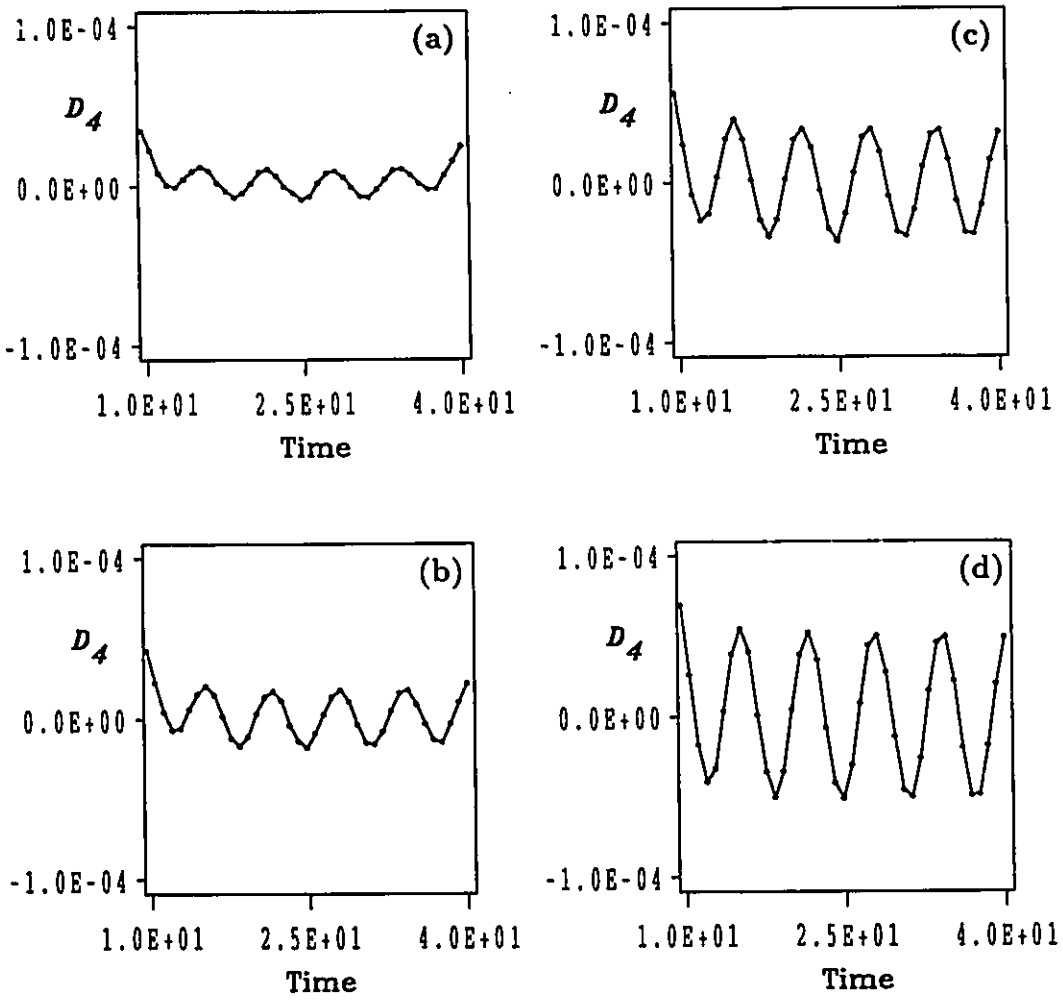

Figure 3.4 Same as for Figure 3.3 but for detail 4.

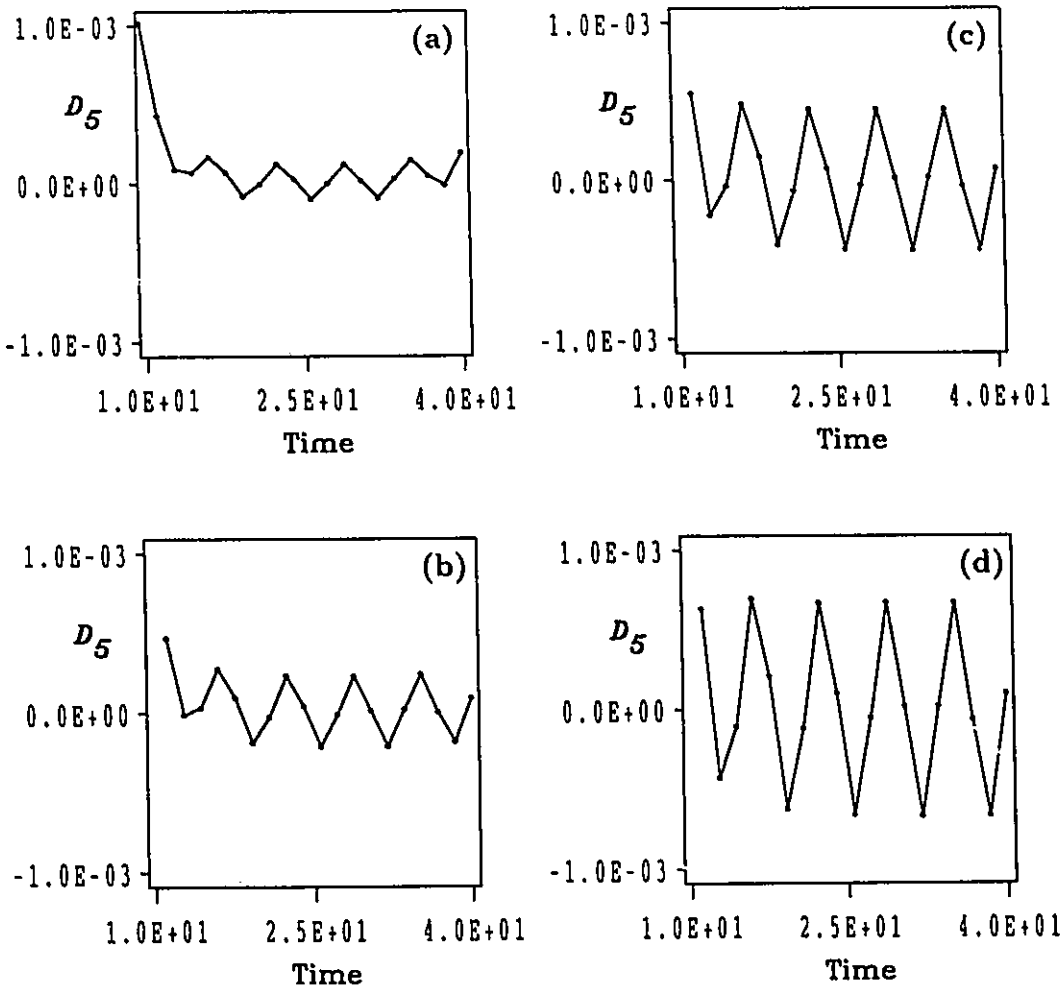

Figure 3.5 Same as for Figure 3.3 but for detail 5.

Figures 3.6(a), (b), (c) and (d) show detail 3 of x(t) for mother functions ψ_4, ψ_6, ψ_8 and ψ_{10} with $\omega = 2.0$ and F = 6.0×10^{-3}. Note that the vertical scale is the same for all mother functions as that used in Figure 3.4, except for Figure 3.6(a) where it is an order of magnitude larger. The plots of detail 3 in Figure 3.6 are predominantly periodic with a period of approximately π, as expected for $\omega = 2.0$. Figures 3.7(a), (b), (c) and (d) show detail 4 of x(t) for the mother functions ψ_4, ψ_6, ψ_8 and ψ_{10} with the vertical scale the same for all mother functions, except for Figure 3.7(a) where it is an order of magnitude larger. Comparison of Figures 3.7 and 3.6 allows the observation that detail 4 is similar to detail 3, although in Figure 3.7

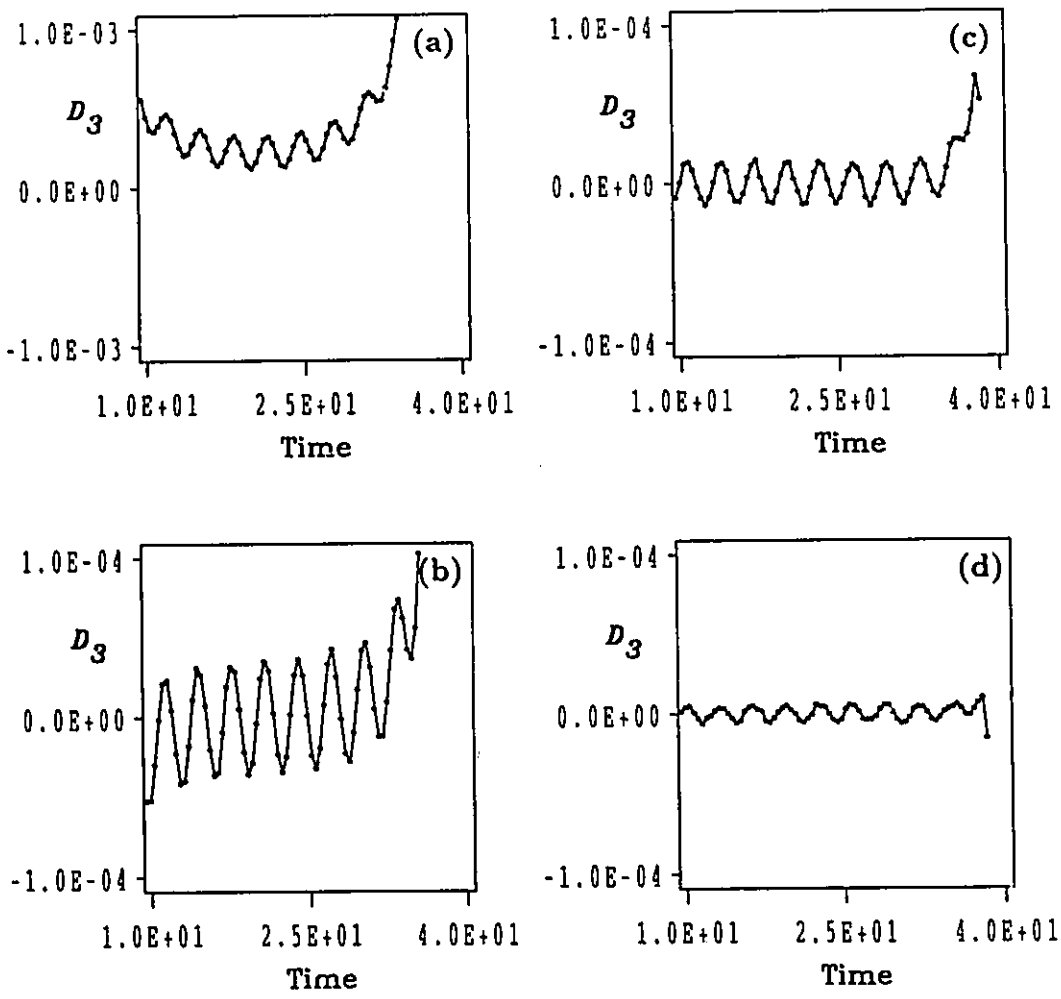

Figure 3.6 Detail 3 of x(t) for t = 10 to 40, $\omega = 2.0$, $F = 6.0 \times 10^{-3}$ and (a) ψ_4; (b) ψ_6; (c) ψ_8; (d) ψ_{10}. Notice that the y axis in (a) is an order of magnitude larger than in the others.

the jaggedness of each detail is more pronounced as there are half as many points and the waveform is undersampled. Comparing results for ψ_8 and $F = 6.0 \times 10^{-3}$, it may be seen that the waveform in Figure 3.6(c) is similar to the waveform in Figure 3.4(d) while Figure 3.7(c) is similar to Figure 3.5(d). Thus for a forcing frequency which is double, the waveforms are similar but at a detail number one lower. This is further illustrated in Figure 3.8 where the left-hand column is for a forcing frequency of $\omega = 0.5$ and the right-hand column is for a forcing frequency of $\omega = 8.0$ with the forcing amplitude the same as before at $F = 6.00 \times 10^{-3}$. In general, it is expected

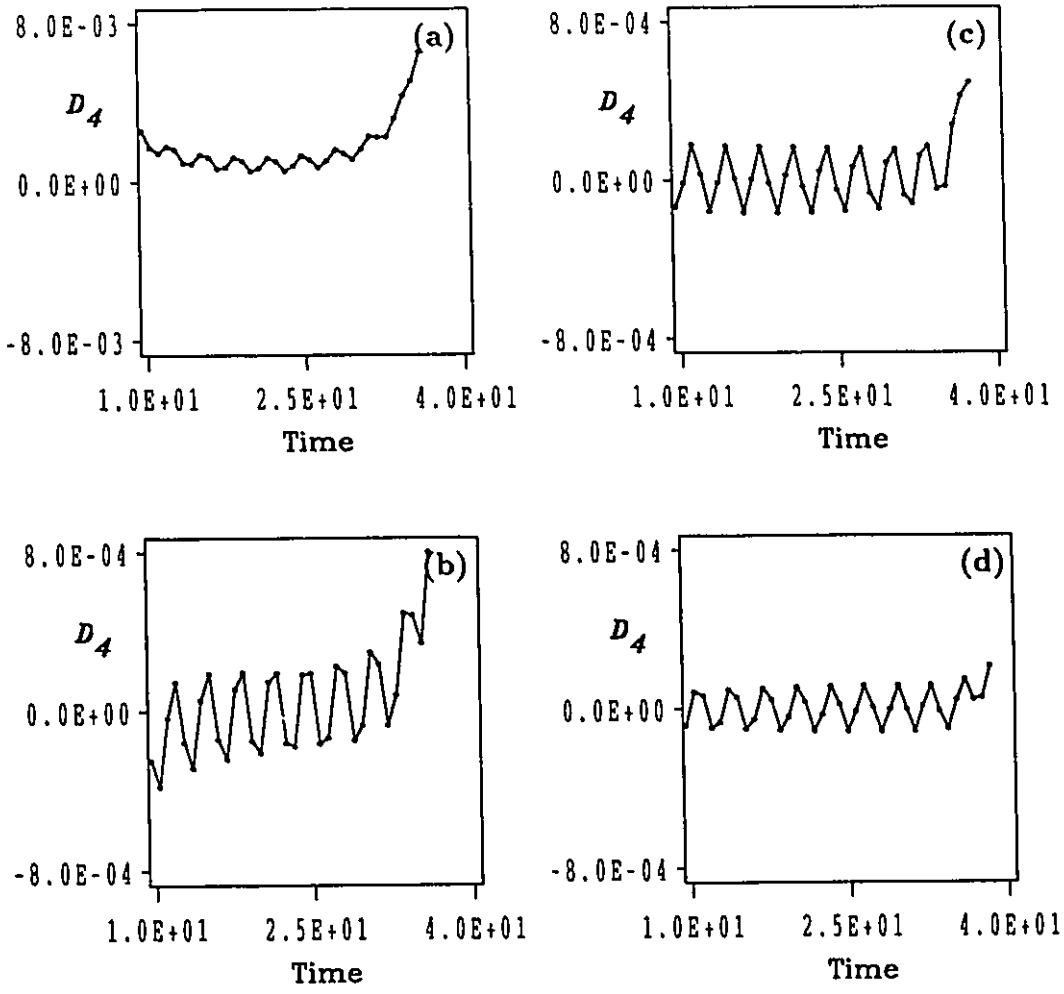

Figure 3.7 Same as for Figure 3.6 but for detail 4.

that for a forcing frequency which is 2^N, the waveforms are similar but at a detail number N lower, although this rule is not followed for a large range of frequencies. For a forcing frequency of 1/2 it would be expected that the waveform that was detected for $\omega = 1.0$ in D_4 of Figure 3.4(d) would only appear in D_5 of Figure 3.8. Although there is a waveform present in D_5 of Figure 3.8(c) it is also still present in D_4 of Figure 3.8(b). However if the magnitudes of the waveform in Figures 3.8(b) and (c) are compared to the magnitudes of the waveform in Figure 3.4(d) one can see that the magnitude of the waveform in Figure 3.8(b) is about 4 times less than that in Figure 3.4(d) but the magnitude of the waveform in Figure 3.8(c) is larger than

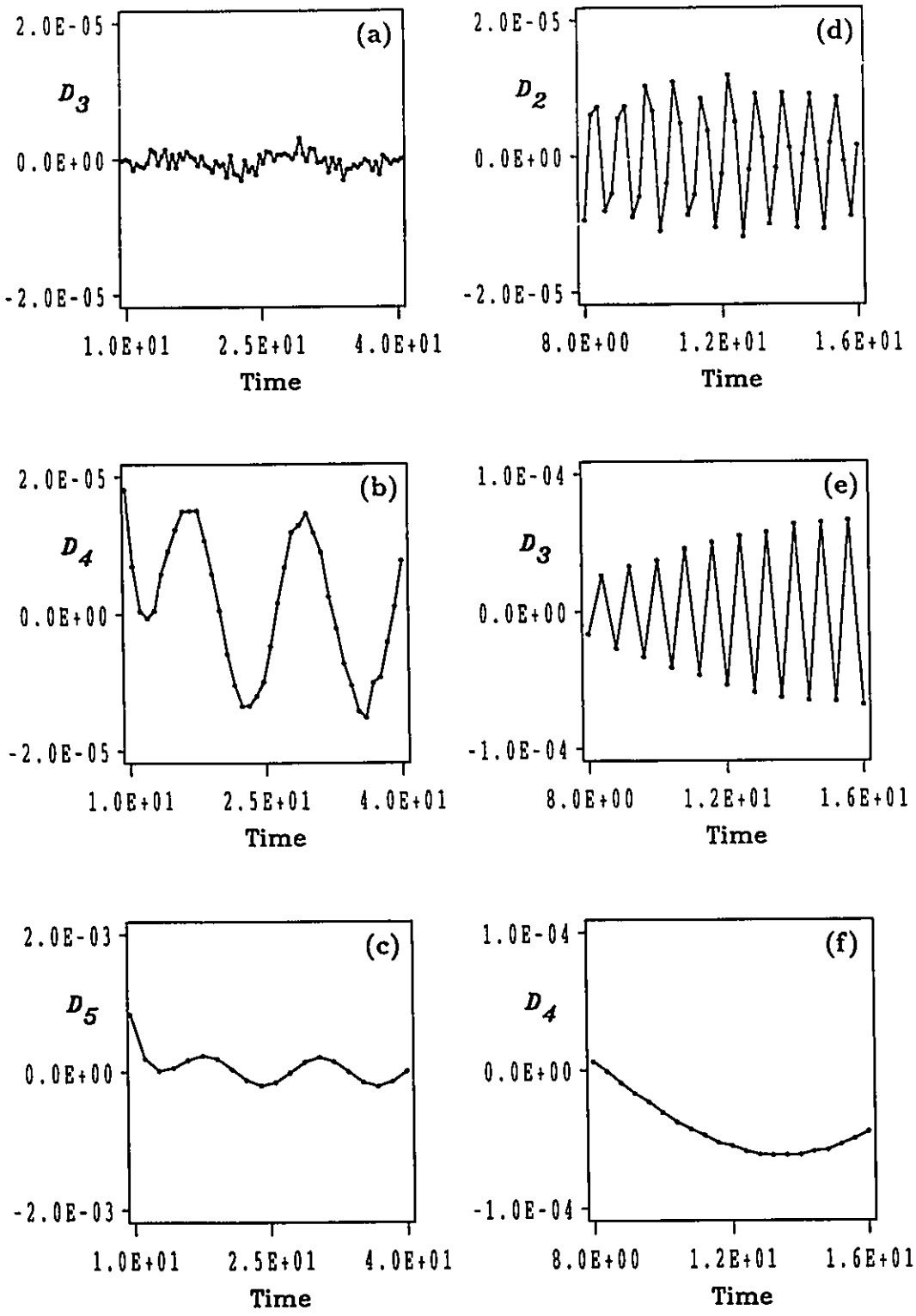

Figure 3.8 Details for a forcing amplitude of $F = 6.00 \times 10^{-3}$. The left hand column is for a forcing frequency $\omega = 0.5$ while the right hand column is for a forcing frequency of $\omega = 8.0$.

that of Figure 3.4(d), by about 2-3 times in fact. The rule has worked, although not perfectly for this case. Notice that there is a partial waveform present in Figure 3.3(d) for the $\omega = 1.0$ case. Therefore there seems to be a set of details that contain the waveform of a specific forcing frequency. The result points in the correct direction, and the waveform is well enough resolved in D_4 and D_5 of Figure 3.8(b) and (c) to see that the period is the expected 4π. In Figure 3.8(d), (e), and (f), details 2, 3, and 4 are shown and the forcing frequency $\omega = 8.0$ is detected although not in the expected detail. Since the forcing frequency in this case is 4 times the $\omega = 2.0$ case it would be expected that the waveform would be detected 2 details lower in number from the D_4 of Figure 3.7(d). In Figure 3.8(d) and (e) the ragged waveform appears, and this result is in the expected range but the waveform was expected to be smoother. The detail number that the frequency appeared in was lower or higher as predicted but the detail number that the waveform appears in is does not follow a ridged rule that can explain exactly where the waveform of a specific forcing frequency will appear. This will be discussed further later in this chapter.

As mentioned previously, the localization of the mother function decreases slowly as M increases and, qualitatively, this accounts for the trends in Figures 3.6 and 3.7. Thus for the most localized mother function, ψ_4 (Figures 3.6(a) and 3.7(a)), the amplitude of the oscillations is greatest but these are superimposed on the largest global variations of the details as the corresponding wavelet basis functions behave in the most independent fashion. Again, it may be more difficult to pick out the weak forcing term.

An advantage of the wavelet analysis becomes clear when results for different total time intervals with forcing frequency $\omega = 2.0$, F= 6.0×10^{-3} and a mother function ψ_8 are considered. Figure 3.9 shows detail 3 of x(t) with the same step size as before (5.00×10^{-2}) but with a longer total time in (a) 8192 steps $\times$ 5.00×10^{-2} =

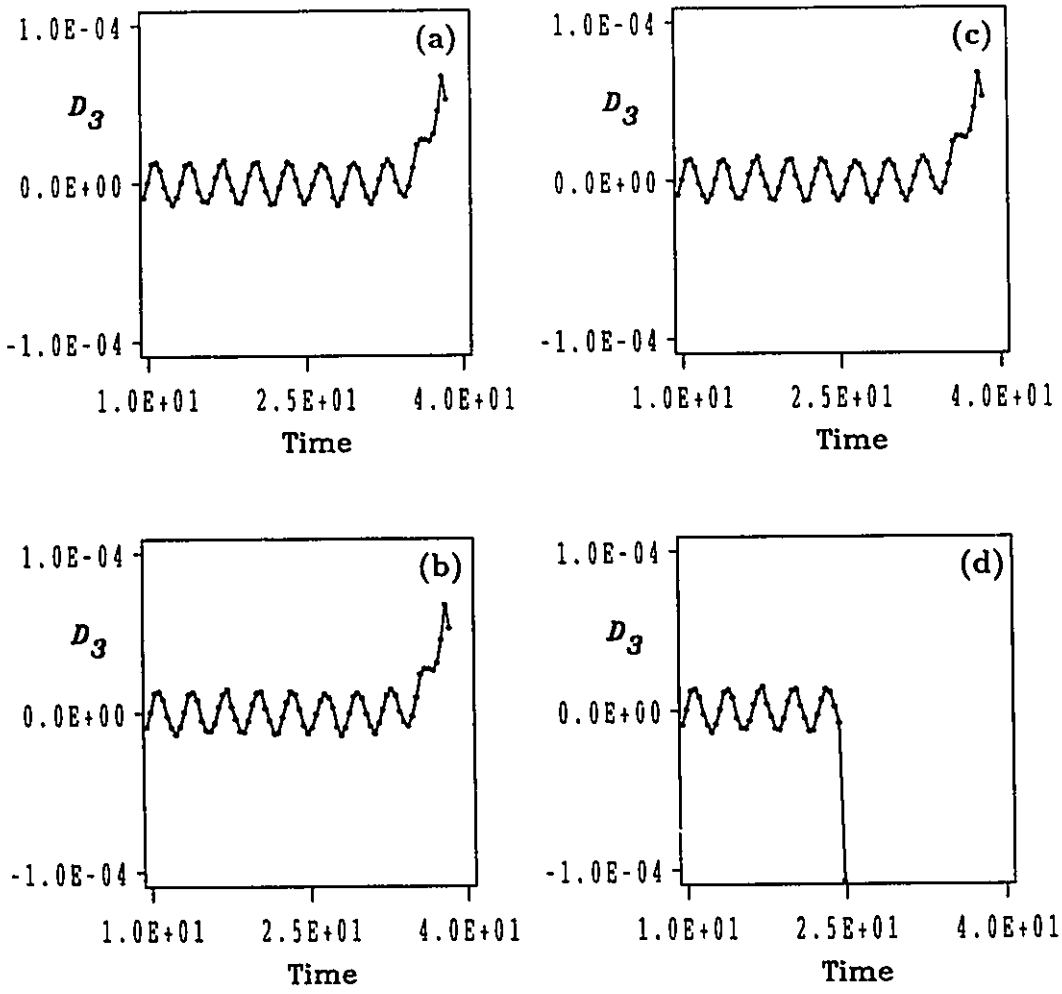

Figure 3.9 Detail 3 of x(t) for t = 10 to 40, $\omega = 2.0$, $F = 6.0 \times 10^{-3}$, ψ_8 and a total time of 0 to (a) 409.6; (b) 102.4; (c) 51.2; (d) 25.6.

409.6 and shorter total times in, (b) 2048 steps $\times$ 5.00×10^{-2} = 102.4, (c) 1024 steps $\times$ $5.00 \times 10^{-2} = 51.2$ and (d) 512 steps $\times$ $5.00 \times 10^{-2} = 25.6$. Comparison of Figure 3.6(c) and Figures 3.9(a), (b), (c) and (d) shows that the waveforms in the D_3 details are essentially the same even for Figure 3.9(d) where the waveform exists for only part of the time interval 10 to 40. The waveforms in the details are not exactly the same because there are edge effects, as seen in Figure 3.9(d) but since the wavelet basis functions are localized, the edge effects are minimal although they are increasingly significant as M increases. Thus better results are not obtained by

increasing the number of data points and leaving the step size the same. That is, increasing the total time has little effect on the wavelet transform results and neither does decreasing the total time.

Table 3.1 Number of data points in detail data files. This is for a total time of 204.8 time units but different step sizes and different total number of data points in the original signal file.

Signal data	step size	Number of data points (column) for respective Detail # 1	2	3	4	5	6	7	8
4096	5.00×10^{-2}	2048	1024	512	256	128	64	32	16
8192	2.50×10^{-2}	4096	2048	1024	512	256	128	64	32
16384	1.25×10^{-2}	8192	4096	2048	1024	512	256	128	64
32768	6.25×10^{-3}	16384	8192	4096	2048	1024	512	256	128

Table 3.1 illustrates that the wavelet transform resolution is step size dependent rather than total time dependent as the Fourier transform is. Table (3.1) shows the complete range of change discussed in this work. It shows that as the step size is halved, while maintaining the same total time, the total number of steps must be increased (doubled). The detail # in which the unchanged forcing frequency can be found will have the same number of data points. Thus as the data step is halved the detail # in which the forcing frequency is detected is increased by 1. For example, D_3 is where the forcing frequency $\omega = 2.0$ with a step size of 5.00×10^{-2} and for 4096 data points, was detected. In Table 3.1, row 1 has 4096 points in the signal file and a set size of 5.00×10^{-2}. Detail 3 was where the waveform with a frequency of $\omega = 2.0$ was detected and in the Table 3.1 detail 3 column intersection with row 1 there is 512 data points in the detail file. For a signal of 8192 points and a step size of 2.50×10^{-2} (row 2), D_4 has 512 data points. Similarly for a signal of 32768 points and a step size of 6.25×10^{-3} (row 4 of Table 3.1) detail 6 has 512 data

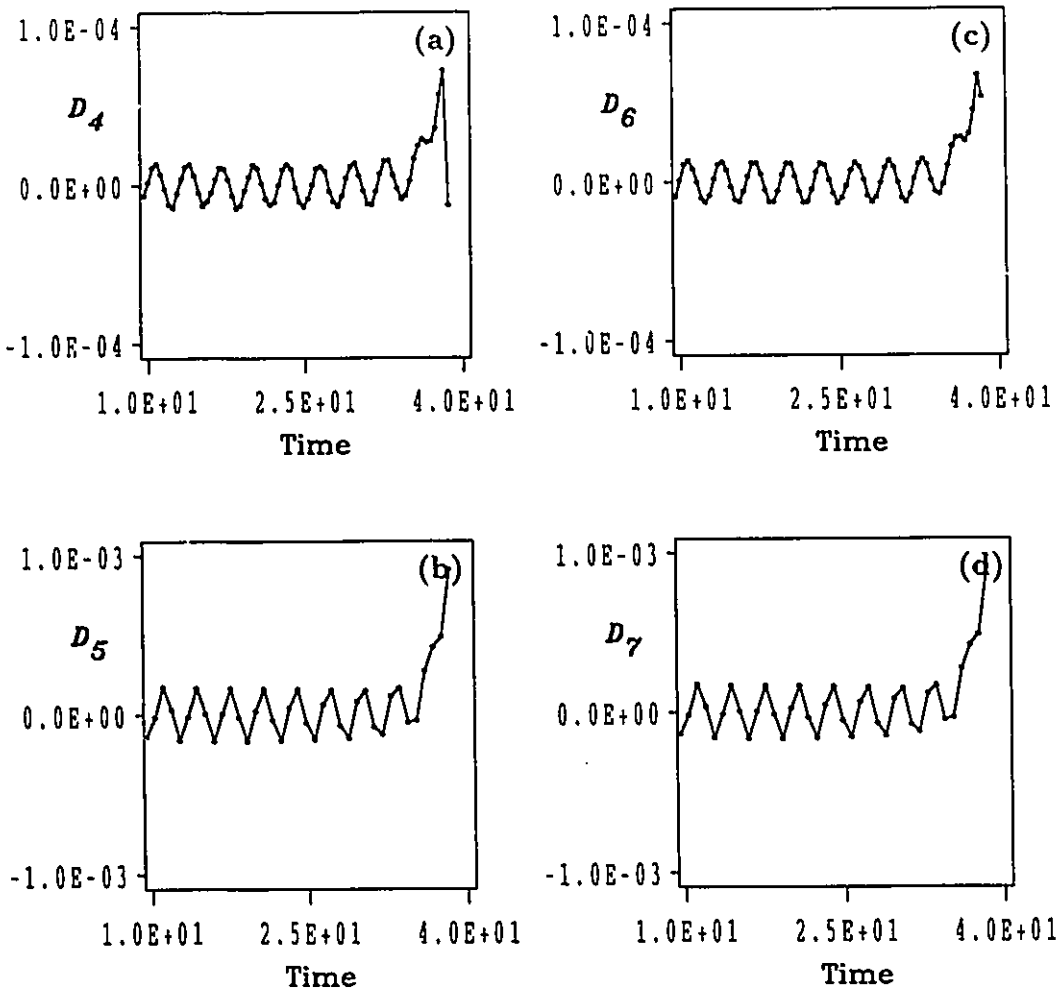

Figure 3.10 (a) and (b) Step size = 2.5×10^{-2}. (c) and (d) Step size = 6.25×10^{-3}. t = 10 to 40, $\omega = 2.0$, F = 6.0×10^{-3}, ψ_8, and total time = 0 to 204.8.

points. Signal files with these parameters were calculated and these are illustrated in Figure 3.10. The left column for step size 2.5×10^{-2} and the right column for step size 6.25×10^{-3}. Compare the waveform in D_3 of Figure 3.6(c) with the waveform in D_4 of Figure 3.10(a) and D_6 of Figure 3.10(c). Also compare the waveform in D_4 of Figure 3.7(c) with the waveform in D_5 of Figure 3.10(b) and D_7 of Figure 3.10(d). In these cases the detail number did change by the expected value as predicted by the information gained from Table 3.1. The detail in which the forcing frequency is detected is determined by the selection of the filter functions. Wavelet analysis can

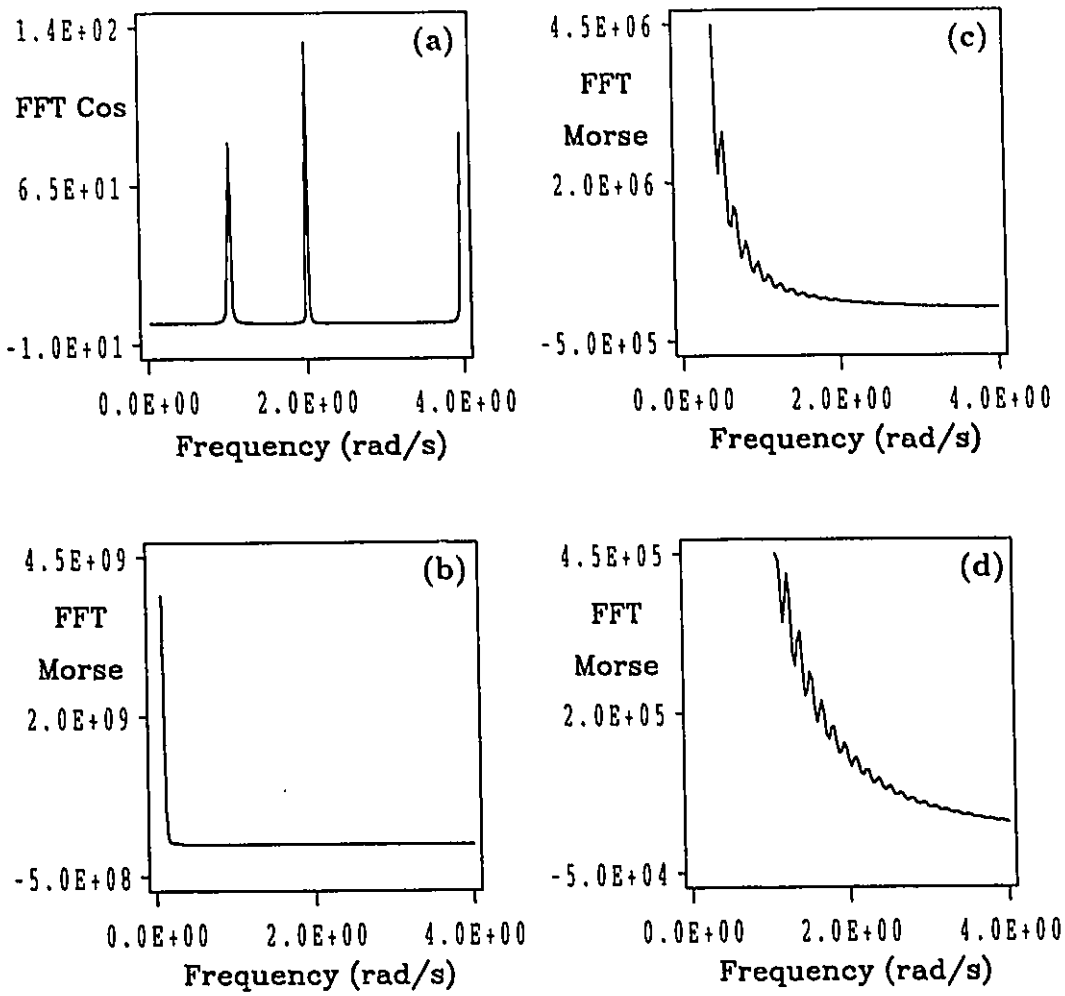

Figure 3.11 Fast Fourier transform of a forcing term which is the sum of three cosine functions ($\omega_1 = 1.0$, $\omega_2 = 2.0$, and $\omega_3 = 4.0$) each with an amplitude of $F = 6.00 \times 10^{-3}$ and a Morse potential with the same forcing conditions.(a) is a plot of the Fast Fourier Transform of the cosine functions, (b) is the fullscale plot of the Fast Fourier Transform of the same forcing conditions coupled with the Morse potential at E = 0.99 of dissociation. (c) is an expansion of the vertical scale, as is (d).

be viewed as selecting a set of filter functions to operate on the digitized (discretized) signal function. Just as the discretization process affects the outcome of an FFT (see the section in this chapter on FFT) so does the discretization cause a change in how the wavelet analysis detects differences in the signal approximation at two different resolutions. Remember that the detail is exactly this difference between the signal at two different approximations, one fuzzier (coarser) that the other.

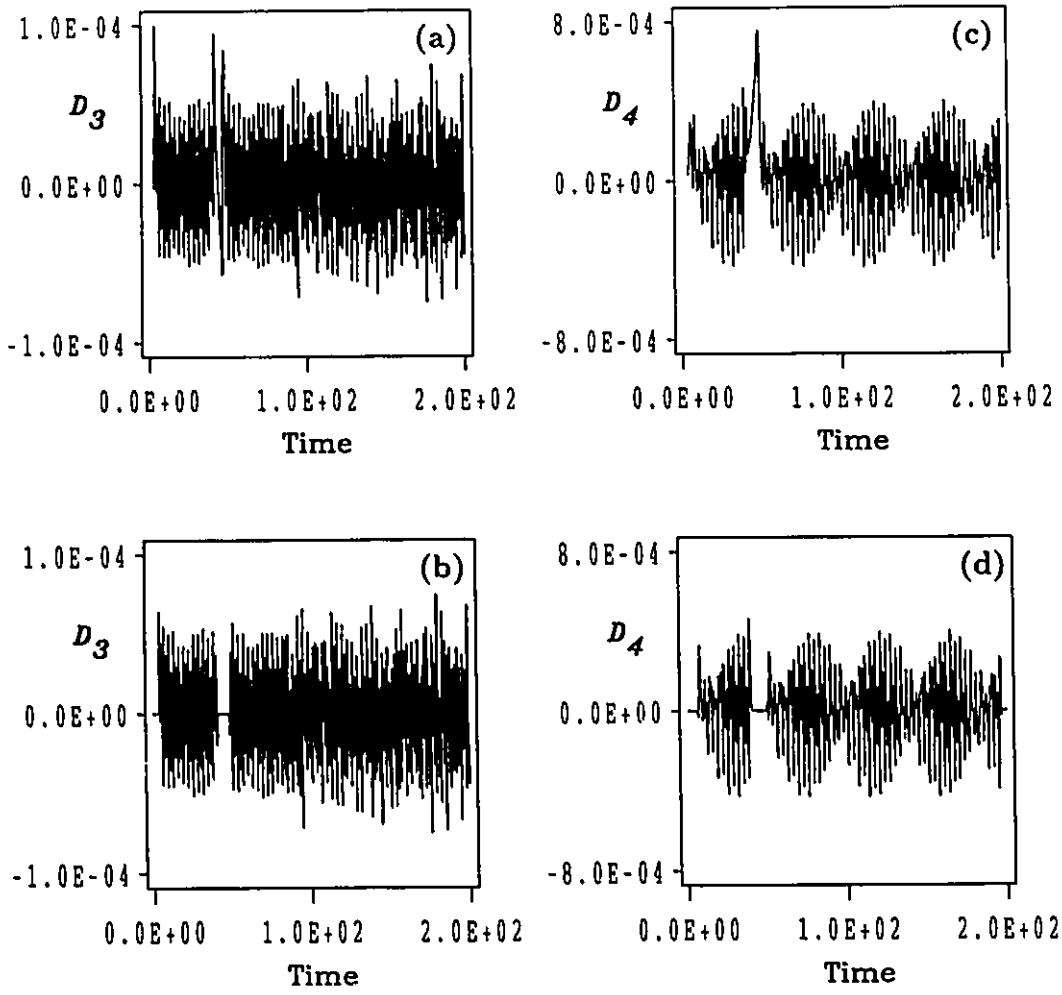

Figure 3.12 Details 3 and 4 for the Morse oscillator with three forcing frequencies as described in the previous figure. (a) is detail 3, (b) is detail 3 that has been "altered", (c) is detail 4, and (d) is detail 4 that has been "altered".

Now, this work turns to developments where the wavelet analysis is not used to replace the Fourier transform but instead is used as a preprocessing function. To illustrate this, instead of using a single forcing frequency the forcing term is the sum of three cosine functions with different frequencies but each has the same amplitude. In Figure 3.11(a) the FFT of three cosine functions with the same amplitude (F= 6.00×10^{-3}) but three different frequencies ($\omega_1 = 1.0$, $\omega_2 = 2.0$, and $\omega_3 = 4.0$) is plotted. The three frequencies are easy to distinguish, and the amplitude differences are explained by the sample rate differences, as discussed earlier in this chapter. The

file was created using a step size of 5.00×10^{-2} for 4096 steps and thus the usual total time of 204.8 time units. These three simple frequencies are easy for the FFT to determine. However, in Figure 3.11(b) the FFT of a Morse potential and an identical forcing term (F= 6.00×10^{-3}, $\omega_1 = 1.0$, $\omega_2 = 2.0$, and $\omega_3 = 4.0$) shows the difficulty that the FFT has in detecting the three weak forcing frequencies when much larger frequencies, due to the Morse potential, are present. Figures 3.11(c) and (d) are expansions of the vertical scale. Even in the case where the scale has been expanded as much as possible it is difficult to detect even one of the three frequencies. This is where wavelet analysis can be used to filter out the unwanted frequencies leaving the weaker forcing frequencies to be detected by the FFT.

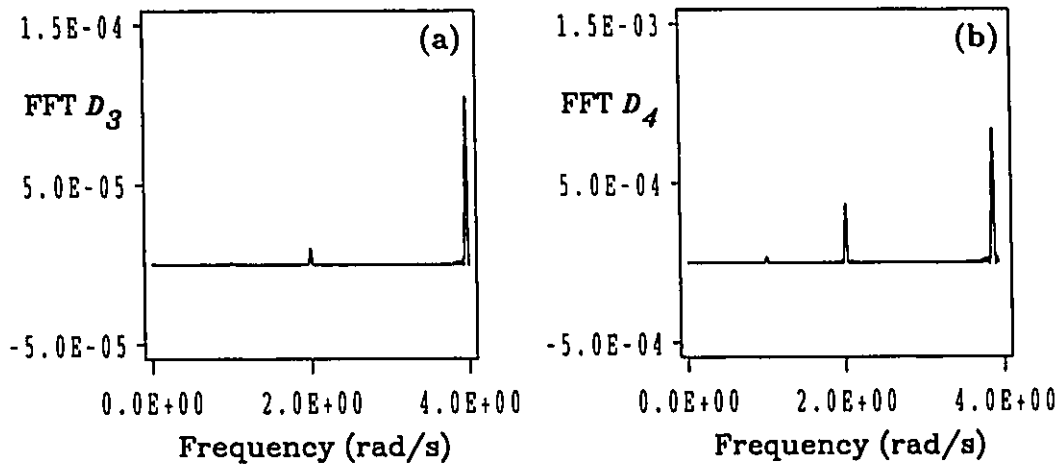

Figure 3.13 FFT of details 3 and 4 that have been "altered".

In Figure 3.12 details 3 and 4 are shown of a wavelet analysis of the above mentioned Morse data file. The details shown in Figures 3.12(b) and (d) are "altered" versions of Figures 3.12(a) and (c) respectively. The data files were "altered"in that any data points that were large deviations from the plotted y-axis scale were set to zero. It is evident that only a few data points have been zeroed, from comparison of 3.12(a) and (b), as well as 3.12(c) and (d). What effect this has on the reconstruction of the signal is discussed in a later section. Figure 3.13(a) is the FFT of

the "altered" detail 3, and 3.13(b) is the FFT of the "altered" detail 4 and the three forcing frequencies are found in these two plots. Note that as stated before the higher frequencies are better represented (detected) in the lower numbered details. This is observed in Figure 3.13(b) where the highest frequency detected is $\omega = 3.85$ and should have been 4.00 radians per second but Figure 3.13(a) correctly identifies the highest frequency. Similar results were obtained for frequencies such as 1.15, 2.15, and 4.15 radians per second. Note that the higher frequencies are incorrectly sampled in the higher numbered detail files which causes aliasing problems.

Now, this work investigates a Morse potential with a forcing term that has nine different frequencies ($\omega_i = i$ with $i = 1, 2, 3, \cdots, 9$). This data was produced using a step size 5.00×10^{-2} and 4096 data points as used previously. Figure 3.14(a) is the FFT of the "altered" D_2 of the Morse coordinate and 5 frequencies at the correct intervals are observed. Figure 3.14(b) is the FFT of the "altered" D_3 and, while frequencies 3 and 4 are observed and frequencies 1 and 2 can be guessed at there are also some extra frequencies observed at 6.8 and 7.8 radians per second due to aliasing. The FFT of an "altered" D_4 is not shown here and in it 1, 2, 3 and 4 radians per second can be seen but the plot is very noisy and other peaks also appear.

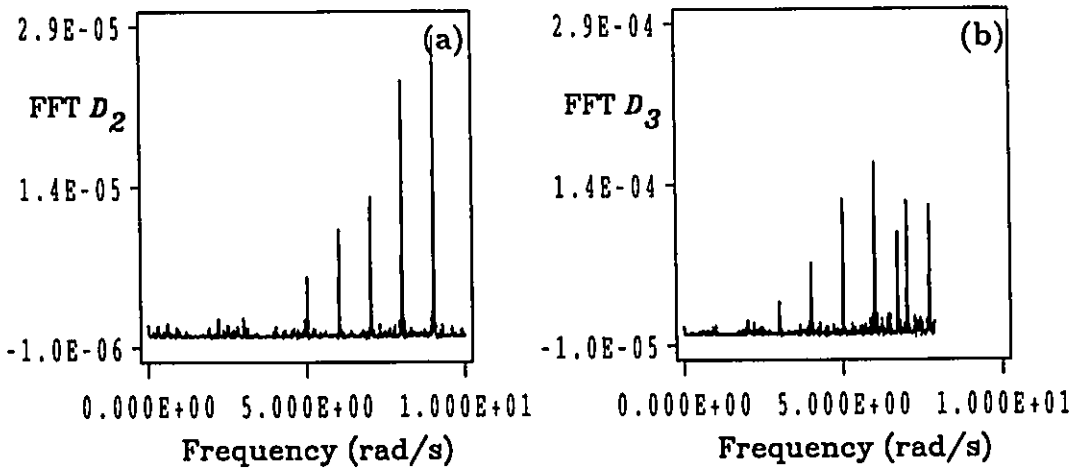

Figure 3.14 FFT of details 2 and 3 that have been "altered" for a Morse signal with 9 forcing frequencies.

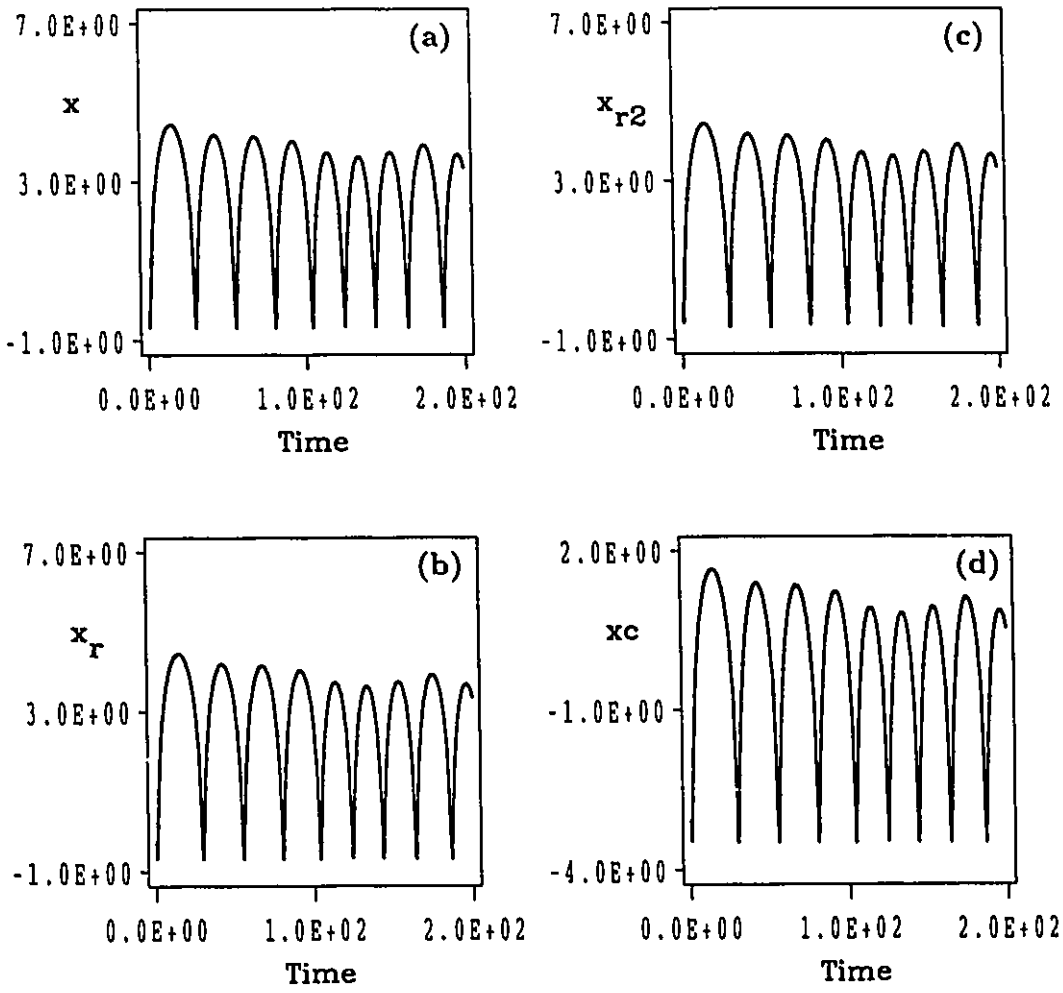

Figure 3.15 Signals for the Morse coordinate with 9 separate forcing frequencies. (a) the original signal, (b) is the usual reconstructed signal, (c) is the reconstructed signal using some details that have been modified, and (d) is the original signal that has been dc adjusted.

Again the detail files were "altered" in that data points that were large excursions from the rest of the data were set to zero. There were four detail files that had been "altered", D_1, D_2, D_3, and D_4. These files were then used to reconstruct the signal so a comparison of reconstruction files could be done. Figure 3.15(a) is a plot of the Morse coordinate with nine separate forcing frequencies ($\omega_i = i$ with $i = 1, 2, 3, \cdots, 9$) each with a forcing amplitude of F $= 6.00 \times 10^{-3}$. Figure 3.15(b) is a plot of the reconstructed coordinate while (c) is a plot of the second reconstructed

signal file which used the first four details that had been "altered" and the other four unedited detail files. The line resulting from a spline fit to the data is what was plotted in Figures 3.15(a)-(d). The actual data points of the original signal and the usual reconstructed file are very similar while the second reconstructed file has some differences. However the overall structure of the coordinate is seen to be unaltered by the second reconstruction process (compare Figures 3.15(a), (b) and (c)).

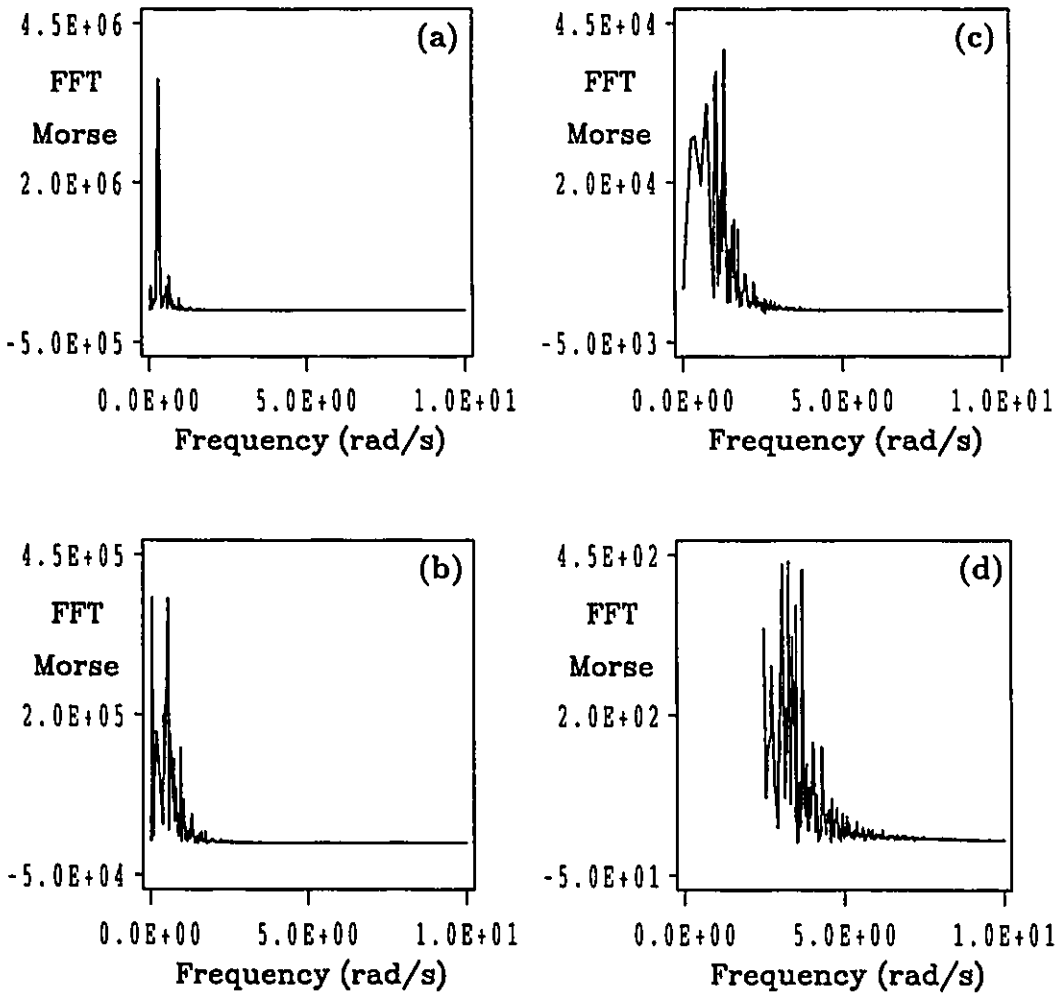

Figure 3.16 FFT of the Morse coordinate from which the constant 2.8 was subtracted. (a) is the fullscale plot, (b) is an expansion, as are (c), and (d).

Figure 3.15(d) is the usual reconstruction file of the original signal but it has been adjusted to decrease the amplitude of the zero frequency component of the

Fourier transform. In this case the value 2.8 was subtracted from all data points of the original signal file. Figure 3.16 is a plot of the FFT of this adjusted file where (a) is the fullscale plot. Note that the zero frequency component has a much smaller amplitude than the plot of the FFT of the Morse coordinate with three forcing frequencies (see Figure 3.11(b)). This "dc" shifting of the data is a common procedure used to minimize the amplitude of the zero component. It was not done for the three frequency situation because the system dissociated after 60 time units. The point is that even after this adjustment has been made there is little chance of being able to detect the 9 frequencies since they are of such small amplitudes compared to the amplitudes of the frequencies that make up the Morse function itself. The reader is referred to chapter two where the approximation to the Morse function was discussed.

Thus the wavelet analysis alone can detect a single frequency that the FFT cannot detect. The combination of wavelet-FFT can detect a combination of frequencies that the FFT could not detect and that the wavelet analysis had difficulty with. This demonstration is not complete since a real signal complete with decay and noise has not been done. It appears that the wavelet analysis that has been outlined so far is not enough to complete this task. There is hope however, in a paper by Delprat, *et al*[71] who have used their algorithm to ratio out the frequencies of interest from a set of frequencies. They then do another analysis of the system and keep ratioing out the frequencies that have been detected and look for other frequencies of interest. Therefore this process is left for future work on the Morse oscillator and other chemical (kinetic) systems.

3.5 Summary

In this work a wavelet analysis of the coordinate of a weakly forced and weakly damped Morse oscillator near dissociation was presented. The coordinate was highly

aperiodic in this highly anharmonic regime and in fact chaotic under some of the conditions presented. It has been shown that the forcing amplitude can be qualitatively determined while the forcing frequency can be quantitatively determined, even for short total times. When the coordinate is highly aperiodic it is not possible to determine these quantities by subtracting off the coordinate of the unforced and undamped Morse oscillator since the unforced undamped coordinate has a completely different period than the forced and damped case. Therefore subtraction of the two cases is not possible. Even magnification of the coordinate as was done in Figure 3.2 does not allow the forcing frequency to be determined. The FFT of the Morse has too many large amplitude frequencies present from the Morse potential and the frequencies of the forcing term are effectively buried.

Since each stage of the wavelet transform uses a different resolution it is termed a multiresolution decomposition. Wavelet basis functions are well localized in both frequency and time for a wide range of frequency and time intervals. Thus a "good" time-frequency window is created using a wavelet transform. The wavelet basis functions used in this work, ψ_{mn}, are automatically orthogonal for different m since they are basis functions for different W_m. Consequently, wavelet basis functions at different stages may be mixed and problems of linear dependence may be minimised. Details of the coordinate at several stages have been compared and a weak forcing term has been detected in certain details when the corresponding wavelet basis functions have the appropriate localization in both frequency and time. The combination of a wavelet transform followed by an FFT of the details has also shown that several frequencies can be detected at the same time. In fact these frequencies can be detected even when their amplitudes are much smaller than the amplitude of the frequencies that make up the Morse potential.

In closing two aspects of wavelet analysis are addressed. First, unlike a Fourier transform, a wavelet transform is not unique. Coifman and Wickerhauser[72] and

others are searching for best fit wavelet basis sets to use for reconstruction purposes and analysis of waveforms. The present work has shown that, for the Morse oscillator system, effective results may be obtained using several of the basis sets of mother functions devised by Daubechies[55].

Second, this work has shown that weak forcing frequencies can be determined only when the rate of change of the coordinate is relatively slow (small). However, researchers are working to overcome this limitation by using newer algorithms and ratioing out detected frequencies[71].

While these remarks may appear to limit the usefulness of wavelet analysis they really should be viewed only as a caution against believing that a wavelet analysis can solve any and all problems. Wavelet analysis is a tool that is evolving and therefore its limitations are still being discovered and overcome. This discovery process is happening at a rather rapid rate and the near future could see a resolution of the problems mentioned in this work.

3.6 Future Work on Wavelets

The wavelet transform has been used, in this work, to resolve a small amplitude forcing term for the Morse oscillator. Mallat[58] has shown that it is possible to determine the fractal dimension of an image. It would be extremely useful to extend the present work and use the wavelet transform to directly measure the fractal dimension of a Morse system under extreme forcing and to eventually apply the technique to experimental data. The section on nonlinear kinetics, in this work, describes the progress that has been made to apply wavelet analysis to experimental data.

However, it is perhaps more important to take the work of several people (Coifman and Wickerhauser[72], Delprat *et al*[71], Mallat and Hwang[73]) and combine it with this work to apply wavelet analysis to real laboratory signals.

4 Nonlinear Kinetics

4.1 Introduction

Shock tube compression has been used for kinetic studies of various chemical systems. This work expands on work that has been done by Cheng [69] on the oscillations observed in shock heated CCl_3F. Cheng has shown that a shock heated compound, with a starting sample pressure near the vapor pressure of the compound which subsequently condenses, displays an oscillating schlieren signal (described below) which is unexpected. Cheng[69] has also shown that shock compressed methane at low pressures, pressures much lower than its vapour pressure, does not have the unexpected oscillations in its schlieren signal. This may be explained by considering that the CH_4's temperature has increased the translational motion of the compound and therefore the collisions are violent enough to overcome the intermolecular forces that are believed to cause condensation, whereas for CCl_3F the intermolecular forces for cluster formation are stronger. Thus, cluster formation and condensation can take place. Another consideration is that even at room temperature methane is above its critical temperature, $T_c = 191$ K, as discussed Cheng[69]. The critical temperature of a gas is the highest temperature at which the gas can still be condensed.

This work changes the focus to another approach that clarifies the oscillations by pursuing a series of compounds instead just of one. Ideally the series would start with CCl_3F, then hydrogens would replace the halogens. The experiments would involve using $CHCl_3$ (chloroform), then CH_2Cl_2 (dichloromethane), and finally CH_3Cl (methylchloride). Each of these experiments would be done with the same diaphragms (see below) but at various pressures up to and including the vapour pressure of each of the compounds. This progression would allow the observation of oscillatory behaviour as a function of hydrogen content as, first the fluorine and then the chlorines would be replaced with hydrogen. One explanation for the expected loss of oscillations

would be that the hydrogen allows a vibrational relaxation (see reference 69) path not available to the molecules with no or fewer hydrogen atoms. Chloroform has the most interesting possibilities since some of its physical properties are close to that of CCl_3F, such as T_b, T_c, and C_{3v} symmetry.

The second innovation of this work is the introduction of a new data collection system. The old data collection system was actually two separated detection systems. One system was for measurement of the velocity and the second was for observing the main signal. These systems and the changes made, are outlined later in this work. Suffice it to say that a complicated collection system and data transfer process is replaced with one system based on a 386/25MHz PC. The limitation of this apparatus will be discussed in the experimental section. The major advantage is that several experimental traces can now be observed for each shock experiment *i.e.* one for each of the new velocity detection stations. The data collection is such that the shock velocity for each of these traces are within 2% of each other, depending upon the intensity of the shock. The lack of reproducibility of the shock velocity, until now, was one of the existing inadequacies of shock compression work. Due to membrane material inconsistencies, the diaphragms did not always burst at exactly the same pressure so there could easily be a 5% difference in velocities of samples run at the same pressure and in the same apparatus. With this new technique up to three experiments can now be compared within a single shock tube compression run, with conditions within 2% of each other. Thus a major inconvenience of shock tube compression work has been overcome.

Third, experiments were carried out with successively higher dilution in Ar. This reduced the thermal feedback, which is an essential aspect of the oscillatory and chaotic behaviour. The unusual dependence of the observations on the degree of dilution is a consequence of nonlinear kinetics, and is modeled numerically also.

The fourth innovation of this work is the application of wavelet analysis to the observed oscillatory signals.

4.2 Nonlinear Kinetic Theory

Gray *et al*[19,23–26] and Scott *et al*[27,28] have shown that complicated chemical systems can be modeled with a set of differential equations. They have also shown how a set of equations can be reduced in number with some loss of information but with little or no loss in topological behaviour. The procedure outlined in their papers also indicated that a chemical system could be well-behaved for a certain set of rate parameters, become oscillatory for others, and the system could even exhibit chaotic behavior. The papers also indicated that if the parameters where increased further the system went through the chaotic region and became well-behaved again. This is a very important development for understanding chemical system behavior. Thus, the work mentioned above can be used to demonstrate that nonlinear systems far from equilibrium can behave in an unexpected manner even to include oscillatory and chaotic behaviour.

4.3 Simulations

In this work, oscillating rates of reaction are modeled using a set of equations that utilize first the formation of vibrationally excited monomers, then the formation of dimers, trimers, tetramers and pentamers.

$$A_1 \xrightarrow{k_1^f} A_1^*$$
$$A_1 + A_1^* \xrightarrow{k_2^f} A_2^*$$
$$A_2^* \xrightarrow{k_2^s} A_2$$
$$A_2 + A_1^* \xrightarrow{k_3^f} A_3^*$$

$$
\begin{aligned}
A_3^* &\xrightarrow{k_3^s} A_3 \\
A_3 + A_1^* &\xrightarrow{k_4^f} A_4^* \\
A_4^* &\xrightarrow{k_4^s} A_4 \\
A_4 + A_1^* &\xrightarrow{k_5^f} A_5^* \\
A_5^* &\xrightarrow{k_5^s} A_5
\end{aligned}
\qquad [4.1]
$$

Table 4.1 Modified Cluster Distribution at Equilibrium

species	300 K	350 K	400 K
y_1	1.763×10^{-1}	1.786×10^{-1}	1.561×10^{-1}
y_2	1.763×10^{-1}	5.100×10^{-2}	1.840×10^{-2}
y_3	4.406×10^{-2}	1.276×10^{-2}	4.590×10^{-3}
y_4	3.085×10^{-2}	8.929×10^{-3}	3.213×10^{-3}
y_5	1.322×10^{-2}	3.827×10^{-3}	1.377×10^{-3}
y_1^*	5.587×10^{-1}	7.446×10^{-1}	8.163×10^{-1}
y_2^*	1.904×10^{-4}	6.735×10^{-5}	2.791×10^{-5}
y_3^*	3.023×10^{-4}	1.276×10^{-4}	5.967×10^{-5}
y_4^*	1.036×10^{-4}	4.885×10^{-5}	2.462×10^{-5}
y_5^*	2.750×10^{-5}	1.393×10^{-5}	7.381×10^{-6}

The oscillations are believed to be caused by the repetitive formation and break up of the n-mers. Cheng[69] has shown the detail of this theory and it is his basic computer program (FORTRAN) that is used for the simulations presented in this work. In the present work, the free energy changes that are used to calculate the equilibrium cluster population distribution has been modified to reflect a situation in which the formation of dimers is less favored as the temperature increases (see Table 4.1). The stabilization of an excited n-mer causes heat release and therefore a temperature rise in the system. This forces the system to overshoot the equilibrium concentration of

dimers and forces the break-up of the dimers. Conversely, the break up of an n-mer is endothermic. This causes a heat loss to the system, a temperature decrease and a subsequent overshoot of the equilibrium concentration. The general shape of the waveform that is observed in the schlieren detection system is temperature-sensitive. The schlieren system is detecting the density gradient of the gas that the HeNe laser beam passes through (see Laser Schlieren Detection section). Therefore, as set up for this work, when the voltage of the signal goes positive it means that the process, if it is chemical, is endothermic. (The small negative peak (see Figure 4.32) and the large positive peak are due to the relatively uninteresting passage of the shock front.) Oscillations in the signal therefore mean that the rate of change of the temperature is an oscillatory function of time.

Cheng's[69] equation for the calculated response of the system of differential equations, as stated below, is proportional to the derivative of the temperature with respect to time.

$$\begin{aligned}\frac{dT}{dt'} = \left(\frac{C'}{y^*_{1,0}} + \beta z_0\right)\Bigg[&\sum_n \frac{k^s_i}{k^f_{2,eq}}(H^*_i - H_i)(y^*_i - f_i y_i) \\ &+ \frac{k^f_2}{k^f_{2,eq}}(2H^*_1 - H^*_2)\left(y^*_1 \frac{y^*_1 C'}{y^*_{1,0}} - \frac{y^*_2}{s g_2}\right) \\ &+ \sum_n (H_i + H^*_1 - H^*_{i+1})\frac{k^f_i}{k^f_{2,eq}}\left(y_{i-1}\frac{y^*_1 C'}{y^*_{1,0}} - \frac{y^*_i}{s g_i f_{i-1}}\right)\Bigg] / \\ &\left[\sum_n (C_{p,i} y_i + C^*_{p,i} y^*_i) + z_0 y^*_{1,0}\frac{C_{p,Ar}}{C'}\right]. \end{aligned} \qquad [4.2]$$

Here $t'$is a dimensionless time scale, $t' = k^f_{2,eq}\,[A^*_1]_0\,t$, and C' is the total normalized concentration of all species, $C' = C/C_0$, where C_0 is the total concentration of all species, excited or otherwise, at time zero. y_n is the mole fraction of the n-mer in other words, $y_n = [A_n]/C$. Also, y^*_n is the mole fraction of the excited n-mer or

$y_n^* = [A_n^*]/C$, and $y_{1,0}^*$ is the initial excited monomer mole fraction, $y_{1,0}^* = [A_1^*]_0/C_0$. $g_n = [A_n^*]_{eq}/[A_{n-1}^*]_{eq}$ and $s = [A_1^*]_0/[A_1^*]_{eq}$. Also, z_0 is the ratio of Ar to CCl_3F concentrations and it can therefore go from zero (no argon) to infinity (no CCl_3F). β is related to the relative collisional efficiency of the stabilizing component Ar and CCl_3F. H_n is the enthalpy of the n-mer species, $C_{p,i}$ is the heat capacity of the i^{th} species, and the rate coefficient k_n^f and k_n^s are presented below. The solution of equation [4.2] requires simultaneous solution of ten differential rate equations for the mole fractions y_n and y_n^* (see Cheng[69]). This work expands on Cheng's[69] work in that dilution experiments and simulations were done and low pressure pure CCl_3F experiments were done. This work starts with a cluster distribution (Table 4.1) that Cheng did not use in his work.

The experimental signals can be represented by $d\rho/dy$ *vs* t. The ideal gas law relates the densityρ to the temperature T, the pressure p and the effective molecular weight μ according to $\rho = p\mu/RT$. Taking $p\mu$ as a constant during the shock,

$$\frac{d\rho}{dt'}\frac{dt'}{dy} = -\frac{p\mu}{R}\frac{dT}{T^2 dt'}\frac{dt'}{dy} \qquad [4.3]$$

hence the observable $d\rho/dt'$ is proportional to $(1/T^2)dT/dt'$ which is plotted in the simulation plots. Hereafter the term observable will be used to refer to the plots of $(1/T^2)dT/dt'$ *versus* $\mathrm{Log_{10}}$ of Gas Time. The rate coefficients, k_n^f and k_n^s can be scaled fairly generally in terms of the base rate coefficients $k_{2,eq}^f$ and $k_2^{s,eq}$.

$$\frac{k_n^f}{k_{2,eq}^f} = ((1+n^{1/3})/(1+2^{1/3}))\sqrt{(2/3)\frac{n+1}{n}}\; e^{B(n-2.0)}\sqrt{\mathrm{T/T_{ini}}} \qquad [4.4]$$

$$\frac{k_1^s}{k_{2,eq}^f} = \frac{k_1^{s,eq}}{k_{2,eq}^f}\; e^{-E_1/RT} \qquad [4.5]$$

$$\frac{k_2^s}{k_{2,eq}^f} = \frac{k_2^{s,eq}}{k_{2,eq}^f}\; e^{-E_2/RT} \qquad [4.6]$$

$$\frac{k_n^s}{k_{2,eq}^f} = \frac{k_2^{s,eq}}{k_{2,eq}^f} e^{A(n-2)} \quad n > 2. \qquad [4.7]$$

For the various rate coefficients stated above, the subscript n refers to the n-mer in question, the superscripts, f, to formation, and s to stabilization. Also, the parameter B relates the formation of the n-mer to that of the dimer while A relates the stabilization of the n-mer to that of the dimer, once formed. Lastly, T_{ini} is the initial temperature, T is the temperature at any time t and T_{int} it the final temperature of the system.

Equation [4.2] is nonlinear and depending upon the choice of s, $y_{1,0}^*$, *etc.*, the y_n and T are also far from equilibrium. Hence, these equations fulfill Gray's criteria for chemical instability: 1) a system far from equilibrium, 2) a system based on nonlinear differential equations, and 3) a system with thermal feedback. Therefore [4.2] is a good example of nonlinear kinetics. The parameters A and B are useful to allow equations [4.4] and [4.7] to describe a large variety of behaviour of cluster formation and stabilization.

Table 4.2 Simulation parameters for a general search of parameter space. Note that k_1^s and k_2^s are ratioed to $k_{2,eq}^f$.

k_1^s	0.1341	13.41	13.41	13410	13.41	10000	20000
k_2^s	0.13	0.13	0.013	0.13	13000	13000	13000
$k_{2,eq}^f$	6810	6810	68.10	6810	6810	6810	6810

A general search of parameter space was carried out, and the values used are listed in Table 4.2. The plots of the observable *vs* $\log_{10}$ of gas time, hereafter referred to as $l_{10}gt$, for the settings in column three of Table 4.2 had oscillations. Therefore these variables were left unchanged for the simulations presented in this work. Figures 4.1

through 4.31 are plots of the observable (abbreviated to Obser) *vs* $l_{10}gt$ (-10.0 to 5.0) with parameters $E_1 = 9800\ kj/mol$, $E_2 = 0.98\ kj/mol$, $k_1^{s,eq} = 13.4076$, $k_2^{s,eq} = 0.0130$, $T_{ini} = 291.15$ K, $k_2^f = 68.1$ and the supersaturation ratio, $s = 0.6160$, while the unitless parameters A, B, and the final integration (int) temperature, T_{int}, are varied. For Figures 4.1-4.10 z_0, the dilution parameter, is set to zero and β the collisional energy transfer efficiency is therefore not included in the calculations. The effect that these terms have on the oscillations of the observable are investigated in a later section (Figures 4.11-4.31).

Table 4.3 Listing of the Figures 4.1-4.10 and the associated simulation parameter settings.

A	B	T_{int}	Tol	y-axis scale			
				$\pm 1.5 \times 10^{-2}$	$\pm 1.5 \times 10^{-3}$	$\pm 1.5 \times 10^{-5}$	$\pm 1.5 \times 10^{-6}$
3.5	1.0	350.15	10^{-12}		4.1(a)	4.1(b)	
7.5	0.5	350.15	10^{-12}		4.2(a)	4.3(a)	
7.5	1.0	325.15	10^{-12}		4.2(b)	4.3(b)	
7.5	1.0	350.15	10^{-12}		4.2(c)	4.3(c)	4.9(a)
7.5	2.0	350.15	10^{-12}	4.4(a)	4.5(a)	4.7(a)	4.9(b)
7.5	2.0	350.15	10^{-10}	4.4(b)		4.7(b)	4.9(c)
11.5	1.0	325.15	10^{-12}		4.6(a)	4.8(a)	
11.5	1.0	350.15	10^{-12}		4.6(b)	4.8(b)	4.10(a)
11.5	2.0	350.15	10^{-12}	4.4(c)	4.5(b)	4.8(c)	4.10(b)

In Figure 4.1 $A = 3.5$ and $B = 1.0$. In Figure 4.1(a) the y-axis value spans the range $\pm 1.5 \times 10^{-3}$; while in Figure 4.1(b) the y-axis is expanded to $\pm 1.5 \times 10^{-5}$. In Figure 4.1(a) the observable starts out at a positive value (even at $l_{10}gt$ = -20.0), and as the system evolves the observable decreases. The decrease starts at approximately $l_{10}gt = -5.0$ and the amplitude of the waveform continues to decrease until $l_{10}gt = -2.5$ whereupon it increases and decreases until the integration stops. In Figure 4.1(b) it is obvious that the observable goes negative only once.

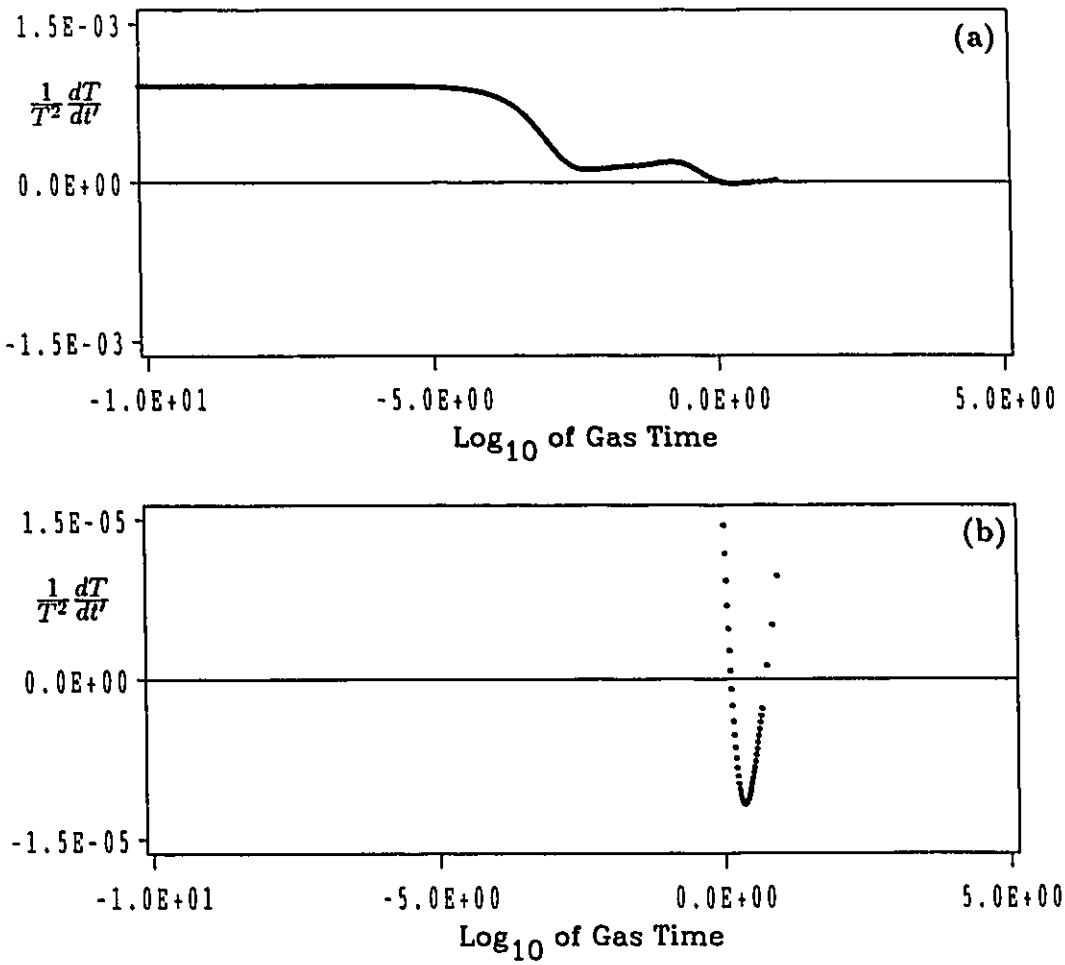

Figure 4.1 Simulation parameters $A = 3.5$, $B = 1.0$, and $T_{int} = 350.14$ K. (a) is a plot with the y-axis scaled to $\pm 1.5^{-3}$ and (b) is a plot with the y-axis scaled to $\pm 1.5 \times 10^{-5}$.

A short discussion of the integration problems must be outlined now. The integration for the simulations was based on Gear's predictor-corrector method. In these routines the step size that is chosen, is just the value at which the integration output would be given not the actual integrator step size. The way that the calculation was done is that a step size and also the number of steps to be done at this step size was chosen. Thus after a predetermined number of steps had been done the program would increase the step size at which a value was output from the integration routine. However, the integration routine always had control over the actual step size used for the integration. The integrator would do its calculation based on its own error

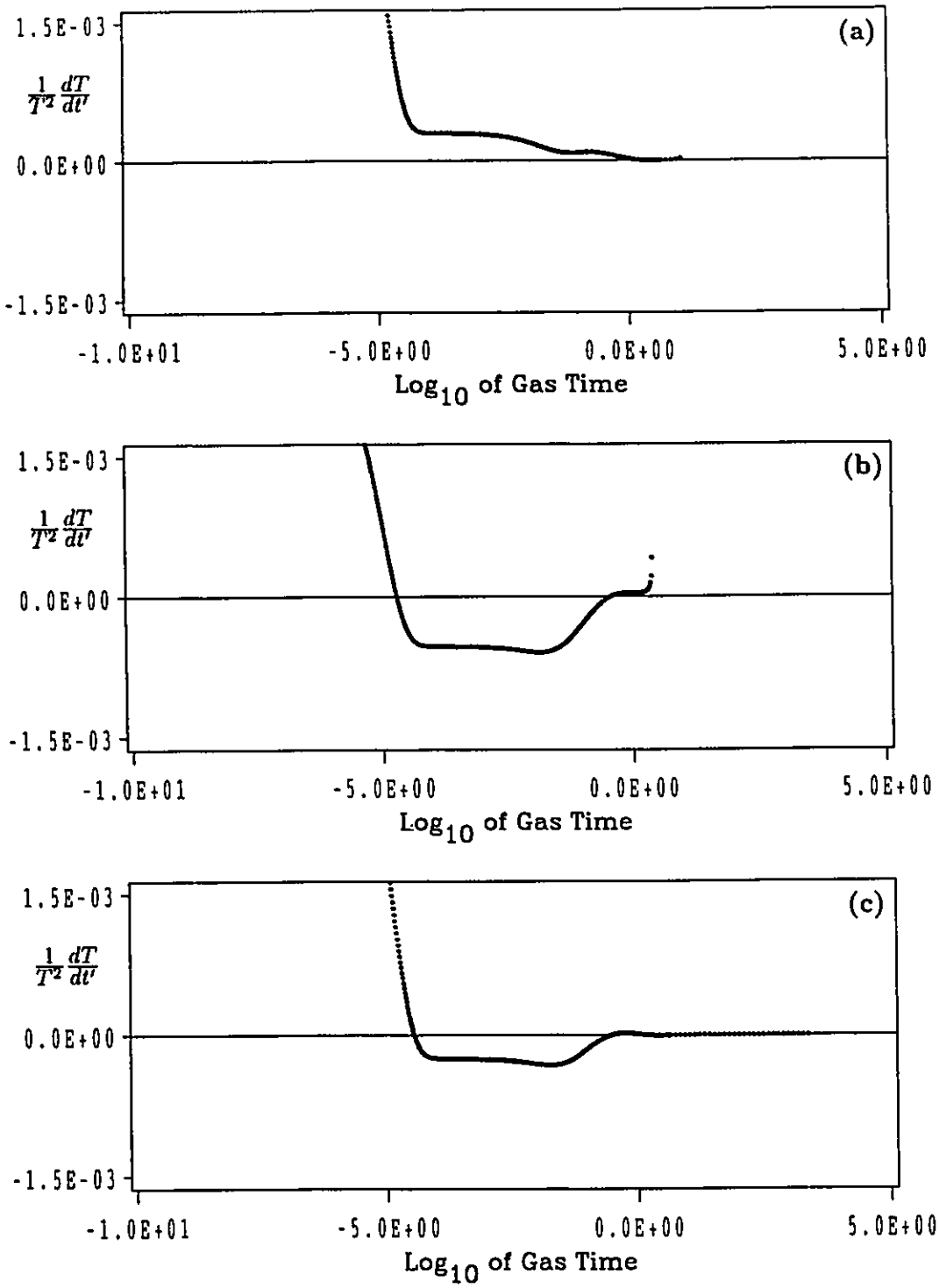

Figure 4.2 The simulation parameter $A = 7.5$ is kept constant while B and T_{int} are varied and the observable is plotted with a y-axis scale of $\pm 1.5 \times 10^{-3}$. (a) $B = 0.5$, and $T_{int} = 350.15$ K; (b) $B = 1.0$, and $T_{int} = 325.15$ K; (c) $B = 1.0$, and $T_{int} = 350.15$ K.

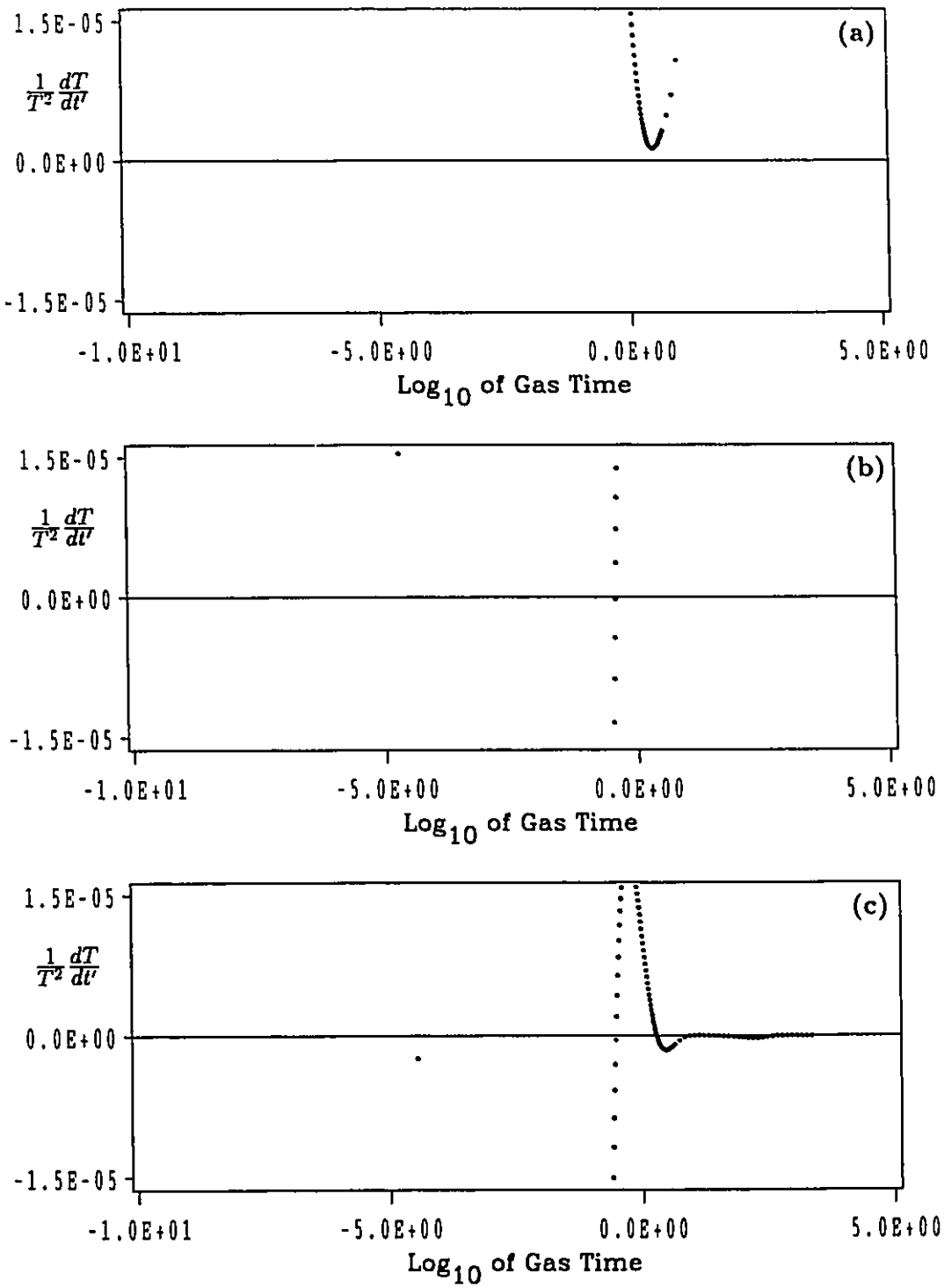

Figure 4.3 The simulation parameter $A = 7.5$ is kept constant while B and T_{int} are varied and the observable is plotted with a y-axis scale of $\pm 1.5 \times 10^{-5}$. (a) $B = 0.5$, and $T_{int} = 350.15$ K; (b) $B = 1.0$, and $T_{int} = 325.15$ K; (c) $B = 1.0$, and $T_{int} = 350.15$ K.

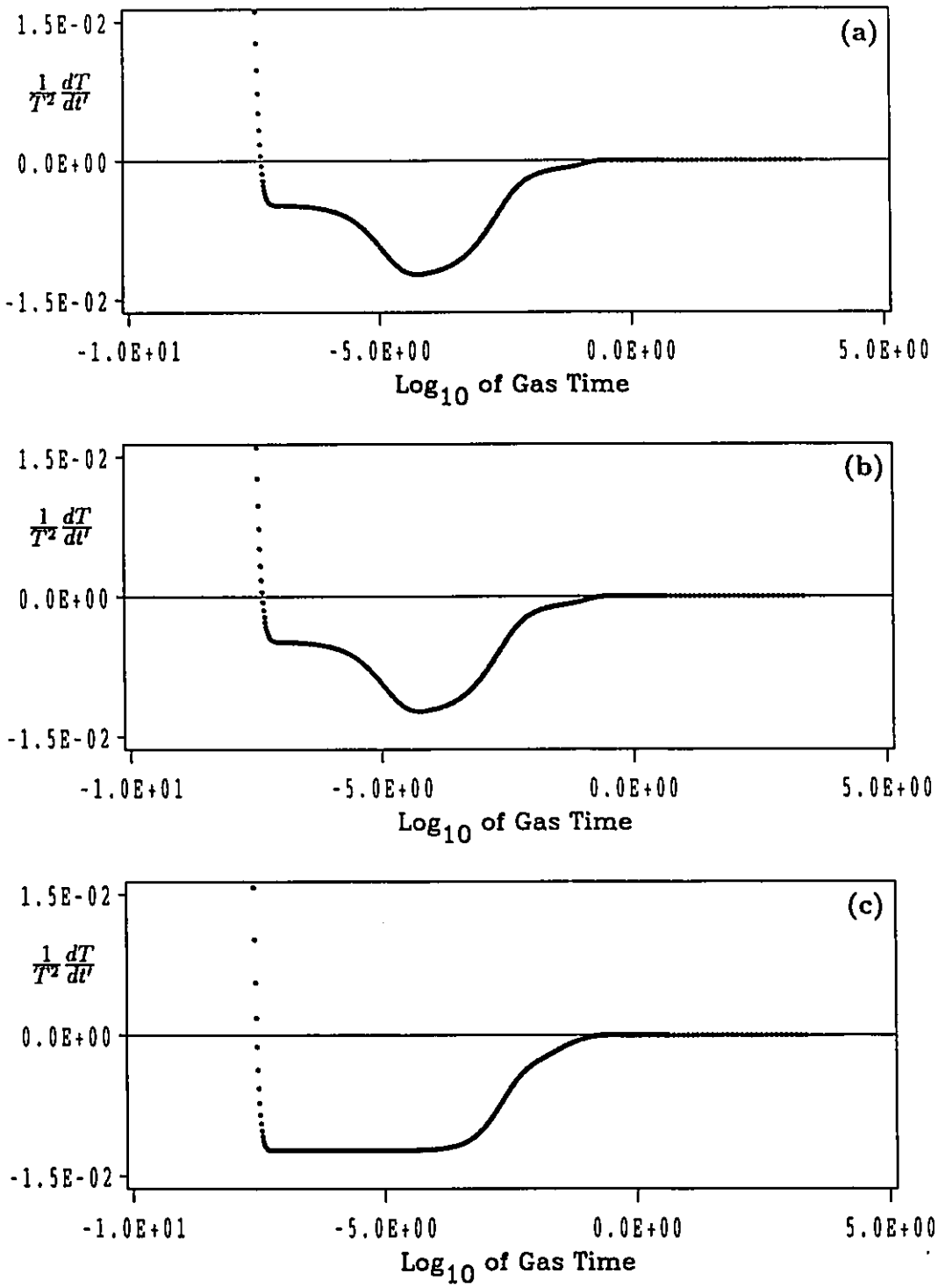

Figure 4.4 Simulation parameters $B = 2.0$ and $T_{int} = 350.15$ K are kept constant, while A and Tol are varied and the observable is plotted with a y-axis scale of $\pm 1.5 \times 10^{-2}$. (a) $A = 7.5$ and $Tol = 10^{-12}$; (b) $A = 7.5$ and $Tol = 10^{-10}$; (c) $A = 11.5$ and $Tol = 10^{-12}$.

analysis and on the relative error that was allowed. In these routines this latter value was called *Tol*. Therefore, if the program determines that the error is larger than *Tol* the program decreases the step size and redoes the integration. This process is only allowed to occur for a limited number of iterations or decreases in step size, beyond which the integration is stopped and an error message is printed out. The integrations for T_{int} = 325.15 K were problematic in that the integration invariably failed the *Tol* check too many times, close to the end of the integration and were stopped prematurely. These calculations were nevertheless still included since the exact values were not needed, only the trend and general shape of the observable were used for the sake of comparison.

In Figure 4.2 only $A = 7.5$ is constant. For Figure 4.2(a) $B = 0.5$ and T_{int} = 350.15 K; for (b), $B = 1.0$ and T_{int} = 325.15 K; and for (c), $B = 1.0$ and T_{int} = 350.15 K. Comparison of Figure 4.2(a) and (c) shows the changes in the observable when changing B from 0.5 to 1.0. The observable goes negative at a much sooner $l_{10}gt$ for $B = 1.0$ than for $B = 0.5$. From equation [4.4] it can be seen that decreasing B to a number less than 1.0 will result in a rate coefficient (ratio) that will disfavour the formation of clusters larger than dimers ($n = 2$). Comparison of Figures 4.2(b) and (c) indicates that the amplitude of the observable decreases when the final integration temperature is decreased from 350.15 K to 325.15 K. Notice that, although, the waveforms in 4.2(b) and 4.2(c) are similar (for $l_{10}gt$ less than 0.0) the observable is actually more negative for a lower T_{int}.

Figure 4.3 shows plots of the observable for the same conditions as in Figure 4.2 except that the y-axis has been expanded to assist in observing the behaviour of the waveforms. The waveform in Figure 4.3(a) does not go negative, while the waveform in 4.3(b) has a large negative amplitude for a $l_{10}gt$ of -5.0 to -1.0 but then the waveform goes positive. The observable in Figure 4.3(c) has definite oscillations present, and

the reasons for the oscillations under these conditions will be discussed in a later section. For now it is sufficient to note that changing B from 0.5 (Figure 4.3(a)) to 1.0 (Figure 4.3(c)) has taken the waveform from above the reference line to below the reference line. Thus the waveform overshoots the reference line and returns to it. This could be expected from the fact that if dimers are not favoured ($B < 1.0$) the waveform will not go negative. The negative part of the waveform is from heat released due to cluster formation.

In Figure 4.4, $B = 2.0$ and $T_{int} = 350.15$ K are kept constant, and the integration is checked by changing Tol from 10^{-12} in Figure 4.4(a), to 10^{-10} in Figure 4.4(b). Further y-axis expansions of these waveforms are shown in Figures 4.7(a) and (b) as well as Figures 4.9(b) and (c). Note that changing Tol from 10^{-12} to 10^{-10} does not change the observable (waveform), and thus the integration is stable. That is the reason that $Tol = 10^{-12}$ is used throughout the present study.

Figure 4.5(a) and (b) are expansions of Figure 4.4(a) and (c), respectively. Therefore in Figure 4.5 the effect, on the observable, of changing A from 7.5 to 11.5 for $B = 2.0$ and $T_{int} = 350.15$ K can be noted. The waveform in Figure 4.5(a) has inflection points that are missing in (b), although it is obvious that both of the waveforms are oscillating around the reference line.

In Figure 4.6 $A = 11.5$ and $B = 1.0$ while T_{int} is changed from 325.15K to 350.15K at a y-axis expansion of $\pm 1.5 \times 10^{-3}$. The observable has a more negative plateau at a lower T_{int}. Also the maximum negative amplitude is larger for the lower T_{int}. This is similar to the case for $A = 7.5$, as can be seen in Figure 4.2(b) and (c) for a similar y-axis expansion.

Comparing Figure 4.1(a), 4.2(c) and 4.6(b) for which all conditions are the same, including the y-axis expansion, except that $A = 3.5$, 7.5 and 11.5, respectively, it is

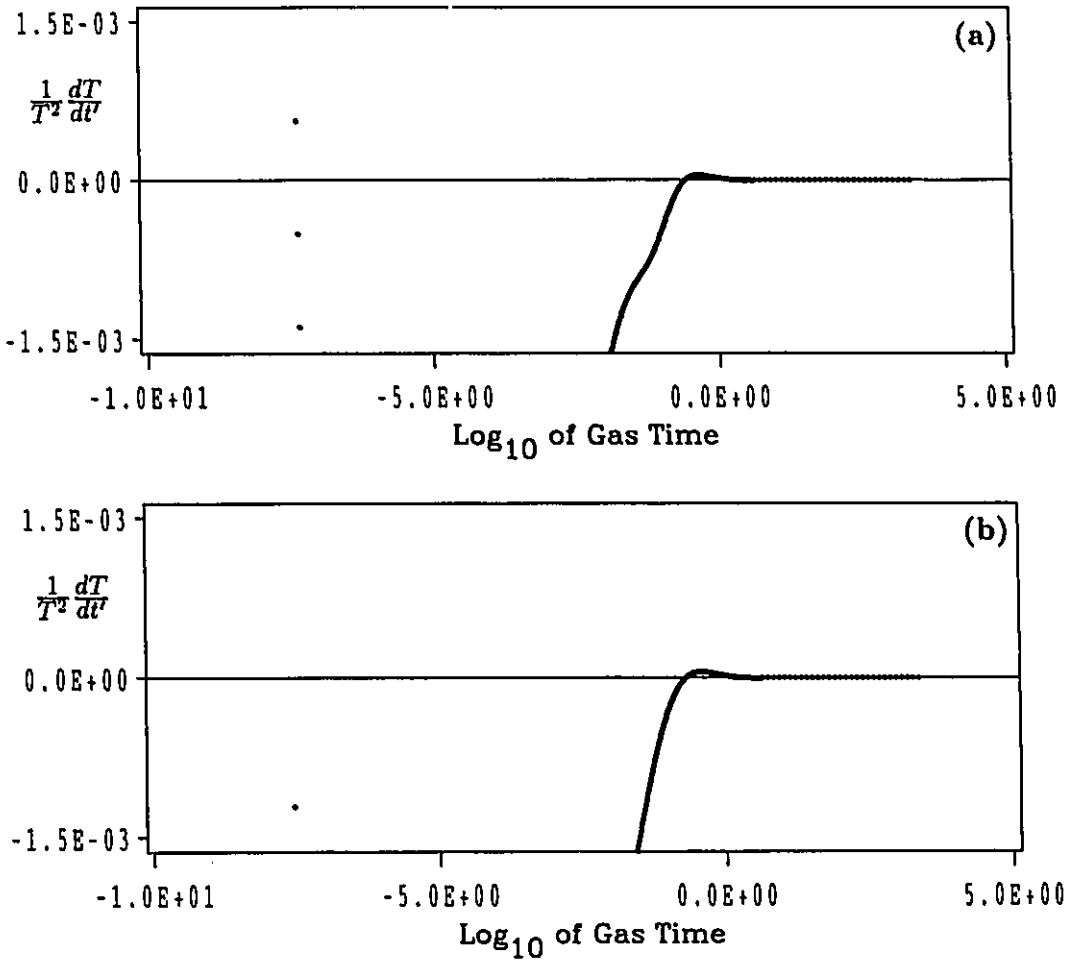

Figure 4.5 Simulation parameters $B = 2.0$, and $T_{int} = 350.15$ K are kept constant, while A is varied. (a) $A = 7.5$ (b) $A = 11.5$. The observable is plotted with a y-axis scale of $\pm 1.5 \times 10^{-3}$.

possible to see what effect changing A has on the amplitude of the observable. For $A = 3.5$, Figure 4.1(a), the observable is on the plot scale for all time shown and only goes negative at approximately $l_{10}gt$ equal to zero. For Figure 4.2(c), $A = 7.5$ and the observable has a larger amplitude but the amplification is decidedly nonlinear. This is emphasized further when Figure 4.6(b) ($A = 11.5$) is compared to 4.2(c) ($A = 7.5$). The waveform in Figure 4.6(b) has a larger negative amplitude but a much different shape than the waveform in Figure 4.2(c). Remember that equation [4.7] indicates that a larger A means a rate coefficient that favours stabilized n-mers ($n > 2$). In addition, comparison of 4.4(a) and (c) show the change in observable with $B = 2.0$

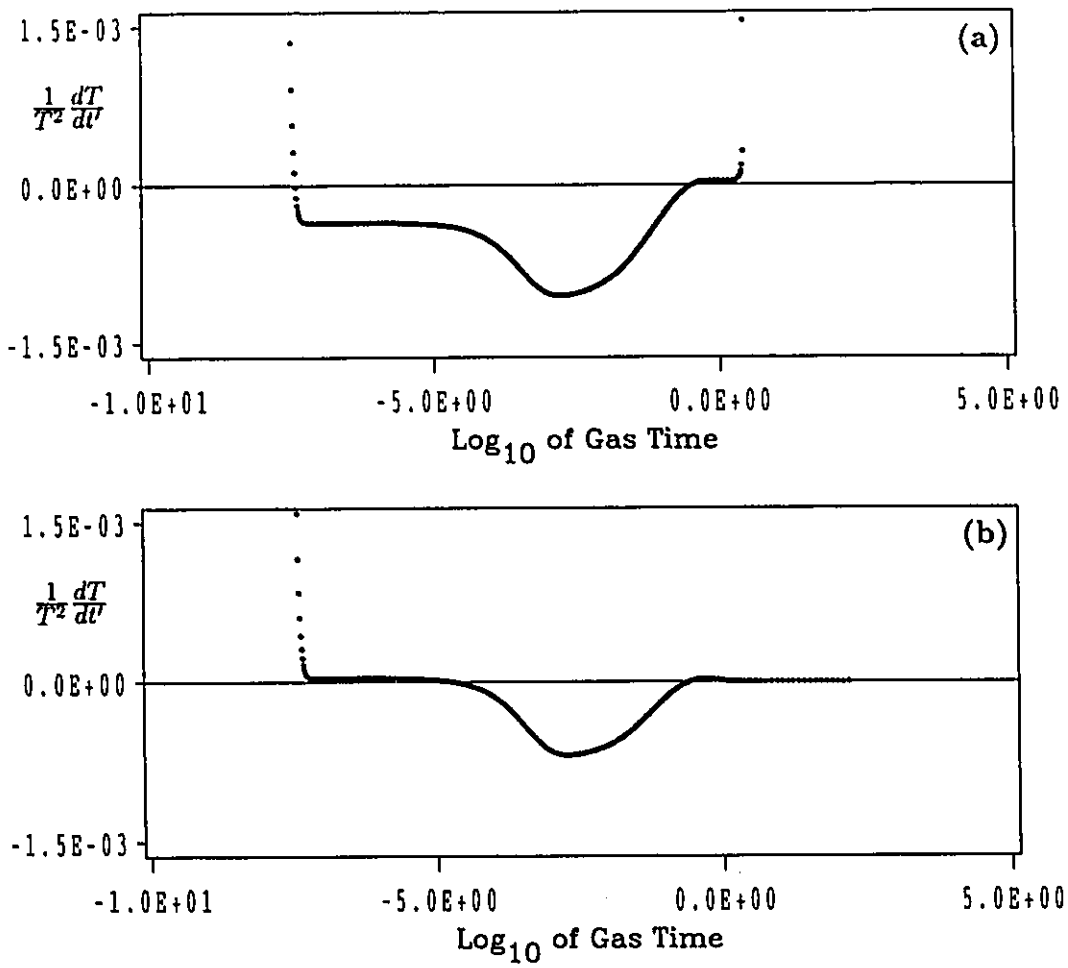

Figure 4.6 Simulation parameters $A = 11.5$, and $B = 1.0$ are kept constant while T_{int} is varied. (a) $T_{int} = 325.15$ K, (b) $T_{int} = 350.15$ K. The observable is plotted with a y-axis scale of $\pm 1.5 \times 10^{-3}$.

and $T_{int} = 350.15$ K constant while A is changed from 7.5 to 11.5, respectively. Not only are the amplitudes different, the shape of the waveforms are different. In fact the inflection points in the negative part of the observable in Figure 4.4(a) seem to be missing from the same part of the waveform in Figure 4.4(c).

Figure 4.7 is for simulation parameters of $A = 7.5$, $B = 2.0$ and $T_{int} = 350.15$ K. Only *Tol* has been changed, from 10^{-12} (Figure 4.7(a)) to 10^{-10} (Figure 4.7(b)), and the waveforms seem to be identical.

Figure 4.8 is a further y-axis expansion with the simulation parameters $A = 11.5$,

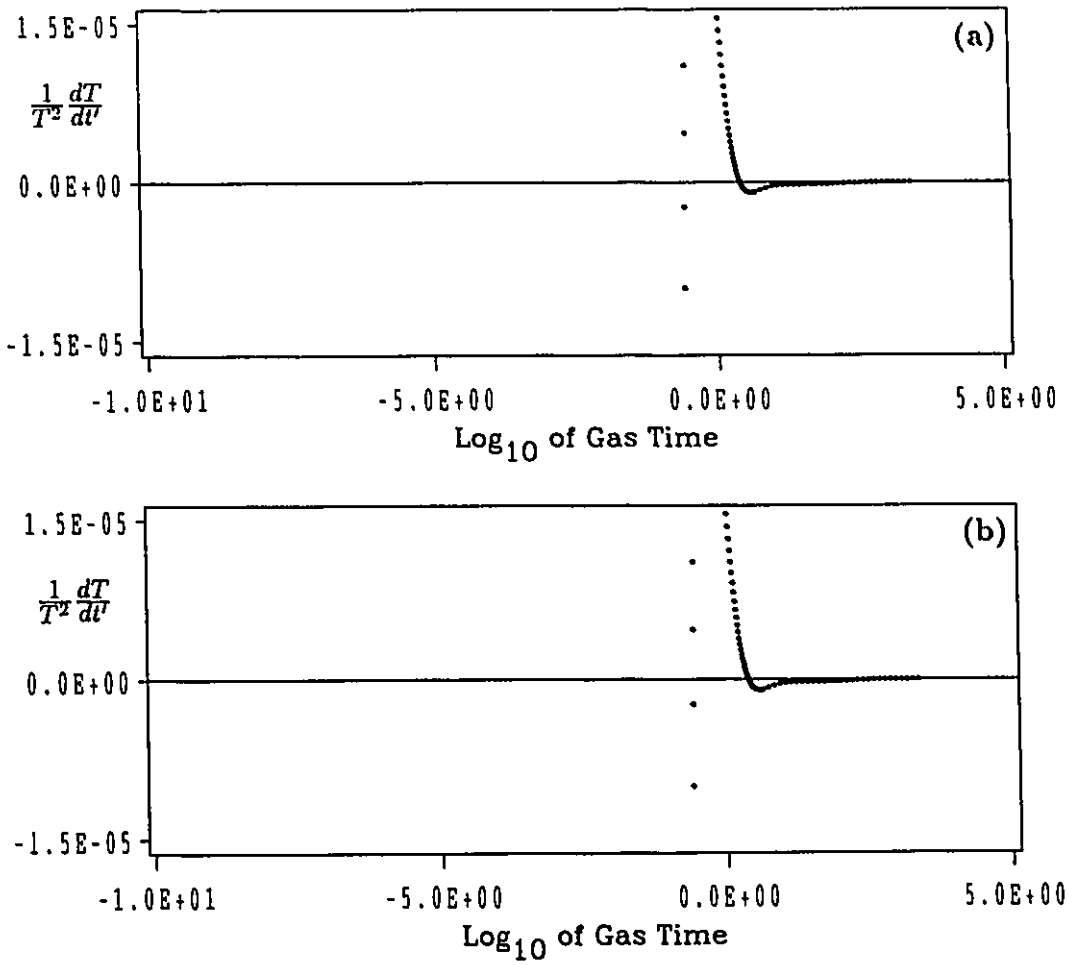

Figure 4.7 Simulation parameters $A = 7.5$, $B = 2.0$ and $T_{int} = 350.15$ K are kept constant, while Tol is varied. (a) $Tol = 10^{-12}$, (b) $Tol = 10^{-10}$. The observable is plotted with a y-axis scale of $\pm 1.5 \times 10^{-5}$.

$B = 1.0$ and $T_{int} = 325.15$ K for (a); $T_{int} = 350.15$ K for (b); while $B = 2.0$ and $T_{int} = 350.15$ K for (c). Comparison of Figures 4.8(b) and (c) shows that the change of B from 1.0 to 2.0 has increased the maximum amplitude of the observable. Thus, increasing the rate constant for formation of n-mers ($n > 2$) increases the maximum observable amplitude.

Figure 4.9 has used simulation parameters $A = 7.5$ and $T_{int} = 350.15$ K for all cases, while $B = 1.0$ and $Tol = 10^{-12}$ for Figure 4.9(a) with $B = 2.0$; $Tol = 10^{-12}$ for Figure 4.9(b); while $B = 2.0$ and $Tol = 10^{-10}$ for Figure 4.9(c). Comparison of

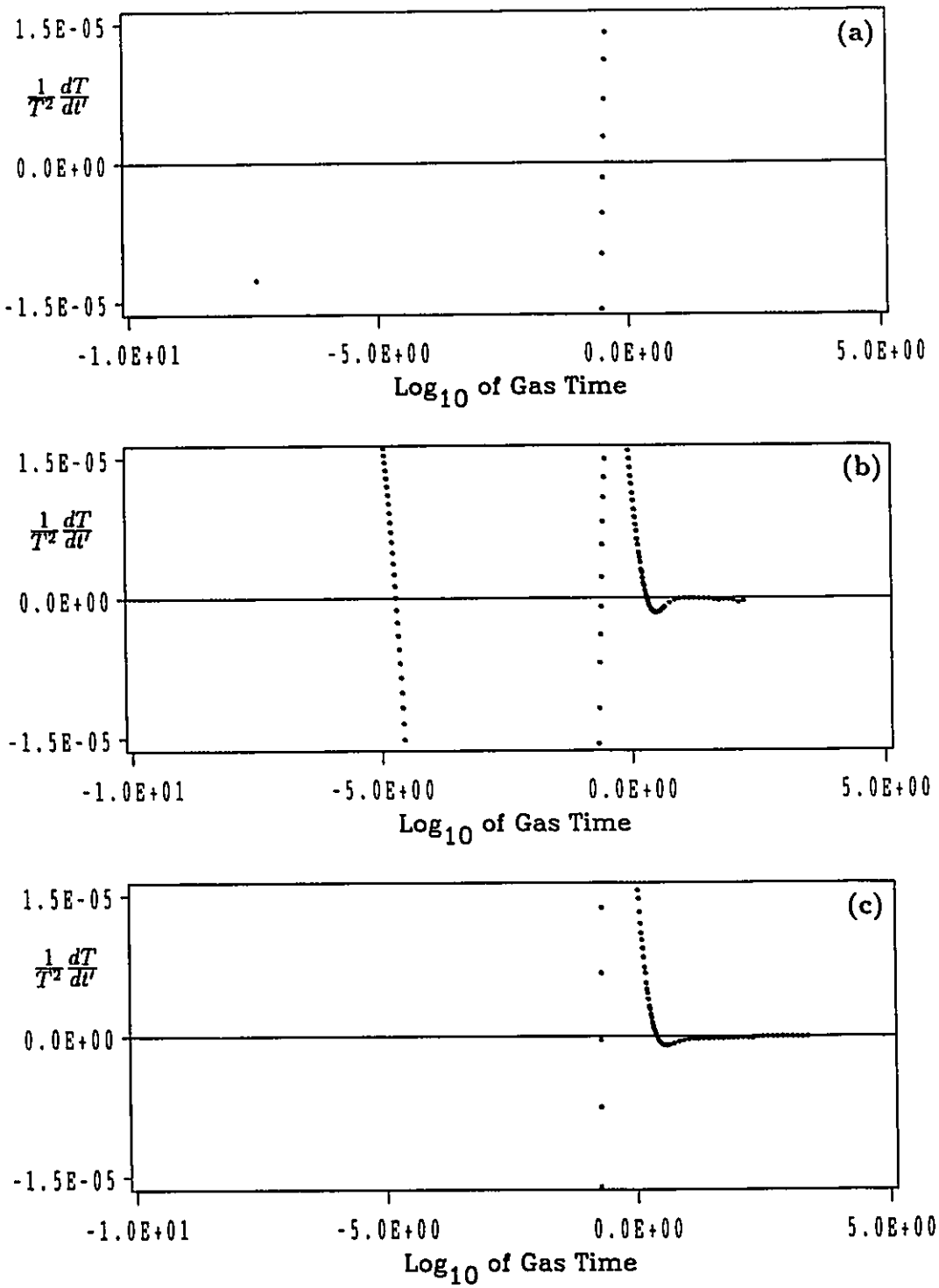

Figure 4.8 Simulation parameter $A = 11.5$ is kept constant while B and T_{int} are varied. The observable is plotted with a y-axis scale of $\pm 1.5 \times 10^{-5}$. (a) $B = 1.0$, and $T_{int} = 325.15$ K; (b) $B = 1.0$ and $T_{int} = 350.15$ K; (c) $B = 2.0$ and $T_{int} = 350.15$ K.

4.9(b) and 4.9(c) at this expansion ($\pm 1.5 \times 10^{-6}$) confirms that there is no change of the waveform for a change in *Tol*. Comparison of 4.9(a) and 4.9(b) shows that as B is increased from 1.0 to 2.0 the amplitude of the oscillations of the observable is decreased and the shape of the waveform changes from a waveform with two negative peaks in 4.9(a) to one negative peak and two inflection points in 4.9(b).

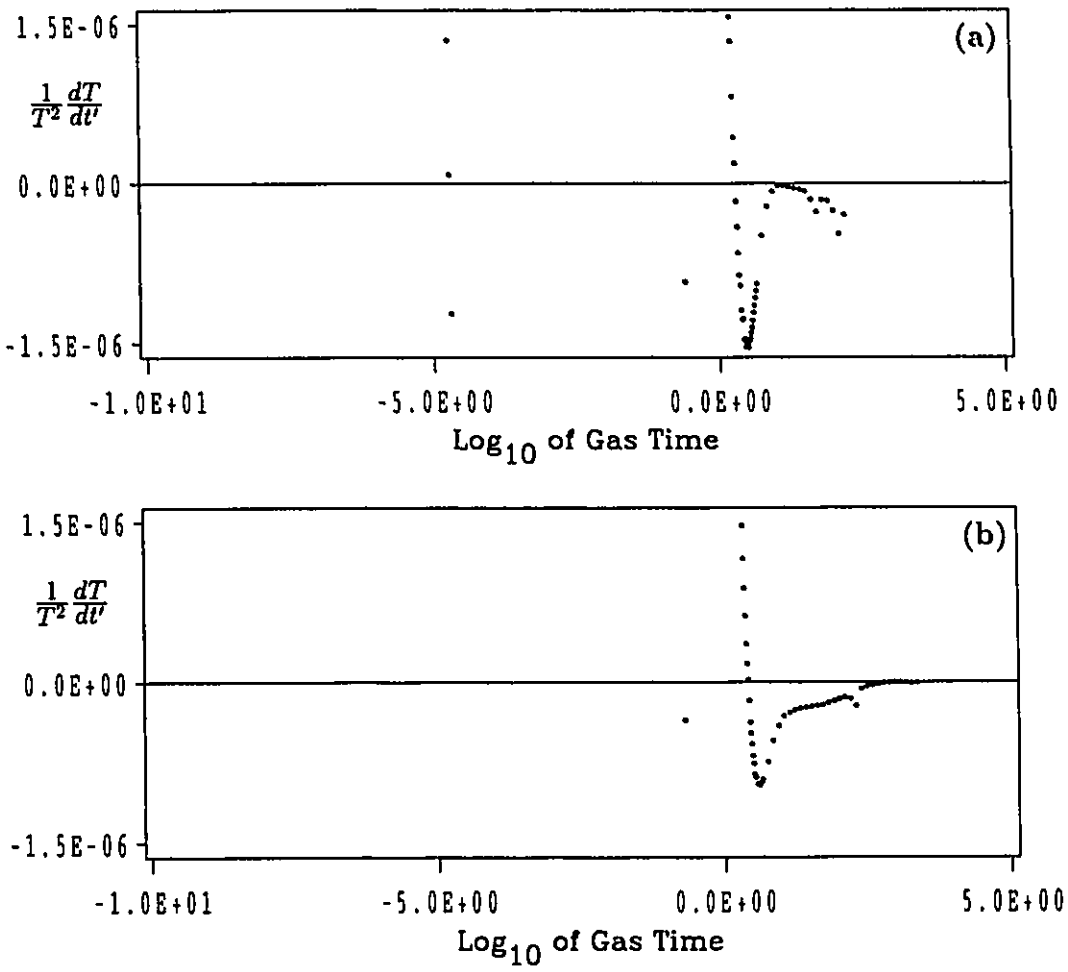

Figure 4.10 Simulation parameters $A = 11.5$ and $T_{int} = 350.15$ K are kept constant, while B is varied. (a) $B = 1.0$, (b) $B = 2.0$. The observable is plotted with a y-axis scale of $\pm 1.5 \times 10^{-6}$.

Figure 4.10 is a final expansion for simulation parameters $A = 11.5$, and $T_{int} = 350.15$ K with B changing from 1.0 to 2.0 for (a) and (b) respectively. The amplitude of the oscillations of the observable decreases as B increases and the waveform also

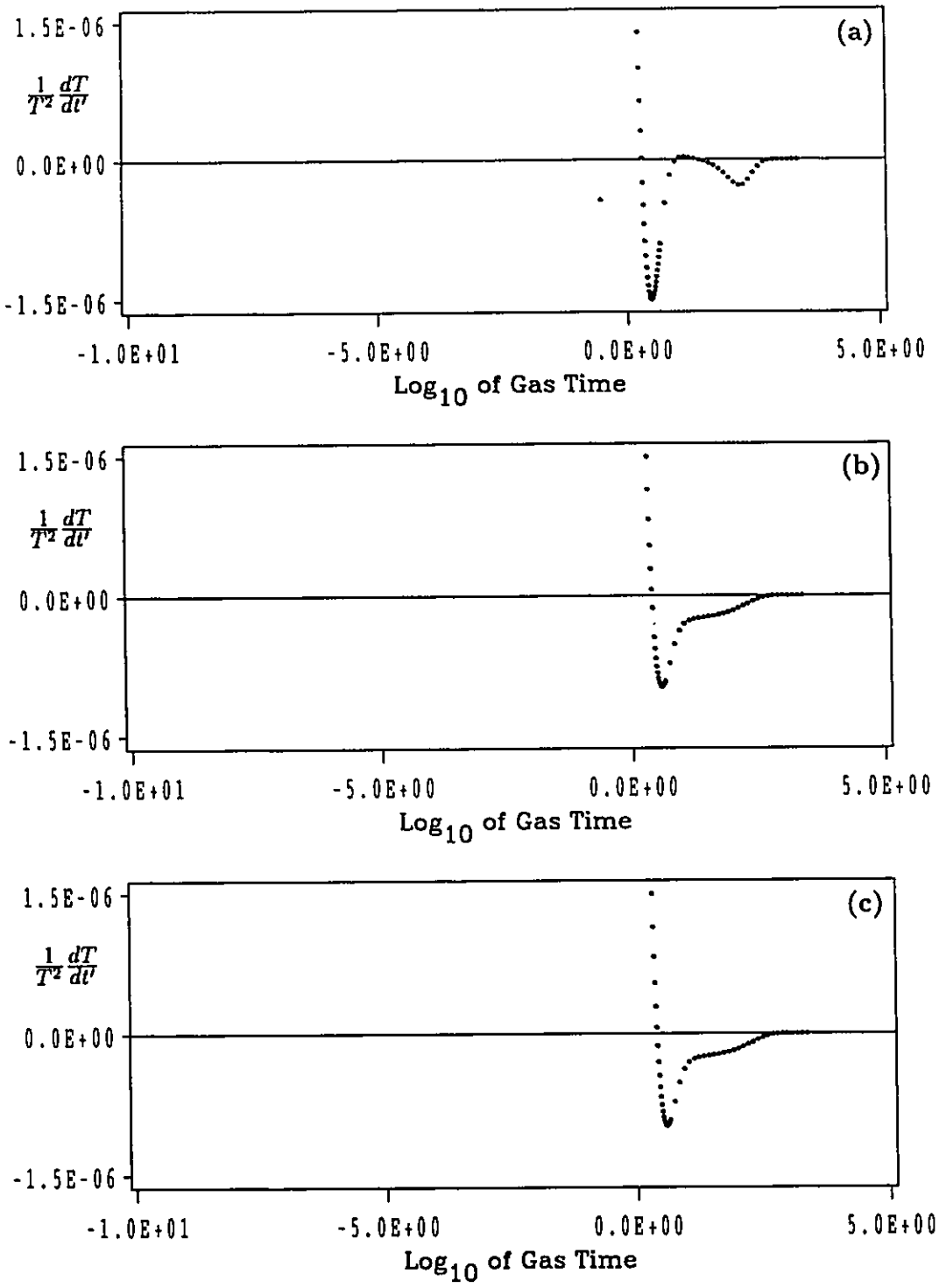

Figure 4.9 Simulation parameters $A = 7.5$ and $T_{int} = 350.15$ K are kept constant, while B and T_{int} are varied. The observable is plotted with a y-axis scale of $\pm 1.5 \times 10^{-6}$. (a) $B = 1.0$ and $Tol = 10^{-12}$; (b) $B = 2.0$ and $Tol = 10^{-12}$; (c) $B = 2.0$ and $Tol = 10^{-10}$.

changes shape. This indicates that the effect is nonlinear, and this has been the case for each of the changes discussed so far.

Comparing Figure 4.2(a) (A = 7.5, T_{int} = 350.15 K, B = 0.5), Figure 4.2(c) (B = 1.0), and Figure 4.5(b) (B = 2.0) it is obvious that as B increases the amplitude of the observable increases, while in Figures 4.9(a) and (b), with B changing from 1.0 to 2.0, the amplitude of the oscillations of the observable have decreased. In Figures 4.6(b) and 4.5(b), with A = 11.5, T_{int} = 350.15 K and B varying from 1.0 to 2.0 respectively, the maximum of the negative amplitude of the observable has increased dramatically but again the oscillations have decreased as shown more clearly in Figures 10(a) and (b). The negative maximum of the amplitude of the observable has increased and at the same time the amplitude of the oscillations has decreased.

Comparing Figures 4.3(c) and 4.8(b) it is easy to see that the amplitude of the waveforms are similar for B = 1.0 while A is changed from 7.5 to 11.5; but the waveform in Figure 4.1(b) does not have the same scale of oscillations. For B = 2.0 comparison of Figures 4.7(a) and 4.8(c) show similar oscillations; however, the waveforms in Figures 4.9(b) and 4.10(b) have slight differences in the oscillations of the amplitude of the observable. Thus B has an effect on the amplitude of the oscillations of the observable while A does not. Therefore, the amplitude of the oscillations of the observable are effected more by the formation of clusters than the stabilization of large clusters, at least for the parameter regime investigated in this work.

For Figures 11-24 the simulation parameters A = 7.5, B = 2.0, T_{int} = 350.15 K, and $Tol = 10^{-12}$ are not altered, while β is varied from 10^{-3} to 10^{0} and z_0 is varied from 3.0 to 300.0. Hereafter for all cases, the figures are grouped to allow direct comparison of plots with the same y-axis expansion.

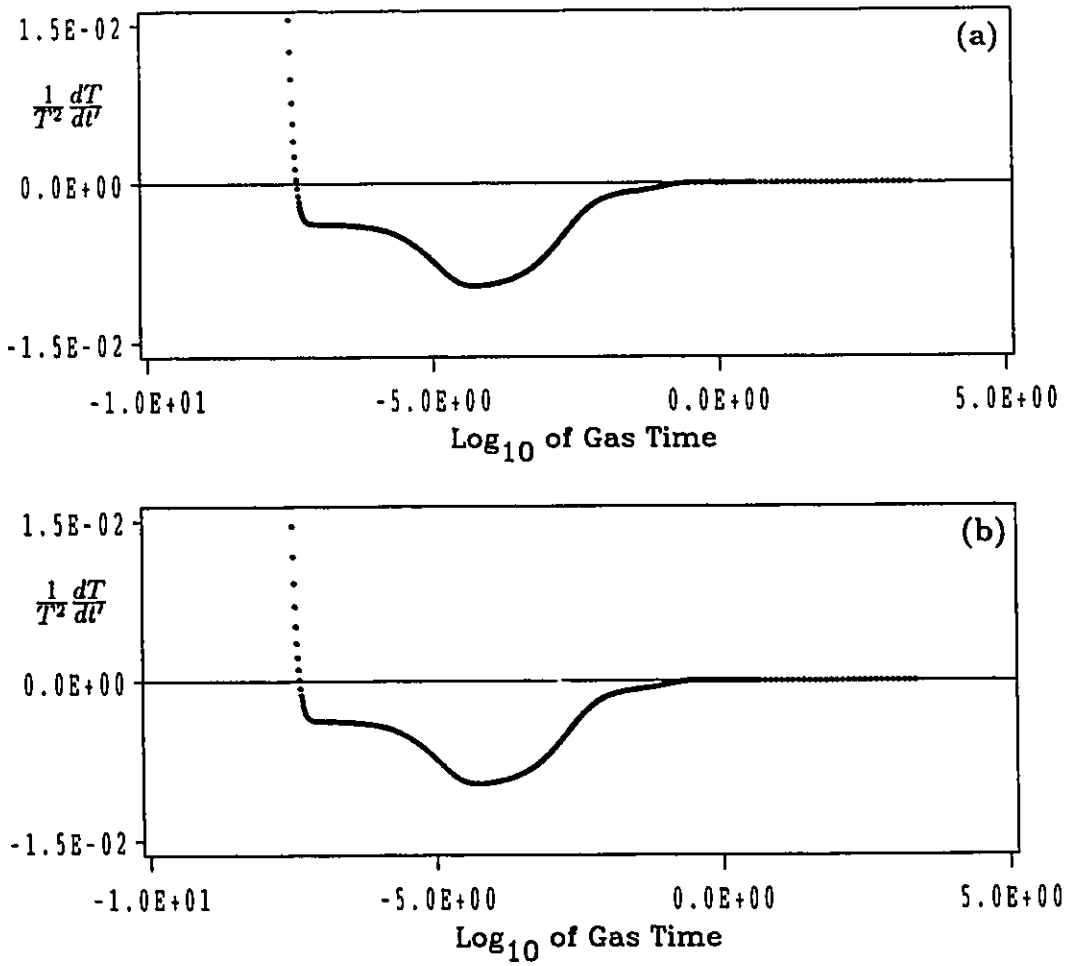

Figure 4.11 Simulation parameters $A = 7.5$, $B = 2.0$, $T_{int} = 350.15$ K, and $z_0 = 3.0$ are kept constant, while β is varied. (a) $\beta = 10^{-3}$, (b) $\beta = 10^{-2}$. The observable is plotted with a y-axis scale of $\pm 1.5 \times 10^{-2}$.

Table 4.4 Listing of the Figures 4.11-4.24 for the simulation parameters $A = 7.5$, $B = 2.0$, and $T_{int} = 350.15$ K remaining constant while β and z_0 are varied.

β	z_0	y-axis scale of $\pm 1.5\times$					
		10^{-2}	10^{-3}	10^{-5}	10^{-6}	10^{-7}	10^{-8}
10^{-3}	3.0	4.11(a)	4.14(a)	4.17(a)	4.20(a)		
10^{-2}	3.0	4.11(b)	4.14(b)	4.17(b)	4.20(b)		
10^{-1}	3.0	4.12(a)	4.15(a)	4.18(a)	4.21(a)		
10^{-0}	3.0	4.12(b)	4.15(b)	4.18(b)	4.21(b)	4.23(a)	
10^{-3}	30.0	4.13(a)	4.16(a)	4.19(a)	4.22(a)	4.23(b)	
10^{-3}	300.0	4.13(b)	4.16(b)	4.19(b)	4.22(b)	4.24(a)	4.24(b)

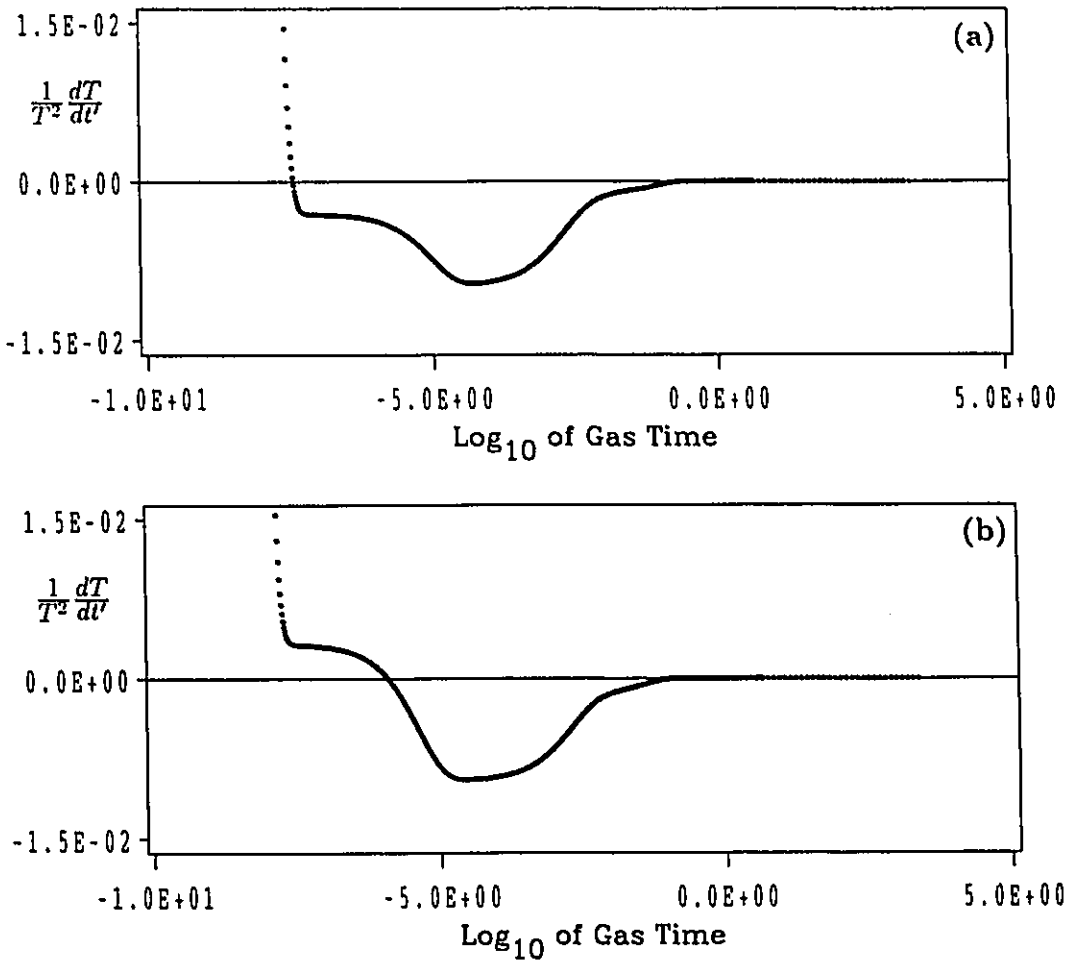

Figure 4.12 Simulation parameters $A = 7.5$, $B = 2.0$, $T_{int} = 350.15$ K, and $z_0 = 3.0$ are kept constant, while β is varied. (a) $\beta = 10^{-1}$, (b) $\beta = 10^{0}$. The observable is plotted with a y-axis scale of $\pm 1.5 \times 10^{-2}$.

The observable (equation [4.2]) can be approximated using:

$$\frac{dT}{dt'} \propto \frac{\left(\frac{C'}{y^*_{1,0}} + \beta z_0\right)}{\left(\sum(C_{p,n}y_n + C^*_{p,n}y^*_n) + z_0 y^*_{1,0}\frac{C_{p,Ar}}{C'}\right)} F_{NonLinear} \qquad [4.8]$$

where $F_{NonLinear}$ is a nonlinear function of time varying cluster mole fractions and rate coefficients which are also explicitly temperature dependent.

Several more approximations can be made for CCl_3F which is a molecule with 5

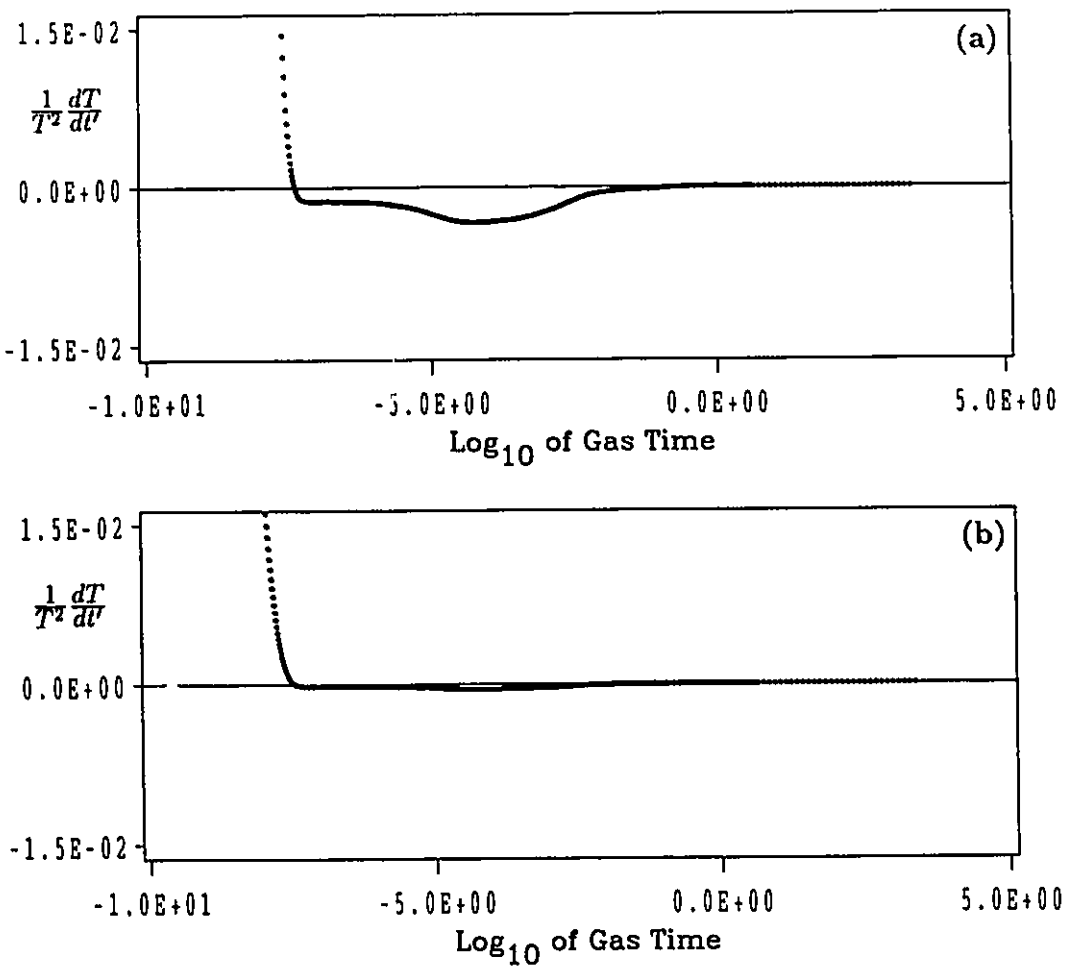

Figure 4.13 Simulation parameters $A = 7.5$, $B = 2.0$, $T_{int} = 350.15$ K, and $\beta = 10^{-3}$ are kept constant, while z_0 is varied. (a) $z_0 = 30.0$, (b) $z_0 = 300.0$. The observable is plotted with a y-axis scale of $\pm 1.5 \times 10^{-2}$.

atoms and therefore has $3 * 5 - 6 = 9$ normal modes of motion. The heat capacity can be approximated as below:

$$C^*_{p_1} = \frac{3}{2}R + \frac{3}{2}R + 9R + R = 13R \qquad [4.9]$$

$$C_{p_1} = \frac{3}{2}R + \frac{3}{2}R + R = 4R \qquad [4.10]$$

$$C_{p_{Ar}} = \frac{3}{2}R + R = \frac{5}{2}R \qquad [4.11]$$

Allowing that the concentration C' should be close to unity, dT/dt' can be approximated with,

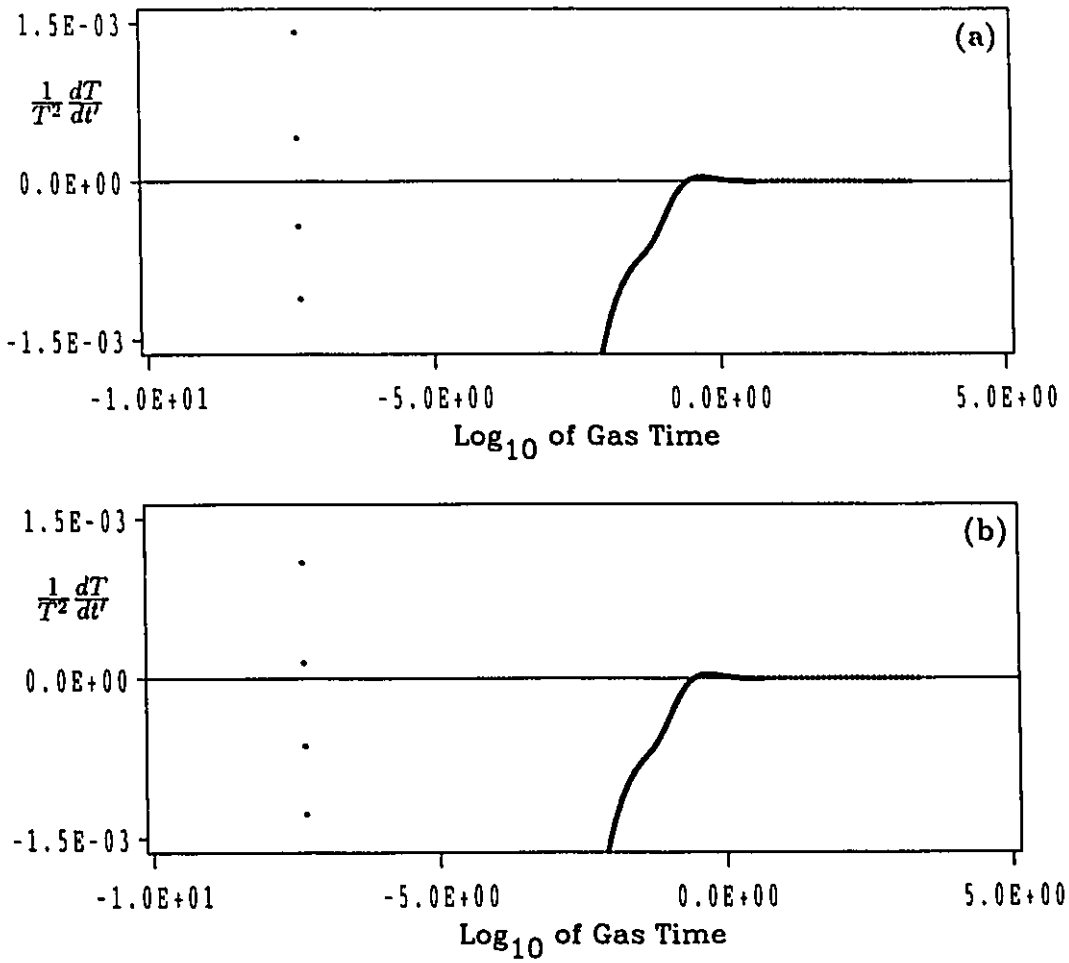

Figure 4.14 Simulation parameters $A = 7.5$, $B = 2.0$, $T_{int} = 350.15$ K, and $z_0 = 3.0$ are kept constant, while β is varied. (a) $\beta = 10^{-3}$, (b) $\beta = 10^{-2}$. The observable is plotted with a y-axis scale of $\pm 1.5 \times 10^{-3}$.

$$\frac{dT}{dt'} \propto \frac{(2.0 + \beta z_0)}{(34.0 + 5.0 z_0)} F_{NonLinear} \qquad [4.12]$$

Keeping the final approximation in mind, there are three cases to be checked.

1. Keep z_0 constant and vary β resulting in $dT/dt' \propto (2.0 + 3.0\beta) F_{NonLinear}$. Thus dT/dt' varies from 2.003 $F_{NonLinear}$ to 5.0 $F_{NonLinear}$ with $z_0 = 3.0$ and varying β from 10^{-3} to 1.0. It is expected that the increase in stabilization efficiency will increase the heat release rate and therefore increase the amplitude of the signal. There may also be nonlinear effects as a result of the increased thermal feedback.

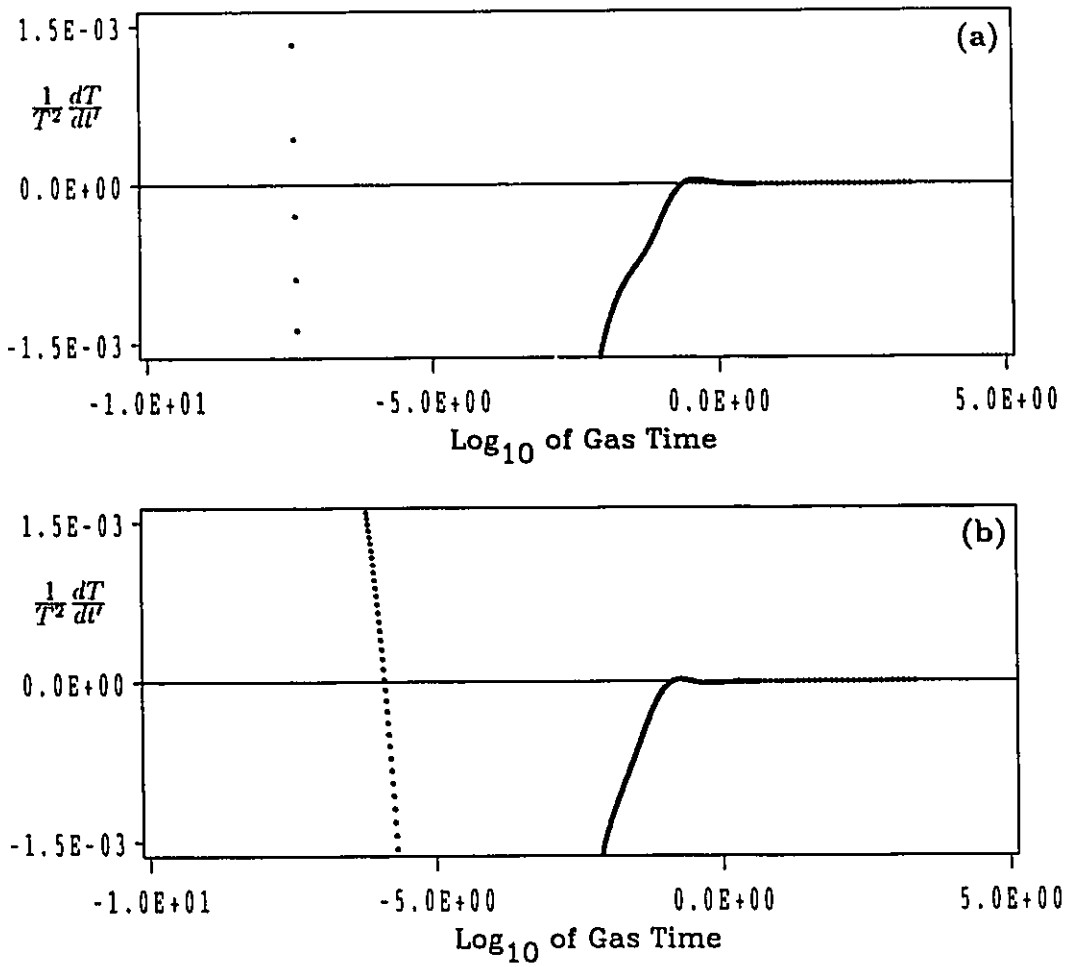

Figure 4.15 Simulation parameters $A = 7.5$, $B = 2.0$, $T_{int} = 350.15$ K, and $z_0 = 3.0$ are kept constant, while β is varied. (a) $\beta = 10^{-1}$, (b) $\beta = 10^{0}$. The observable is plotted with a y-axis scale of $\pm 1.5 \times 10^{-3}$.

2. Keep βz_0 constant, and vary z_0. This, of course, means that β has to vary inversely to z_0. Then $dT/dt' \propto F_{NonLinear}/(34.0 + 5.0z_0)$ and since z_0 is varied from basically 3.0 to 300.0 dT/dt' varies from $F_{NonLinear}/49$ to $F_{NonLinear}/1534$. Increased heat dilution (increasing $[Ar]$) should decrease the amplitude of the signal and there may also be reduced nonlinear effects.

3. Keep β constant and vary z_0. $dT/dt' \propto ((2.0 + 10^{-3}z_0)/(34.0 + 5.0z_0)) * F_{NonLinear}$. β is kept at 10^{-3} but z_0 is changed from 3 to 300.0 in one set of circumstances and from 0 to 1.0 in another set of circumstances. dT/dt' is expected to vary from 0.0408 $F_{NonLinear}$ to 0.0015 $F_{NonLinear}$ for the first set (a factor of 27) and it should vary from 0.0588 $F_{NonLinear}$ to 0.0513 $F_{NonLinear}$ or a factor of 1.1465(*i.e* not much) in the second set of circumstances.

These cases will be discussed after all examples have been presented. Figures 4.11-

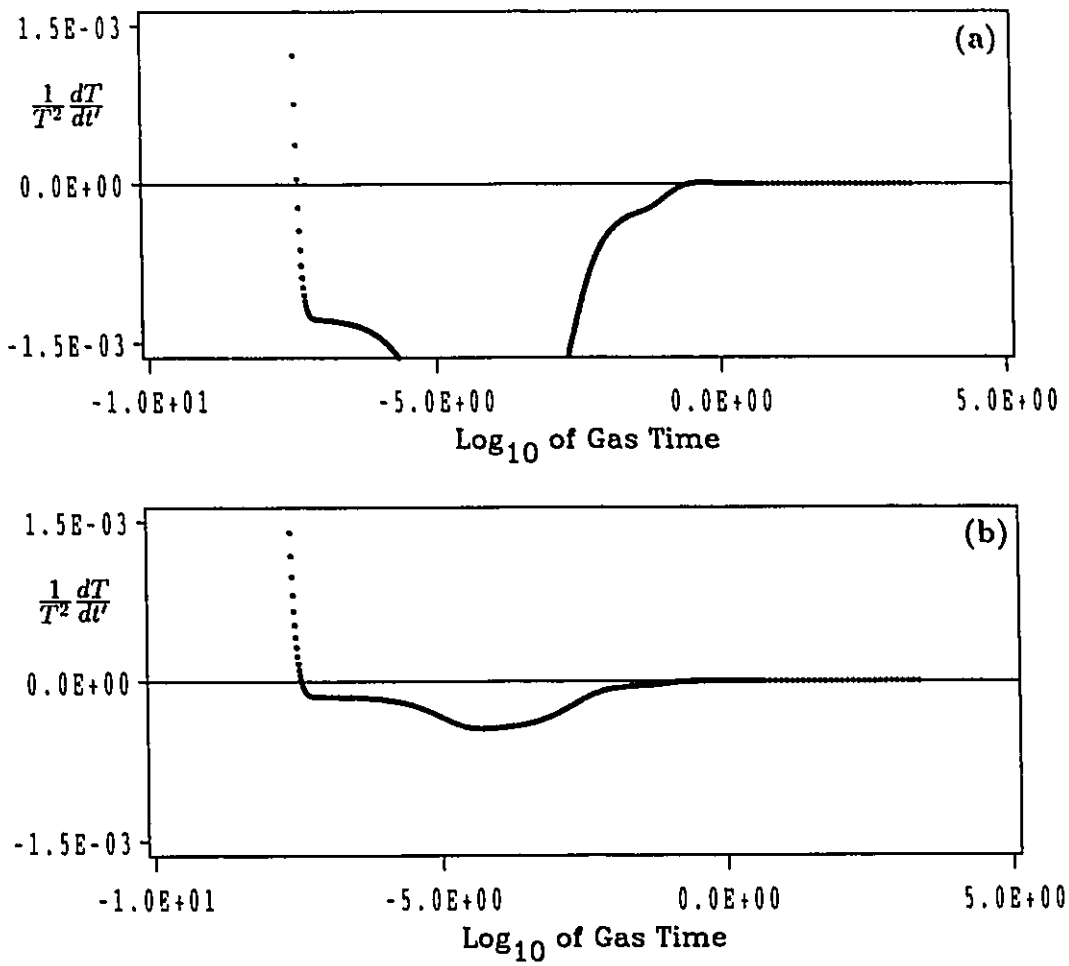

Figure 4.16 Simulation parameters $A = 7.5$, $B = 2.0$, $T_{int} = 350.15$ K, and $\beta = 10^{-3}$ are kept constant, while z_0 is varied. (a) $z_0 = 30.0$, (b) $z_0 = 300.0$. The observable is plotted with a y-axis scale of $\pm 1.5 \times 10^{-3}$.

4.24 are examples of all three cases for $A = 7.5$, $B = 2.0$ and $T_{int} = 350.15$ K, while Figures 4.25-4.31 are examples of case 3 only with $A = 11.5$, $B = 1.0$ and $T_{int} = 350.15$ K. These parameter regimes are, of course, a natural extension of the previous work.

Comparing Figure 4.4(a), where $A = 7.5$, $B = 2.0$, and $T_{int} = 350.15$ K but $z_0 = 0.0$, to Figure 4.11(a) where z_0 was changed to 3.0 and therefore $\beta = 10^{-3}$ was brought into play, the effect of changing z_0 can be seen. That is, the first minimum is slightly smaller in amplitude. In Figure 4.12(a) β has been increased to 0.1 with

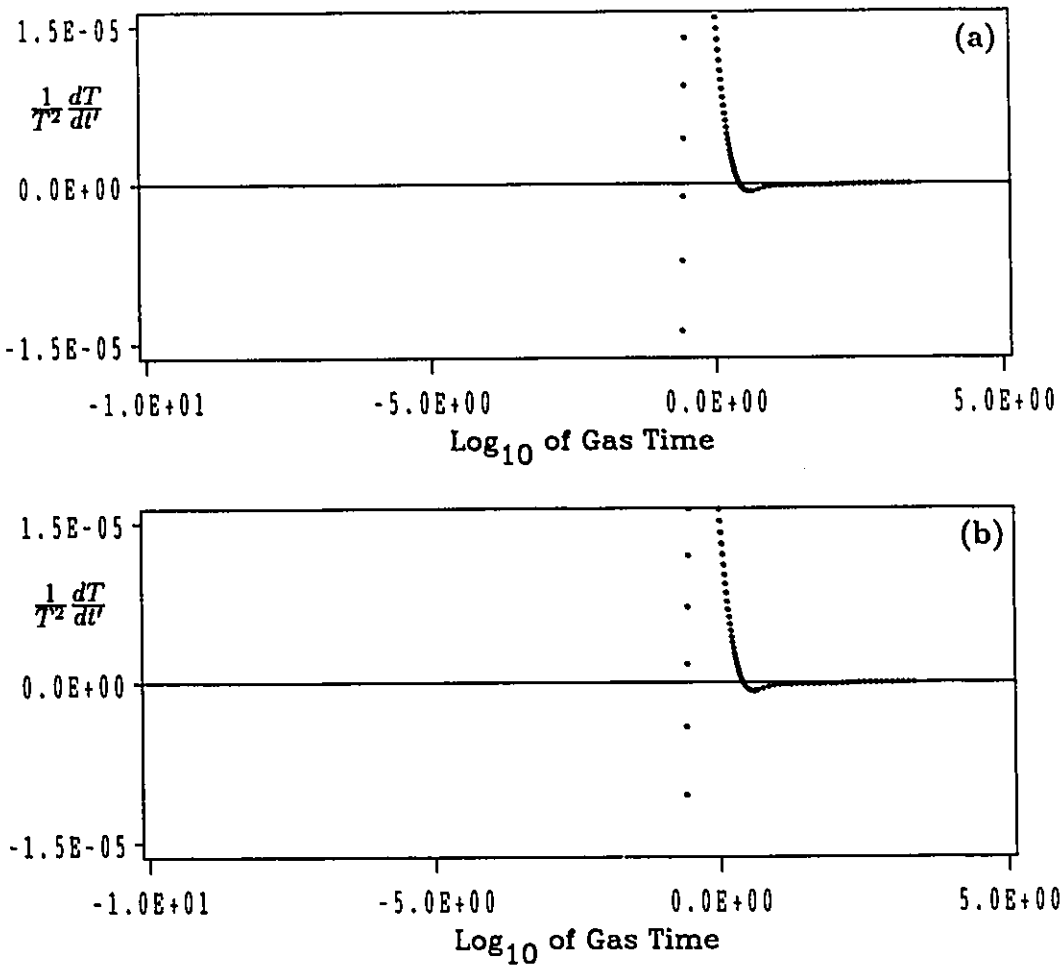

Figure 4.17 Simulation parameters $A = 7.5$, $B = 2.0$, $T_{int} = 350.15$ K, and $z_0 = 3.0$ are kept constant, while β is varied. (a) $\beta = 10^{-3}$, (b) $\beta = 10^{-2}$. The observable is plotted with a y-axis scale of $\pm 1.5 \times 10^{-5}$.

a further shift of the first negative part of the waveform becoming more positive but not crossing over yet. The waveform has crossed over in Figure 4.12(b) where β has been increased to 1.0. Note that the second peak has not changed while the other change was occurring.

In Figure 4.13(a), where z_0 is increased to 30.0 and in Figure 4.13(b) where z_0 is increased to 300.0 the decrease of the amplitude of the observable is much more pronounced than the change of z_0 from 0 to 3.0 indicates.

Figure 4.14(a) and (b) are y-axis expansions of the plots presented in 4.11(a) and

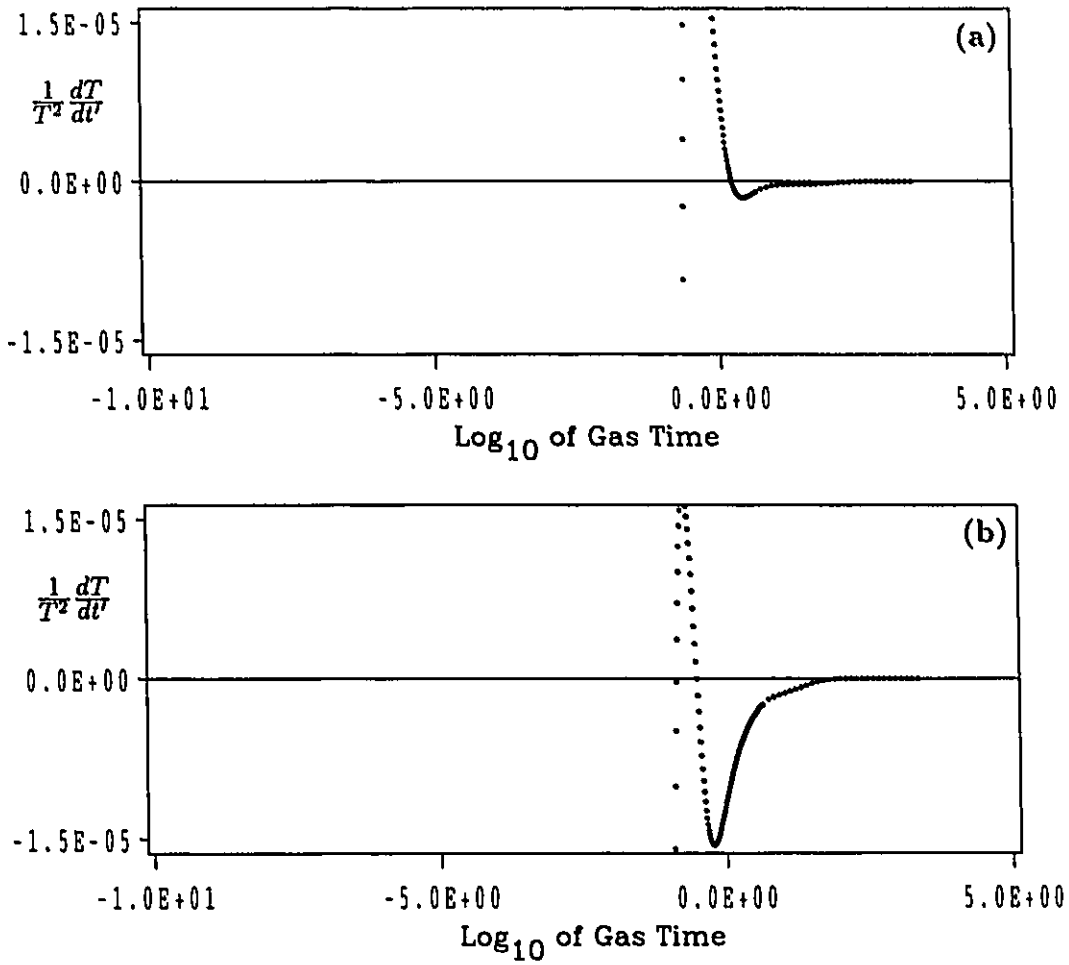

Figure 4.18 Simulation parameters $A = 7.5$, $B = 2.0$, $T_{int} = 350.15$ K, and $z_0 = 3.0$ are kept constant, while β is varied. (a) $\beta = 10^{-1}$, (b) $\beta = 10^{0}$. The observable is plotted with a y-axis scale of $\pm 1.5 \times 10^{-5}$.

(b), respectively, with $\beta = 10^{-3}$ and $z_0 = 3.0$. There seems to be little change in the inflection points and oscillations that were observed in Figure 4.14(a) and (b) or in Figure 4.5(a) where $z_0 = 0.0$ and β was therefore not included in the calculation.

Comparison of Figures 4.15(a) and (b) shows that, although, there are several inflection points in the waveform in 4.15(a) for $\beta = 10^{-1}$, when β is increased to 1.0, 4.15(b), these inflection points are no longer present. They may have been converted to oscillations of the waveform about the zero reference line but this does not seem to have been the case for in Figure 4.18(a) and (b), 4.21(a) and (b), and Figure 4.31(a)

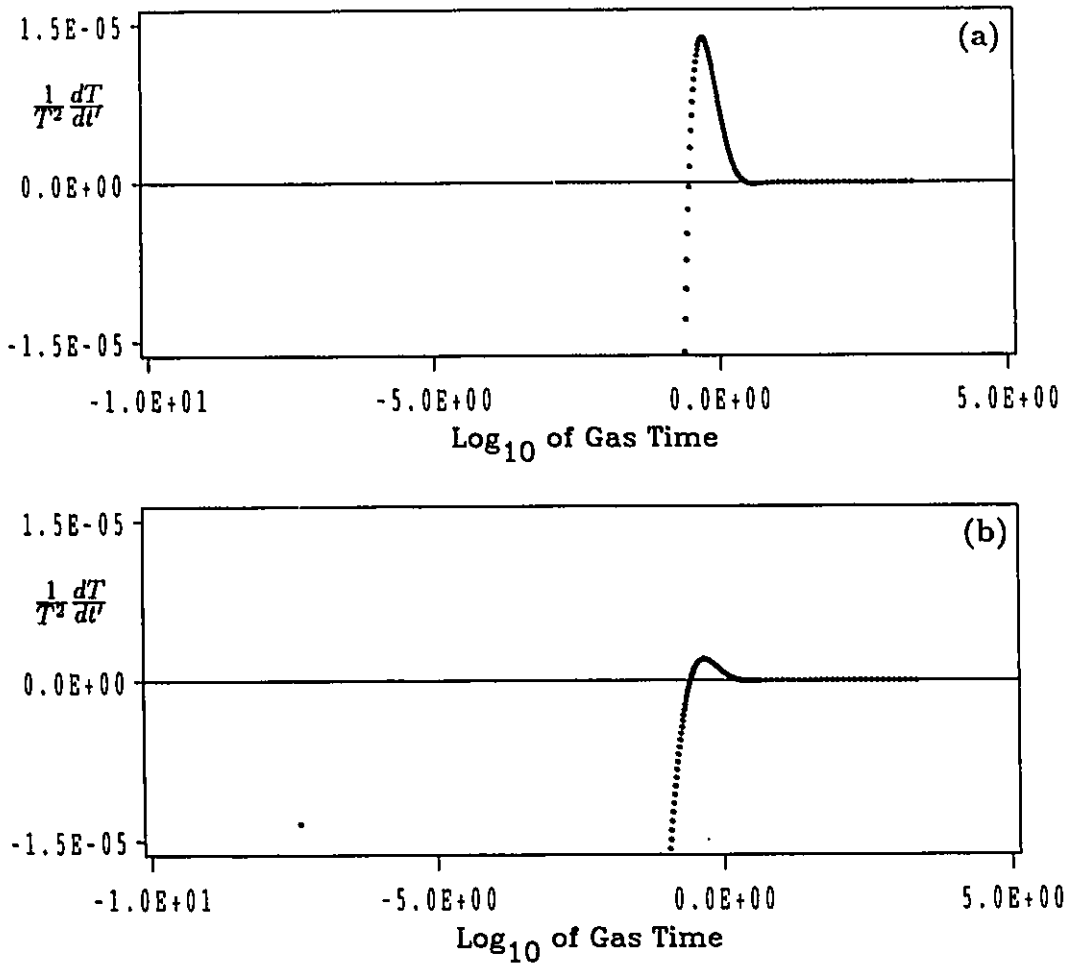

Figure 4.19 Simulation parameters $A = 7.5$, $B = 2.0$, $T_{int} = 350.15$ K, and $\beta = 10^{-3}$ are kept constant, while z_0 is varied. (a) $z_0 = 30.0$, (b) $z_0 = 300.0$. The observable is plotted with a y-axis scale of $\pm 1.5 \times 10^{-5}$.

there seems to be no increase in the number of oscillations of the observable.

Figure 4.16(a) and (b) are for $A = 7.5$, $B = 2.0$, $T_{int} = 350.15$ K, and $\beta = 10^{-3}$, while z_0 varies from 30.0 to 300.0, respectively, and the y-axis expansion is for $\pm 1.5 \times 10^{-3}$. The observable amplitude has decreased dramatically with the increase of z_0 from 30.0 to 300.0, which is only an order of magnitude change.

In Figure 4.17, with $A = 7.5$, $B = 2.0$, $T_{int} = 350.15$ K, and $z_0 = 3.0$ are kept constant while β is changed from 10^{-3} in 4.17(a) to 10^{-2} in 4.17(b), and the y-axis expansion is for $\pm 1.5 \times 10^{-5}$. Once again it is hard to see any change of the amplitude

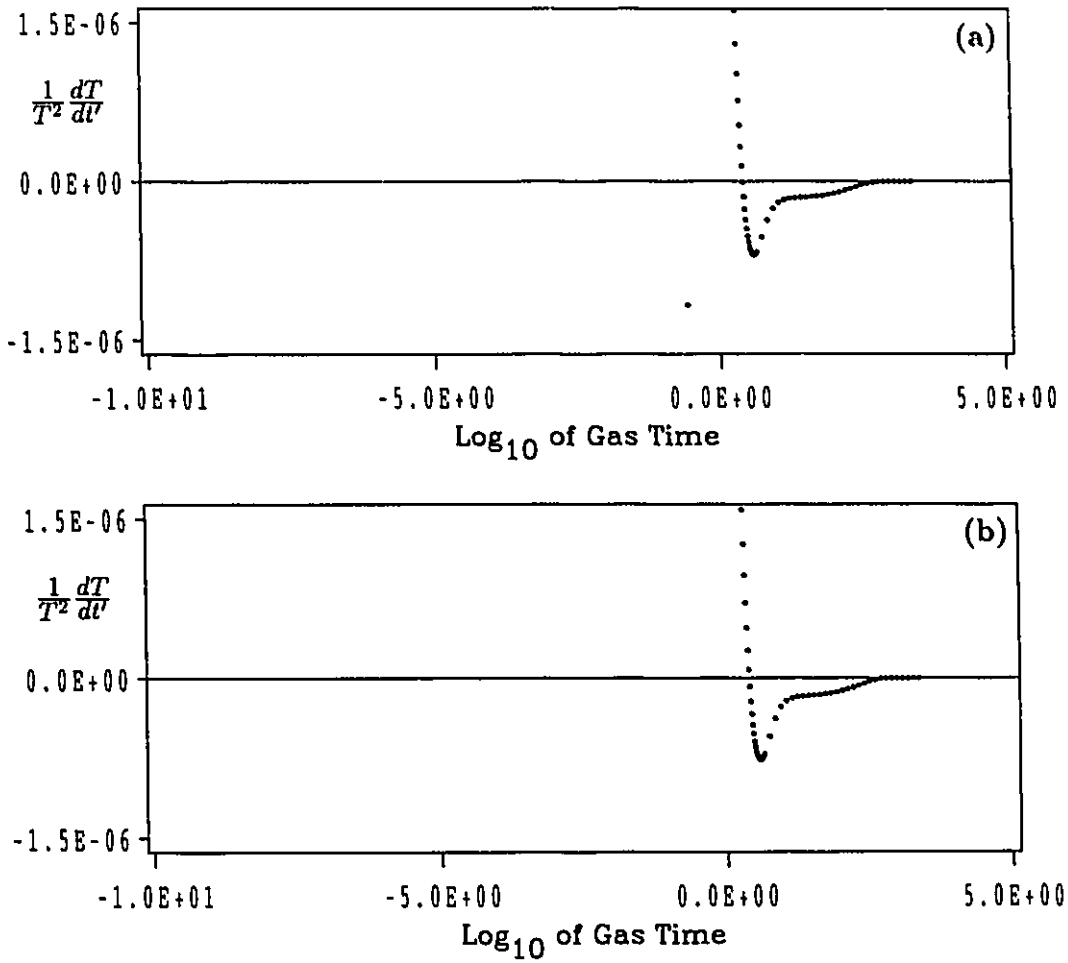

Figure 4.20 Simulation parameters $A = 7.5$, $B = 2.0$, $T_{int} = 350.15$ K, and $z_0 = 3.0$ are kept constant, while β is varied. (a) $\beta = 10^{-3}$, (b) $\beta = 10^{-2}$. The observable is plotted with a y-axis scale of $\pm 1.5 \times 10^{-6}$.

of the observable for this increase of β by an order of magnitude.

In Figure 4.18 all parameters are kept constant including $z_0 = 3.0$ while β is changed from 0.1 to 1.0. A rather large decrease of the amplitude of the observable can be seen when comparing Figure 4.18(a) and 4.18(b), for this order of magnitude change for z_0. In fact, it is much more dramatic than the small change of the observable when comparing Figures 4.17(b) and 4.18(a), which are also for an order of magnitude change of z_0, 10^{-2} to 10^{-1}.

In Figure 4.19 the parameters $A = 7.5$, $B = 2.0$,$T_{int} = 350.15$ K, and $\beta = 10^{-3}$

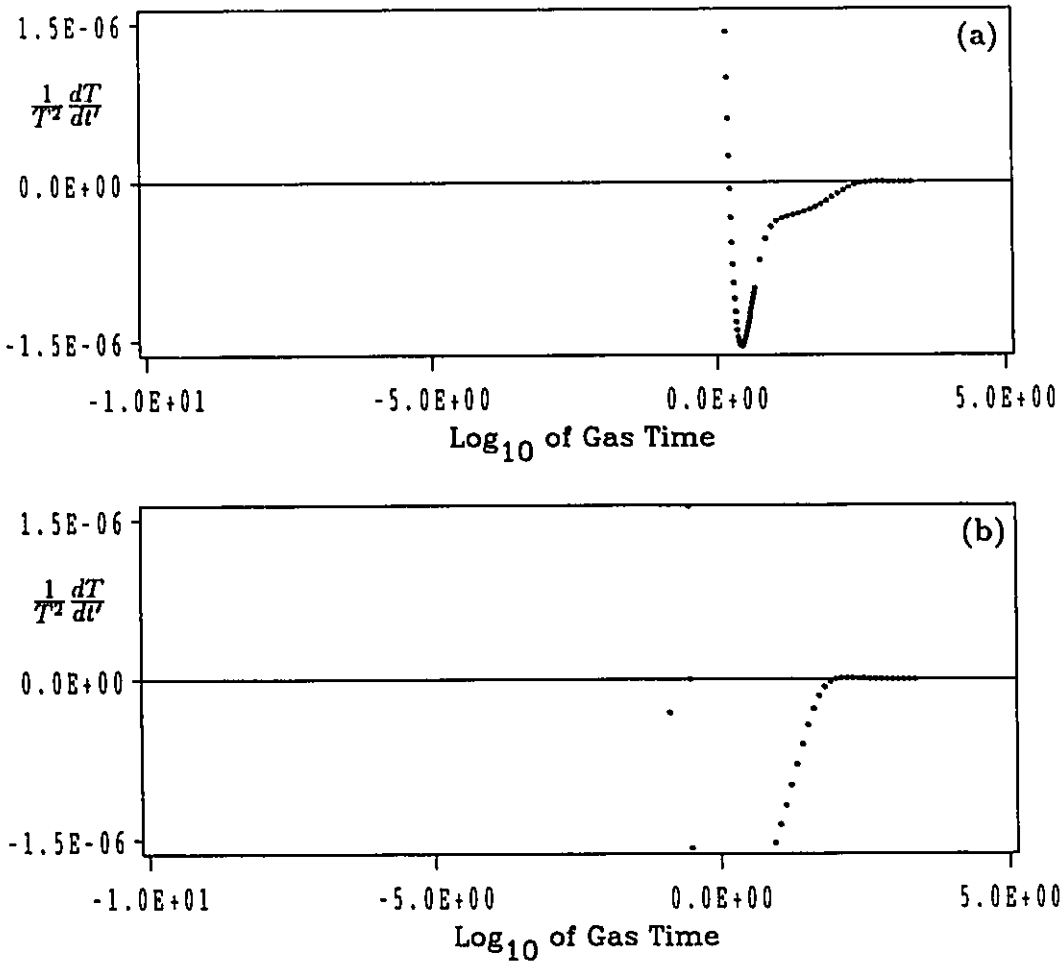

Figure 4.21 Simulation parameters $A = 7.5$, $B = 2.0$, $T_{int} = 350.15$ K, and $z_0 = 3.0$ are kept constant, while β is varied. (a) $\beta = 10^{-1}$, (b) $\beta = 10^{0}$. The observable is plotted with a y-axis scale of $\pm 1.5 \times 10^{-6}$.

are kept constant, while z_0 is changed from 30.0 to 300.0 for a y-axis expansion of $\pm 1.5 \times 10^{-5}$. The waveform in 4.19(a) has a larger amplitude that the waveform in 4.19(b) which is expected for this order of magnitude increase of z_0, as was first shown in Figures 4.13(a) and (b).

Close inspection of Figure 4.20(a) and (b) reveals that the negative amplitude of the waveform in (b) is more than 10% larger than the waveform amplitude of (a). Thus an order of magnitude increase in β has caused a small increase in the observable amplitude at this expansion.

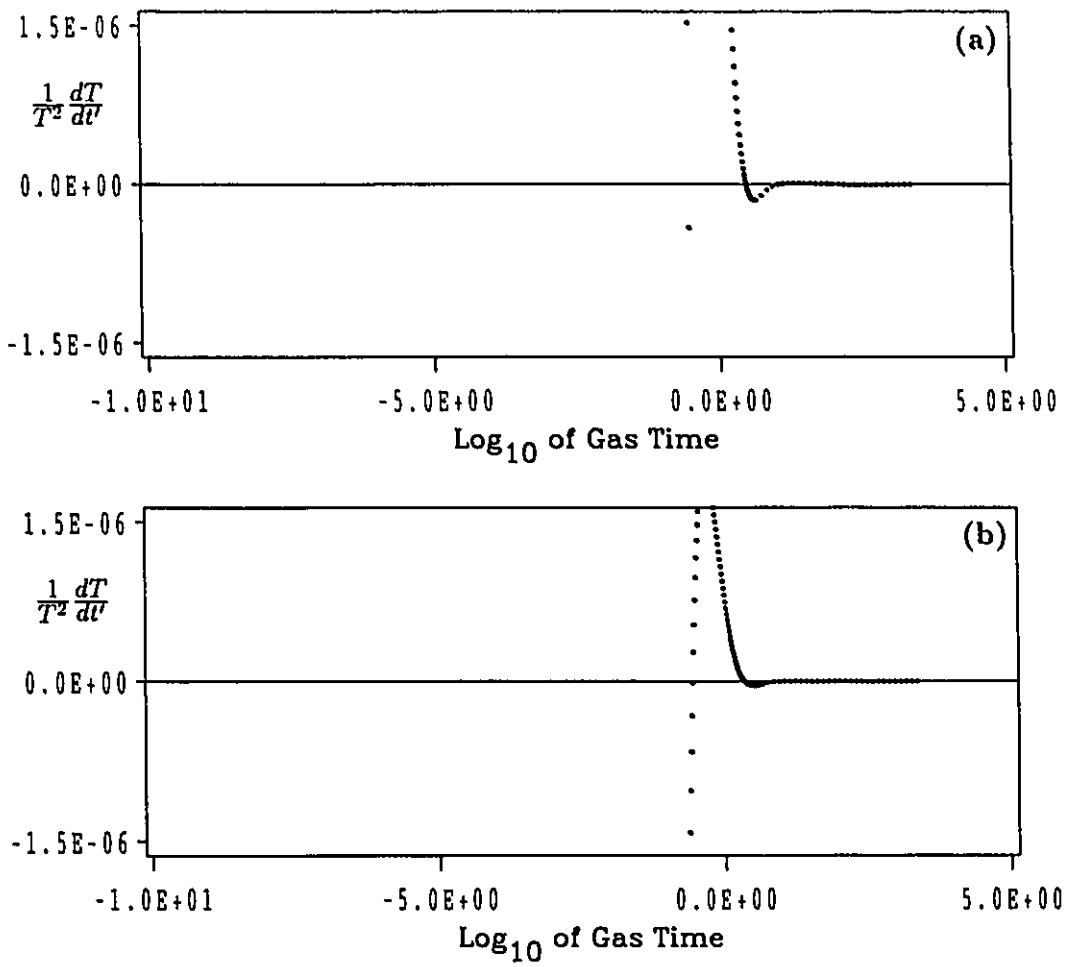

Figure 4.22 Simulation parameters $A = 7.5$, $B = 2.0$, $T_{int} = 350.15$ K, and $\beta = 10^{-3}$ are kept constant, while z_0 is varied. (a) $z_0 = 30.0$, (b) $z_0 = 300.0$. The observable is plotted with a y-axis scale of $\pm 1.5 \times 10^{-6}$.

It is obvious that the waveform in Figure 4.21(b) has a much larger negative amplitude than the waveform in Figure 4.21(a). However, it is interesting that the overall shape of the waveform in Figure 4.21(a) is decidedly similar to the waveforms in Figures 4.20(a) and (b). There is a larger increase of the amplitude of the observable for changing β from 0.1 to 1.0 than for the change from 10^{-3} to 10^{-2} or 10^{-2} to 10^{-1}. A decidedly nonlinear response to a linear change of β but the change is in the correct direction. As stated in case one, the amplitude of the signal is expected to increase with increasing stabilization.

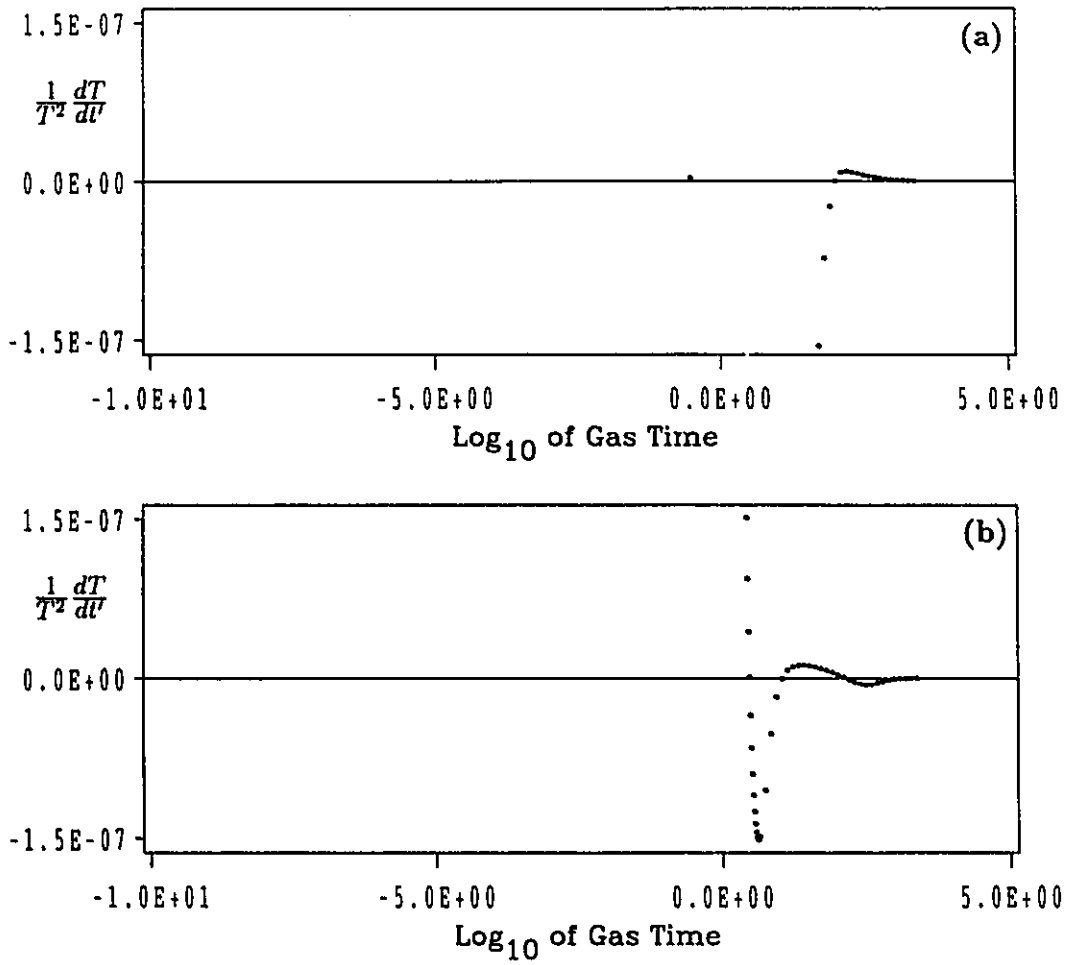

Figure 4.23 Simulation parameters $A = 7.5$, $B = 2.0$, and $T_{int} = 350.15$ K are kept constant, while β and z_0 are varied. (a) $\beta = 10^0$ and $z_0 = 3.0$, (b) $\beta = 10^{-3}$ and $z_0 = 30.0$. The observable is plotted with a y-axis scale of $\pm 1.5 \times 10^{-7}$.

Figure 4.23(a), with $\beta = 1.0$, and $z_0 = 3.0$, an expansion of Figure 4.22(b), showing that the waveform does go positive. Although the same expansion of the waveform for $\beta = 10^{-1}$ is not shown it has similar features to those seen in Figure 4.23(a). In Figure 4.23(b) it is obvious that the amplitude of the waveform has decreased when z_0 is increased from 3.0 to 30.0, but there has also been an increase in the number of oscillations present in the waveform.

Comparison of Figure 4.23(b) and 4.24(a) shows that the amplitude of the wave-

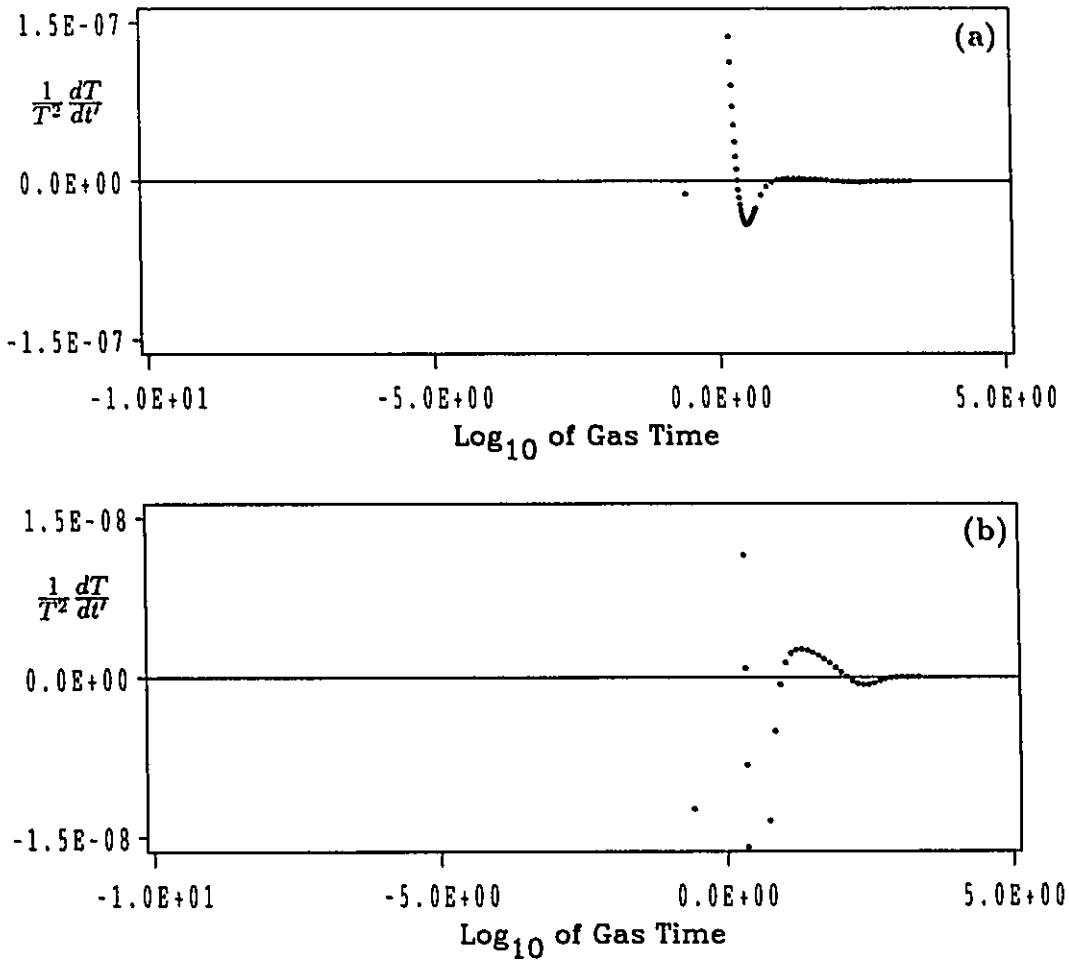

Figure 4.24 Simulation parameters $A = 7.5$, $B = 2.0$, $T_{int} = 350.15$ K, $\beta = 10^{-3}$ and $z_0 = 300.0$ are kept constant, and the observable is plotted with a y-axis of $\pm 1.5 \times 10^{-7}$, (a), and $\pm 1.5 \times 10^{-8}$, (b).

form has decreased when increasing z_0 from 30.0 to 300.0. The y-axis of Figure 4.24(b) is an order of magnitude larger than Figure 4.23(b) and the waveform in 4.24(b) in not on scale, thus it has not decreased linearly. Comparison of Figure 4.23(b) and 4.24(b) shows that the change of the parameter, z_0, by an order of magnitude does not change the amplitude by an order of magnitude. However it should be pointed out that the waveform in Figure 4.24(b) still has oscillations present.

For Figures 4.25-4.31 the simulation parameters $A = 11.5$, $B = 1.0$, $T_{int} = 350.15$ K, $Tol = 10^{-12}$ and $\beta = 10^{-3}$ are not changed, while z_0 is changed from 1.0 to 300.0.

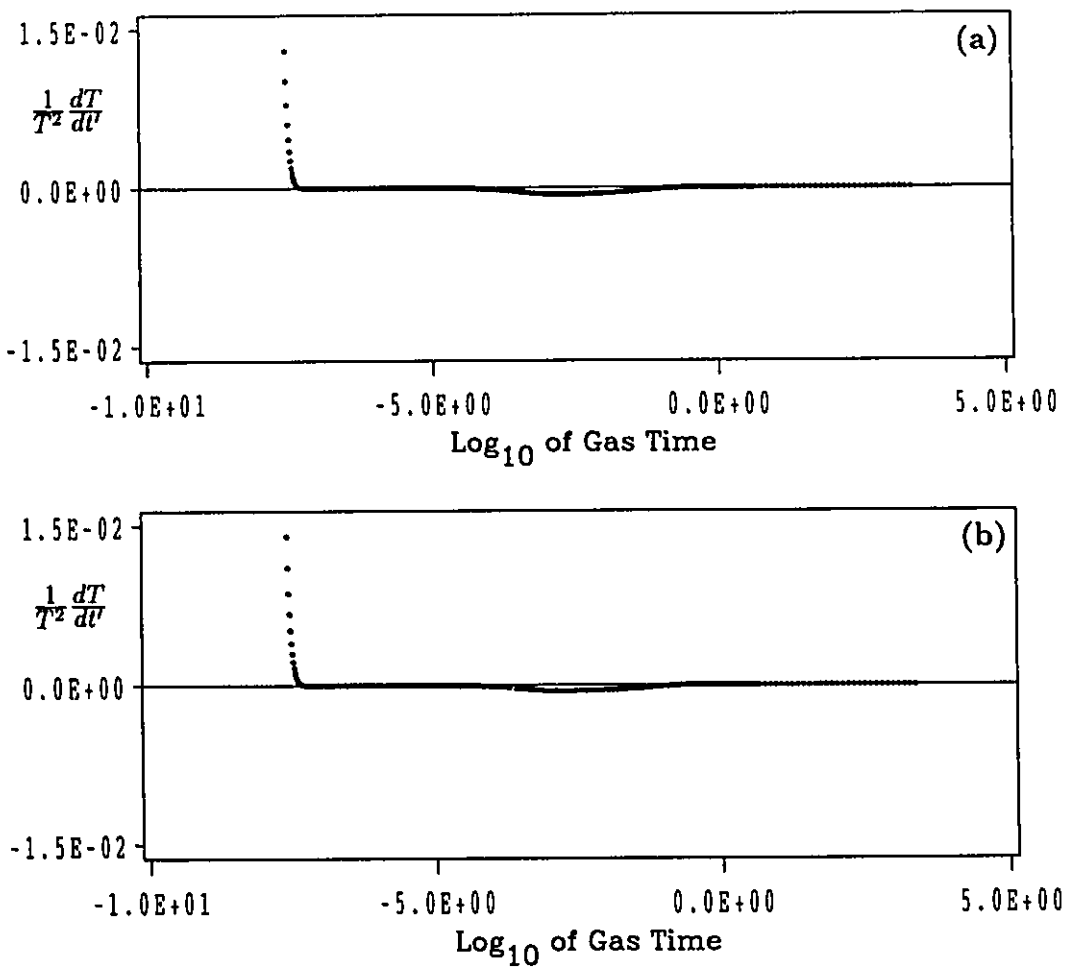

Figure 4.25 Simulation parameters $A = 11.5$, $B = 1.0$, $T_{int} = 350.15$ K, and $\beta = 10^{-3}$ are kept constant but z_0 is varied. (a) $z_0 = 1.0$, (b) $z_0 = 3.0$. The observable is plotted with a y-axis scale of $\pm 1.5 \times 10^{-2}$.

Table 4.5 Listing of the Figures 4.25-4.31 for the simulation parameters $A = 11.5$, $B = 1.0$, $T_{int} = 350.15$ K, and $\beta = 10^{-3}$ while z_0 is varied.

β	z_0	y-axis scale			
		$\pm 1.5 \times 10^{-2}$	$\pm 1.5 \times 10^{-3}$	$\pm 1.5 \times 10^{-5}$	$\pm 1.5 \times 10^{-6}$
10^{-3}	1.0	4.25(a)	4.27(a)	4.29(a)	4.31(a)
10^{-3}	3.0	4.25(b)	4.27(b)	4.29(b)	4.31(b)
10^{-3}	30.0	4.26(a)	4.28(a)	4.30(a)	
10^{-3}	300.0	4.26(b)	4.28(b)	4.30(b)	

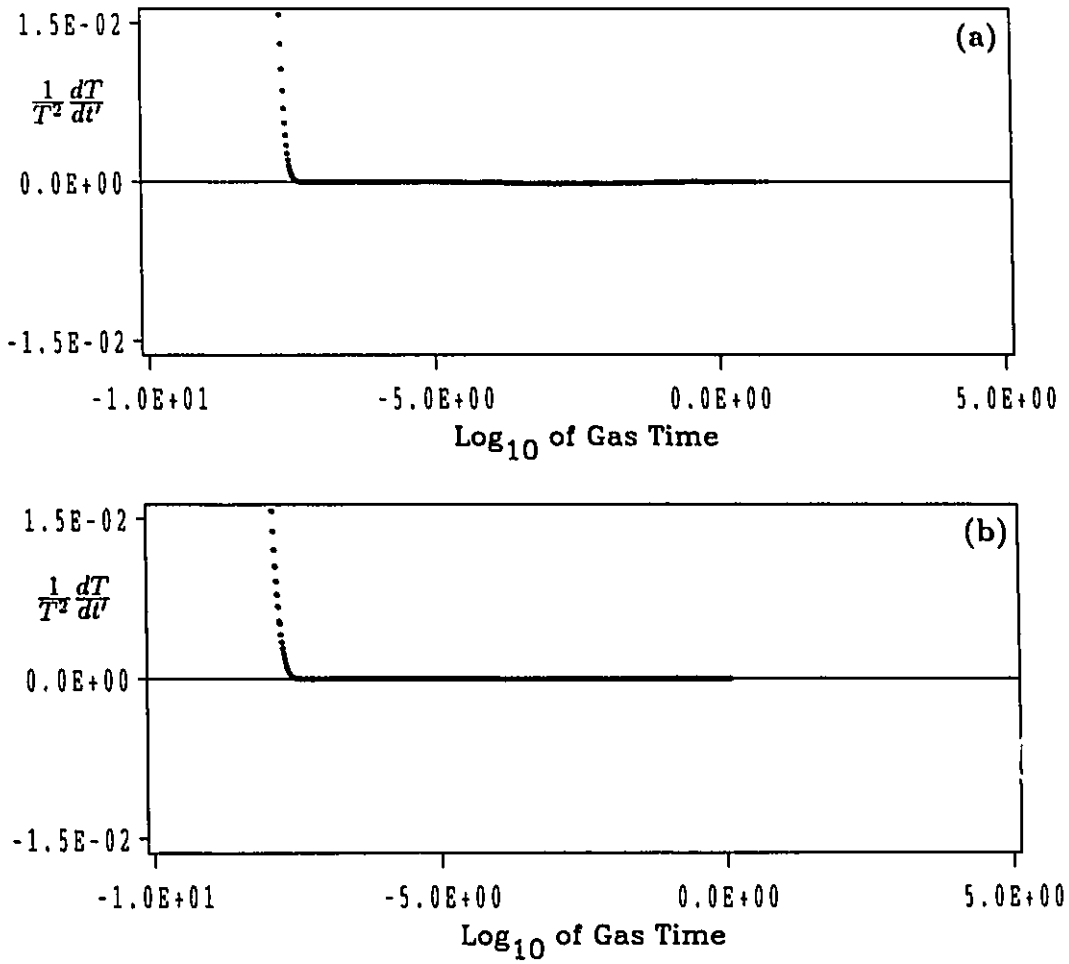

Figure 4.26 Simulation parameters $A = 11.5$, $B = 1.0$, $T_{int} = 350.15$ K, and $\beta = 10^{-3}$ are kept constant but z_0 is varied. (a) $z_0 = 30.0$, (b) $z_0 = 300.0$. The observable is plotted with a y-axis scale of $\pm 1.5 \times 10^{-2}$.

Comparison of Figure 4.25(a) and (b), where the parameter z_0 has been changed by a factor of 3 while keeping $A = 11.5$, $B = 1.0$, $T_{int} = 350.15$ K, $\beta = 10^{-3}$, and $Tol = 10^{-12}$ fixed, shows a slight change in the negative part of the waveform. Further amplification is needed to understand what has changed, and this is indicated later.

This is also the case for Figure 4.26 since the amplification is not large enough to see a change. However the waveform in Figure 4.26(a) is at least different from the waveform in Figure 4.25(b).

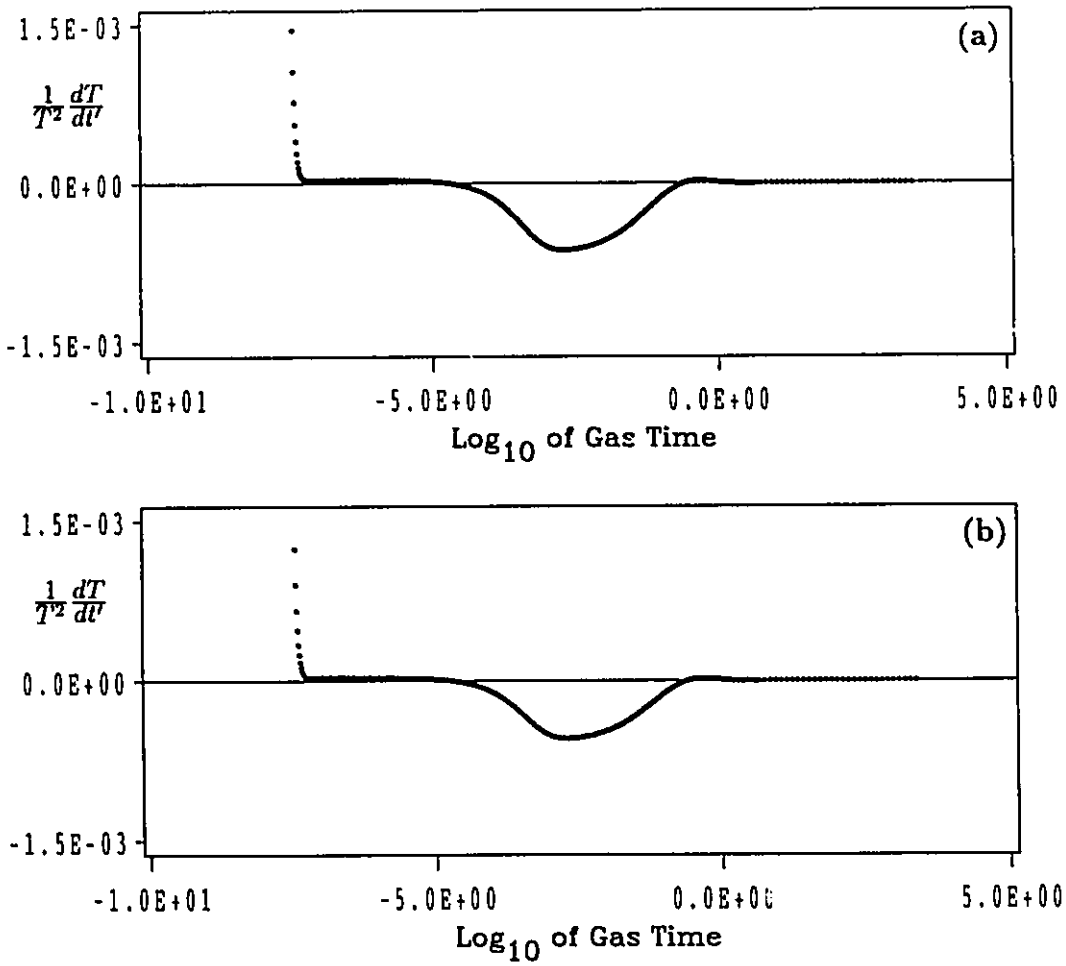

Figure 4.27 Simulation parameters $A = 11.5$, $B = 1.0$, $T_{int} = 350.15$ K, and $\beta = 10^{-3}$ are kept constant but z_0 is varied. (a) $z_0 = 1.0$, (b) $z_0 = 3.0$. The observable is plotted with a y-axis scale of $\pm 1.5 \times 10^{-3}$.

Comparing Figure 4.27(a) to Figure 4.6(b) shows that the depth of the well has decreased when increasing z_0 from 0.0 to 3.0 although not much change is seen for the 1.0 case.

Figures 4.28(a) and (b) indicate that increasing z_0 from 30.0 to 300.0 causes the amplitude of the waveform to decrease. However, Figures 4.30 (a) and (b) allow for an evaluation of the case of increasing z_0 from 30.0 to 300.0, and these expansions clearly show the decrease in amplitude of the waveform.

Note that z_0 is the ratio Ar/CCl_3F, and therefore as the ratio is increased there

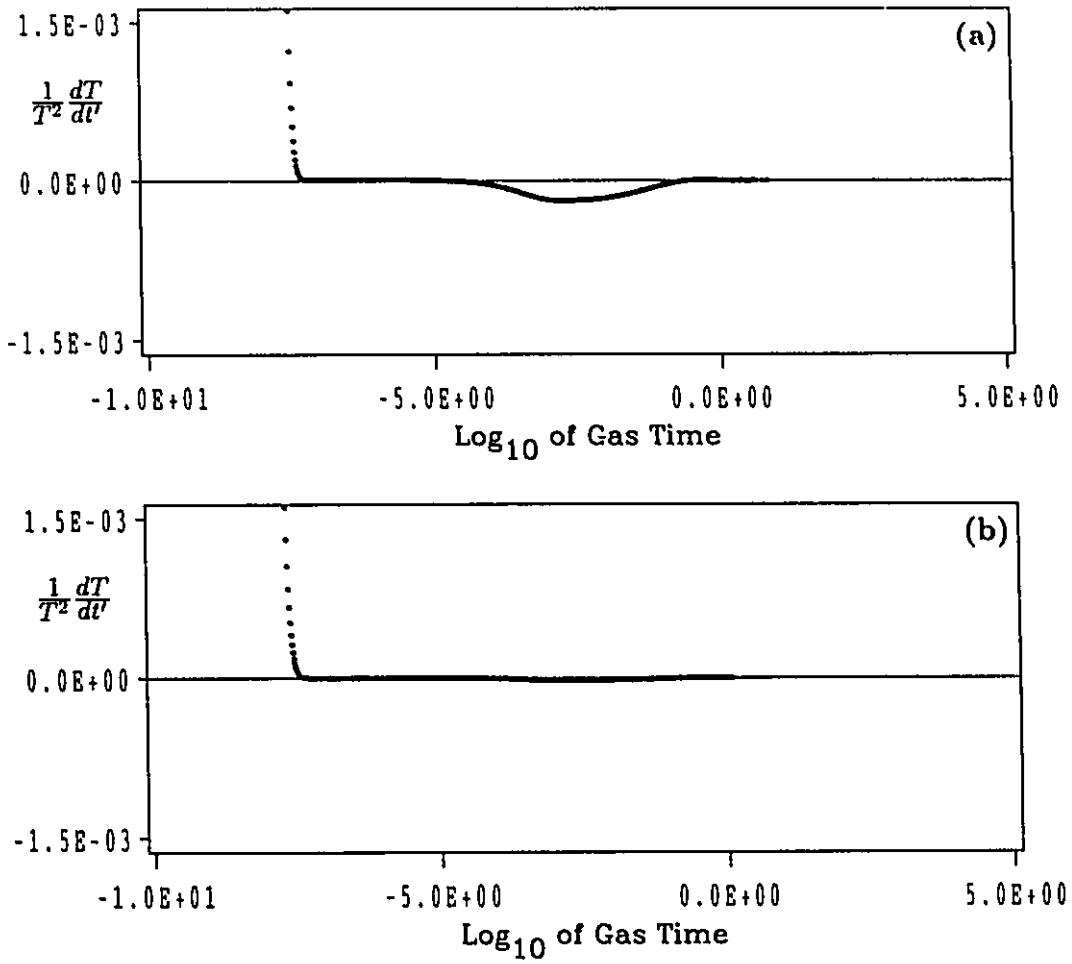

Figure 4.28 Simulation parameters $A = 11.5$, $B = 1.0$, $T_{int} = 350.15$ K, and $\beta = 10^{-3}$ are kept constant but z_0 is varied. (a) $z_0 = 30.0$, (b) $z_0 = 300.0$. The observable is plotted with a y-axis scale of $\pm 1.5 \times 10^{-3}$.

is more argon present and the result is that the waveform is less negative. Remember that the negative part of the waveform is a measure of the rate of heat release. It can be expected that part of the decrease of the waveform amplitude will be due to less CCl_3F present to form clusters. Part may also be due to Ar's poor ability to stabilise the clusters resulting in a lower amplitude of the negative part of the waveform. The overall shape (*i.e.* oscillations) are affected by this dilution factor, which has the additional subtle effect of controlling the thermal feedback to the rate coefficients and to the equilibrium mole fractions.

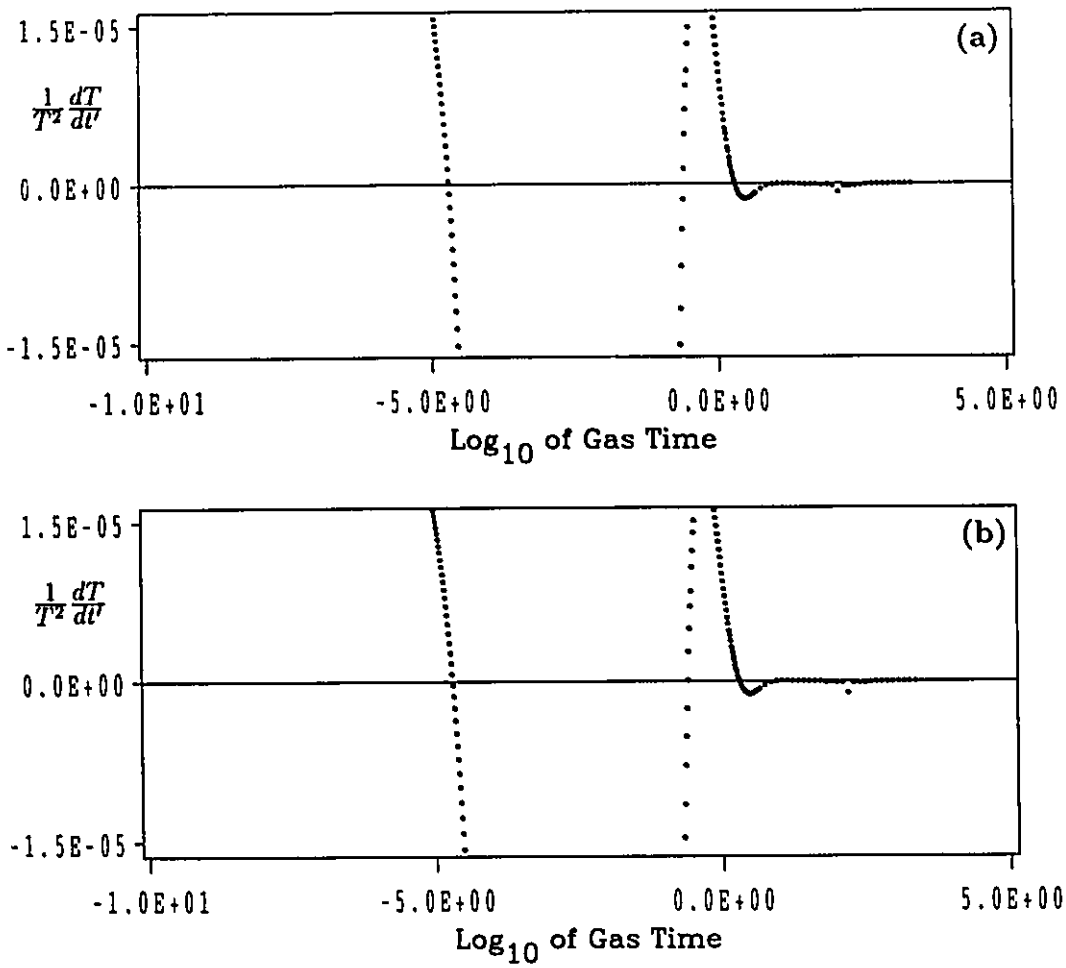

Figure 4.29 Simulation parameters $A = 11.5$, $B = 1.0$, $T_{int} = 350.15$ K, and $\beta = 10^{-3}$ are kept constant but z_0 is varied. (a) $z_0 = 1.0$, (b) $z_0 = 3.0$. The observable is plotted with a y-axis scale of $\pm 1.5 \times 10^{-5}$.

Comparison of Figures 4.29(a) and (b) to Figure 4.8(b) again shows that there is a slight change of the waveform for a change of z_0 from 0.0 to 1.0 and a larger change of the waveform when z_0 is increased to 3.0.

Comparing Figures 4.10(a) and 4.31, where z_0 has increased from 0.0 (Figure 4.10(a)) to 1.0 (Figure 4.31(a)) to 3.0 (Figure 4.31(b)) and it can be seen that the amplitude has decreased but that the shape of the waveform has also changed.

Overall these simulations have shown manifestations of nonlinear effects since the waveforms have changed shape, and the amplitude has not changed proportionally.

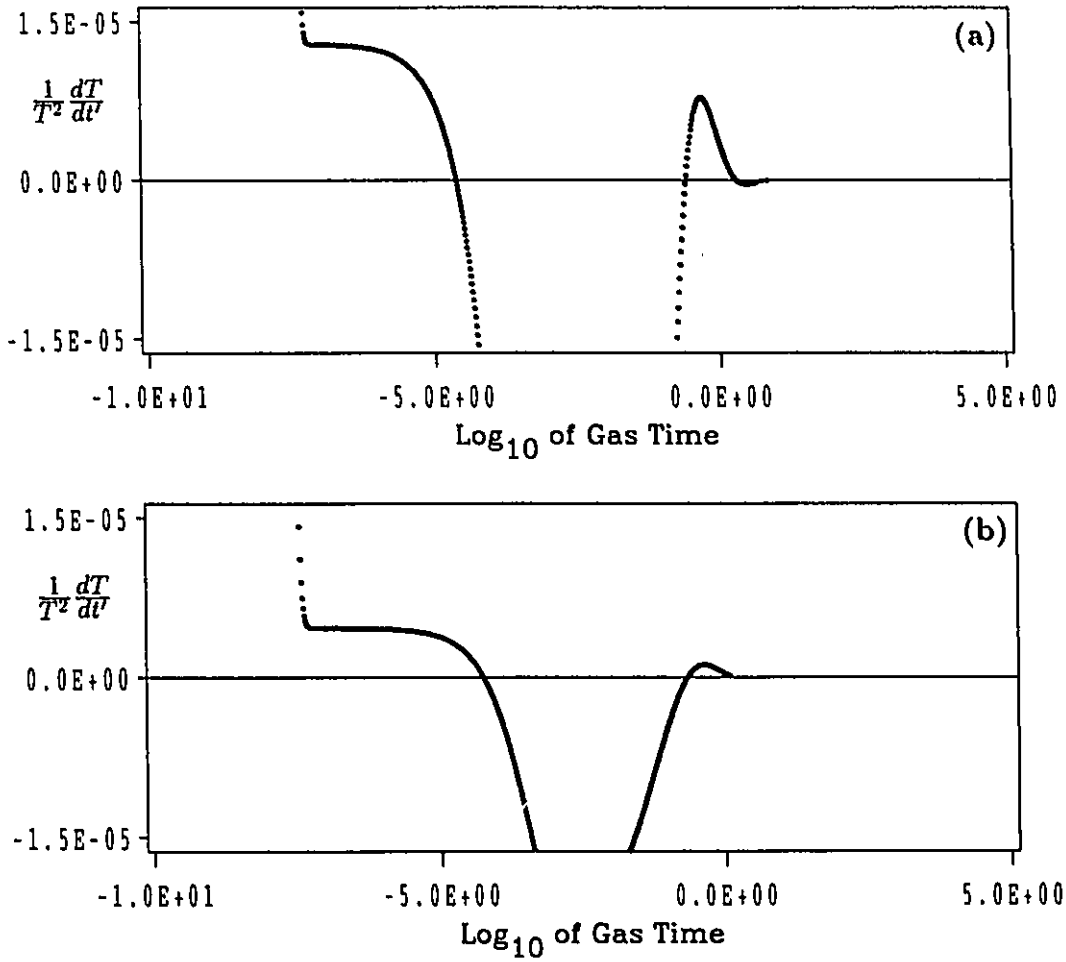

Figure 4.30 Simulation parameters $A = 11.5$, $B = 1.0$, $T_{int} = 350.15$ K, and $\beta = 10^{-3}$ are kept constant but z_0 is varied. (a) $z_0 = 30.0$, (b) $z_0 = 300.0$. The observable is plotted with a y-axis scale of $\pm 1.5 \times 10^{-5}$.

For case one, as mentioned earlier for z_0 being constant, Figure 4.21(a) is compared to Figure 4.18(b) where the y-axes are an order of magnitude different and the waveform is on scale in both plots. However the approximated rate equation indicates that there should only have been a change of amplitude by a factor of 2.5, not an order of magnitude. Furthermore, the shape has changed. Therefore this is another indication that there are nonlinear effects.

For case two, where $z_0 * \beta = 0.3$, a comparison of Figure 4.12(a) and 4.16(b) where the y-axes are an order of magnitude different shows similarity of shape. A simple

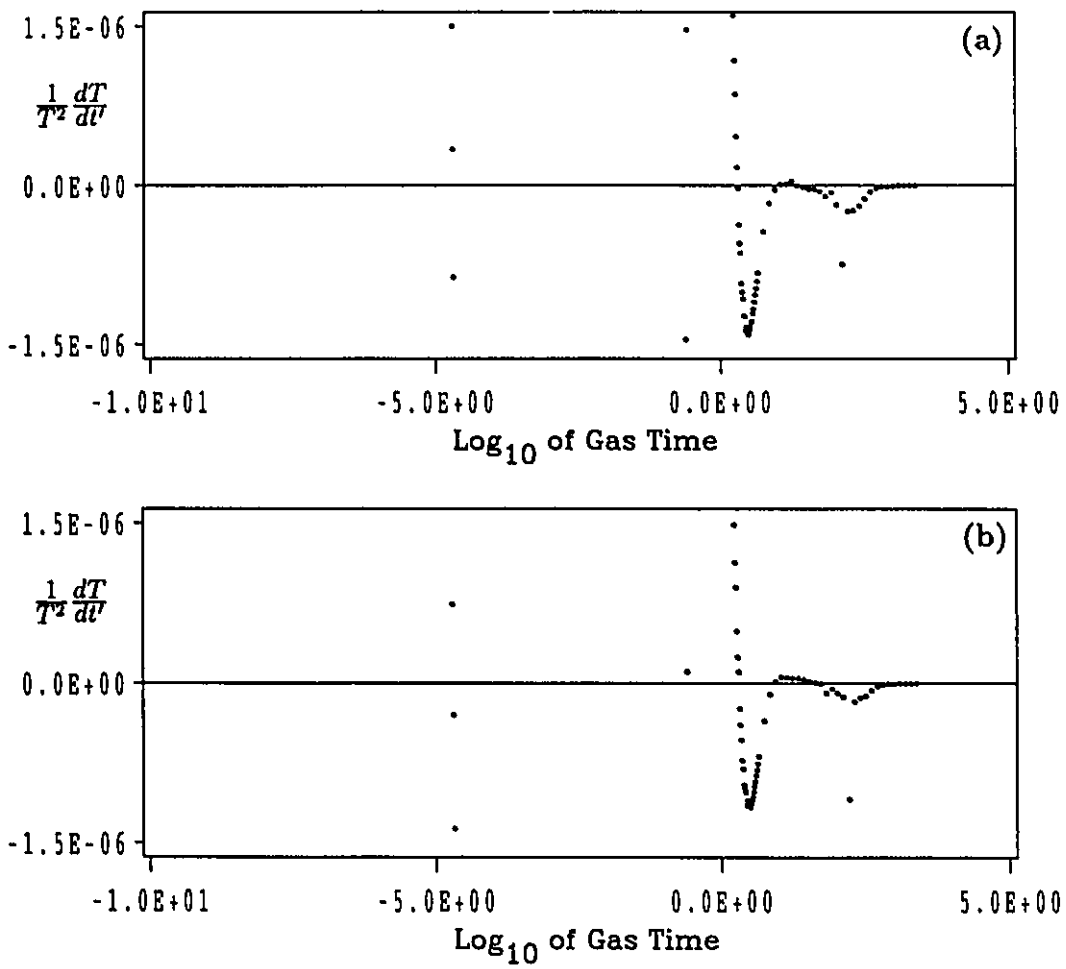

Figure 4.31 Simulation parameters $A = 11.5$, $B = 1.0$, $T_{int} = 350.15$ K, and $\beta = 10^{-3}$ are kept constant but z_0 is varied. (a) $z_0 = 1.0$, (b) $z_0 = 3.0$. The observable is plotted with a y-axis scale of $\pm 1.5 \times 10^{-6}$.

measurement of the depth of the well in both figures gives a ratio of 23.3 not the expected 30. However, comparison of expansions of these figures, as in Figures 21(a) and 4.24(a) respectively, shows that the factor of 30 difference is evident, but so is the shape change.

For case 3, where $\beta = 10^{-3}$ and z_0 is varied from 3.0 to 300.0 and from 3.0 to 0.0, the comparison of Figure 4.11(a) and Figure 4.16(b) shows that the amplitude changes by about a factor of 21 and not the expected 27. In the expansions of those plots, that is Figure 4.20(a) and Figure 4.24(a) the ratio is only about 19 times not the 27

times that was predicted. For $A = 11.5$ and $B = 1.0$ comparison of Figures 4.6(b) for $z_0 = 0.0$ and 4.27(a) for $z_0 = 1.0$ and 4.27(b) for $z_0 = 3.0$ show little or no change of the gross features. However, for the expansions, as in Figures 4.10(a) and 4.31(a) and (b) it is possible to see a change in amplitude of about the expected 1.147, but most important is the change in waveform shape. Even the slight change of z_0 from 1.0 (Figure 4.31(a)) to 3.0 (Figure 4.31(b)) has changed the amplitude of the waveform and the oscillations of the waveform.

4.4 Experimental Apparatus

The experimental apparatus is a shock tube for doing temperature jump experiments. Although the T-jump is unlimited, the apparatus used in the present work has been used in the past for $\Delta T = 0 \rightarrow 4000$ K. The temperature jump occurs in 1-2 nanoseconds. The shock tube is made up of two chambers separated by a diaphragm. The driver section is made from iron pipe which is 15 centimeters in diameter and 380 centimeters long. The sample section is made from stainless steel plate, which is approximately 10 centimeters to a side and is 1100 centimeters long. The test gas is placed in the sample section and then driver gas, usually helium, is added to the driver section until the diaphragm bursts. The magnitude of the temperature jump is controlled by selecting the diaphragm thickness. As one would expect, the thicker the diaphragm the greater the temperature jump. There can be as much as 5-8% difference in the experimental temperature for a constant test pressure since not every diaphragm bursts at exactly the same pressure.

The sample chamber has eight sets of quartz windows, in opposite walls and one of these sets is used to detect the main signal via a laser-schlieren detection system (described below). Three of the remaining sets of quartz windows are used to determine the velocity of the shock front using three more schlieren detectors. The velocity of the shock front is calculated by measuring the time interval between the detector signals and by dividing it into the known inter-detector distance ($vel = dist/time$). At each schlieren detector a 5mW He-Ne laser beam passes perpendicularly through a set of quartz windows in the sample section and impinges on the centre of a quadrant photodetector. The electronics of the photodetector system is set up such that the currents from each of the quadrants are balanced against each other. Therefore when the laser beam is centred on the four quadrants each will have equal laser intensity on it producing equal current, and the resulting output from the photodetector electronics will be zero. Therefore this configuration will indicate if the beam has moved and

in which direction it has moved. The schlieren detection system allows the density gradient of the shock heated gas to be measured, as described below. The density gradient is then related to physical and chemical properties of the sample gas.

4.4.1 Laser Schlieren Detector

This work will present a summary of the schlieren detection system as initiated by Kiefer and Lutz[74] and then improved upon by Dove and Teitelbaum[75] and further improved upon by Baalbaki and Teitelbaum[76]. The schlieren detection system as outlined by Kiefer and Lutz[74] used a single HeNe (helium-neon) laser, a 25% transmitting mirror, two photomultiplier tubes, one microscope optic and a knife-edge. The HeNe laser beam was incident on the 25% transmitting mirror and the reflected portion of the beam was passed through optical quality, glass windows in opposing sides of the test section of a shock tube. Once the laser light had passed through the second window it was focussed, using a microscope optic, onto a knife-edge (a razor blade) 7 meters away. Only one-half of the beam was blocked by the razor's edge; the rest fell onto a photomultiplier tube and the resulting signal was amplified and sent to a Tektronix oscilloscope. The transmitted beam (see above) was sent on to a second photomultiplier tube, and the resulting signal was amplified, and sent to a second Tektronix oscilloscope. This second signal was used to do background correction. Both signals, once displayed on the oscilloscope screens, were photographed using appropriate camera attachments for the oscilloscopes. The fastest time base for these oscilloscopes was 0.1 μsecond per division. Since these were analog oscilloscopes, the easiest and cheapest way that the data could be recorded was by the use of cameras. The reader is referred to the original papers for the exact details of the setup. This initial setup of Kiefer and Lutz[74] was improved upon by Dove and Teitelbaum[75] by replacing the photomultipliers and knife edge with a quadrant photodiode detector. The preceding discussion was for the main signal of the shock

tube, and the velocity detection was done using gold film thermal sensors inside the tube. This was replaced by Baalbaki and Teitelbaum[76] with sets of laser-schlieren detectors, but the velocity signals were sent to one channel of a Nicolet Explorer *III* digital oscilloscope which had only 4096 data points. Baalbaki and Teitelbaum also captured the main signal with a transient waveform recorder (Biomation 8100) with 2048 data points. The Biomation waveform recorder has a minimum step size of 10 nanoseconds and therefore for 2048 data points the total time of the waveform must be $\leq 10 \times 10^{-9} \times 2048 \approx 20.5\mu$seconds. However, if the total time of a waveform to be studied is $\approx 800\mu$seconds and there are only 2048 data points, the data step used must be 0.4μseconds, not 10 nanoseconds, in order to capture the whole signal ($2048 \times 400 \times 10^{-9}$seconds $\approx 820\mu$seconds). The transient waveform recorder was used to trigger the capture of the velocity data and its own data. The velocity data would then be recorded on a double-sided double density (2DD) 5.25" disk. Next the information from the transient waveform recorder was sent to the digital oscilloscope and recorded on 5.25"/2DD disks. The information was backed up in this manner and could be sent on to an XT-clone and then transferred to the mainframe computer for analysis and plotting.

In the following description the quadrant photodetector array is labeled A, B, C, and D, in a clockwise manner starting with A at the top most left corner of the circle (See Figure 4.32(d)). In the system used by Dove and Teitelbaum[75] and by Baalbaki and Teitelbaum[76], the output voltage was collected from two differential video amplifiers $V_1 = V_a - V_c$ and $V_2 = V_b - V_d$ which were then subtracted to give $V = V_1 - V_2 = V_a + V_d - V_b - V_c$. The result is just the left half of the photodiode array minus the right half of the photodiode array. The video amplifiers were used because, at the time (early 1970s) these were the fastest responding differential amplifiers available. They have been replaced in the present study with operational amplifiers (OP-64) which have a faster response (130V/μs) than the video amplifiers and which

have a lower bandwidth thus picking up less high frequency noise. The OP-64 has a Gain-Bandwidth product of 80 MHz (typical) and therefore at the amplification of 10 that is used in this work, the Bandwidth is about 8-10 MHz. Also, the OP-64 has a high current output and therefore can be used directly to drive 50 ohm (Ω) cable. It also has one more feature that makes it ideal for this work and that is the ability to disable the amplifier with a supply voltage signal. Thus the amplifier can be shut off at any time by a timing circuit that is included in the power supply-mixing board setup. The timing circuit is triggered at a predetermined voltage of 200 millivolts (which can be changed if need be), and the width of timing gate (from 40.0 μseconds to 2.0 milliseconds) is set by the resistance value of a 20-turn potentiometer. Schematics are supplied in Appendix C.

The new detection system uses preamplifier circuit boards which are configured to allow easy mounting and removal of the quadrant photodiode (PIN SPOT 9D made by United Detector Technology Sensors, Inc.). This is the same quadrant photodiode array used by Dove and Teitelbaum[75] in the early 1970s and by Baalbaki and Teitelbaum[76] in the 1980s. The present preamplifier circuits use the OP-64 operational amplifier (with the disable function) to amplify the input from the photodiode array by a factor of ten. The circuit is laid out in such a manner that the PIN SPOT 9D can either be connected in the $V_a - V_c$ and $V_b - V_d$ arrangement (quad) or in a $V_{a+d} - V_{b+c}$ arrangement (semicircle). See Appendix C.

For the new main signal preamplifier, the $V_1 = V_a - V_c$, $V_2 = V_b - V_d$ arrangement (quad) was used. This signal is then expected to be fed into a system that will allow subtraction of the two signals such as the Biomation 8100 waveform recorder. The new main signal is not used in the present work.

The new velocity signal detectors used the preamplifier set up in the semicircular mode ($V_{a+d} - V_{b+c}$), and thus the output is a complete schlieren millivolt signal. The

output of each preamplifier is sent to the mixing board where they are added to each other at the input of another OP-64 amplifier (gain of ten). The output of the mixing board is sent to a BNC connector that is terminated at 50 ohms. Since each velocity signal is a separate system any number of velocity detectors could be added to the overall system. However, in this case since there were only five HeNe lasers available the mixing board was only set up to work with five inputs. It should be added at this point that the mixing board is set up to use quadrant inputs if two OP-64 circuits have been wired up in the preamplifier (See Appendix C, preamplifier schematic). At the present time this is not the case but the preamplifier circuit boards and the main mixing board are all set up to accept the necessary components.

The separate photodiode preamplifier signals can be calibrated to give the same response for the same deflection. Note that the system has not been calibrated for this work, but the procedure is presented for future reference. This calibration is needed because not every laser will give the exact same intensity output and the mirrors are not identical and the photodiode arrays are not identical. The components described may be of different age and therefore have a dissimilar response. The first step is to measure and tabulate the maximum voltage from each photodiode in a single quadrant. Then a comparison could be made of the measured values. The lowest value is the most important at this stage. The input resistors of the mixing board could be changed in such a fashion so that each of the inputs from the various preamplifiers result in the same output value from the mixing board amplifier. This means that the photodiode preamplifier with the highest ouput voltage will have the largest resistor placed at its input to the mixing board amplifier. Therefore all preamplifiers would then deliver the same voltage to the mixing board amplifier input for the same deflection of the laser beam. Thus the systems would be calibrated to give the same response for the same deflection of the respective laser beams.

4.4.2 Laser Schlieren Signals

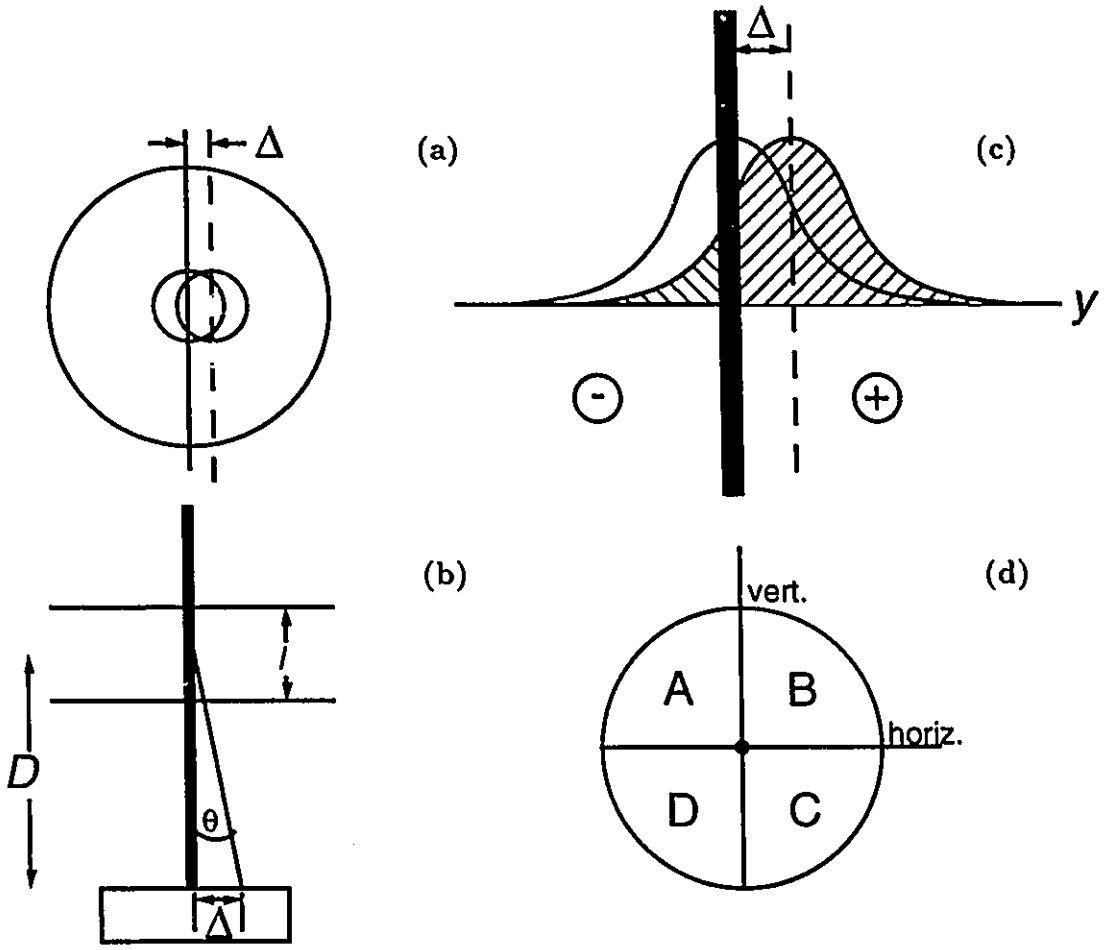

Figure 4.32 Plot of laser beam impinging on quadrant photodiode array.

Teitelbaum[77] has given a detailed explanation and derivations relating the schlieren detection system to the density gradient. Below is a summary of that detailed explanation and the reader is referred to Teitelbaum's work for a full description.

The HeNe laser beam intensity is expected to have a Gaussian distribution (approximated in Figure 4.32(c)),

$$I(r) = \frac{2P_0}{\pi a^2} \exp\left\{\frac{-2}{a^2} r^2\right\} \qquad [4.13]$$

where r is the radial coordinate of the beam, a is the beam radius at the e^{-2} intensity points, and P_0 is the laser power at the surface of the photodiode measured in one quadrant. In fact, usually the term, V_0, the voltage output of the photodiode when the laser is in one quadrant, is used rather than laser power and will be used hereafter in this work.

The laser beam passes through two optical windows in the shock tube before coming in contact with the photodiode. The diameter of the shock tube is taken to be, l, the distance from the centre of the shock tube to the surface of the photodiode is, D, the angle of deflection is, θ, and the pathlength of the movement of the laser beam on the photodiode is, Δ. It is well known that a laser beam in a medium of varying refractive index, will deflect towards a region of higher refractive index, n. If the refractive index, is $n \approx 1$, the deflections of the laser beam are kept small and the laser beam is incident perpendicular to the shock flow, then the deflection angle can be approximated by,

$$\theta = l\frac{\mathrm{d}n}{\mathrm{d}y} \qquad [4.14]$$

where y is the axial coordinate, in the same plane as Δ (see Figure 4.32(b)).

The refractivity, β, and density of the gas, ρ, are related to refractive index, n, by $n = 1 + \beta\rho$. Therefore the deflection angle can be determined by,

$$\theta = \beta l\frac{\mathrm{d}\rho}{\mathrm{d}y} \qquad [4.15]$$

Since θ is expected to be very small (sub-milliradians) $\tan\theta \approx \theta$ and therefore the deflection of the laser beam at the photodiode is,

$$\begin{aligned}\Delta &\approx D\theta \\ &= D\beta l\frac{\mathrm{d}\rho}{\mathrm{d}y}\end{aligned} \qquad [4.16]$$

For the purposes of this work it is enough to realize that when the laser beam is deflected from the centre of the photodiode the deflection will be small, i.e. $\Delta \ll a$ and in only the y direction (see Figure 4.32(b)). Therefore the intensity of the laser beam can be approximated by

$$I(y) = V_0\sqrt{\frac{2}{\pi a^2}} \quad e^{(-2y^2/a^2)}. \qquad [4.17]$$

Upon deflection, the centre of the gaussian distribution of the intensity is shifted from the centre of the photodiode to Δ (Figure 4.32(a)). The integration of an unshifted gaussian distribution of a laser beam, on the centre of a photodiode would result in zero volts output (Figure 4.32(c) unshaded section). However when the laser beam is shifted there is in intensity imbalance (Figure 4.32(c) shaded part). The integration can be broken into two portions one for each half of the photodiode,

$$V = -\int_{-\infty}^{-\Delta} V_0\sqrt{\frac{2}{\pi a^2}} \quad e^{(-2y^2/a^2)}dy + \int_{-\Delta}^{+\infty} V_0\sqrt{\frac{2}{\pi a^2}} \quad e^{(-2y^2/a^2)}dy. \qquad [4.18]$$

Due to the symmetry of the gaussian waveform the negative part of the signal $\int_{-\infty}^{-\Delta}$ is equal to the positive part of the signal $\int_{+\Delta}^{+\infty}$.This leaves $\int_{-\Delta}^{+\Delta}$ which, again due to symmetry, is just $2\int_0^{+\Delta}$(Figure 4.32(c)). Therefore the voltage generated by the photodiode can be represented by,

$$V = 2V_0\sqrt{\frac{2}{\pi a^2}}\int_0^{\Delta} \quad e^{(-2y^2/a^2)}dy. \qquad [4.19]$$

Now if the exponential is expanded using a Taylor series the voltage now becomes

$$V = V_0\sqrt{\frac{8}{\pi a^2}}\int_0^{\Delta} \quad \left[1 - \frac{2y^2}{a^2} + \frac{1}{2}\left(\frac{2y^2}{a^2}\right)^2 \cdots\right]dy. \qquad [4.20]$$

Remembering that $\Delta \ll a$ it can be seen that the higher powers of the expansion will not contribute much,

$$\begin{aligned} V \quad &\approx V_0\sqrt{\frac{8}{\pi a^2}} \quad \left[y - \frac{2y^3}{3a^2}\right]_0^{\Delta} \\ &\approx \Delta V_0\sqrt{\frac{8}{\pi a^2}} \quad \left[1 - \frac{2}{3}\left(\frac{\Delta}{a}\right)^2\right]. \end{aligned} \qquad [4.21]$$

Since $\Delta \ll$ a the last term is close to zero, and therefore the voltage can be represented by

$$V = V_0\sqrt{\frac{8}{\pi a^2}} \quad \Delta. \qquad [4.22]$$

The displacement of the laser beam, Δ, has been defined above and so the relationship of voltage to density is,

$$V = V_0\sqrt{\frac{8}{\pi a^2}}\, D\beta l\frac{d\rho}{dy}. \qquad [4.23]$$

Finally,

$$V \propto \frac{d\rho}{dy} = \frac{d\rho}{u_0 dt} \propto -\frac{1}{T^2}\frac{dT}{dt} \qquad [4.24]$$

where it is assumed that the gas pressure is approximately constant. Also of note is the fact that $dt_g/dt_l = \rho_e/\rho_0$ so the gas time, t_g, used in the simulations can be related to lab time, t_l, via the ratio of post-shock density to pre-shock density.

Lastly, $D \approx 1$ meter, $l = 11.0$ cm, and the refractivity of the gas is dependent upon the test gas used,

$$\beta = \frac{\sum_i \beta_i x_i \mu_i}{\sum_i x_i \mu_i} \qquad [4.25]$$

where x_i and μ_i are the mole fraction and molecular weight of the respective species, i, in the mixture. In this work Ar and CCl_3F are used with β's of 0.1589 and 0.229 cm^3/g, respectively.

4.4.3 Data Collection

The old data collection system was of a very low resolution, in that the four laser schlieren velocity signals together only had 4096 data points. This has been updated and the new system now captures three velocity signals and stores them on a Compuscope card which is manufacture by Gage Applied Science, Montreal,

Canada. The Compuscope is a digital oscilloscope on a card that is inserted in an available slot of an IBM PC, or IBM PC clone. The card used in this work, CS220, collects 256k of data points (262 144) at a sampling rate up to 40 Million Samples Per Second (40MSPS). The new data collection system collects at least 16 data points for each data point collected in the previous system. In an ideal case, 32 data points would be collected in the new system for each data point of the previous system. Thus, there is an increase in the sampling of the waveform.

With the redesigned velocity data collection system, the data can now be used not only for calculating the velocity but also used for comparison of each detector station signal with the main signal (if available) and each other. The velocity signals are essentially at similar but slightly different velocities and thus at different initial conditions but hopefully within 2-4% of each other. This is important since the parameter regime that the experiments are being done at result in signals that oscillate and are even chaotic at times. Since it is well known that systems in a chaotic parameter regime are sensitive to initial conditions, comparing results of a system with very similar initial conditions is a productive and desirable pursuit.

In this work, the output of the mixing board was ac coupled to the CompuScope card and the card was set do a MID capture of the data. In other words, the trigger was set to fire and capture, and display the data so that the centre of the data would be the central data point. The trigger voltage was received from the mixing board and it was usually selected off of the second photodiode signal. The amplification on the card was set to $2\times$ and therefore the voltage was doubled before being sent to the AD (analog-to-digital) converter. This is the reason that the maximum peak is not on full scale (see Figure 4.33).

Photodiode detection stations 1 and 2 were 304.3 ± 0.5 mm apart while stations 2 and 3 were 292.3 ± 0.5 mm apart. The velocities were calculated using time between

shock front peaks obtained from a plot of the signal at a 50μsecond per division expansion. These plots were screen dumps done using the CompuScope software and a 9 pin dot matrix printer.

The photodiode detectors were on an optical table (2000 lbs cement block on rubber) that damped out all frequencies greater than 12 Hz. There were still some technical problems that were overcome by having the photodiodes at a negative value. Thus as each one of the photodiodes (PD) was disabled, in turn, the baseline would increase in value (see Figure 4.33). Note that the photodiode preamplifier outputs are DC coupled to the mixing board amplifier input.

4.5 Data

A program, developed by in H. Teitelbaum's laboratory by Su[82], was used to calculate shock parameters (post shock temperature, pressure and density), and for this work it was modified to use curves fitted to the enthalpy data presented in JANAF tables for ideal gases[78]. The ideal gas law was used since most of the pure compounds were at relatively low partial pressures and the mixtures were mostly Argon. The enthalpy of the mixture at a certain temperature was calculated by summing the mole fraction of each component times the enthalpy of the component at the specified temperature. Also, in the same manner the molecular weight of the gas mixtures was calculated.

The shock parameter program uses the enthalpy, h, of the gas or mixture of gases to calculate the velocity, u_0 at a given post shock temperature, T_e and from an initial temperature, T_0. The velocity is also used to calculate the post shock pressure, p, before complete equilibration and after complete equilibration has occurred, that is after the system has reached its equilibrium Boltzmann distribution (for a given temperature). A set of data is created for a range of post shock temperatures and shock velocities. Once the shock velocity, u_0, is matched with the measured velocity then the other parameters are read from the table of calculated data. The parameters used have a subscript, $_e$ for post shock conditions after equilibration, $_0$ for initial conditions, $_a$ for vibrationally and rotationally frozen, and $_b$ for vibrationally frozen. The hydrodynamic equations are listed below.

$$\rho_0 u_0 = \rho_e u_e = \rho_a u_a = \rho_b u_b \qquad [4.26]$$

$$p_0 + \rho_0 u_0^2 = p_e + \rho_e u_e^2 = p_a + \rho_a u_a^2 = p_b + \rho_b u_b^2 \qquad [4.27]$$

$$h_0 + \frac{1}{2}u_0^2 = h_e + \frac{1}{2}u_e^2 = h_a + \frac{1}{2}u_a^2 = h_b + \frac{1}{2}u_b^2 \qquad [4.28]$$

$$\frac{p_0\mu_0}{\rho_0 T_0} = \frac{p_e\mu_0}{\rho_e T_e} = \frac{p_a\mu_0}{\rho_a T_a} = \frac{p_b\mu_0}{\rho_b T_b} = R \qquad [4.29]$$

where ρ is the density, u is the flow velocity in shock-stationary coordinates, p is the pressure, h is the enthalpy of the mixture, and T is the temperature of the system.

Equation [4.26] states that mass flux is conserved; equation [4.27] states that momentum flux is conserved; and equation [4.28] states that energy flux is conserved. Note that equation [4.28] is a reordering of the ideal gas law, $PV = nRT$, to $R = (P/T)(V/n)$ where $V/n = \mu/\rho$. That is, the volume divided by the number of moles is the same as the molecular weight divided by the density of the gas mixture.

The calculation of shock velocity, u_0, is performed by first choosing T_e, given T_0 and solving for ρ_0/ρ_e from

$$\rho_0/\rho_e = \frac{1}{2T_0}\left\{-(2y - T_e + T_0) + \sqrt{(2y - T_e + T_0)^2 + 4T_eT_o}\right\} \qquad [4.30]$$

with

$$y = \frac{\mu_0}{R}(h_e - h_0). \qquad [4.31]$$

Then

$$u_0 = \sqrt{\frac{2(h_e - h_0)}{(1 - \rho_0^2/\rho_e^2)}}. \qquad [4.32]$$

Using the first set of equalities in equation [4.27],

$$\frac{p_e}{p_0} = 1 + \frac{\rho_0}{p_0}u_0^2 - \frac{\rho_e}{p_0}u_e^2. \qquad [4.33]$$

Substituting equation [4.26] ($\rho_0 u_0 = \rho_e u_e$), which restated means $\frac{\rho_0}{\rho_e}u_0 = u_e$, into equation [4.33], results in

$$\frac{p_e}{p_0} = 1 + \frac{\rho_0 u_0^2 - (\rho_0 u_0)(\frac{\rho_0}{\rho_e})u_0}{p_0} \qquad [4.34]$$

which can be restated as

$$\frac{p_e}{p_0} = 1 + (1 - \rho_0/\rho_e)u_0^2(\frac{\rho_0}{p_0}). \qquad [4.35]$$

Lastly, keeping in mind equation [4.29] which relates density, pressure, molecular weight and temperature to the gas constant, equation [4.35] takes on the form,

$$\frac{p_e}{p_0} = 1 + (1 - \rho_0/\rho_e)u_0^2(\frac{\mu_0}{RT_0}). \qquad [4.36]$$

Therefore once the velocity is calculated for a certain temperature, T_e, and knowing the p_0, it is relatively easy to calculate p_e.

Shock compression experiments were done on pure CCl_3F (six), SF_6 (three), CCl_3H (two), and Ar (one). There were three mixtures prepared, 5.05%, 5.08%, and 25.05% CCl_3F in Ar.

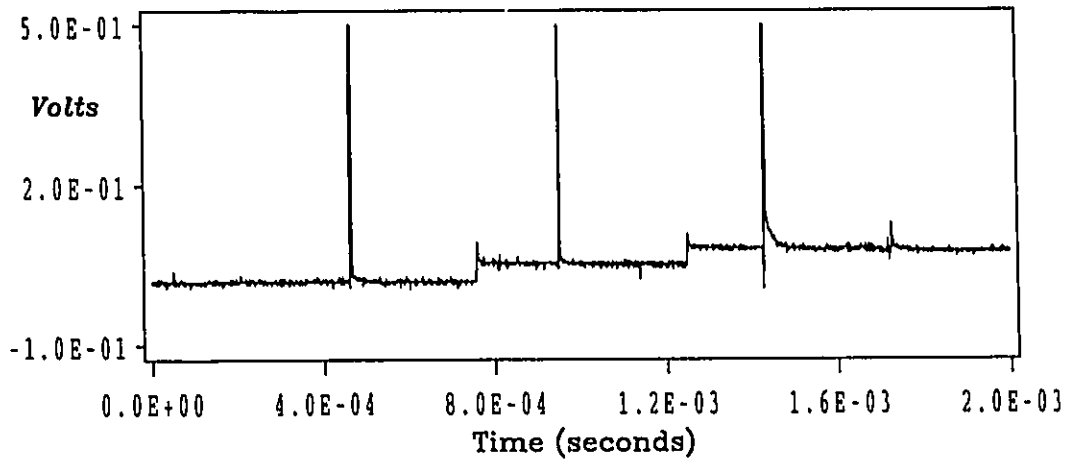

Figure 4.33 Plot of schlieren millivolt signal (from all three velocity stations) *versus* time (seconds) for shock compression of pure Ar with $p_0 = 63.0$ Torr, $T_0 = 295.15$ K, $p_e = 279.7$ Torr, and $T_e = 589.58$ K (average values).

In general the plots of the data presented here are for all three schlieren millivolt signals for the three photodiode detection stations. In all but a few cases, which will be pointed out when they occur, the first photodiode preamplifier is shut-off before the shock front reaches the next photodiode station. The same circumstances exist for photodiodes two and three. This "turning off" of the preamplifier can be observed as a shifting of the baseline which is illustrated in Figure 4.33 for a shock compression of

Table 4.6 Shock velocities, u_0, for gases studied in this work as obtained from three photodiode stations, PD1, 2, and 3. All pressures are in Torr and temperatures are in Kelvin (K).

sample	mixture ratio	sample pressure	p_0	u_0(m/s) PD#1-2	PD#2-3	Ave.	$\Delta u_0\%$
Argon	pure		63.0	624.21	615.37	619.8	−1.44
SF_6	pure		24.0	341.91	333.10	337.5	−2.64
SF_6	pure		100.0	211.32	207.30	209.3	−1.94
SF_6	pure		360.0		163.75	163.8	
CCl_3H	pure		5.0	599.61	590.50	595.0	−1.55
CCl_3H	pure		6.0	857.18	811.94	834.6	−5.57
CCl_3F	pure		5.0	574.15	573.14	573.6	−0.17
CCl_3F	pure		9.5	473.98	472.98	473.5	−0.21
CCl_3F	pure		22.0	342.68	337.92	340.3	−1.41
CCl_3F	pure		29.0	331.66	324.78	328.2	−2.12
CCl_3F	pure		61.0	238.67	235.73	237.2	−1.25
CCl_3F	pure		196.0	192.59	190.17	191.4	−1.27
CCl_3F	5.05%	188.0	9.49	380.38	377.16	378.8	−0.85
CCl_3F	5.05%	250.5	12.65	361.19	358.65	359.9	−0.71
CCl_3F	5.05%	435.0	21.97	332.57	330.28	331.4	−0.69
CCl_3F	5.08%	188.0	9.55	382.77	377.16	380.0	−1.49
CCl_3F	5.08%	188.5	9.58	447.50	444.56	446.0	−0.66
CCl_3F	5.08%	100.0	5.08	496.82	491.26	494.0	−1.13
CCl_3F	25.05%	188.0	47.09	296.59	293.47	295.0	−1.06
CCl_3F	25.05%	253.0	63.38	285.73	283.78	284.8	−0.69
CCl_3F	25.05%	435.0	108.97	258.98	255.28	257.1	−1.45

63.0 Torr of Ar with $T_0 = 295.15$ K, and average post shock conditions of $p_e = 279.7$ Torr, and $T_e = 589.58$ K. These conditions are the second most severe in this study. (All conditions used in this study are presented in Tables 4.6, and 4.7.)

In Figure 4.33, at about 1.45 milliseconds, there is a negative going peak then a larger positive peak. This is the case for all of the waveforms in Figure 4.33 and all other figures in this section. Since only a small portion of the data points can be printed, due to technical limitations of the usual 300 dpi (dot per inch) laser printer, the negative peak is quite often not seen on the plot, but it does exist in the data set captured. The negative peak is due to the shock front encountering the laser beam

Table 4.7 Post shock pressure, p_e and temperature, T_e. All pressures are in Torr and temperatures are in Kelvin (K).

sample	mixture ratio	sample pressure	p_0	p_e(Torr)			T_e (K)		
				PD1-2	PD2-3	Ave.	PD1-2	PD2-3	Ave.
Argon	pure		63.0	284.0	275.5	279.7	594.74	584.45	589.58
SF_6	pure		24.0	159.0	150.8	154.9	374.65	370.64	372.64
SF_6	pure		100.0	249.6	240.0	244.8	322.05	320.63	321.34
SF_6	pure		360.0		532.4	532.4		305.53	305.53
CCl_3H	pure		5.0	81.9	79.4	80.6	584.39	576.27	580.32
CCl_3H	pure		6.0	201.9	181.1	191.4	858.63	803.42	830.59
CCl_3F	pure		5.0	87.6	87.2	87.4	544.44	543.62	544.02
CCl_3F	pure		9.5	113.0	112.5	112.8	469.30	468.61	468.96
CCl_3F	pure		22.0	135.9	132.1	134.0	387.56	384.96	386.26
CCl_3F	pure		29.0	167.6	160.7	164.1	381.58	377.92	379.74
CCl_3F	pure		61.0	180.7	176.1	178.4	336.46	335.16	335.81
CCl_3F	pure		196.0	373.8	364.3	368.9	317.00	316.02	316.50
CCl_3F	5.05%	188.0	9.49	17.8	17.5	17.7	370.34	367.66	369.00
CCl_3F	5.05%	250.5	12.65	21.1	20.8	21.0	354.46	352.38	353.42
CCl_3F	5.05%	435.0	21.97	30.4	29.9	30.1	330.88	328.98	329.92
CCl_3F	5.08%	188.0	9.55	18.2	17.6	17.9	372.42	367.76	370.08
CCl_3F	5.08%	188.5	9.58	25.8	25.4	25.6	427.76	425.16	426.46
CCl_3F	5.08%	100.0	5.08	17.1	16.7	16.9	472.70	467.49	470.08
CCl_3F	25.05%	188.0	47.09	88.2	86.2	87.2	343.58	341.56	342.57
CCl_3F	25.05%	253.0	63.38	109.5	107.9	108.7	336.58	335.34	335.96
CCl_3F	25.05%	435.0	108.97	151.9	147.1	149.5	319.28	316.86	318.06

so swiftly that the beam is deflected completely off of the photodiode surface. The following large positive peak is due to physical processes of the shock front and is not discussed further in this work. In other words, these peaks are due to the shock front and will be referred to hereafter in that manner.

The schlieren millivolt signals of shock compressed pure CCl_3F, at various initial pressures (p_0 from 5.0 to 196.0 Torr), are presented in Figures 4.34-38.

In Figure 4.34(a) the conditions for shock compression of pure CCl_3F are, $p_0 =$ 5.0 Torr, $T_0 = 295.15$ K, $p_e = 87.4$ Torr and $T_e = 544.02$ K. It is quite noticeable when the preamplifier is turned off for the first photodiode detection station at $\approx 8.5 \times 10^{-4}$

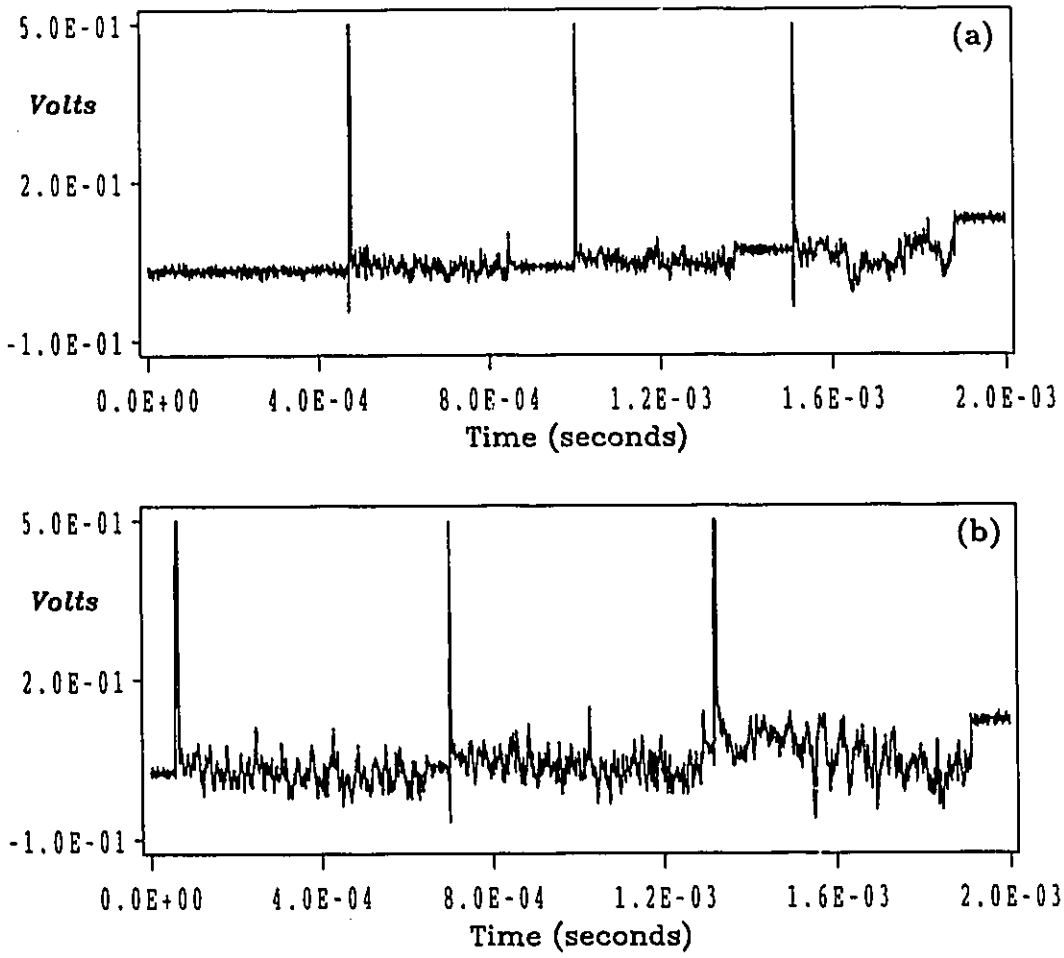

Figure 4.34 Plot of schlieren millivolt signal *versus* time (seconds) for shock compression of pure CCl_3F. For (a) $p_0 = 5.0$ Torr, $T_0 = 295.15$ K, $p_e = 87.4$ Torr, and $T_e = 544.02$ K (average values) and for (b) $p_0 = 9.5$ Torr, $T_0 = 295.15$ K, $p_e = 112.8$ Torr, and $T_e = 468.96$ K (average values).

seconds. In this case there is also a spike present which is an artifact of the preamplifier since it takes a short amount of time to actually reduce the preamplifier output to zero. The advantage of being able to turn off the preamplifier is evident from comparison of the waveform at time 4.0×10^{-4} seconds in Figure 4.34(a) and the time of 9.0×10^{-4} seconds for the same figure. Comparison of these baselines allows the observer to see that there is definitely some chemical activity taking place at the first photodiode station from the time 5.0×10^{-4} to 8.0×10^{-4} seconds. This turning off of the preamplifiers in turn also allows for isolation of each photodiode signal into separate

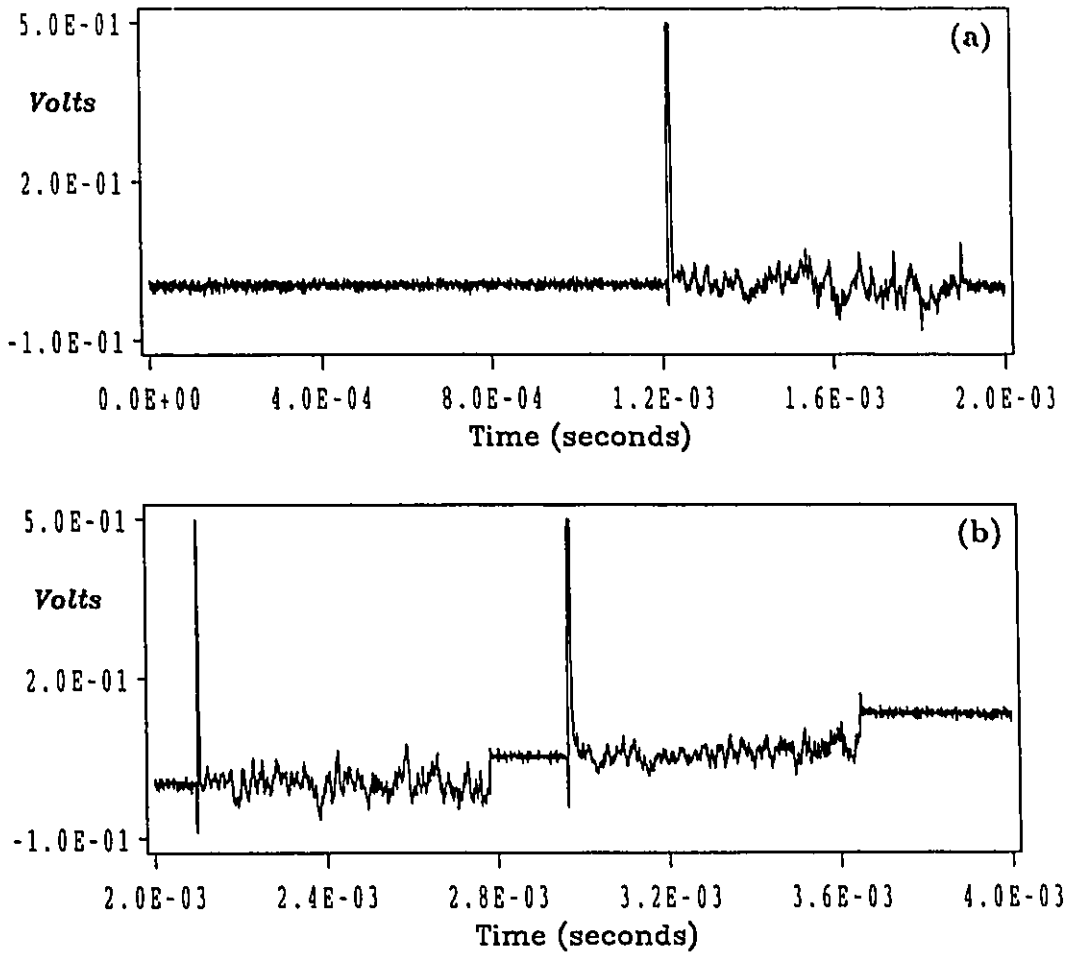

Figure 4.35 Plot of schlieren millivolt signal *versus* time (seconds) for shock compression of pure CCl_3F with $p_0 = 22.0$ Torr, $T_0 = 295.15$ K, $p_e = 134.0$ Torr, and $T_e = 386.26$ K (average values). (a) is for 0.0 to 2.0 milliseconds and (b) is for 2.0 to 4.0 milliseconds.

signals that do not interfere with each other. This is illustrated later with signals that have the timing circuit bypassed. Table 4.6 also lists the relative decrease of velocity from photodiode stations 1-2 and 2-3 and in almost all cases the decrease of velocity is less than 1% over a distance of $\approx$ 60 cm.

Note that in Figure 4.34(a) the three millivolt signals are not identical even though the conditions are similar but the third photodiode signal seems to represent the most severe deviation of the three. This is not always the case as will be pointed out in later discussions.

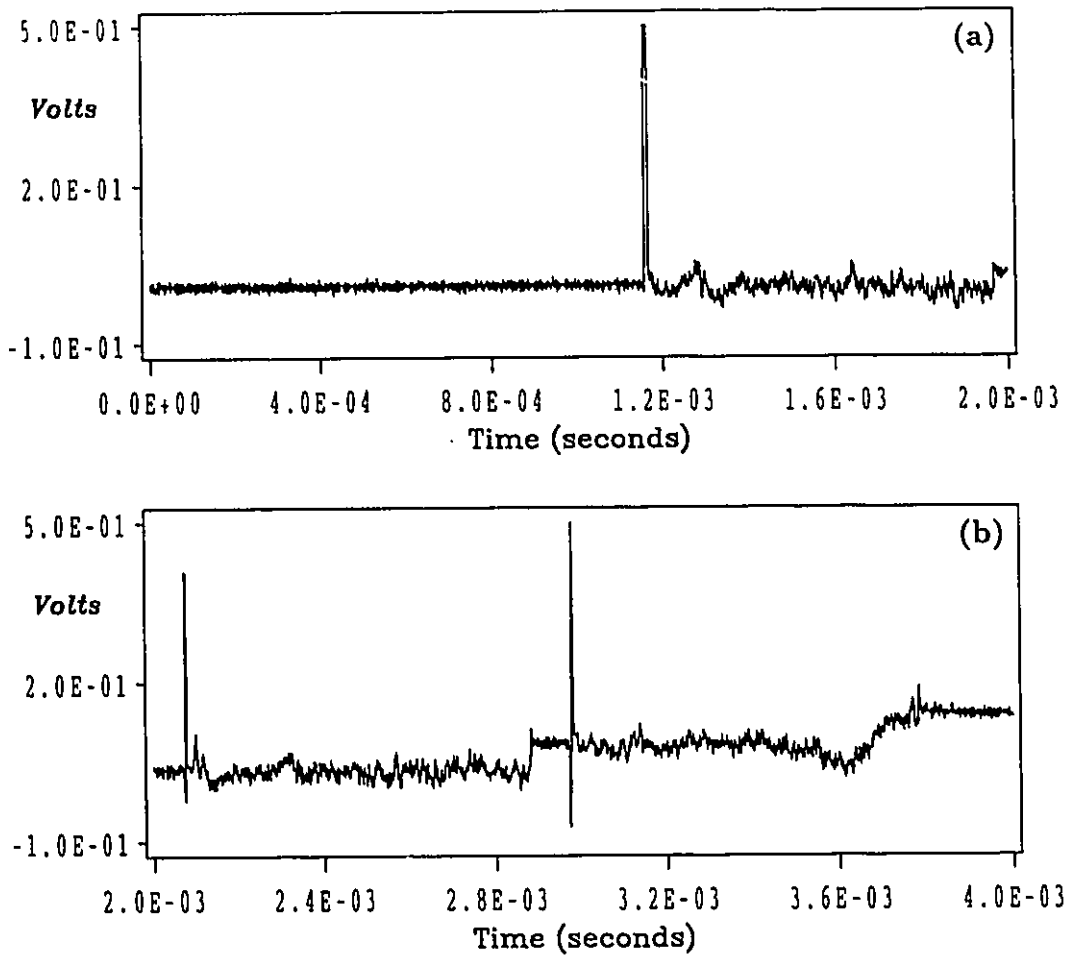

Figure 4.36 Plot of schlieren millivolt signal *versus* time (seconds) for shock compression of pure CCl_3F with p_0 = 29.0 Torr, T_0 = 295.15 K, p_e = 164.1 Torr, and T_e = 379.74 K (average values). (a) is for 0.0 to 2.0 milliseconds and (b) is for 2.0 to 4.0 milliseconds.

In Figure 4.34(b) the shock conditions are p_0 = 9.5 Torr, T_0 = 295.15 K, p_e = 112.8 Torr, and T_e = 468.96 K which is a decrease in the post shock temperature of 75.06 degrees, as expected for a lower velocity. Note that the time between positive peaks in 4.34(a) and 4.34(b) are different in that the Δt is larger in 4.34(b) than 4.34(a). This is expected since the velocity is lower and therefore it must take more time for the shock front to travel between the photodiode detection stations. Although the shock conditions are less severe (lower T_e) the nonperiodic oscillations present in the baseline of Figure 4.34(b) are larger in amplitude than in Figure 4.34(a). These

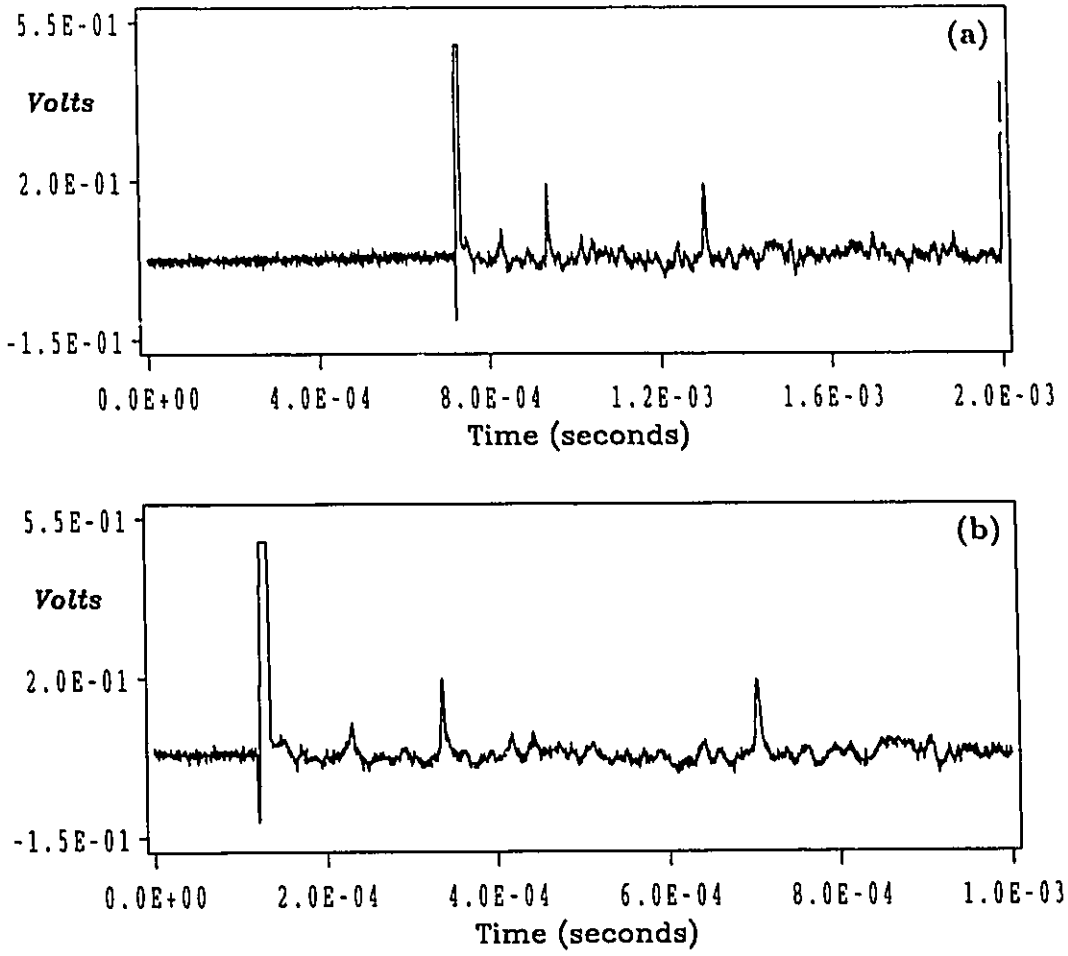

Figure 4.37 Plot of schlieren millivolt signal *versus* time (seconds) for shock compression of pure CCl_3F with p_0 = 61.0 Torr, T_0 = 295.15 K, p_e = 178.4 Torr, and T_e = 335.81 K (average values). (a) is for 0.0 to 2.0 milliseconds and shows the total time between the first two photodiode detection stations. (b) is an x-axis expansion for 1.0 millisecond of the first photodiode schlieren millivolt signal.

are discussed later in this section.

In Figure 4.35 the conditions for the shock compression of pure CCl_3F are p_0 = 22.0 Torr, T_0 = 295.15 K, p_e = 134.0 Torr, and T_e = 386.26 K. Thus the post shock conditions are even less harsh than for the case of p_0 = 9.5 of Figure 4.34(b) but the oscillations of the waveform have even larger amplitudes. In fact there are also some spikes appearing at around one millisecond of the signal from photodiode #1 (see Figure 4.35(a)). In Figure 4.35(b) the schlieren millivolt signal of photodiode

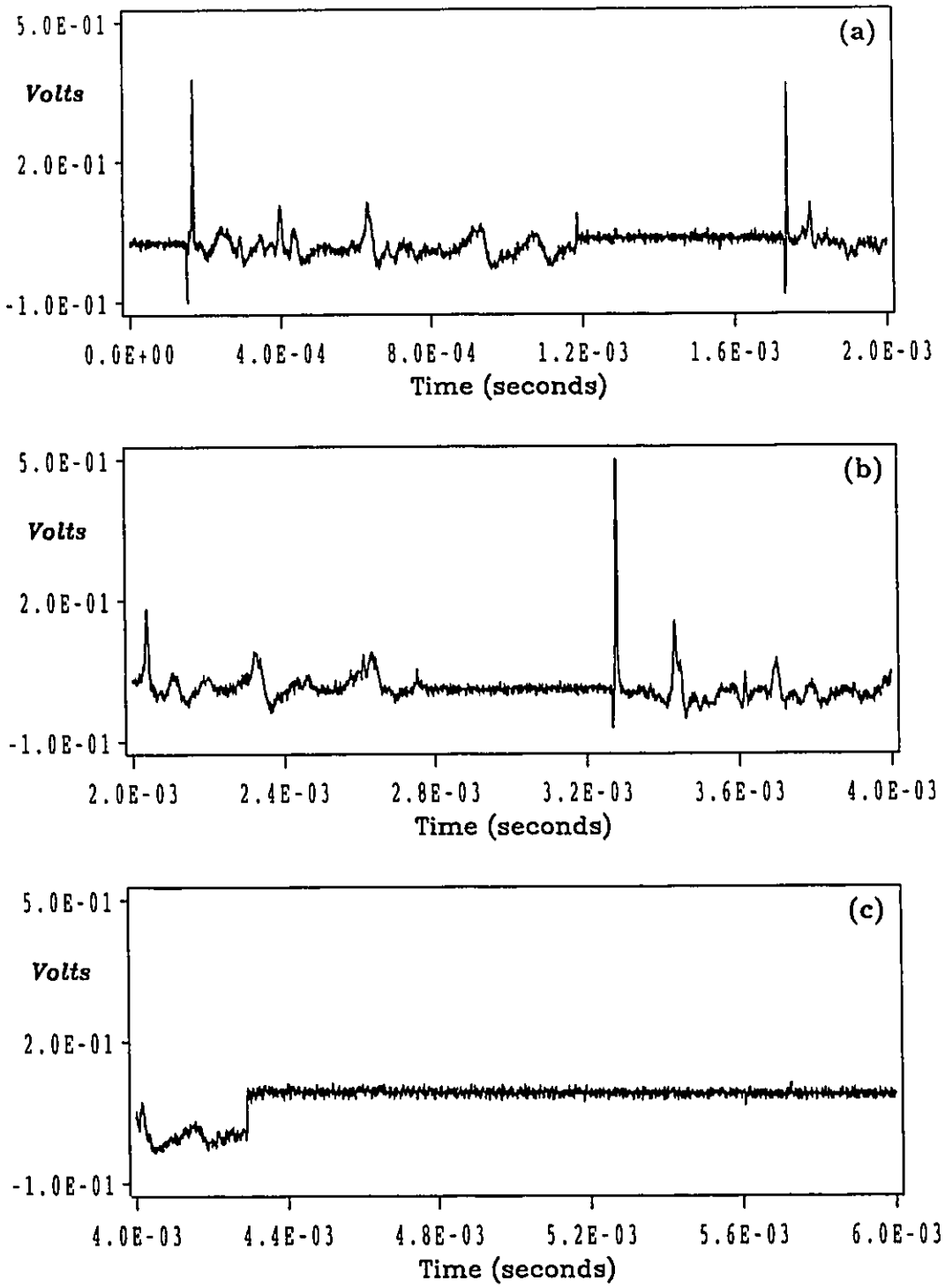

Figure 4.38 Plot of schlieren millivolt signal *versus* time (seconds) for shock compression of pure CCl_3F with $p_0 = 196.$ Torr, $T_0 = 295.15$ K, $p_e = 368.9$ Torr, and $T_e = 316.50$ K (average values). (a) is for 0.0 to 2.0 milliseconds, (b) is for 2.0 to 4.0 milliseconds, and (c) is for 4.0 to 6.0 milliseconds .

detectors 2 and 3 are presented. Note that the first and second signals are similar but the third signal has much smaller amplitude changes.

In Figure 4.36 the schlieren millivolt signal of shock compressed pure CCl_3F is presented for the conditions $p_0 = 29.0$ Torr, $T_0 = 295.15$ K, $p_e = 164.1$ Torr, and $T_e = 379.74$ K. Note that there are spikes present in Figures 4.36(b) at ≈ 2.15 milliseconds. However, the amplitudes of the waveforms and the periodicity of the waveforms are much reduced in intensity even though the post shock conditions are only slightly changed ($\Delta T_e = 6.52$ degrees) from the previous case. This is an indication that the behaviour is extremely sensitive to initial conditions.

In Figure 4.37 the conditions for shock compression of pure CCl_3F are $p_0 = 61.0$ Torr, $T_0 = 295.15$ K, $p_e = 178.4$ Torr, and $T_e = 335.81$ K. In 4.37(a) the schlieren millivolt signal for the time between photodiode detection stations 1 and 2 is shown. In Figure 4.37(b) the millivolt signal for photodiode detector 1 is expanded to illustrate the spikes that are present. Note that although T_e is now as low as 335.81 K, there are definite oscillations present.

In Figure 4.38 the schlieren millivolt signal of shock compressed pure CCl_3F is presented for $p_0 = 196.0$ Torr, $T_0 = 295.15$ K, $p_e = 368.9$ Torr, and $T_e = 316.50$ K. There are definite spikes present in 4.38(a), (b) and (c). Each of the signals are distinctly different, and, since the post shock velocities for all three signals are within 1% of each other, this means that the system is extremely sensitive to the post shock conditions. (Note that all three signals have the negative peak of the shock front displayed in this case.)

In general the trend was for the amplitude of the waveform to increase with increasing initial pressure but at the same time the post shock temperature was decreasing. Therefore the result is not attributable to changing only one parameter.

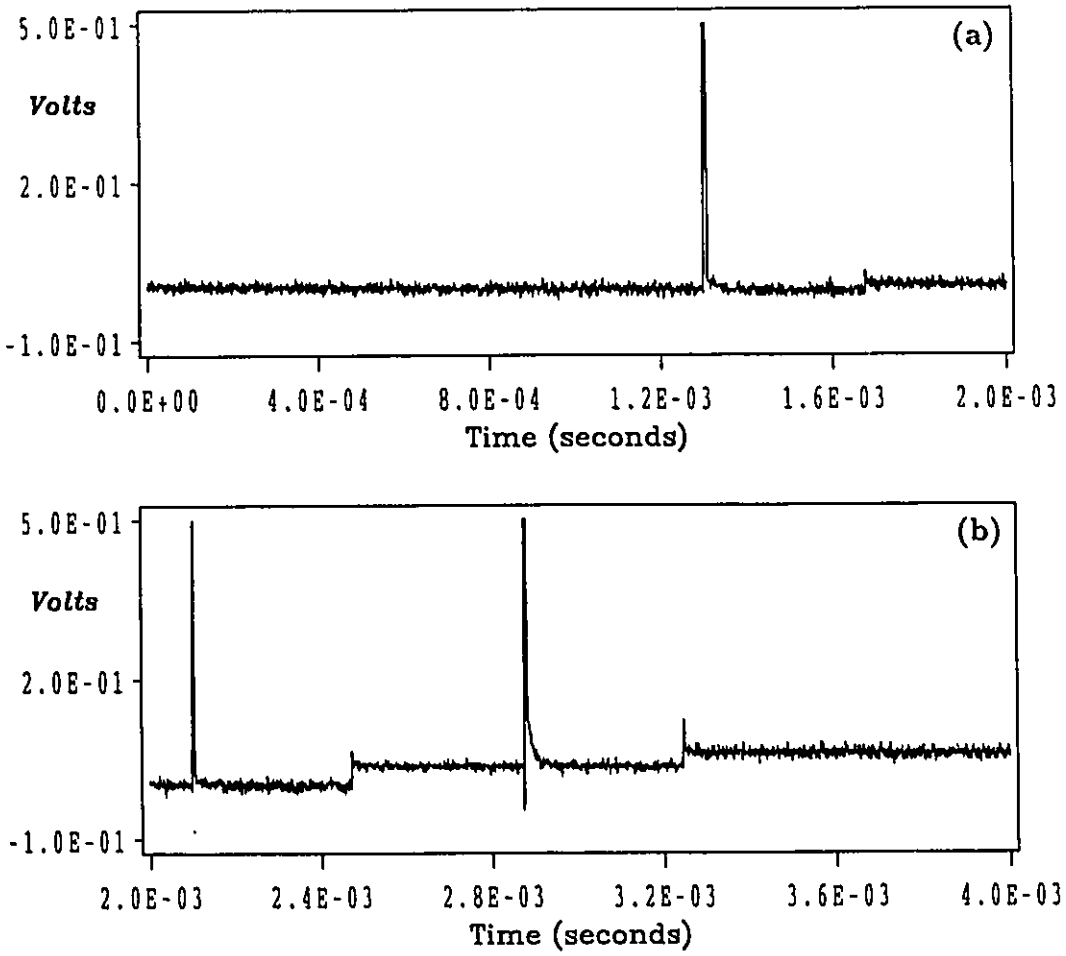

Figure 4.39 Plot of schlieren millivolt signal *versus* time (seconds) for shock compression of 188.0 Torr of a 5.05% mixture of CCl_3F in Ar with $p_0 = 9.5$ Torr, $T_0 = 295.15$ K, $p_e = 17.7$ Torr, and $T_e = 369.00$ K (average values). (a) is for 0.0 to 2.0 milliseconds and (b) is for 2.0 to 4.0 milliseconds.

Figures 4.39 to 4.48 are plots of the schlieren millivolt signal for shock compression of mixtures of CCl_3F in Ar (5.05%, 5.08% and 25.05%).

In Figure 4.39 the conditions for shock compression of 188.0 Torr of a 5.05% mixture of CCl_3F in Ar are $p_0 = 9.5$ Torr, $T_0 = 295.15$ K, $p_e = 17.7$ Torr, and $T_e = 369.00$ K. It is obvious from comparison of 4.39(a) and (b) that no chemistry has taken place, as revealed by any of the photodiode signals. There is the expected jump in baseline for the preamplifier shut-off but otherwise the baseline has the same amount of noise across the 4.0 milliseconds of time displayed for both 4.39(a) and

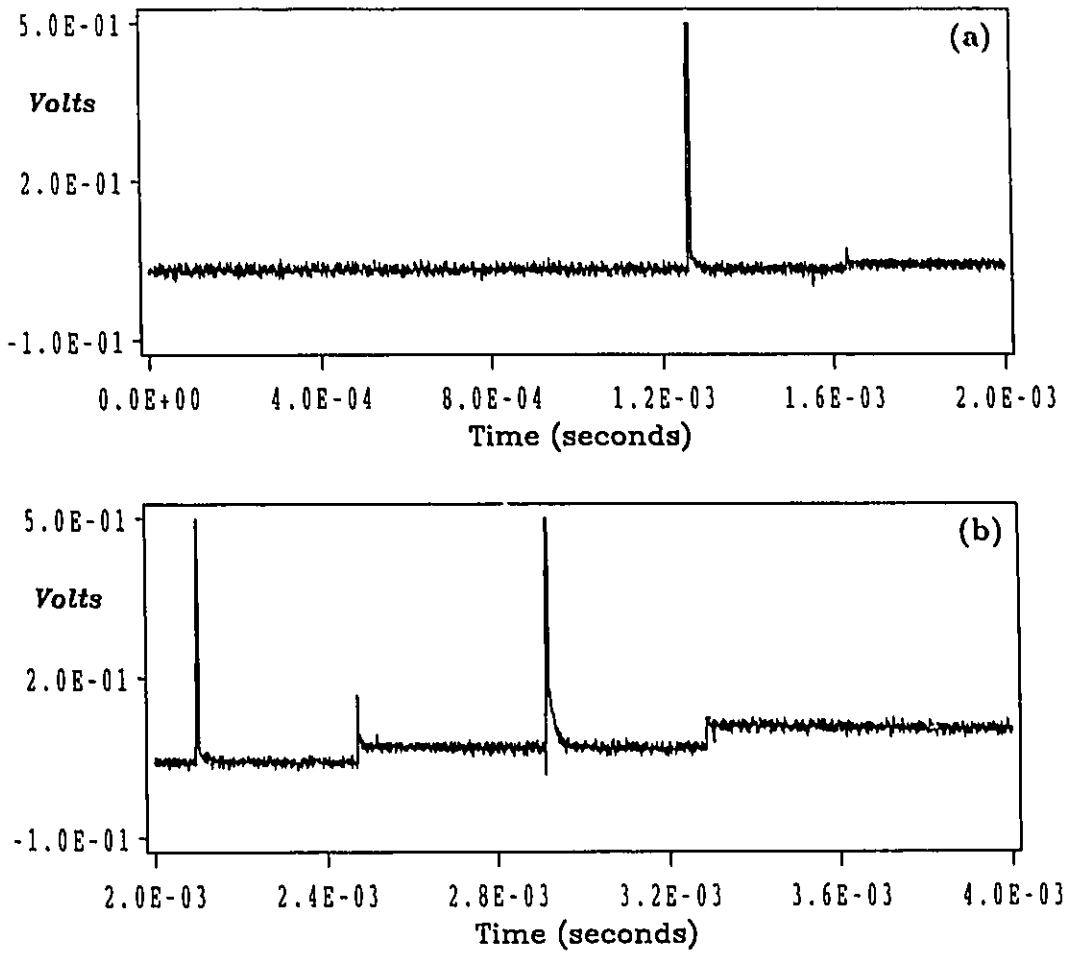

Figure 4.40 Plot of schlieren millivolt signal *versus* time (seconds) for shock compression of 250.5 Torr of a 5.05% mixture of CCl_3F in Ar with $p_0 = 12.6$ Torr, $T_0 = 295.15$ K, $p_e = 21.0$ Torr, and $T_e = 353.42$ K (average values). (a) is for 0.0 to 2.0 milliseconds and (b) is for 2.0 to 4.0 milliseconds.

(b). Also note the spikes present upon shutting down the preamplifier circuit (at 1.7, 2.5, and 3.25 milliseconds).

In Figure 4.40 the conditions for shock compression of 250.5 Torr of a 5.05% mixture of CCl_3 in Ar are $p_0 = 12.6$ Torr, $T_0 = 295.15$ K, $p_e = 21.0$ Torr, and $T_e = 353.42$ K. The only noticeable features are those due to the shock front (large positive peaks) and some spikes which are artifacts of the shutoff of the preamplifier circuit.

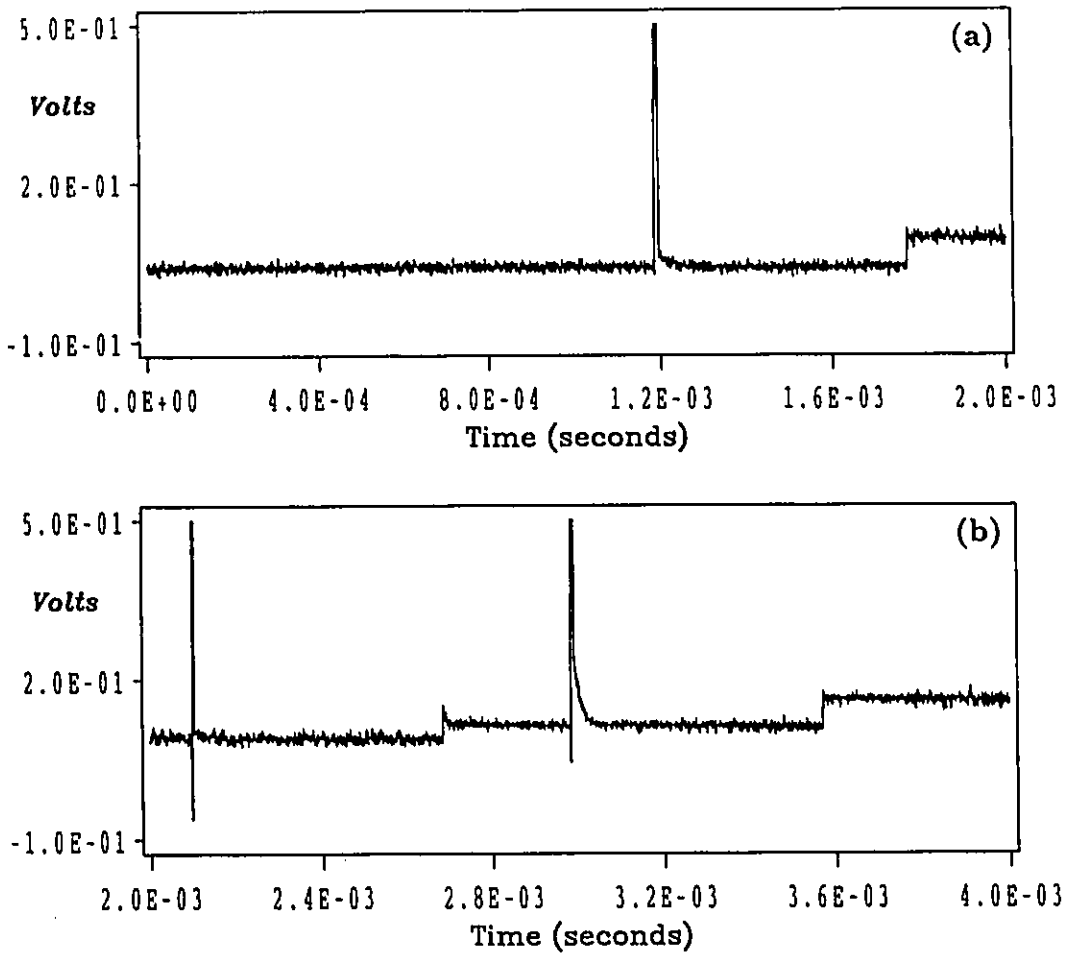

Figure 4.41 Plot of schlieren millivolt signal *versus* time (seconds) for shock compression of 435.0 Torr of a 5.05% mixture of CCl_3F in Ar with $p_0 = 22.0$ Torr, $T_0 = 295.15$ K, $p_e = 30.1$ Torr, and $T_e = 329.92$ K (average values). (a) is for 0.0 to 2.0 milliseconds and (b) is for 2.0 to 4.0 milliseconds.

In Figure 4.41 the conditions for shock compression of 435.0 Torr of a 5.05% mixture of CCl_3 in Ar are $p_0 = 22.0$ Torr, $T_0 = 295.15$ K, $p_e = 30.1$ Torr, and $T_e = 329.92$ K. The schlieren millivolt signals in these plots are very similar to the two previous plots. The waveform has very similar features before and after the shock front has passed.

What is evident from Figures 4.39, 4.40, and 4.41 is that no chemical activity, or at least no heat release, has occurred as was seen in the pure CCl_3F shock compression experiments shown in plots 4.34-4.38. However comparison of Figures 4.39-4.41 with

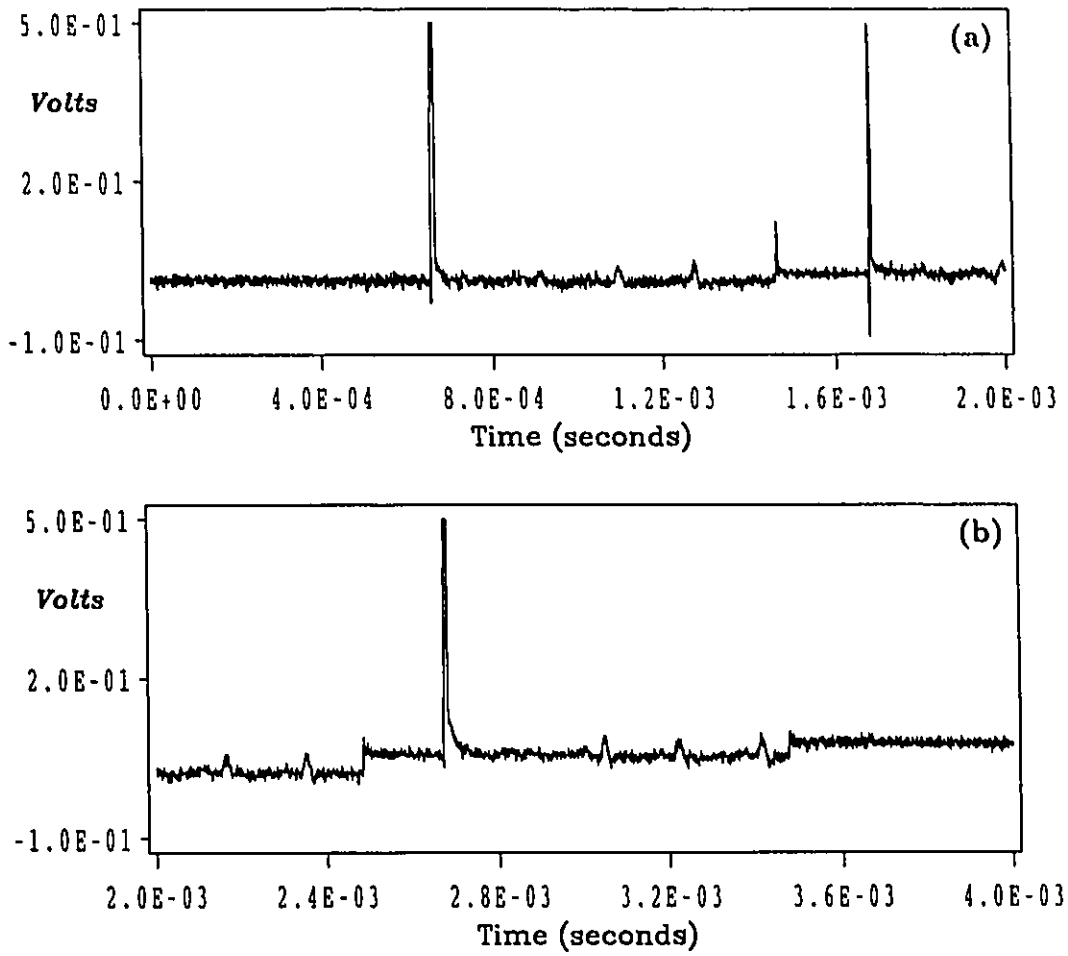

Figure 4.42 Plot of schlieren millivolt signal *versus* time (seconds) for shock compression of 188.0 Torr of a 25.05% mixture of CCl_3F in Ar with $p_0 = 47.1$ Torr, $T_0 = 295.15$ K, $p_e = 87.2$ Torr, and $T_e = 342.57$ K (average values). (a) is for 0.0 to 2.0 milliseconds and (b) is for 2.0 to 4.0 milliseconds.

4.33 allows the observer to see the similarity of the photodiode signals. For example, comparing the third photodiode signal of Figure 4.33 (at $\approx$ 1.52 milliseconds) with Figure 4.39(b) (at $\approx$ 2.9 milliseconds), Figure 4.40(b) (at $\approx$ 2.9 milliseconds), and Figure 4.41(b) (at $\approx$ 3.0 milliseconds) it is possible to see that the photodiode response is very similar for the decay of the shock front.

The post shock temperature is considered to be an important parameter for the characterization of the conditions of the system. However it must be pointed out that plots 4.39 to 4.41 with a range of $T_e = 369.00$ to 329.92 K, shows no structural

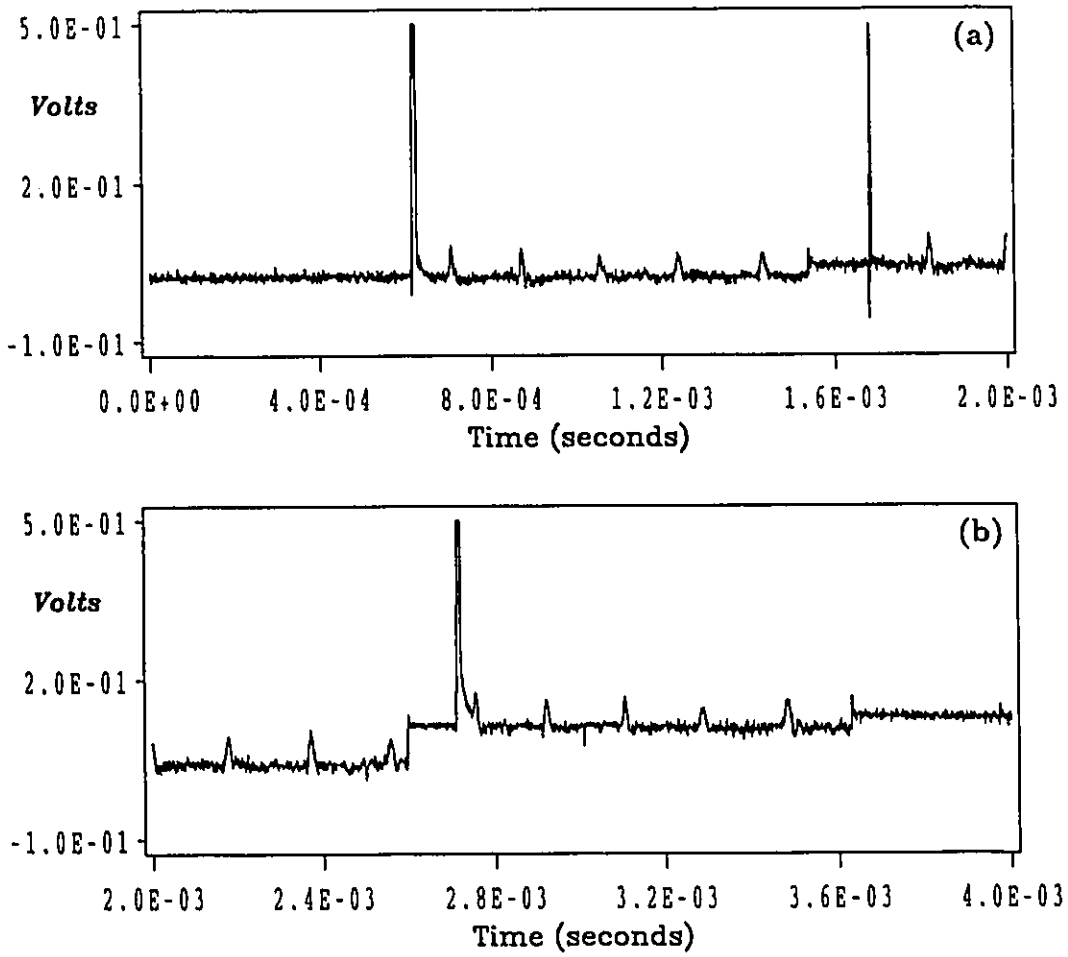

Figure 4.43 Plot of schlieren millivolt signal *versus* time (seconds) for shock compression of 253.0 Torr of a 25.05% mixture of CCl_3F in Ar with $p_0 = 63.4$ Torr, $T_0 = 295.15$ K, $p_e = 108.7$ Torr, and $T_e = 335.96$ K (average values). (a) is for 0.0 to 2.0 milliseconds and (b) is for 2.0 to 4.0 milliseconds.

behaviour; yet Figures 4.34-4.38, with an overlapping range of $T_e = 544.02$ to 316.50 K show a nonperiodic behaviour, and are thus an indication that the post shock temperature is not the only parameter that should be considered. Thus it seems that the argon itself must play a role in "quieting" down the schlieren millivolt signals.

Further evidence for this is the change in behaviour shown in Figure 4.42 where the conditions for shock compression of 188.0 Torr of a 25.05% mixture of CCl_3 in Ar are $p_0 = 47.1$ Torr, $T_0 = 295.15$ K, $p_e = 87.2$ Torr, and $T_e = 342.57$ K. In Figures 4.42(a) and (b) one can see that after the shock front has passed there are

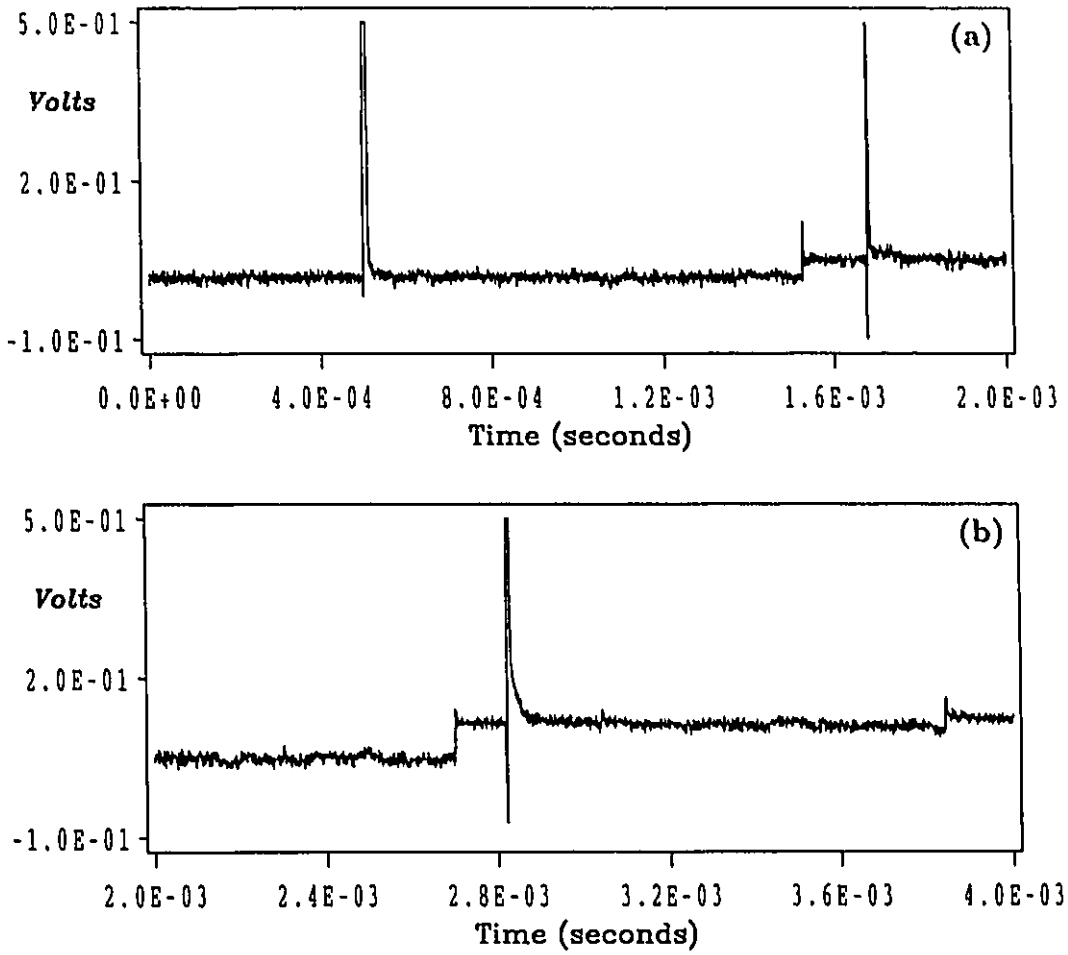

Figure 4.44 Plot of schlieren millivolt signal *versus* time (seconds) for shock compression of 435.0 Torr of a 25.05% mixture of CCl_3F in Ar with p_0 = 109.0 Torr, T_0 = 295.15 K, p_e = 149.5 Torr, and T_e = 318.06 K (average values). (a) is for 0.0 to 2.0 milliseconds and (b) is for 2.0 to 4.0 milliseconds.

prominent spikes appearing regularly on the baseline. The baseline itself seems to have the same amount of noise present before and after the shock front has passed.

Again this is shown in Figure 4.43, where the conditions for shock compression of 253.0 Torr of a 25.05% mixture of CCl_3 in Ar are p_0 = 63.4 Torr, T_0 = 295.15 K, p_e = 108.7 Torr, and T_e = 335.96 K. Obviously the shock velocity is less than for Figure 4.42 (see Tables 4.6 and 4.7 for the exact differences) but the amplitude of the spikes has increased and are more distinct. Analysis of this waveform is done in a later section of this work.

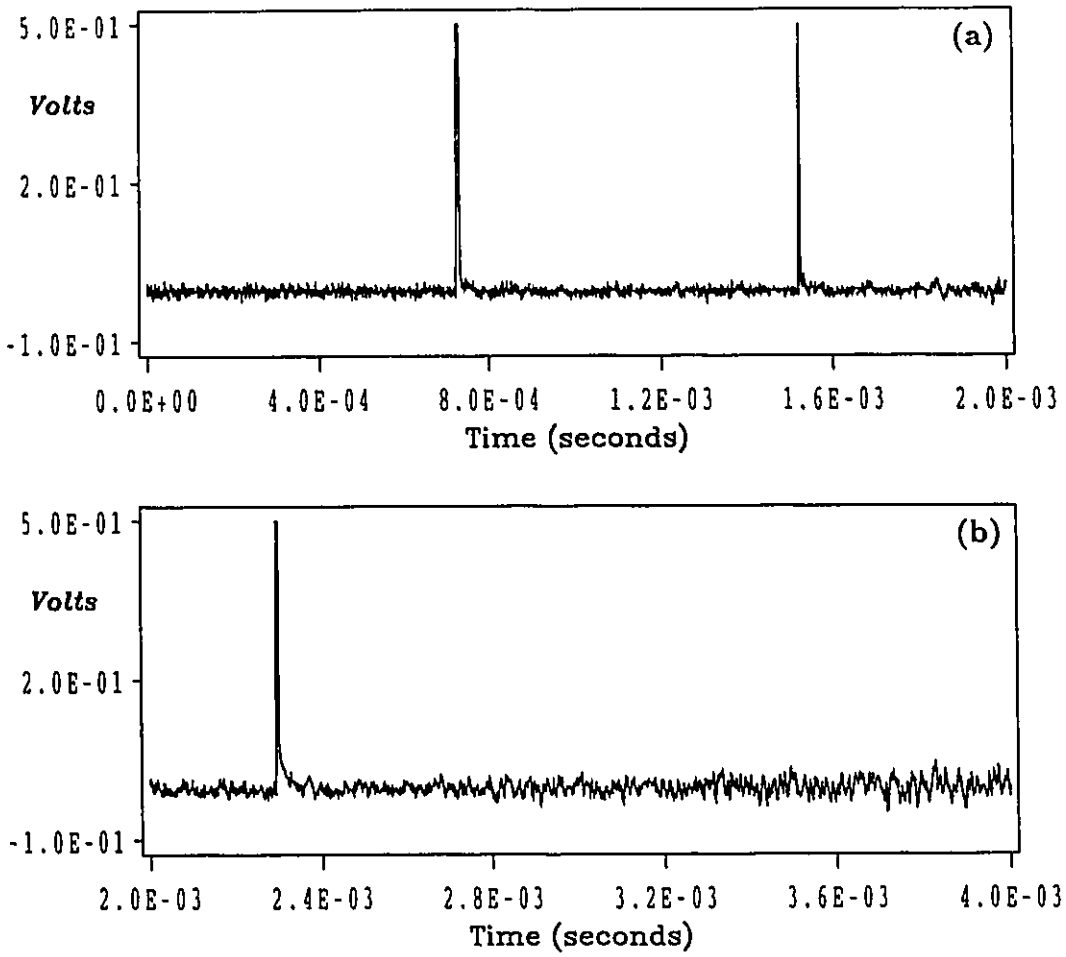

Figure 4.45 Plot of schlieren millivolt signal *versus* time (seconds) for shock compression of 188.0 Torr of a 5.08% mixture of CCl_3F in Ar with $p_0 = 9.6$ Torr, $T_0 = 295.15$ K, $p_e = 17.9$ Torr, and $T_e = 370.08$ K (average values). (a) is for 0.0 to 2.0 milliseconds and (b) is for 2.0 to 4.0 milliseconds.

What is now surprising is that in Figure 4.44, where the conditions for shock compression of 435.0 Torr of a 25.05% mixture of CCl_3 in Ar are $p_0 = 109.0$ Torr, $T_0 = 295.15$ K, $p_e = 149.5$ Torr, and $T_e = 318.06$ K, the spikes have decreased dramatically. In fact there are only slight variations in the baseline evident in Figures 4.44(a) and (b), after the shock front has passed.

Now this study returns to a mixture with lower CCl_3F content, as in Figure 4.45 where the conditions for shock compression of 188.0 Torr of a 5.08% mixture of CCl_3 in Ar are $p_0 = 9.6$ Torr, $T_0 = 295.15$ K, $p_e = 17.9$ Torr, and $T_e = 370.08$ K. Note that

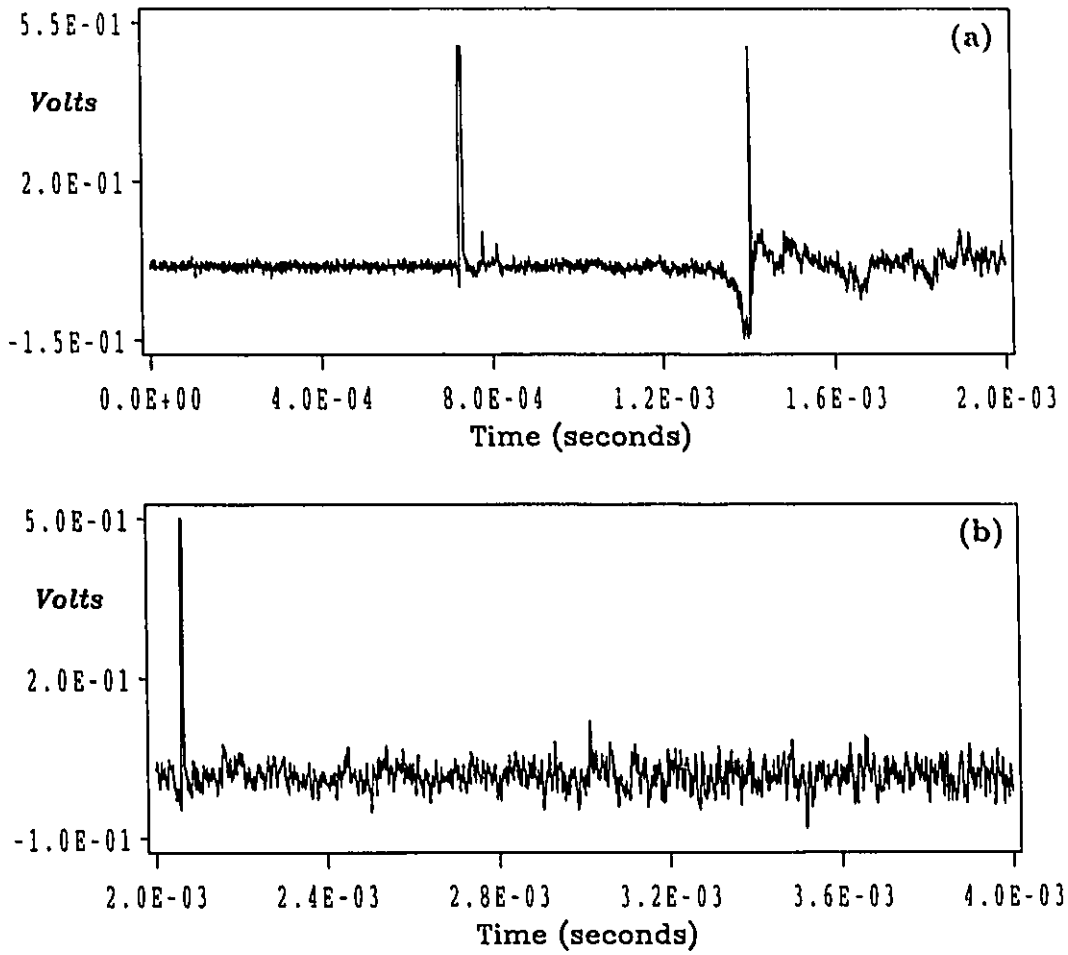

Figure 4.46 Plot of schlieren millivolt signal *versus* time (seconds) for shock compression of 188.5 Torr of a 5.08% mixture of CCl_3F in Ar with $p_0 = 9.6$ Torr, $T_0 = 295.15$ K, $p_e = 25.6$ Torr, and $T_e = 426.46$ K (average values). (a) is for 0.0 to 2.0 milliseconds and (b) is for 2.0 to 4.0 milliseconds.

the timing circuit has been bypassed and therefore only the first photodiode signal of Figure 4.45(a) is independent of the others. Notwithstanding this, there seems to be some small baseline oscillations of the first photodiode signal but these are only slightly different than the baseline noise before the shock front, and evidently the entire process is stable.

In Figure 4.46 where the conditions for shock compression of 188.5 Torr of a 5.08% mixture of CCl_3 in Ar are more intense than in Figure 4.45 *i.e.*, $p_0 = 9.6$ Torr, $T_0 = 295.15$ K, $p_e = 25.6$ Torr, and $T_e = 426.46$ K. The spikes have suddenly

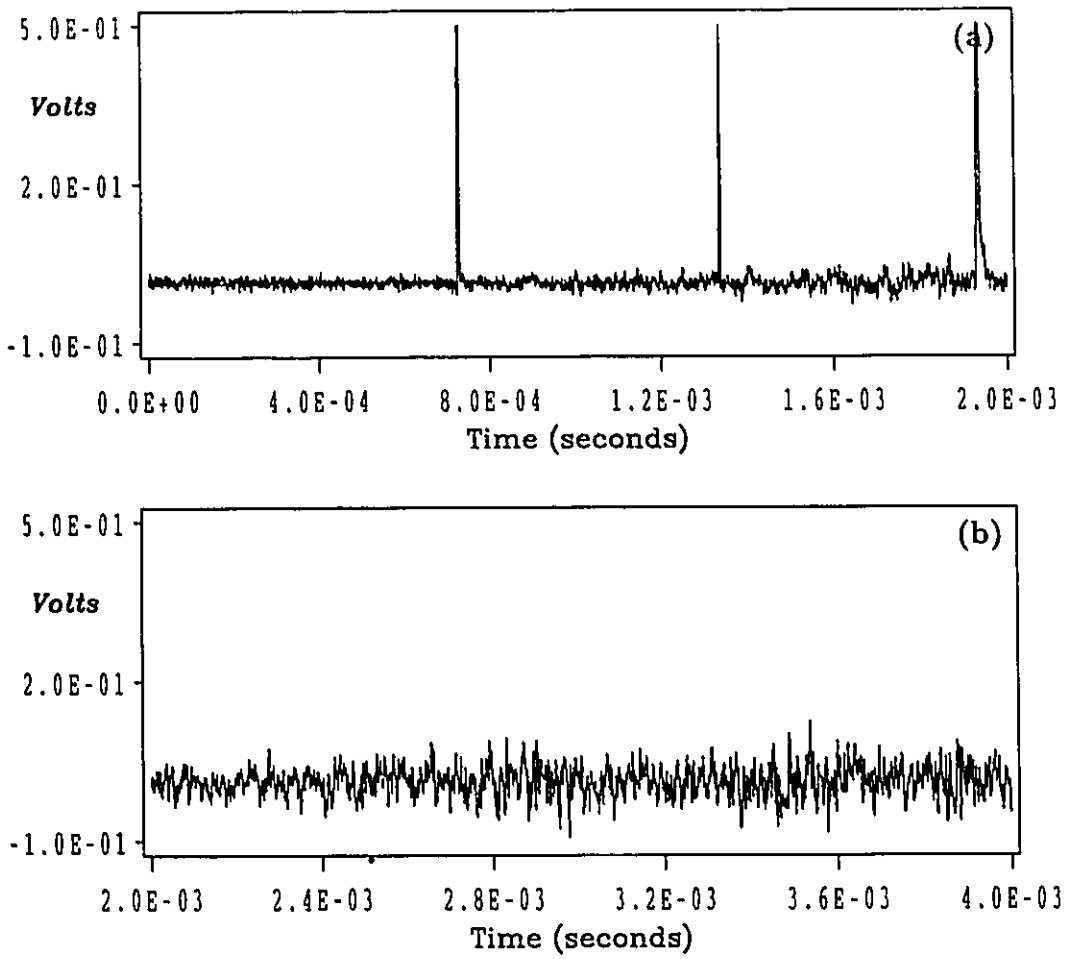

Figure 4.47 Plot of schlieren millivolt signal *versus* time (seconds) for shock compression of 100.0 Torr of a 5.08% mixture of CCl_3F in Ar with $p_0 = 5.1$ Torr, $T_0 = 295.15$ K, $p_e = 16.9$ Torr, and $T_e = 470.08$ K (average values). (a) is for 0.0 to 2.0 milliseconds and (b) is for 2.0 to 4.0 milliseconds.

occurred again, just after the shock front in the first photodiode signal at about 0.8 milliseconds (see Figure 4.46(a)). The rest of the waveform present in Figure 4.46(a) and (b) is used for the calculation of the velocity only, as the millivolt signal of the first photodiode is superimposed on the second. This is also the case for the third photodiode signal which is affected by the addition of the signal from the first two photodiodes.

When the conditions become even more extreme (a further increase in velocity), as in Figure 4.47 where the conditions for shock compression of 100.0 Torr of a 5.08%

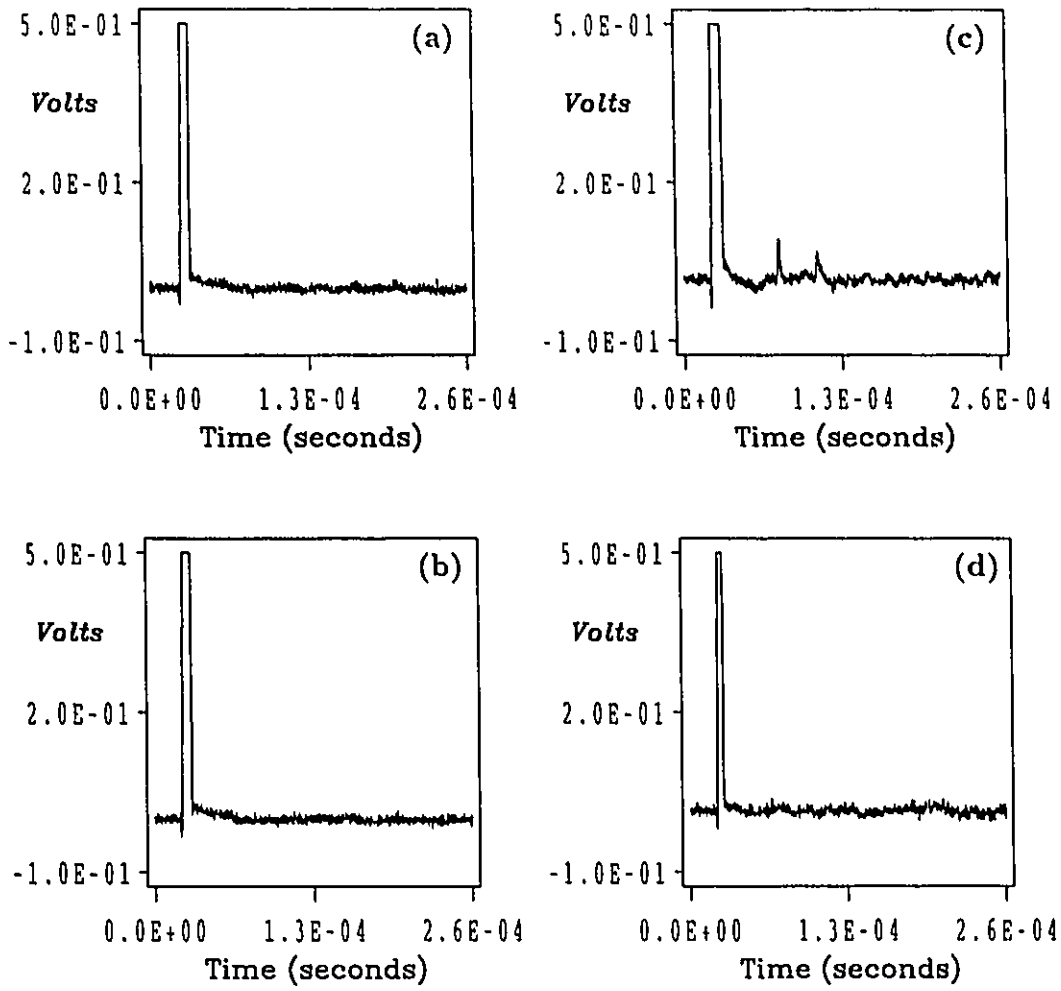

Figure 4.48 Plot of schlieren millivolt signal *versus* time (seconds) for shock compression of approximately a 5% mixture of CCl_3F in Ar with different velocities and therefore different post shock conditions (p_e and T_e are average values). The x-axis is expanded to display from 0.0 to 0.26 milliseconds. (a) p_0 = 9.5 Torr, T_0 = 295.15 K, p_e = 17.7 Torr, and T_e = 369.00 K; (b) p_0 = 9.6 Torr, T_0 = 295.15 K, p_e = 17.9 Torr, and T_e = 370.08 K; (c) p_0 = 9.6 Torr, T_0 = 295.15 K, p_e = 25.6 Torr, and T_e = 426.46 K; (d) p_0 = 5.1 Torr, T_0 = 295.15 K, p_e = 16.9 Torr, and T_e = 470.08 K.

mixture of CCl_3 in Ar are p_0 = 5.1 Torr, T_0 = 295.15 K, p_e = 16.9 Torr, and T_e = 470.08 K, the oscillations or spikes are reduced in amplitude again. This is also a case where the timing circuit was bypassed and the photodiode preamplifiers were not turned off in sequence.

In Figure 4.48 a direct comparison can be made between experiments with simi-

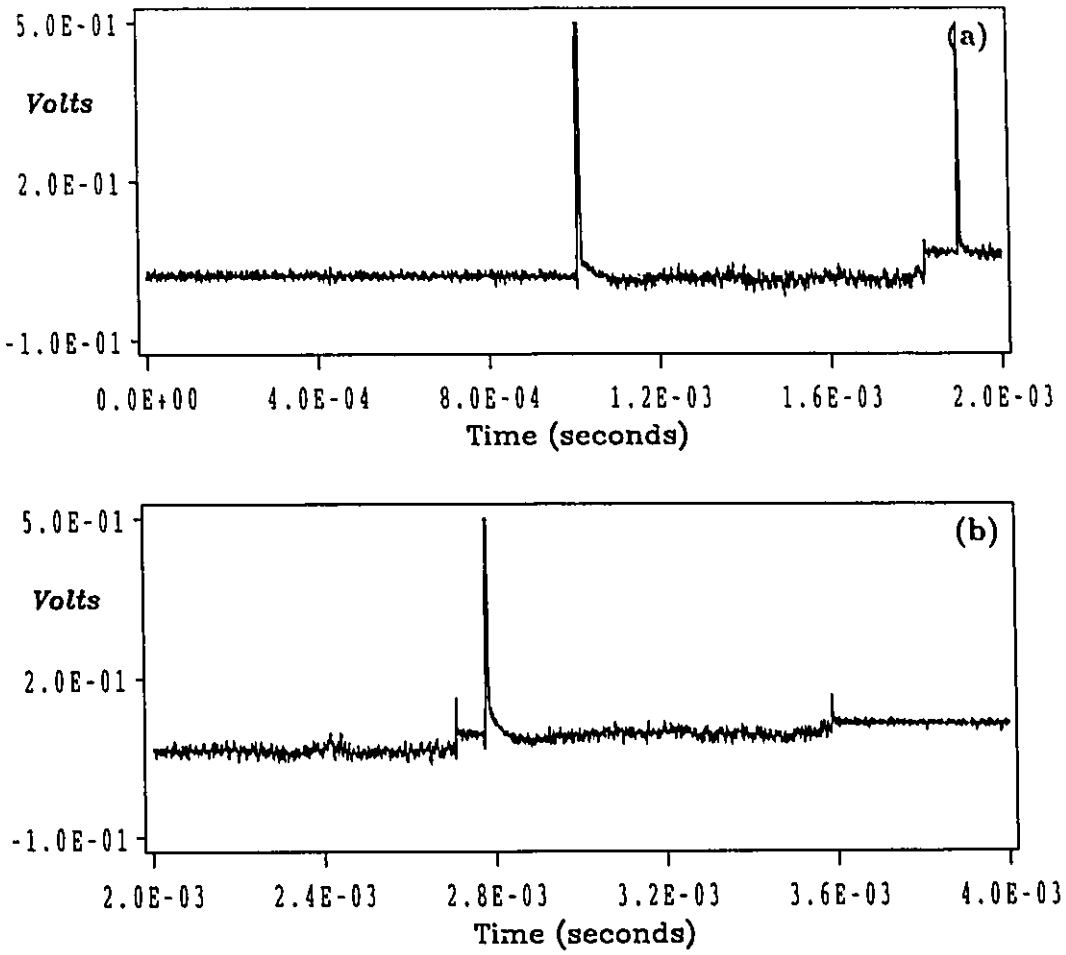

Figure 4.49 Plot of schlieren millivolt signal *versus* time (seconds) for shock compression of pure SF_6 with $p_0 = 24.0$ Torr, $T_0 = 295.15$ K, $p_e = 154.9$ Torr, and $T_e = 372.64$ K (average values). (a) is for 0.0 to 2.0 milliseconds and (b) is for 2.0 to 4.0 milliseconds.

lar initial conditions and slightly different post shock conditions. Figure 4.48(a) is an expansion of the first photodiode signal of Figure 4.39(a) between 0.0 to 0.26 milliseconds, while Figure 4.48(b) is a similar expansion of Figure 4.45(a). Figure 4.48(c) is a similar expansion of Figure 4.46(a), and Figure 4.48(d) is a similar expansion of Figure 4.47(a). Thus it can be seen that the baseline of Figure 4.48(a), and (b) are very similar. Except for the spikes present in Figure 4.48(c) its baseline is also very similar to the baseline of Figure 4.48(d). The baselines in the latter two have more fluctuations than the baselines in Figures 4.48(a) and (b).

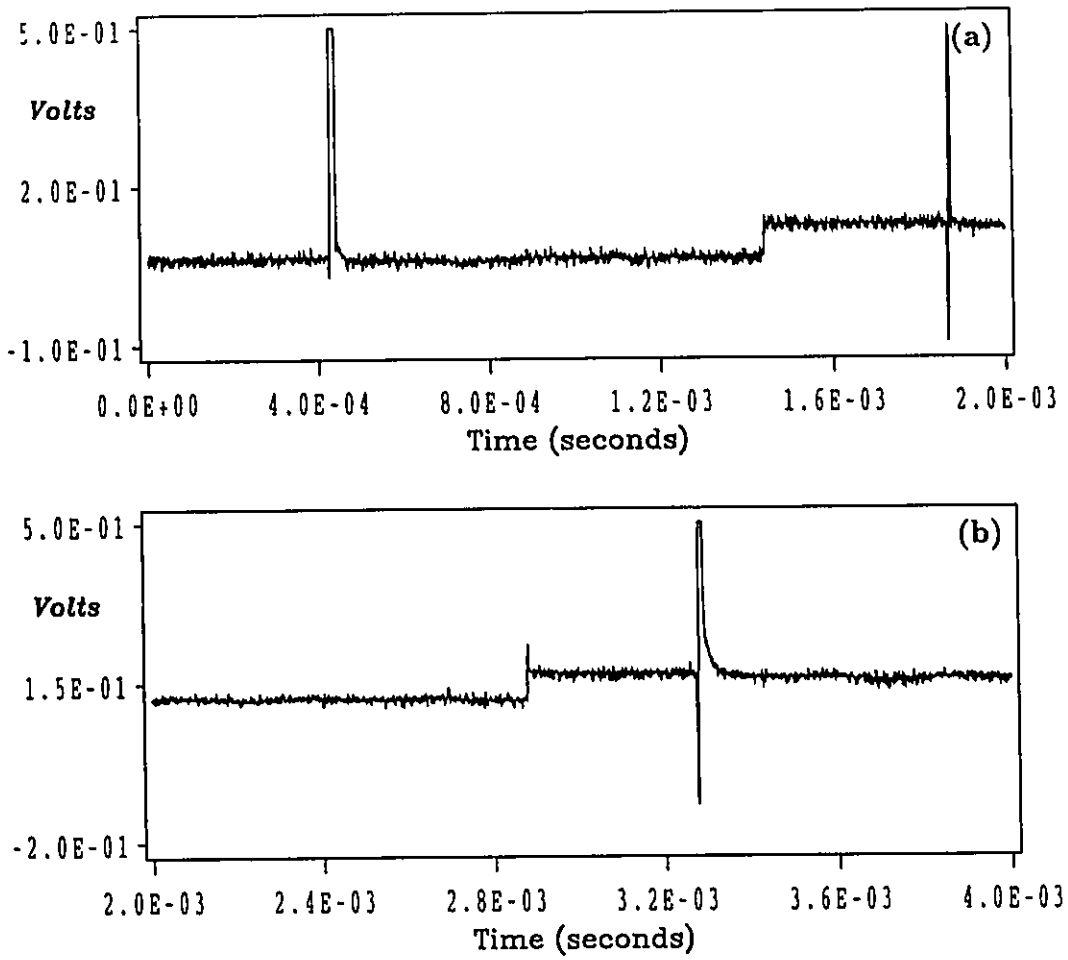

Figure 4.50 Plot of schlieren millivolt signal *versus* time (seconds) for shock compression of pure SF_6 with p_0 = 100.0 Torr, T_0 = 295.15 K, p_e = 244.8 Torr, and T_e = 321.34 K (average values). (a) is for 0.0 to 2.0 milliseconds and (b) is for 2.0 to 4.0 milliseconds.

This work now shows the same or at least similar effects for compounds other than CCl_3F. In Figure 4.49, where the conditions for shock compression of pure SF_6 are p_0 = 24.0 Torr, T_0 = 295.15 K, p_e = 154.9 Torr, and T_e = 372.64 K, the baseline has a slight oscillation to it for each of the separate schlieren millivolt signals. This oscillating baseline is also present in Figure 4.50, where the conditions for shock compression of pure SF_6 are p_0 = 100.0 Torr, T_0 = 295.15 K, p_e = 244.8 Torr, and T_e = 321.34 K. Note that the post-shock baseline seems to be quieter in Figure 4.50 than in Figure 4.49.

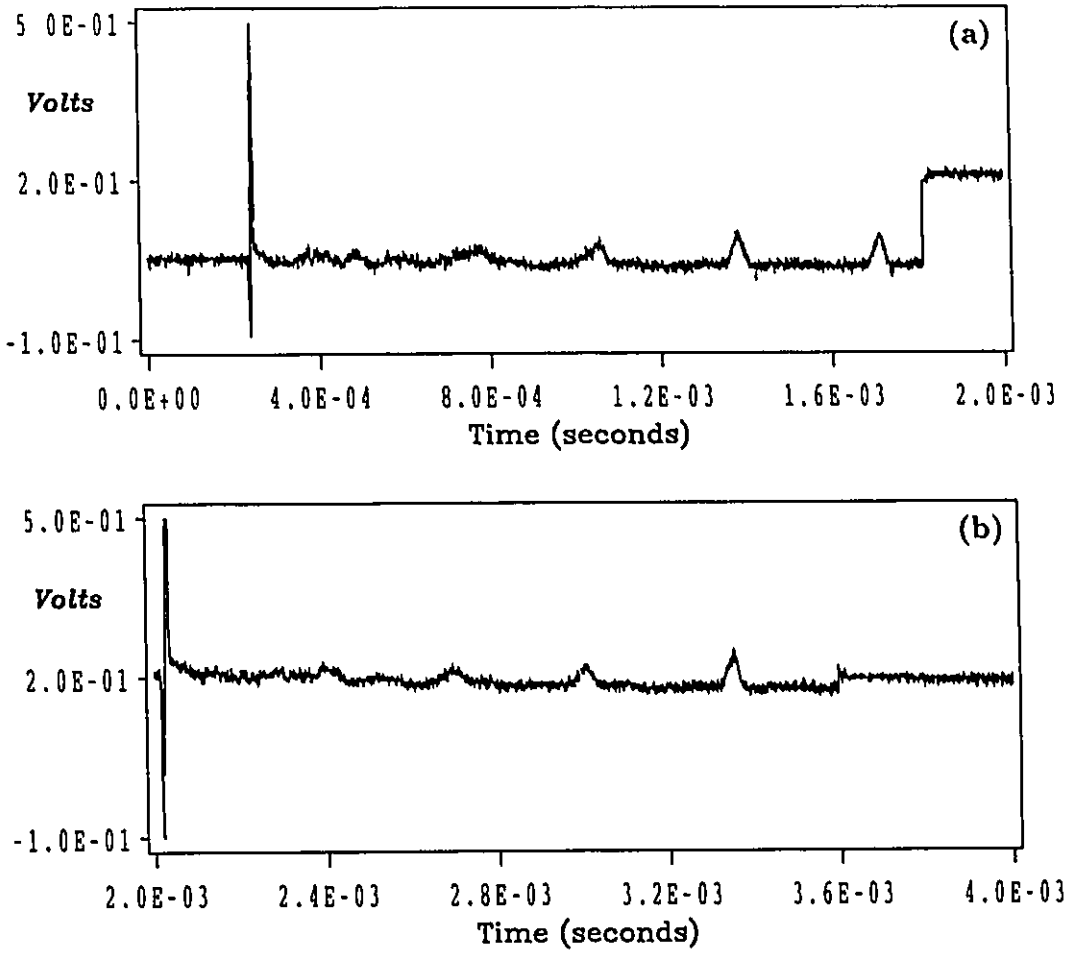

Figure 4.51 Plot of schlieren millivolt signal *versus* time (seconds) for shock compression of pure SF_6 with p_0 = 360.0 Torr, T_0 = 295.15 K, p_e = 532.4 Torr, and T_e = 305.53 K (average values). (a) is for 0.0 to 2.0 milliseconds and (b) is for 2.0 to 4.0 milliseconds.

Finally, at least for SF_6, in Figure 4.51, where the conditions for shock compression of pure SF_6 are p_0 = 360.0 Torr, T_0 = 295.15 K, p_e = 532.4 Torr, and T_e = 305.53 K, there are suddenly oscillations present again. The signal shown originates from the second and third photodiode detection stations since an error in data collection caused the loss of the first part of the first photodiode signal. Analysis of this signal will be presented in a later section.

In Figure 4.52(a), the conditions for shock compression of pure CCl_3H are p_0 = 5.0 Torr, T_0 = 295.15 K, p_e = 80.6 Torr, and T_e = 580.32 K, while for Figure 4.52(b),

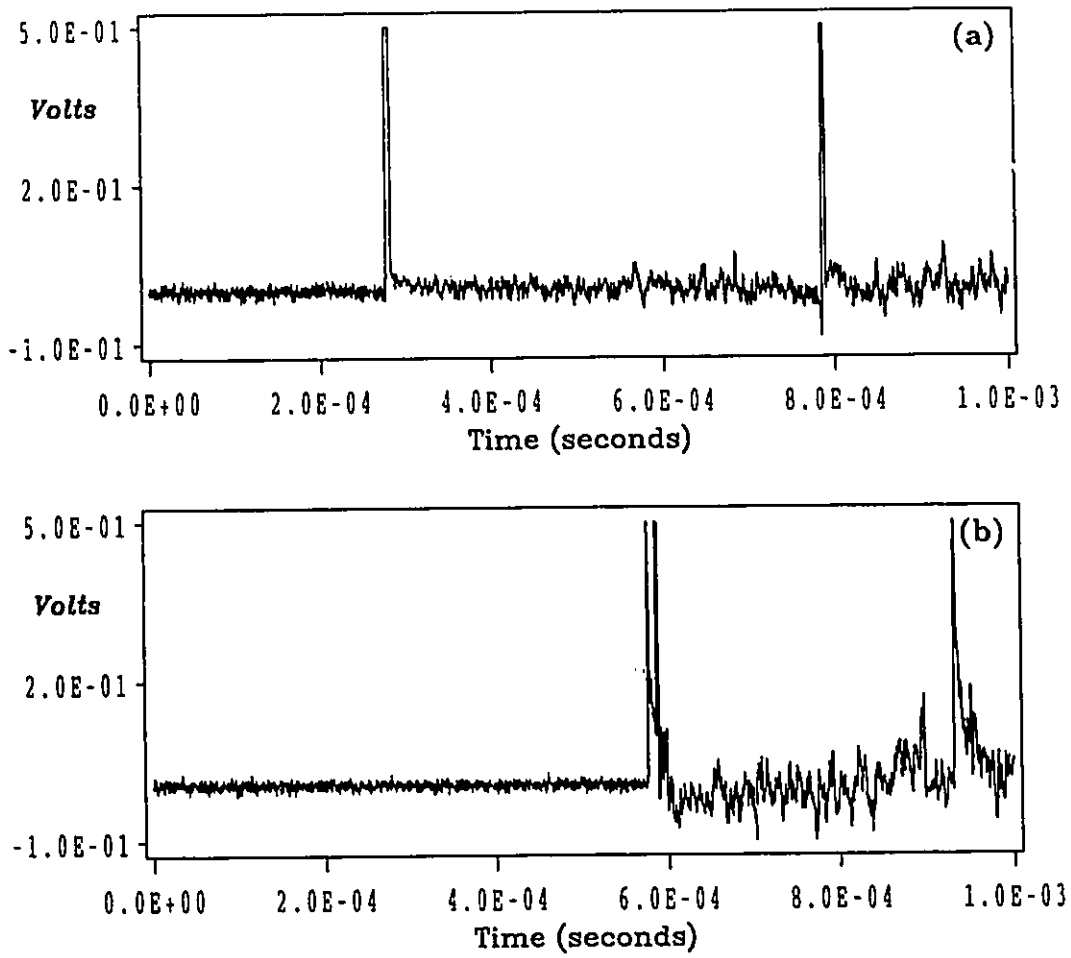

Figure 4.52 Plot of schlieren millivolt signal *versus* time (seconds) for shock compression of pure CCl_3H with different velocities and therefore different post shock conditions (p_e and T_e are average values). The x-axis is expanded to display from 0.0 to 1.0 milliseconds. (a) p_0 = 5.0 Torr, T_0 = 295.15 K, p_e = 80.6 Torr, and T_e = 580.32 K; (b) p_0 = 6.0 Torr, T_0 = 295.15 K, p_e = 191.4 Torr, and T_e = 830.59 K.

the conditions for shock compression of pure CCl_3H are p_0 = 6.0 Torr, T_0 = 295.15 K, p_e = 191.4 Torr, and T_e = 830.59 K. In both cases the timing circuit for the preamplifier shutoff has been disabled and that is the reason that only the first two photodiode schlieren millivolt signals are shown. Note that the baseline in Figure 4.52(a) and (b) are very different after the shock front has passed and are decidedly different from each other.

Figure 4.53 is for the same conditions of Figure 4.52 but the x-axes have been

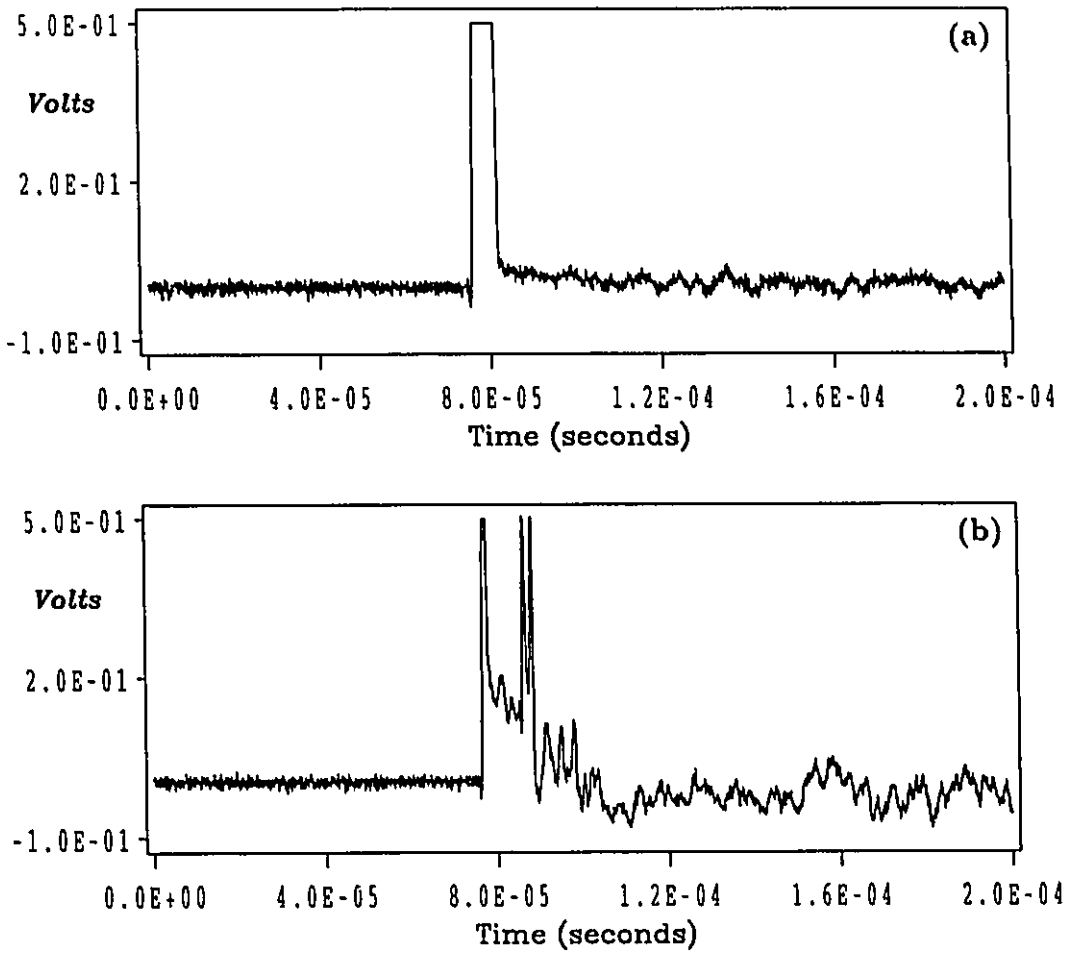

Figure 4.53 Plot of schlieren millivolt signal *versus* time (seconds) for shock compression of pure CCl_3H with different velocities and therefore different post shock conditions (p_e and T_e are average values). The x-axis is further expanded to display from 0.0 to 0.2 milliseconds. (a) p_0 = 5.0 Torr, T_0 = 295.15 K, p_e = 80.6 Torr, and T_e = 580.32 K; (b) p_0 = 6.0 Torr, T_0 = 295.15 K, p_e = 191.4 Torr, and T_e = 830.59 K.

expanded to allow observation of the oscillations in both 4.52(a) and (b). Thus it can be seen that the baseline of 4.53(a) has definite nonperiodic behaviour just as has been seen in the series of plots presented for pure CCl_3F of Figures 4.34-4.36. Figure 4.53(a) appears to be most similar to Figure 4.34(a) whose pressure is close to the initial pressure of CCl_3F, *i.e* 5.0 Torr. The post shock conditions are also similar, see Tables 4.6 and 4.7, rows five and seven. The velocities are within 3.7% of each other, but the post shock temperatures differ by 6.7% from each other while

the post shock pressures differ by 7.8% from each other. Despite this similarity, Figure 4.53(b) indicates, that there are extremely irregular effects present since the oscillations (Figure 4.53(b)) are rather pronounced compared to those that have been shown so far. These kinds of oscillations were also observed by Cheng[69].

Since most of the experiments were carried out with the same thickness of diaphragm a comparison of experiments with the same initial total pressure can be done. This involves a comparison of 196.0 Torr of pure CCl_3F, (Figure 4.38), 188.0 Torr of a 5.05% mixture of CCl_3F in Ar (Figure 4.39), 188.0 Torr of a 5.08% mixture of CCl_3F in Ar (Figure 4.45), and 188.0 Torr of a 25.05% mixture of CCl_3F in Ar (Figure 4.42). Of these four situations, Figure 4.38 (196.0 Torr of pure CCl_3F) shows the most dramatic oscillations, spikes and irregular baseline. 196.0 Torr of pure CCl_3F is also a very low post shock temperature situation, 316.50 K. The next most severely oscillatory system is displayed in Figure 4.42 for 188.0 Torr of a mixture of 25.05% CCl_3F in Ar. Its post shock temperature, 342.57 K, is slightly higher than in the previous case (316.50 K). Both 5% mixtures of CCl_3F in Ar have no oscillations present and are at post shock temperatures of $\approx$ 370 K.

There are three criteria for complicated behaviour and even chaotic behaviour[69]: (1) nonlinear equations or terms (see the rate equations outlined in the simulation section); (2) a system far from equilibrium. (In this work the system is taken from a Boltzmann distribution at one temperature to a new temperature, and the system must then evolve to a new Boltzmann distribution for the new temperature.); and (3) thermal feedback, (positive feedback) which can lead to oscillations and chaotic response. This is shown in this work as well. In fact in this work the thermal feedback seems to be controlled by the presence of Ar. At a certain dilution factor the Ar turns off the feedback and the oscillations, or spikes disappear. This work has presented the idea (as outlined by Cheng[69]) that the heat release and take up in the system

is from the formation, stabilization or break up of clusters. Thus the argon seems to collisionally deactivate the dissociation process. Figures 4.48(b) and 4.48(c) show that the thermal feedback can be turned "on". Figures 4.48(c) and 4.48(d) show that the thermal feedback has been turned "off".

If the notion of post shock pressure is used to compare experiments, referring to Table 4.7, it is possible to see that for the experiments involving CCl_3F comparison of 5.0 Torr of pure CCl_3F (row seven), and 188.0 Torr of 25.05% mixture of CCl_3F in Ar (row nineteen) should be done. Thus comparing Figures 4.34(a) and 4.42(a) it is possible to see that there are no similarities at all in the schlieren millivolt signals of the two cases.

Similarly, the signal for 9.5 Torr of CCl_3F (p_e = 112.8) and 253.0 Torr of a 25.05% mixture of CCl_3F (p_e = 108.7) in Ar can be compared. Figures 4.34(b) and 4.43(a)/4.43(b) again show that there are no similarities between the two cases.

If T_e, the post shock temperature, is chosen as a basis for comparison then the experiment with 435.0 Torr of a 25.05% mixture of CCl_3F in Ar (T_e = 318.06 K) can be compared with 196.0 Torr of pure CCl_3F (T_e = 316.50 K). Again there is nothing similar about these waveforms. Alternatively a comparison can be made of 253.0 Torr of a 25.05% mixture of CCl_3F in Ar (T_e = 335.96 K), with 435 Torr of a 5.05% mixture of CCl_3F in Ar (T_e = 329.92 K) and with 61.0 Torr of pure CCl_3F (T_e = 335.81 K). Thus comparing Figures 4.43, 4.41, and 4.37, respectively, it can be seen that although the waveforms in both Figures 4.43 and 4.37 have oscillations, the waveforms are quite different. The waveform in Figure 4.41 has no oscillations and is similar to the signal represented by pure argon in Figure 4.33.

If comparison is made on the basis of the initial partial pressure, p_0, then 5.0 Torr of pure CCl_3F can be compared to 100 Torr of a 5.08% mixture of CCl_3F in

Ar. Thus comparing Figures 4.34(a) with 4.47(a) it can be seen that, even though there are more severe post shock conditions for Figure 4.47(a), the baseline after the shock front is much quieter that the baseline in Figure 4.34(a). Thus the Ar has apparently stabilized the thermal feedback originating from collisional equilibration of the excited dimers.

Comparison could also be made of 22.0 Torr of pure CCl_3F and 435 Torr of a 5.05% mixture of CCl_3F in Ar. Thus comparison of Figures 4.35 and 4.41, respectively, shows again that for similar p_0 (of CCl_3F) the results are very different. The argon seems to have again stabilized the situation, and the baseline after shock front passage is very similar to that before (see Figure 4.41); whereas for Figure 4.35 there is definitely nonperiodic behaviour after shock front passage.

There is, however, a curious situation. With $p_0 = 61.0$ Torr, $T_e = 335.81$ K (Figure 4.37) and with $p_0 = 63.4$ Torr, $T_e = 335.96$ K (Figure 4.43) some similar spiking occurs.

Instead of comparing T_es, comparison of T_e to the critical temperature, T_c, of the compound could be done. In other words the reduced temperature, T_e/T_c might be a relevant parameter. Voronel [83] has pointed out that the behaviour of liquids should be investigated with more attention to the critical point of the compound. In fact on page 364 of reference 83 he states:

> "Different physical magnitudes not only have different singularities near T_c (different exponents), but are also distorted in different ways by the same distorting factors. $\cdots$ The location of the singular point is better determined by anomalies in kinetic quantities than by thermodynamic. In contrast to extensive thermodynamic quantities, which are averaged over the vessel and smooth out the real anomaly, the relaxation times of the various parts of the system do not add up."

This work investigates the nonlinear kinetic properties of shock compressed compounds and the pre-cursor conditions to condensation. Since the critical temperature is defined as the highest temperature at which the compound can condense (form a liquid), T_c is important to this work.

For CCl_3F with $T_e << T_c(\approx 472$ K) as in Figure 4.37, where $T_e = 335.81$ K, and in Figure 4.38, where $T_e = 335.81$ K, spikes or oscillations, are present. In Figure 4.36 with $T_e = 379.74$ K, and in Figure 4.35 where, $T_e = 386.26$ K, the spikes or oscillations, when present are similar in amplitude to the other nonperiodic baseline behaviour. Finally, in Figure 4.34(b) with $T_e = 468.96$ K, which is just slightly less than T_c, there is a large amplitude variation of the baseline, and in Figure 4.34(a) with $T_e = 544.02$ K $> T_c$ the baseline is not a flat line, but it is much quieter than for other temperatures.

The work done with SF_6 also seems to follow the general trend that if $T_e > T_c(\approx$ 319 K) then the baseline is relatively smooth (see Figures 4.49 and 4.50). While when $T_e < T_c$ (see Figure 4.51) the spikes, or oscillations, are present.

Now this work turns its attention to CCl_3H ($T_c \approx 537$ K). The results plotted in Figures 4.53(a) and (b) are for situations where $T_e > T_c$, 580.32 K and 830.59 K, respectively. The reason for the dramatic oscillations present in 4.53(b) are most likely due to hydrogen bonding which produces more strongly bonded $n-$mers than for the other compounds. Since there is a stronger bond therefore a stronger shock is needed to interrupt dimer formation.

4.6 Data Analysis

The Fourier Transform and the Fast Fourier Transform (FFT) are known to be good methods for analyzing repetitive signals[66,67] but these methods have some limitations when it comes to analyzing transient signals. There are ways to overcome some of these limitations. This work will not pursue those techniques however, but will instead show a wavelet analysis in conjunction with a FFT, of the millivolt signal presented in Figure 4.43.

4.6.1 FT Analysis

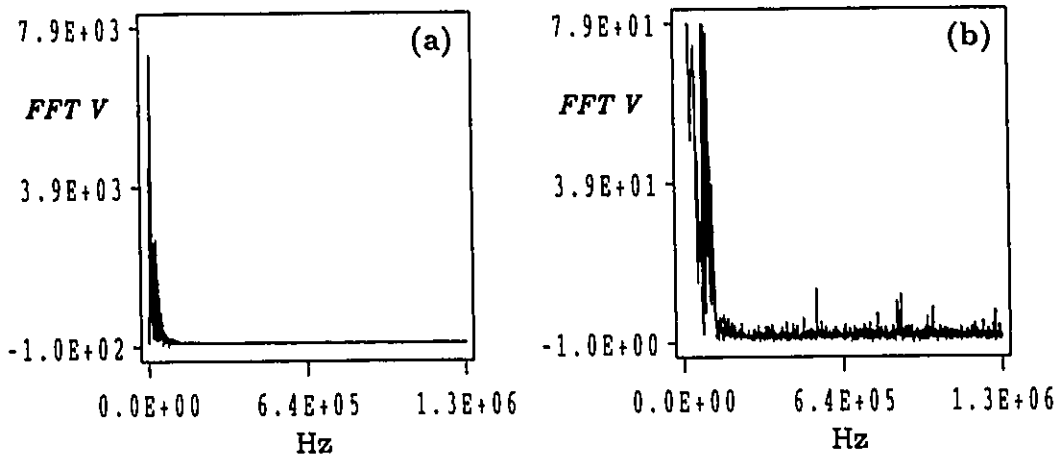

Figure 4.54 The Fast Fourier Transform of the complete millivolt signal (32, 768 data points) lasting 819.2 μseconds. (a) is the fullscale plot for 0 to 1.3 MHz, (b) is a vertical scale expansion by a factor of 100.

The FFT of the millivolt signal (Figure 4.43) is shown in Figure 4.54 and the maximum amplitude is approximately 7200, (a), while the the zero frequency component amplitude is approximately 1. Figure 4.54(b) is a vertical scale expansion by a factor of 100. There are several frequencies present, and the frequencies that the FFT of the details resolves are present with lower amplitudes. Thus they are buried in the background of the system.

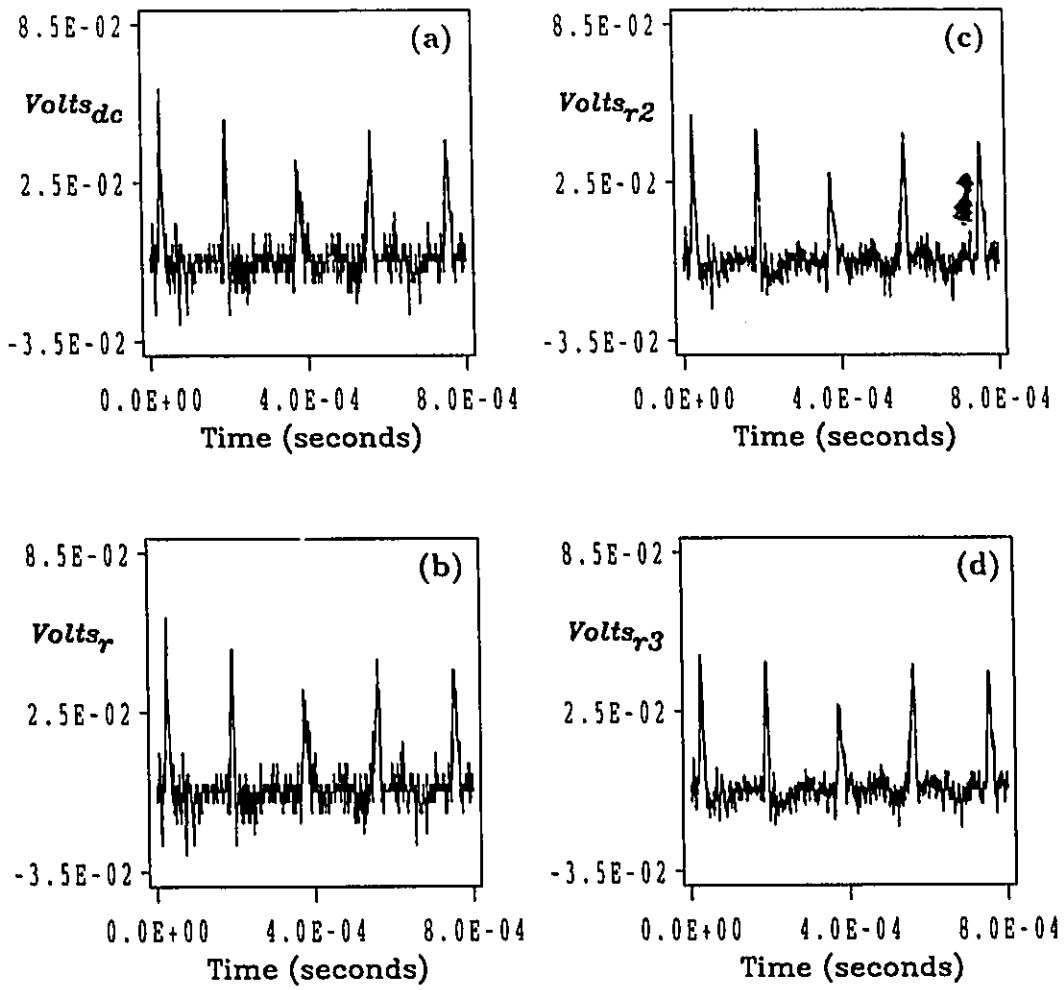

Figure 4.55 Plot of the millivolt signal from Schlieren detection system of the shock tube apparatus. Smoothed data, only 1024 points were plotted (a) $dc(-25 \times 10^{-3})$ shifted voltage, (b) waveform reconstructed from the wavelet analysis, (c) waveform reconstructed from "altered" details D_1, D_2, D_3 and D_4 and the unaltered details of the previous analysis, and (d) waveform reconstructed from the D_1, D_2, D_3, and D_4 details from a wavelet analysis using the ψ_4 wavelet but the rest of the unaltered details.

4.6.2 Wavelet Analysis

The data that is shown in this work is for 32, 768 data points *i.e.* 819.4 μseconds. The signal that is plotted in this work is a subset of these collected data points. Every eighth data point was kept and the wavelet analysis was performed on these remaining 4096 data points. This procedure of keeping every eighth data point could

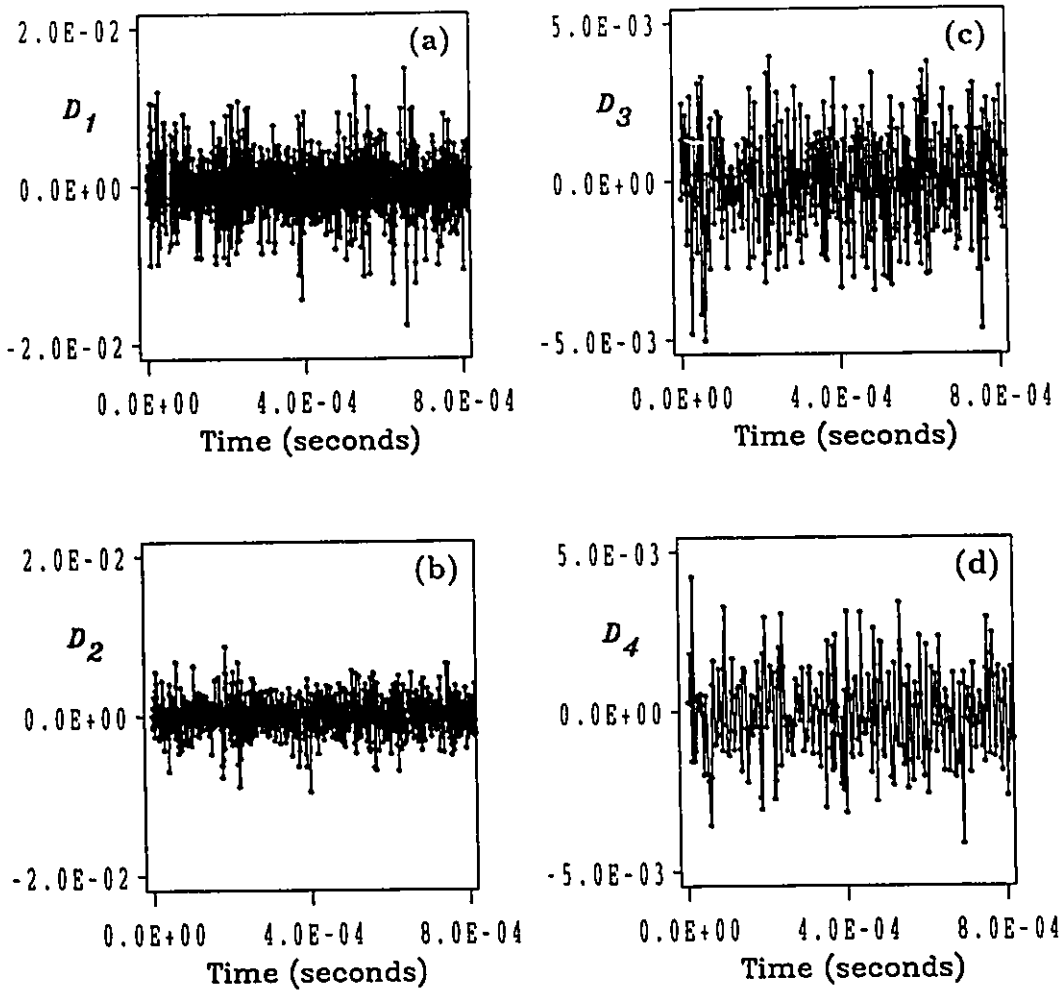

Figure 4.56 The unaltered detail files (D_1 to D_4) of a wavelet analysis of the signal shown in previous figure (a), calculated using a ϕ_8 wavelet.

be considered a smoothing of the original data. In fact, a wavelet analysis was also performed on a data set that was obtained from keeping every second data point of the original 32, 768 data points. That wavelet analysis did not work as well as the wavelet analysis of the 4096 data set, which are the only plots that are presented here.

In Figure 4.55 the millivolt signal is plotted at various stages of the process. Figure 4.55(a) is the millivolt signal that had been reduced to 4096 of the original 32, 768 data points. In Figure 4.55(b) the millivolt signal has been *dc* shifted by

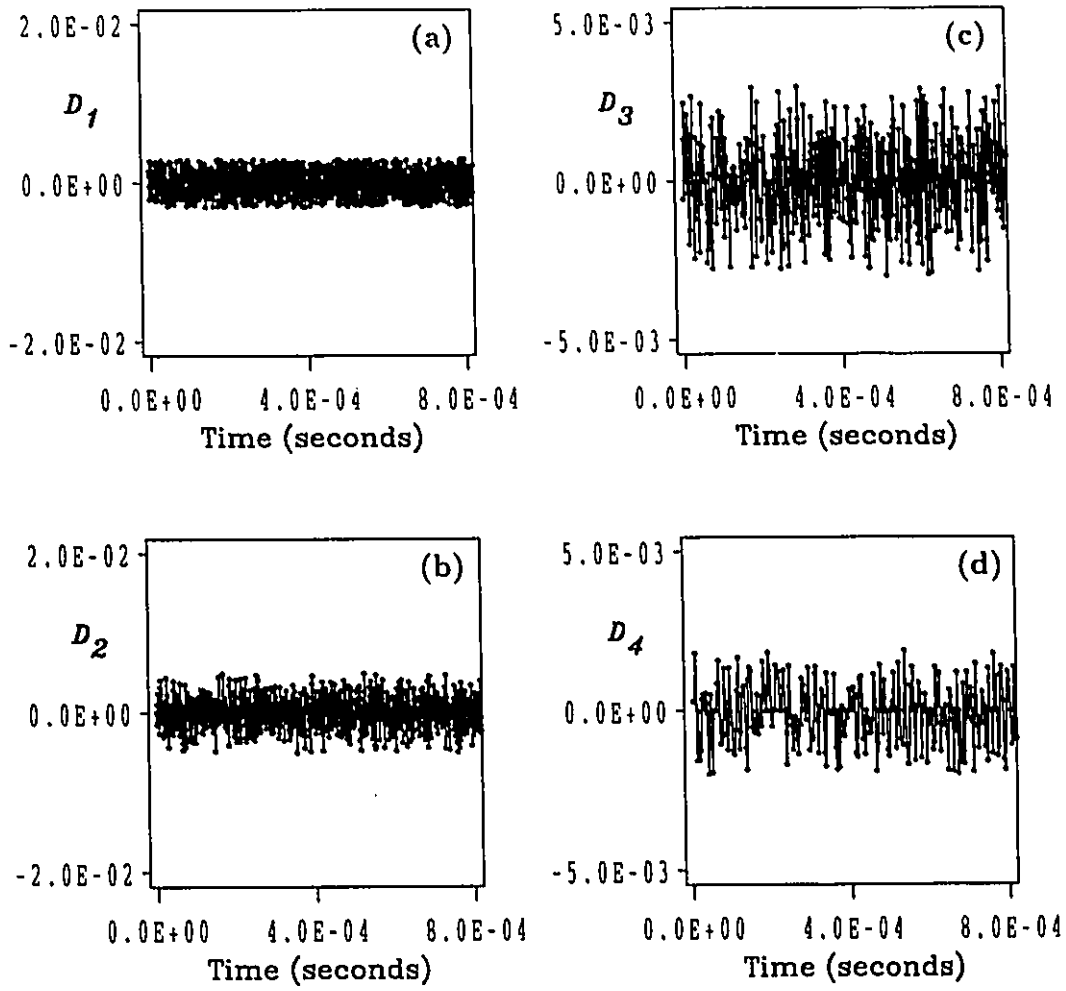

Figure 4.57 The edited detail files (D_1 to D_4).

-25×10^{-3} volts. This shifting was done to decrease the amplitude of the zero frequency component of the FFT of the millivolt signal. This is a common FFT practice as described by Brigham[67].

The wavelet analysis is then performed on the *d.c.* shifted 4096 data point signal of Figure 4.55(b). Since each of the resulting detail data files has a different number of data points (see Figure 4.56), each file is filled with zeros added at the end to make up a total of 4096, and then an FFT is calculated. To resolve separate frequencies a procedure is used, stated in an earlier section, of setting a threshold value of the amplitude of the detail data. If the detail amplitude is larger than the threshold value

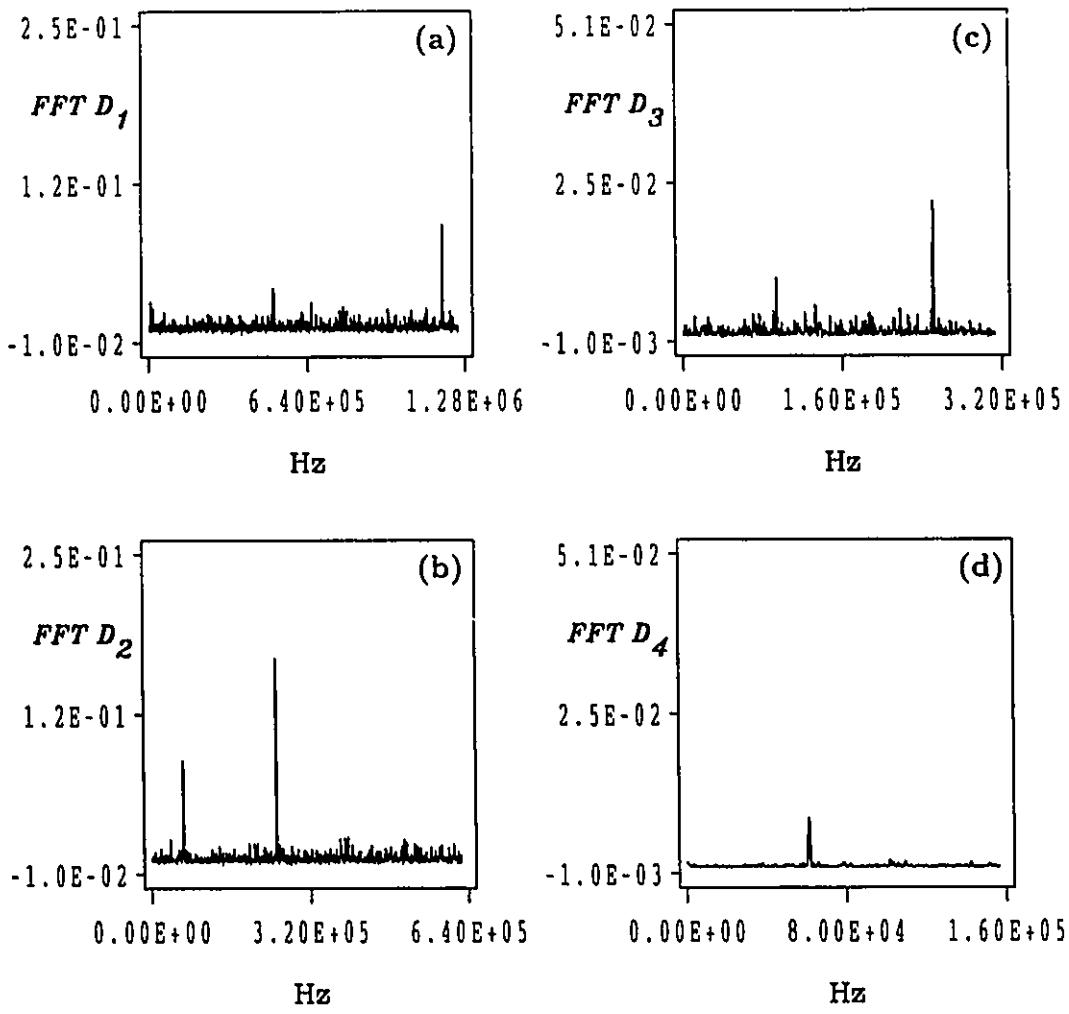

Figure 4.58 Plots of the Fast Fourier Transform of the detail data files with threshold settings slightly different for each detail (db08). (a) FFT of D_1. (b) FFT of D_2, (c) FFT of D_3, and (d) FFT of D_4.

the data point value is set to zero. The threshold value is decided upon by observing the amplitude of the detail plot. Usually the waveform in the detail has a central set of values with only a few values exceeding this amount. This is illustrated in Figure 4.58 for D_1, D_2, D_3, and D_4. This center value is then used as the threshold value in the FFT program. Several threshold values near this selected value are chosen to see if the FFT output changes. If there are only minor changes for an order of magnitude change of the threshold value, and if the amplitude of the zero Hz component is relatively small (a tool used in FFT analysis) then that threshold

value is kept. The edited detail data file is also saved in this process to be used in the second reconstruction of the original signal.

The procedure uses eight detail files to reconstruct the original signal. The reconstructed signal is shown in Figure 4.55(c) and is for all intents and purposes, identical to Figure 4.55(b). (In fact the data files agree to the three significant figures supplied by the original 8 bit A/D.) In the second reconstruction the first four edited detail files and the four remaining unedited detail files are used to produce the waveform in Figure 4.55(d). Notice that Figure 4.55(d) has a significant signal-to-noise improvement over Figure 4.55(b) and reveals an underlying oscillation which is otherwise not evident in the original Figure 4.55(a) or (b) because of the high amount of noise present. Since the second reconstructed waveform is different from the original waveform, in theory, it should be possible to repeat the process.In fact, this is not the case at all. A subsequent wavelet-FFT of the second reconstructed waveform results in the already known frequencies and no new information. Although it does provide an increase in the signal-noise-ratio, unfortunately the decrease of the noise is not as dramatic as that shown from a comparison of Figures 4.55(c) and (d). Thus, there is a sense of diminishing returns.

In Figure 4.56 the detail files are presented with vertical scales which are the same for D_1 and D_2 and the same for D_3 and D_4. The detail data points are plotted and a line is drawn between them to guide the eye. There is too much information present to able to detect a single frequency in the waveform, and that is one reason for performing an FFT on the waveform. The threshold values used for the FFT are, $\pm 3.0 \times 10^{-3}$ for D_1, $\pm 5.0 \times 10^{-3}$ for D_2, $\pm 3.0 \times 10^{-3}$ for D_3, and $\pm 2.0 \times 10^{-3}$ for D_4. Figure 4.57 contains the edited detail files with the settings indicated above.

In Figure 4.58 the FFT of the details, as described above, are plotted. In Figure 4.58(a) frequencies of 1.18 MHz, and 500 KHz are observed while in (b) 250 KHz

and 63.17 KHz are the observed frequencies.In Figures 4.58(c) and (d) the frequencies are 251 KHz, 94.15 KHz and 61.42 KHz respectively. These are more dramatically pronounced than in the simple FFT's of Figure 4.54. A wavelet analysis of a 16, 382 data point file was performed but only a few of the higher frequencies were observed and then only when the threshold values were set extremely low.

The success of the WFFT analysis of this work in "denoising" the signal can be explained by referring to Mallat and Hwang[73]. They have developed a special algorithm to push the "denoising" process even further. However, their basic explanation will suffice for this work. Mallat and Hwang[73] point out that when the wavelet analysis is performed on the derivative of a signal the higher details actually contain information pertaining to the location of the edges of the original waveform. In our work the higher numbered details are not edited. The second and third reconstruction processes, of this work, edit only the lower number details. It is evident, from Figure 4.58, that the higher frequencies are present in the lower numbered details and decreasing the amplitude of some of the points in the detail eliminate high frequency noise. Since the higher numbered details are unedited the relatively low frequencies needed to build up the original signal are unaffected. Thus, as pointed out earlier, this process has broken the original signal into frequency bands, some of which have been edited to remove noise, while the remainder have been left unaltered.

Unfortunately, when this process was tried on the millivolt signal presented in Figure 4.38, 196.0 Torr of pure CCl_3F, the analysis produced very similar frequencies to the case of Figure 4.58. Further investigation, as in a wavelet analysis of the baseline present in Figure 4.38(c) after all three photodiodes have been turned off, produced the same frequencies again. The FFT of 8.192×10^{-4} seconds of baseline, from 4.4 milliseconds to 5.2 milliseconds, shown in Figure 4.38(b), is presented in Figure 4.59. Checking the HeNe laser manual confirmed that these high frequencies

are probably due to a 0.1% rms background signal produced by the HeNe lasers. It is expected to give frequencies from 10kHz up to 10 MHz. This work does not use a process, such as outlined by Delprat *et al*[71] for ratioing out known frequencies. Therefore further wavelet analysis of the schlieren millivolt signals is not possible at this time. Nevertheless, it has been shown that it is possible to denoise single shot experimental signals using wavelet analysis. Daubechies[61] has stated that a wavelet analysis is good for picking out high frequencies. It has done so here even when the amplitudes are extremely small. The signals of chemical interest here are actually low frequencies for which wavelet analysis presents no particular advantage over FFT. This work therefore continues with the FFT analysis.

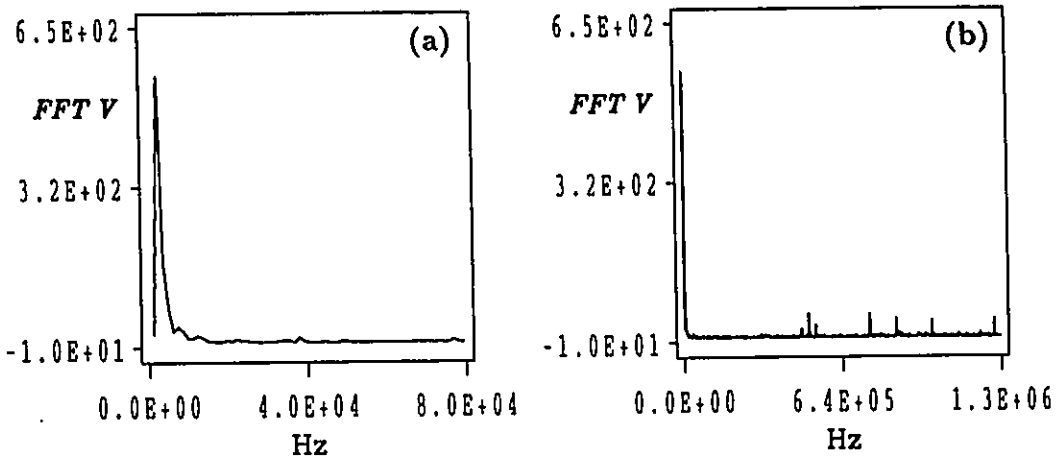

Figure 4.59 Plot of the FFT of 8.192×10^{-4} seconds of baseline, from 4.4 milliseconds to 5.2 milliseconds, shown in Figure 4.38(b). (a) is for 0 to 80kHz and (b) is for 0 to 1.3MHz.

4.6.3 FT Analysis Revisited

The four plots in Figure 4.60 are not all for the same total time and therefore have a different frequency step size. For Figure 4.60(a) the total time of the signal is only 4.096×10^{-4} seconds, which is approximately all of the time of the first photodiode in Figure 4.34(b), and the frequency step size is 2441.4 Hz. The other three signals

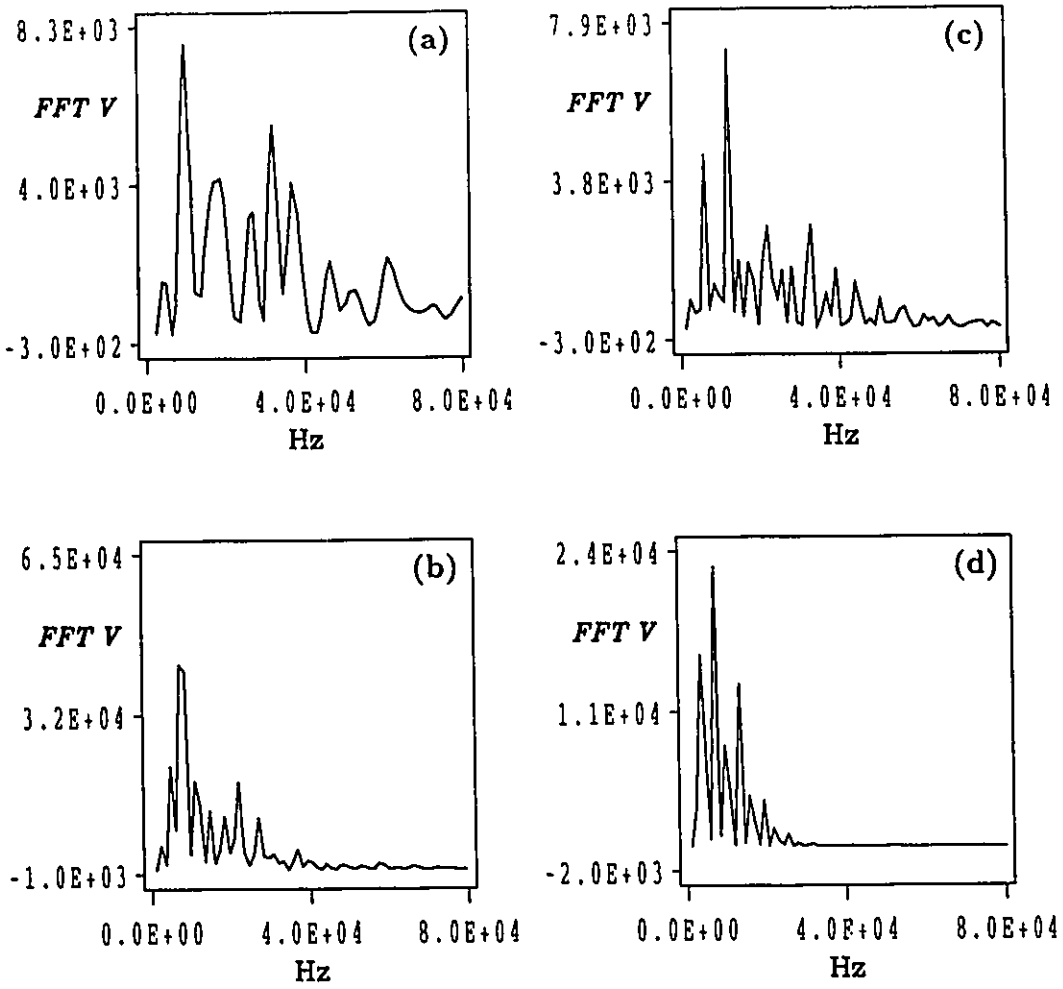

Figure 4.60 Plots of the FFT of schlieren millivolt signals for 0 to 80k Hz. (a) is for p_0 = 9.5 Torr of pure CCl_3F, (b) is for p_0 = 196.0 Torr of pure CCl_3F, (c) is for 253.0 Torr of a 25.05 % mixture of CCl_3F in Ar, p_0 = 63.4 Torr, and (d) is for p_0 = 360.0 Torr of pure SF_6.

(Figure 4.60(b), (c), and (d)) are for 8.192×10^{-4} seconds, and therefore the frequency step size is 1220.7 Hz. Table 4.8 lists the amplitudes, and the respective frequencies, for the four cases presented in Figure 4.60.

There are a large number of frequencies present in Figure 4.60(a) and this is expected, since the post shock temperature of 9.5 Torr of pure CCl_3F (T_e =468.96) is very close to T_c = 471 K. It is interesting to note that there are similar frequencies present in all three CCl_3F experiments show in Figure 4.60. Comparing the pure

Table 4.8 Frequencies for FFT of the schlieren millivolt signals for 9.5 and 196.0 Torr of pure CCl_3F, 253.0 Torr of a 25.05% mixture of CCl_3F in Ar, and 360 Torr of pure SF_6. Amplitude is abbreviation to Amp. and Hertz is abbreviated to Hz.

9.5		196.0		253.0		360.0	
Hz	Amp.	Hz	Amp.	Hz	Amp.	Hz	Amp.
4883	$1.36\times10^{+3}$	4883	$2.16\times10^{+4}$	6103	$4.50\times10^{+3}$	3662	$1.57\times10^{+4}$
9766	$7.88\times10^{+3}$	8545	$4.11\times10^{+4}$	8545	$1.14\times10^{+3}$	7324	$2.28\times10^{+4}$
12207	$1.11\times10^{+3}$	10986	$1.86\times10^{+4}$	12207	$7.23\times10^{+3}$	9766	$8.26\times10^{+4}$
14648	$2.33\times10^{+3}$	12207	$1.35\times10^{+4}$	14648	$1.77\times10^{+3}$	13428	$1.34\times10^{+4}$
17089	$4.09\times10^{+3}$	14648	$1.24\times10^{+4}$	17089	$1.66\times10^{+3}$	15869	$3.99\times10^{+3}$
19531	$3.61\times10^{+3}$	18310	$1.12\times10^{+4}$	18310	$1.26\times10^{+3}$	19531	$3.58\times10^{+3}$
26855	$3.27\times10^{+3}$	21973	$1.83\times10^{+4}$	21973	$2.58\times10^{+3}$	21973	$1.43\times10^{+3}$
31738	$5.66\times10^{+3}$	26855	$1.08\times10^{+4}$	25635	$1.45\times10^{+3}$		
36621	$4.03\times10^{+3}$			28076	$1.60\times10^{+3}$		
46387	$1.90\times10^{+3}$			32959	$2.68\times10^{+3}$		
				39063	$1.54\times10^{+3}$		

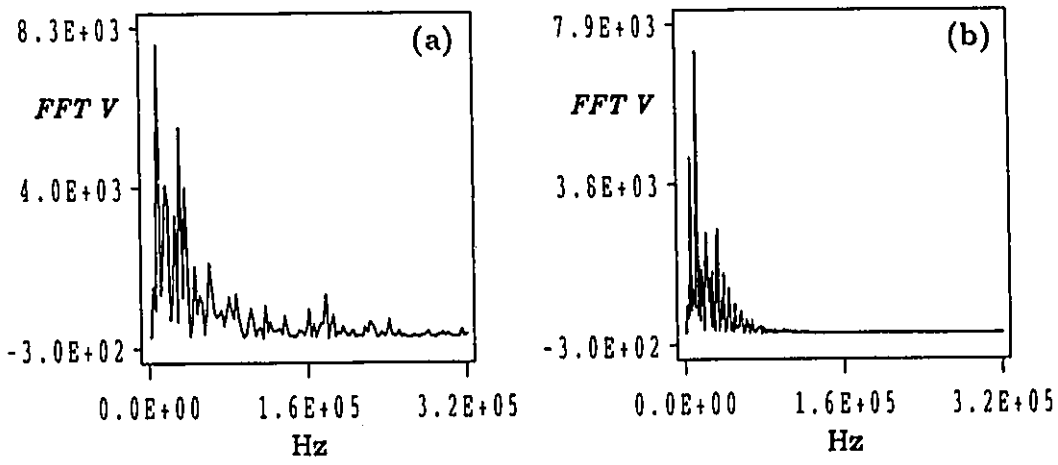

Figure 4.61 Plots of the FFT of schlieren millivolt signals for 0 to 320k Hz. (a) is for $p_0 = 9.5$ Torr of pure CCl_3F, (b) is for 253.0 Torr of a 25.05 % mixture of CCl_3F in Ar, $p_0 = 63.4$ Torr.

systems first, it can be seen that Figures 4.60(a) and (b) (9.5 and 196.0 Torr of pure CCl_3F) have similar peaks at 4883, 12207, 14648, and 26855 (see Table 4.8). Comparing Figures 4.60(b) and (c) (196.0 Torr of of pure CCl_3F and 253.0 Torr of a

25.05% mixture of CCl_3F in Ar), it can be seen that there are similar peaks at 8545, 12207, 14648, 18310, and 21973 (see Table 4.8). Comparing Figures 4.60(a) and (c), it can be seen that the similar peaks are at 12207, 14648, and 17089. Finally frequencies that are present in all three cases are, 12207, and 14648. Of course the amplitudes of the frequencies present in each of the three CCl_3F cases are NOT the same. This different weighting of the frequency components results in different waveforms as seen in the original figures (Figure 4.34(b), 4.38, and 4.43). However, the similar frequency components means that some features are expected to be similar even if at different amplitudes. For example the spikes present in Figure 4.43 are related to similar spikes in both 4.38 and 4.34(b).

Note that Berge *et al*[1] and Thompson *et al*[2] have shown that as a waveform becomes more aperiodic the distinct frequencies of an FFT disappear until eventually only a noisy sloped baseline is left. This is illustrated in Figure 4.61(a).

Figure 4.61(a) is for the same conditions as Figure 4.60(a) and Figure 4.61(b) is for the same conditions as Figure 4.60(c), but both are for abscissae of 0 to 320 kHz. Figure 4.61(a) shows that for the post shock conditions of 9.5 Torr of pure CCl_3F (T_e =468.96), there are a large number of higher frequencies present which is expected for the nonperiodic behaviour of the schlieren signal in Figure 4.34(b). Inspection of Figure 4.61(b), for the quieter case of 253.0 Torr of a 25.05 % mixture of CCl_3F in Ar (T_e = 335.96 Figure 4.43), shows that these higher frequency components are not present for the more well-behaved schlieren signal of Figure 4.43.

Although is has been shown that it is possible to extract characteristic frequencies from the present non-linear chemical reaction, interpretation of these frequencies in terms of rate coefficients for cluster formation and stabilization is the subject of another study[69].

4.7 Summary

The work that has been presented in this chapter on nonlinear kinetics has several components to it. The simulations basically prove that a model of cluster formation via addition of a vibrationally equilibrated monomer to an existing n-mer is workable. The calculated observable has the negative going shape expected from a system with heat release. The oscillations were shown to have a large dependence upon experimental conditions with the dilution parameter being able to turn the thermal feedback off and on.

A new data collection system has been described. This new system has improved the detection of the schlieren signal since the first stage of amplification is close to the photodiode quadrant array, thus increasing the signal-to-noise ratio. The new system allows each photodiode preamplifier to be disabled which makes sure that the signals do not interfere with each other. The system also increases the number of data points collected, and therefore the waveform is sampled at a much higher rate. With this new system comparison of data sets that have a velocities within 2%, and sometimes less, of each other is possible. This was not the case for the previous system. Another aspect of this data collection system is that, presently, three data sets are collected for each experiment.

The schlieren millivolt signals of shock compressed CCl_3F, pure and mixtures, show oscillatory, and chaotic behaviour as did the schlieren millivolts signals of shock compressed SF_6 and CCl_3H. Since the rate of heat release is related to the schlieren signal these oscillations or chaotic behaviour, are related to the rate of heat release. The model proposed in this work describes what occurs when a room temperature distribution of clusters (dimer to pentamer) is then heated suddenly to a new temperature. An irregular approach to a new Boltzmann distribution of clusters results.

Dilution with argon seems to switch off the thermal feedback in the simulations and explains why argon quiets down the schlieren signals.

A wavelet analysis of a schlieren millivolt signal was able to pick out the high frequency background present in the HeNe laser system used, but was not useful in doing an analysis of the low frequencies present in the signal. However, it was shown that under certain circumstances the wavelet analysis technique can be used to greatly reduce the amount of noise present in the schlieren millivolt signal.

The FFT analysis that was done indicated that there are several similar frequency components in three cases of CCl_3F with some similarity in the schlieren millivolt signals.

This work has shown that nonlinear effects are important in understanding the processes involved in cluster formation of CCl_3F.

Summarizing, it has been shown experimentally that shock compression of CCl_3F and other gases below their critical temperatures results in a quasi-periodic and/or chaotic approach to equilibrium. The sensitivity of the observations to initial conditions, and the effect of increasingly turning off the thermal feedback (by dilution with Ar), the sensitivity of the observations to extent from equilibrium (severity of shock), and the ability to model some of the instabilities numerically according to a nonlinear chemical scheme, all attest to the likelihood that the system studied experimentally (here CCl_3F cluster formation) is an example of nonlinear physico-chemical kinetics. It is an unusual example because transient decay is superimposed. "Chaotic approach to equilibrium" is a contradiction in terms. However, it must be noted that those chemical systems which are recognized as representing chaos (see reference 26 and others), and which do not approach equilibrium, actually are a manifestation of this apparent contradiction as well. It is only because such experiments are carried out in

flow systems (*i.e.* thermodynamically open systems) where reagents are constantly being replenished that they appear not to approach equilibrium. The same chemistry and rate equations would apply in a closed system such as ours, and should still be classified as chaotic. This question requires further study.

A Appendix A: Hartree Atomic Units

Atomic units, as set out by Hartree[4], are used throughout this work. Hartree was interested in a single electron "in a central non-Coulomb field of force" and so he set the values of mass, energy and charge to those of the electron. The result is that $\hbar$ is set to unity. The unit of energy is a Hartree which is exactly "twice the ionization energy of the normal state of the hydrogen atom"[4] (twice the Rydberg constant). This leads to a very simple way of determining the unit of time since $\hbar$ is energy times time; and since the energy is known, time can be calculated. The atomic unit of time is $2.418\ 884 \times 10^{-17}$ seconds, which is about 24.2 atto (10^{-18}) seconds. The unit of energy is 27.211 396 electron-volts and; in this case the velocity of light becomes 137.035 990 a.u.. This was important to Hartree, and he stated that this allowed a way to inform one of the effect of relativistic velocities. "For an atom of atomic number N, velocities (in atomic units) are of the order of N^2: so relativistic effects are of order $(N/137)^2$, and therefore are small for light atoms."[4] Hartree also noted that " it is not possible to choose a set of units so that the measures of c, $\hbar$, and e^2 are all unity."[4] Where e^2 is the square of the charge on the electron. Hartree also believed that this set of units was best since it was independent of the measured values and the inaccuracies of those measurements.

B Appendix B: The Effect of the Forcing Term

The forcing term used in this work is a harmonic function, $F\sin(\omega t)$. The derivatives of the sine function are well known. That is if $x = F\sin(\omega t)$, then the first four derivatives are, $x^{(1)} = F\cos(\omega t)\omega$, $x^{(2)} = -F\sin(\omega t)\omega^2$, $x^{(3)} = -F\cos(\omega t)\omega^3$ and $x^{(4)} = F\sin(\omega t)\omega^4$. Thus after four derivatives the cycle is complete and a positive sine function is produced and the general rule is $x^{(N)} = F\sin(\omega t)\omega^{(N)}$. In this appendix, the plots are similar to those in chapter 2 in that the higher derivative is plotted *versus* the lower derivative as in $x^{(N)} - x^{(N-1)}$.

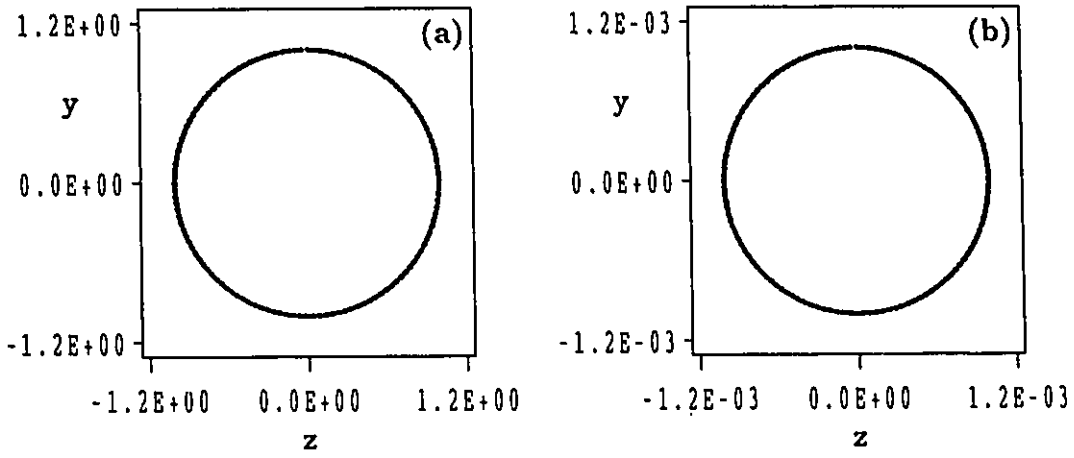

Figure B.1 A plot of $y = A_c\cos(\omega t)$ *versus* $z = A_s\sin(\omega t)$, where $A_c = F\omega^N$ and $A_s = F\omega^{N-1}$ with $N = 1$, $\omega = 1$ and $F = 1$ in (a) while $F = 10^{-3}$ in (b).

It is well know that the plot of a cosine function *versus* a sine function (or *vice versa*) produces a circular plot with a radius the size of the amplitude of the two functions. Therefore, if the amplitude is F, then the radius of the circle is F (see Figure B.1). The sign of the function determines in which quadrant the plotting starts. That is if both functions have positive magnitude the the plot starts in the $(+,+)$ quadrant, top right hand. If both have negative magnitude, $(-,-)$, the plot starts in the bottom left-hand quadrant. A plot of cosine *versus* sine is plotted in a

clockwise direction and a plot of sine *versus* cosine is plotted in a counter-clockwise direction. In these static plots the directional difference can not be realized and therefore the plots in this appendix are all of the cosine it versus the sine function.

Since $A_c = \mathrm{F}\omega^N$ is plotted *versus* $A_s = \mathrm{F}\omega^{N-1}$, as stated above the higher derivative is plotted *versus* the lower derivative, the y axis is affected more by the value of ω than the z axis is, except when $\omega = 1$ and then the axes scales are the same for any value of N. If $\omega < 1$ the axes are going to be smaller than if $\omega > 1$ since a number less than one, when taken to any non-negative power is smaller than one. So as the power of the forcing frequency is raised the magnitude of the axes involved will decrease dramatically.

Table B.1 Amplitude terms of cosine and sine forcing functions.See text.

F	ω	N	$A_c = \mathrm{F}\ \omega^N$	$A_s = \mathrm{F}\ \omega^{N-1}$
1	1	1	1	1
10^{-3}	1	1	10^{-03}	10^{-03}
10^{-3}	10^{-1}	1	10^{-04}	10^{-03}
10^{-3}	10^{-2}	1	10^{-05}	10^{-03}
10^{-3}	10^{-1}	3	10^{-06}	10^{-05}
10^{-3}	10^{-2}	3	10^{-09}	10^{-07}
10^{-3}	10^{-1}	9	10^{-12}	10^{-11}
10^{-3}	10^{-2}	9	10^{-21}	10^{-19}

In chapter one the Morse equation of motion was stated in equation [1.32] and it is already a second derivative with respect to time. If the α parameter of equation [1.32] is set to zero, the forcing term is the same as used here and no derivative has been taken. When the fifth derivative of the Morse equation is discussed that is actually only the third derivative of the forcing term and the eleventh derivative of the Morse equation of motion is only the ninth derivative of the forcing term. In this

appendix those are $N = 3$ and $N = 9$ respectively. The amplitudes resulting from changes of F, N, and ω are tabulated in Table B.1.

Looking at row 1 and 2 of Table B.1 it can be seen that with $N = 1$ and $\omega = 1$ the value of A_c or A_s is directly dependent upon F. However, in row 3 and 4 of Table B.1 with F the same as in row 1 and 2, but $\omega = 0.1$ in row 3 and 0.01 in row 4, it can be seen that A_c is much more affected by ω than is A_s. Next in row 5 and 6 of Table B.1 N has be changed from 1 to 3 while F is the same and ω is again 0.1 and 0.01 respectively. Again there are dramatic changes but now these are due to increasing the power that the forcing frequency, ω, is taken to. Comparison of row 3 and 5 of Table B.1 shows a change of 2 orders of magnitude for both A_c and A_s. This is exactly the increase of the power, N. Comparison of row 4 and 6 of Table B.1 ($\omega = 0.01$) shows an increase of both A_c and A_s by 4 orders of magnitude. This is again due to ω^2 with $\omega = 0.01$. The last two rows of Table B.1 are for $N = 9$, F the same at 10^{-3}, and $\omega = 0.1$ and 0.01, respectively. These results illustrate the affect that increasing N to 9 has on the amplitude of A_c and A_s.

For HF parameters, $\omega = (1.791\ 735 \times 10^{-2}$, F $= (1.067\ 605 \times 10^{-3})$ and the dipole moment factor is (0.29769). For $N = 3$ the amplitude for the y axis is $1.828\ 084 \times 10^{-09}$ and for the z axis is $1.020\ 287 \times 10^{-07}$. Which would be the expected scales of the plot for the Morse fifth-order phase plot. For $N = 9$ the amplitude for the y axis is $6.048\ 327 \times 10^{-20}$ and for the z axis $3.375\ 709 \times 10^{-18}$. Which would be the expected amplitudes for the eleventh-order phase plot of the Morse oscillator.

Therefore by using a change of variable and scaling time to get t' and a forcing frequency ω' these complications are avoided. Yes some information is lost but as seen at the end of the chapter on higher-order phase plots the global behaviour is as expected. At some point in the future further work could be done to investigate this complicated behaviour.

C Appendix C: The Optodetector Schematics

The following diagrams outline the schematics for the new photodetection system. There are schematics for the preamplifier boards, the mixing board, and the timing circuit on the mixing board.

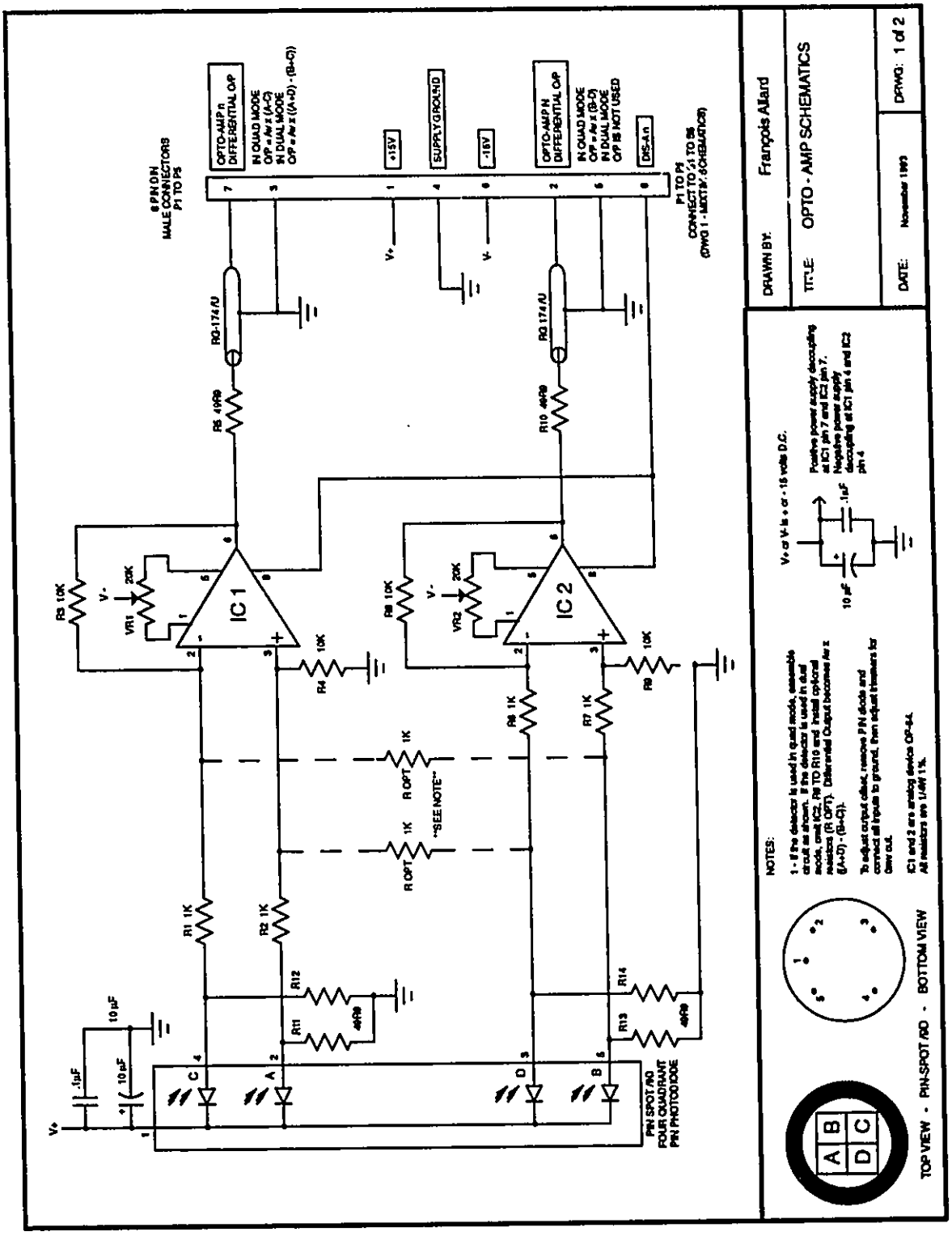

Figure C.1 OPTO-AMP schematic for the preamplifier circuit.

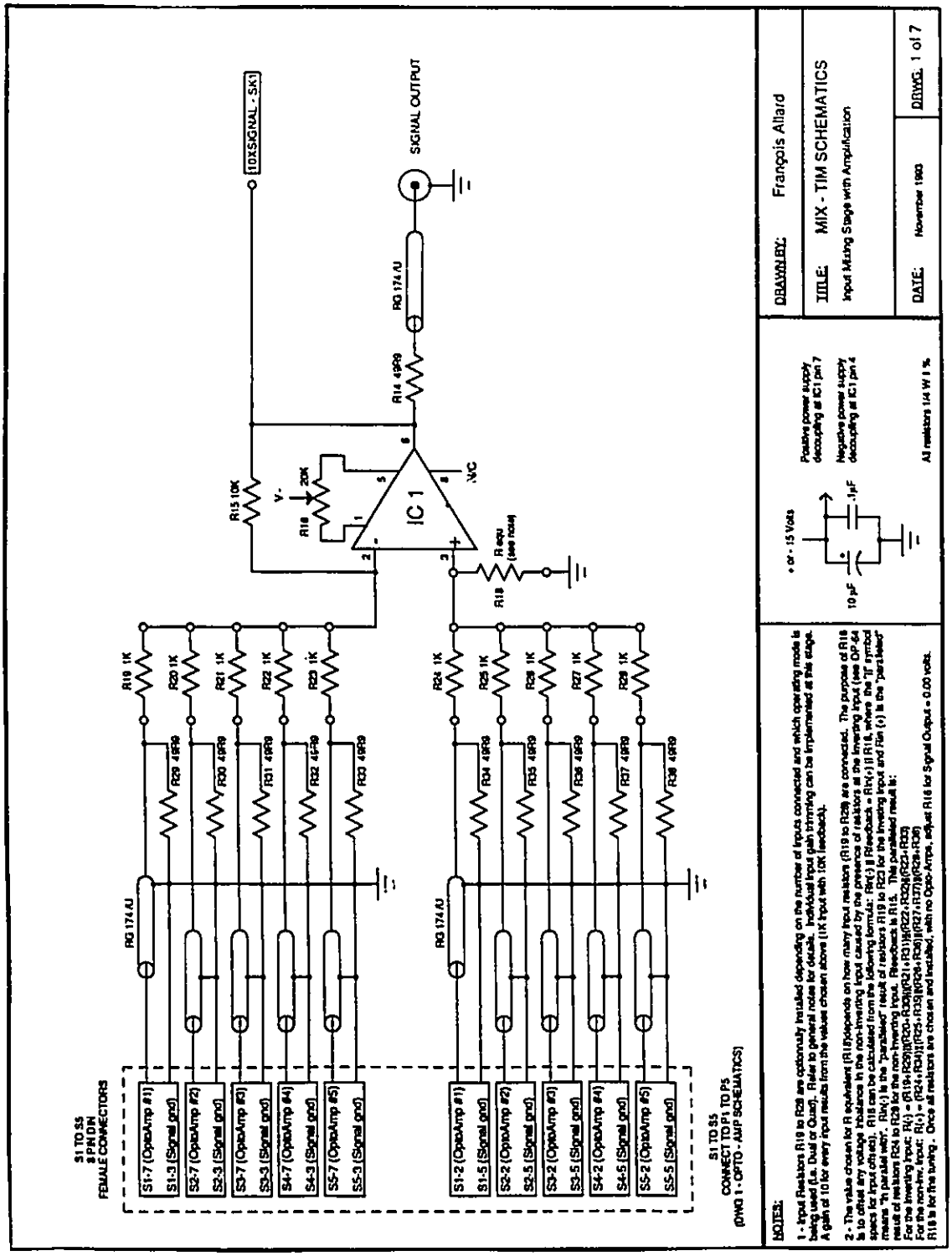

Figure C.2 OPTO-AMP schematic for the input to the mixing ciruit board.

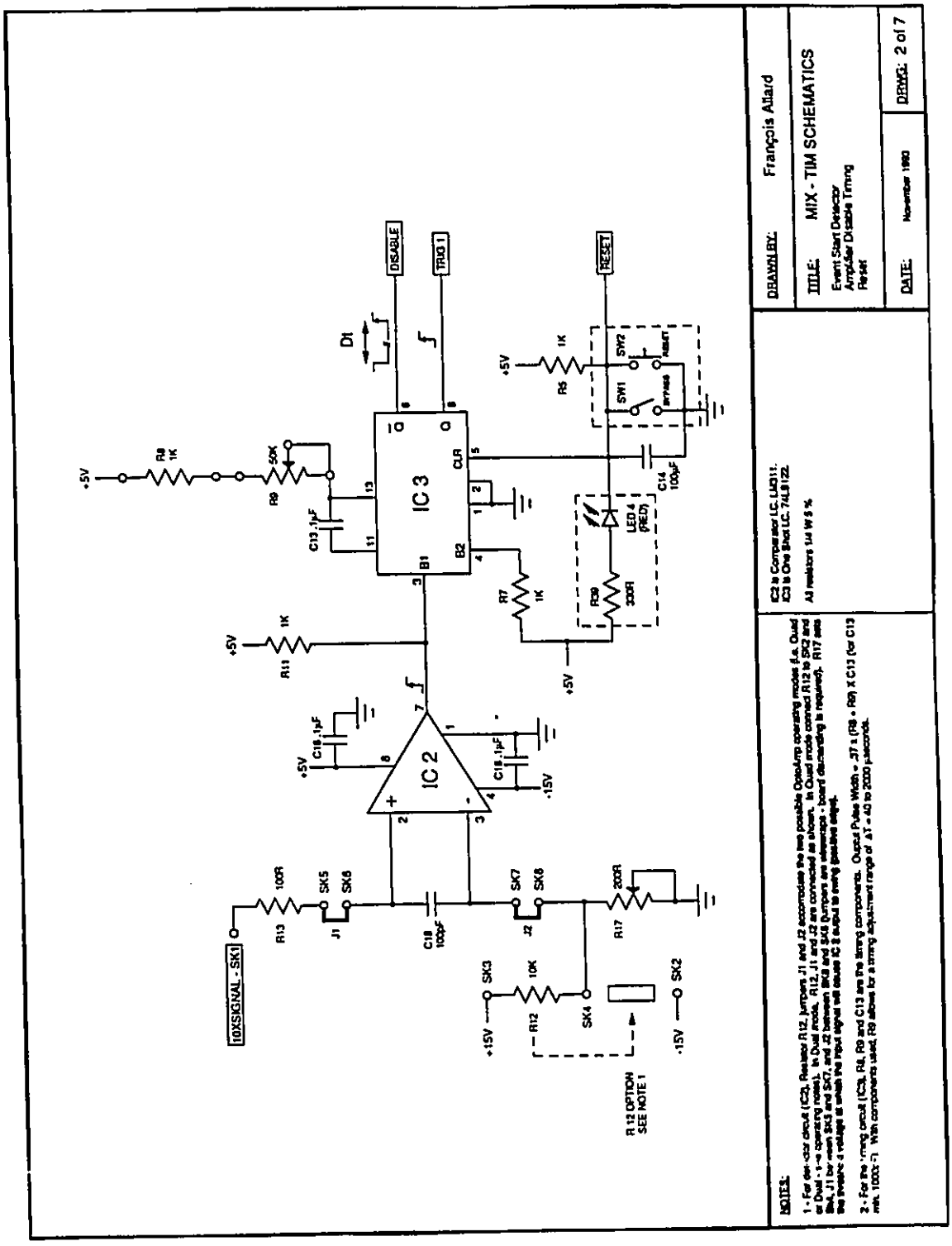

Figure C.3 OPTO-AMP schematic for the timing ciruit.

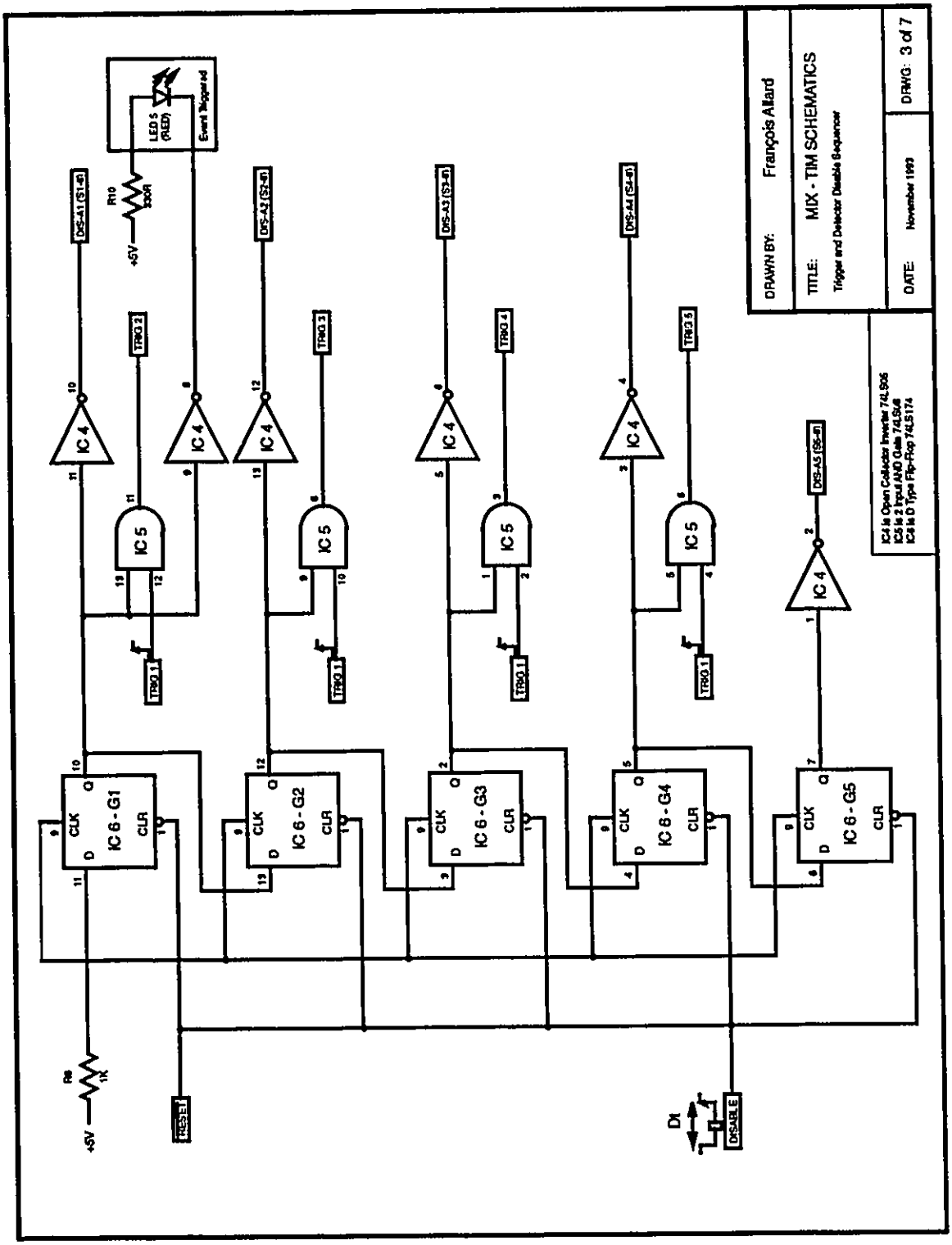

Figure C.4 OPTO-AMP schematic for the logic ciruit for disable signal.

D Appendix D: Fortran Code

All of the Fortran code presented in this chapter, and used in this work, was run on an IBM mainframe or an IBM mainframe-clone (Amdhal). This requires that an *.exec file be used to define the filenames that are related to the file numbers used in the code. Also, this work uses IMSL libraries and subroutines licensed to the University of Ottawa. The Gear integrator complete with its set up routines as well as the FFT routines are examples of such routines. These routines could be replaced by *Numerical Recipes*[81] routines but this work has not used them. The wavelet code[81] used in this work is not listed here, since the copyright is retained by Froment and Mallat, but it is available from the ftp node stated in reference 81.

D.1 Morse Oscillator Code

```
      INTEGER        NEQ,NPARM,IDO,IEND,IMETH,INORM,NOUT,KSTEP,KIIN,IIN
      PARAMETER      (NEQ=2, NPARM=50)
      DOUBLE PRECISION A(1,1),HINIT,PARM(NPARM),Y(NEQ),STEP,YINIT1,XO,
     1YPRIME(NEQ),X,SK,C,MFDX(11),TOL,XEND,H,AE,D,F,V,YINIT2
      COMMON SK,C,AE,D,F
      EXTERNAL       FCN,FCNJ,FCNP,DIVPAG,SSET
      READ(4,106) YINIT1,YINIT2,STEP,XO,SK,C,KSTEP,TOL,AE,D,F
C 106 FORMAT(6E11.3,I6,E8.0)
C     KSTEP   = 2*KSTEP
      IF (STEP.EQ.3.142D0) THEN
       STEP=4.D0*DATAN(1.0D0)
         WRITE(6,*) STEP
      END IF
      Y(1)    = YINIT1
      YINIT2=YINIT2-D*(1.D0-DEXP(-AE*Y(1)))**2
      Y(2)    = -DSQRT(2*SK*D*YINIT2)
C     TOL     = 1.0D-6
      HINIT   = TOL
      IMETH   = 1
      INORM   = 2
      IDO     = 1
      CALL SSET (NPARM, 0.0, PARM, 1)
      PARM(1) = HINIT
      PARM(4) = 1.D+3*KSTEP
      PARM(10)= INORM
      PARM(12)= IMETH
      X       = XO
      XEND    = XO
      IIN     = 0
      KIIN    = KSTEP/10
      DO 10 K=1,KSTEP
          XEND = XEND+STEP
      CALL DIVPAG (IDO,NEQ,FCN,FCNJ,AE,X,XEND,TOL,PARM,Y)
      CALL FCN (NEQ,X,Y,YPRIME)
      CALL FCNP (NEQ,X,Y,YPRIME,MFDX)
C      V  =  D*(1.D0-DEXP(-AE*Y(1)))**2
C I JUST USED THE SAME SYMBOL AS BEFORE BUT NOW THIS SHOULD BE
C THE TOTAL ENERGY.
       V  =  D*(1.D0-DEXP(-AE*Y(1)))**2  + Y(2)**2/(2.D0)
      WRITE(7,100) Y(1),Y(2),YPRIME(2),MFDX(3),MFDX(4),MFDX(5),X
```

```
C     WRITE(9,100) MFDX(6),MFDX(7),MFDX(8),MFDX(9),MFDX(10),MFDX(11),X
C     WRITE(5,101) V,Y(1)
      WRITE(5,101) V,X
        IIN = IIN + 1
       IF (IIN.EQ.KIIN) THEN
         WRITE(6,*) K
         IIN = 0
       END IF
  100 FORMAT(7D14.6)
  101 FORMAT(2D14.6)
  106 FORMAT(6E11.3,I6,E8.0,3E11.3)
 1000 FORMAT(1D15.12)
   10 CONTINUE
C
      STOP
      END
      SUBROUTINE       FCN (NEQ,X,Y,YPRIME)
      INTEGER          NEQ
      DOUBLE PRECISION Y(NEQ),YPRIME(NEQ),X,SK,C,AE,D,F
      COMMON SK,C,AE,D,F
      X = X
      YPRIME(1) = Y(2)
      YPRIME(2) = -C*Y(2)
     1- 2.D0*SK*D*AE*(1.D0 - DEXP(-AE*Y(1)))*DEXP(-AE*Y(1))
     1+ F*DSIN(X)
      RETURN
      END
C
      SUBROUTINE       FCNJ (NEQ,X,Y,DYPDY)
      INTEGER          NEQ
      DOUBLE PRECISION Y(NEQ),DYPDY(NEQ,NEQ),X
      RETURN
      END
C
      SUBROUTINE       FCNP (NEQ,X,Y,YPRIME,MFDX)
      INTEGER          NEQ
      DOUBLE PRECISION Y(NEQ),YPRIME(NEQ),X,SK,C,MFDX(11),AE,D,F
      COMMON SK,C,AE,D,F
      X = X
      MFDX(1) = Y(2)
      MFDX(2) = YPRIME(2)
      MFDX(3)  = - C*MFDX(2)
     1- 2.D0*SK*D*AE**2*MFDX(1)*DEXP(-2.D0*AE*Y(1))
     1+ 2.D0*SK*D*AE**2*(1.D0 - DEXP(-AE*Y(1)))*MFDX(1)*DEXP(-AE*Y(1))
     1+ F*DCOS(X)
      MFDX(4)  = - C*MFDX(3)
     1- 2.D0*SK*D*AE**2*MFDX(2)*DEXP(-2.D0*AE*Y(1))
     1+ 6.D0*SK*D*AE**3*MFDX(1)**2*DEXP(-2.D0*AE*Y(1))
     1+ 2.D0*SK*D*AE**2*(1.D0 - DEXP(-AE*Y(1)))*MFDX(2)*DEXP(-AE*Y(1))
     1- 2.D0*SK*D*AE**3*(1.D0
     1- DEXP(-AE*Y(1)))*MFDX(1)**2*DEXP(-AE*Y(1))
     1- F*DSIN(X)
      MFDX(5)  = - C*MFDX(4)
     1- 2.D0*SK*D*AE**2*MFDX(3)*DEXP(-2.D0*AE*Y(1))
     1+ 18.D0*SK*D*AE**3*MFDX(2)*DEXP(-2.D0*AE*Y(1))*MFDX(1)
     1- 14.D0*SK*D*AE**4*MFDX(1)**3*DEXP(-2.D0*AE*Y(1))
     1+ 2.D0*SK*D*AE**2*(1.D0 - DEXP(-AE*Y(1)))*MFDX(3)*DEXP(-AE*Y(1))
     1- 6.D0*SK*D*AE**3*(1.D0
     1- DEXP(-AE*Y(1)))*MFDX(2)*MFDX(1)*DEXP(-AE*Y(1))
     1+ 2.D0*SK*D*AE**4*(1.D0
     1- DEXP(-AE*Y(1)))*MFDX(1)**3*DEXP(-AE*Y(1))
     1- F*DCOS(X)
C
       MFDX(6)= - C*MFDX(5)
     1 - 2.D0*SK*D*AE**2*MFDX(4)*DEXP(-2.D0*AE*Y(1))
     1+ 24.D0*SK*D*AE**3*MFDX(3)*DEXP(-2.D0*AE*Y(1))*MFDX(1)
     1- 84.D0*SK*D*AE**4*MFDX(2)*DEXP(-2.D0*AE*Y(1))*MFDX(1)**2
     1+ 18.D0*SK*D*AE**3*MFDX(2)**2*DEXP(-2.D0*AE*Y(1))
     1+ 30.D0*SK*D*AE**5*MFDX(1)**4*DEXP(-2.D0*AE*Y(1))
     1+ 2.D0*SK*D*AE**2*(1.D0 - DEXP(-AE*Y(1)))*MFDX(4)*DEXP(-AE*Y(1))
     1- 8.D0*SK*D*AE**3*(1.D0
     1- DEXP(-AE*Y(1)))*MFDX(3)*MFDX(1)*DEXP(-AE*Y(1))
     1- 6.D0*SK*D*AE**3*(1.D0
```

```
1- DEXP(-AE*Y(1)))*MFDX(2)**2*DEXP(-AE*Y(1))
1+ 12.D0*SK*D*AE**4*(1.D0
1- DEXP(-AE*Y(1)))*MFDX(2)*MFDX(1)**2*DEXP(-AE*Y(1))
1- 2.D0*SK*D*AE**5*(1.D0
1- DEXP(-AE*Y(1)))*MFDX(1)**4*DEXP(-AE*Y(1)) + F*DSIN(X)
  MFDX(7)= 2.D0*SK*D*AE**2*(1.D0
1- DEXP(-AE*Y(1)))*MFDX(5)*DEXP(-AE*Y(1))
1- 10.D0*SK*D*AE**3*(1.D0
1- DEXP(-AE*Y(1)))*MFDX(4)*MFDX(1)*DEXP(-AE*Y(1))
1- 20.D0*SK*D*AE**3*(1.D0
1- DEXP(-AE*Y(1)))*MFDX(3)*MFDX(2)*DEXP(-AE*Y(1))
1+ 20.D0*SK*D*AE**4*(1.D0
1- DEXP(-AE*Y(1)))*MFDX(3)*MFDX(1)**2*DEXP(-AE*Y(1))
1+ 30.D0*SK*D*AE**4*(1.D0
1- DEXP(-AE*Y(1)))*MFDX(2)**2*MFDX(1)*DEXP(-AE*Y(1))
1- 20.D0*SK*D*AE**5*(1.D0
1- DEXP(-AE*Y(1)))*MFDX(2)*MFDX(1)**3*DEXP(-AE*Y(1))
1+ 2.D0*SK*D*AE**6*(1.D0
1- DEXP(-AE*Y(1)))*MFDX(1)**5*DEXP(-AE*Y(1))
1- 2.D0*SK*D*AE**2*MFDX(5)*DEXP(-2.D0*AE*Y(1))
1+ 30.D0*SK*D*AE**3*MFDX(4)*DEXP(-2.D0*AE*Y(1))*MFDX(1)
1+ 60.D0*SK*D*AE**3*MFDX(3)*DEXP(-2.D0*AE*Y(1))*MFDX(2)
1- 140.D0*SK*D*AE**4*MFDX(3)*DEXP(-2.D0*AE*Y(1))*MFDX(1)**2
  MFDX(7) = MFDX(7)
1- 210.D0*SK*D*AE**4*MFDX(2)**2*DEXP(-2.D0*AE*Y(1))*MFDX(1)
1+ 300.D0*SK*D*AE**5*MFDX(2)*DEXP(-2.D0*AE*Y(1))*MFDX(1)**3
1- 62.D0*SK*D*AE**6*MFDX(1)**5*DEXP(-2.D0*AE*Y(1))
1+ F*DCOS(X) - C*MFDX(6)
  MFDX(8) = - 210.D0*SK*D*AE**4*MFDX(2)**3*DEXP(-2.D0*AE*Y(1))
1+ 30.D0*SK*D*AE**6*(1.D0
1- DEXP(-AE*Y(1)))*MFDX(2)*MFDX(1)**4*DEXP(-AE*Y(1))
1+ 126.D0*SK*D*AE**7*MFDX(1)**6*DEXP(-2.D0*AE*Y(1))
1- 2.D0*SK*D*AE**7*(1.D0
1- DEXP(-AE*Y(1)))*MFDX(1)**6*DEXP(-AE*Y(1))
1- 2.D0*SK*D*AE**2*MFDX(6)*DEXP(-2.D0*AE*Y(1))
1+ 90.D0*SK*D*AE**3*MFDX(4)*DEXP(-2.D0*AE*Y(1))*MFDX(2)
1+ 60.D0*SK*D*AE**3*MFDX(3)**2*DEXP(-2.D0*AE*Y(1))
1+ 2.D0*SK*D*AE**2*(1.D0 - DEXP(-AE*Y(1)))*MFDX(6)*DEXP(-AE*Y(1))
1+ 36.D0*SK*D*AE**3*MFDX(1)*DEXP(-2.D0*AE*Y(1))*MFDX(5)
1- 12.D0*SK*D*AE**3*(1.D0
1- DEXP(-AE*Y(1)))*MFDX(5)*MFDX(1)*DEXP(-AE*Y(1))
1- 30.D0*SK*D*AE**3*(1.D0
1- DEXP(-AE*Y(1)))*MFDX(4)*MFDX(2)*DEXP(-AE*Y(1))
1- 210.D0*SK*D*AE**4*MFDX(1)**2*DEXP(-2.D0*AE*Y(1))*MFDX(4)
  MFDX(8) =MFDX(8)
1+ 30.D0*SK*D*AE**4*(1.D0
1- DEXP(-AE*Y(1)))*MFDX(4)*MFDX(1)**2*DEXP(-AE*Y(1))
1- 20.D0*SK*D*AE**3*(1.D0
1- DEXP(-AE*Y(1)))*MFDX(3)**2*DEXP(-AE*Y(1))
1- 840.D0*SK*D*AE**4*MFDX(1)*DEXP(-2.D0*AE*Y(1))*MFDX(3)*MFDX(2)
1+ 120.D0*SK*D*AE**4*(1.D0
1- DEXP(-AE*Y(1)))*MFDX(3)*MFDX(2)*MFDX(1)*DEXP(-AE*Y(1))
1+ 600.D0*SK*D*AE**5*MFDX(1)**3*DEXP(-2.D0*AE*Y(1))*MFDX(3)
1- 40.D0*SK*D*AE**5*(1.D0
1- DEXP(-AE*Y(1)))*MFDX(3)*MFDX(1)**3*DEXP(-AE*Y(1))
1+ 30.D0*SK*D*AE**4*(1.D0
1- DEXP(-AE*Y(1)))*MFDX(2)**3*DEXP(-AE*Y(1))
1+ 1350.D0*SK*D*AE**5*MFDX(1)**2*DEXP(-2.D0*AE*Y(1))*MFDX(2)**2
1- 90.D0*SK*D*AE**5*(1.D0
1- DEXP(-AE*Y(1)))*MFDX(2)**2*MFDX(1)**2*DEXP(-AE*Y(1))
1- 930.D0*SK*D*AE**6*MFDX(1)**4*DEXP(-2.D0*AE*Y(1))*MFDX(2)
1- C*MFDX(7) - F*DSIN(X)
  MFDX(9) = + 140.D0*SK*D*AE**4*(1.D0
1- DEXP(-AE*Y(1)))*MFDX(3)**2*MFDX(1)*DEXP(-AE*Y(1))
1+6300.D0*SK*D*AE**5*MFDX(1)**2*DEXP(-2.D0*AE*Y(1))*MFDX(3)*MFDX(2)
1- C*MFDX(8)
1- 70.D0*SK*D*AE**5*(1.D0
1- DEXP(-AE*Y(1)))*MFDX(4)*MFDX(1)**3*DEXP(-AE*Y(1))
1+ 1050.D0*SK*D*AE**5*MFDX(1)**3*DEXP(-2.D0*AE*Y(1))*MFDX(4)
1+ 210.D0*SK*D*AE**4*(1.D0
1- DEXP(-AE*Y(1)))*MFDX(4)*MFDX(2)*MFDX(1)*DEXP(-AE*Y(1))
1- 70.D0*SK*D*AE**3*(1.D0
1- DEXP(-AE*Y(1)))*MFDX(4)*MFDX(3)*DEXP(-AE*Y(1))
```

```
1- 42.D0*SK*D*AE**3*(1.D0
1- DEXP(-AE*Y(1)))*MFDX(5)*MFDX(2)*DEXP(-AE*Y(1))
1+ 42.D0*SK*D*AE**4*(1.D0
1- DEXP(-AE*Y(1)))*MFDX(5)*MFDX(1)**2*DEXP(-AE*Y(1))
1- 14.D0*SK*D*AE**3*(1.D0
1- DEXP(-AE*Y(1)))*MFDX(6)*MFDX(1)*DEXP(-AE*Y(1))
1+ 2.D0*SK*D*AE**2*(1.D0 - DEXP(-AE*Y(1)))*MFDX(7)*DEXP(-AE*Y(1))
1- 980.D0*SK*D*AE**4*MFDX(3)**2*DEXP(-2.D0*AE*Y(1))*MFDX(1)
  MFDX(9) =MFDX(9)
1- 294.D0*SK*D*AE**4*MFDX(1)**2*DEXP(-2.D0*AE*Y(1))*MFDX(5)
1- 1470.D0*SK*D*AE**4*MFDX(4)*DEXP(-2.D0*AE*Y(1))*MFDX(2)*MFDX(1)
1+ 126.D0*SK*D*AE**3*MFDX(5)*DEXP(-2.D0*AE*Y(1))*MFDX(2)
1+ 210.D0*SK*D*AE**3*MFDX(4)*DEXP(-2.D0*AE*Y(1))*MFDX(3)
1+ 42.D0*SK*D*AE**3*MFDX(6)*DEXP(-2.D0*AE*Y(1))*MFDX(1)
1+ 2.D0*SK*D*AE**8*(1.D0
1- DEXP(-AE*Y(1)))*MFDX(1)**7*DEXP(-AE*Y(1))
1- 2.D0*SK*D*AE**2*MFDX(7)*DEXP(-2.D0*AE*Y(1))
1- 254.D0*SK*D*AE**8*MFDX(1)**7*DEXP(-2.D0*AE*Y(1))
1- 42.D0*SK*D*AE**7*(1.D0
1- DEXP(-AE*Y(1)))*MFDX(2)*MFDX(1)**5*DEXP(-AE*Y(1))
1+ 2646.D0*SK*D*AE**7*MFDX(1)**5*DEXP(-2.D0*AE*Y(1))*MFDX(2)
1+ 70.D0*SK*D*AE**6*(1.D0
1- DEXP(-AE*Y(1)))*MFDX(3)*MFDX(1)**4*DEXP(-AE*Y(1))
1+ 210.D0*SK*D*AE**6*(1.D0
1- DEXP(-AE*Y(1)))*MFDX(2)**2*MFDX(1)**3*DEXP(-AE*Y(1))
1- 1470.D0*SK*D*AE**4*MFDX(2)**2*DEXP(-2.D0*AE*Y(1))*MFDX(3)
1+ 3150.D0*SK*D*AE**5*MFDX(2)**3*DEXP(-2.D0*AE*Y(1))*MFDX(1)
  MFDX(9) = MFDX(9)
1- 6510.D0*SK*D*AE**6*MFDX(1)**3*DEXP(-2.D0*AE*Y(1))*MFDX(2)**2
1- 210.D0*SK*D*AE**5*(1.D0
1- DEXP(-AE*Y(1)))*MFDX(2)**3*MFDX(1)*DEXP(-AE*Y(1))
1- 420.D0*SK*D*AE**5*(1.D0
1- DEXP(-AE*Y(1)))*MFDX(3)*MFDX(2)*MFDX(1)**2*DEXP(-AE*Y(1))
1- F*DCOS(X)
1- 2170.D0*SK*D*AE**6*MFDX(1)**4*DEXP(-2.D0*AE*Y(1))*MFDX(3)
1+ 210.D0*SK*D*AE**4*(1.D0
1- DEXP(-AE*Y(1)))*MFDX(3)*MFDX(2)**2*DEXP(-AE*Y(1))
  MFDX(10) = 840.D0*SK*D*AE**6*(1.D0
1- DEXP(-AE*Y(1)))*MFDX(2)**3*MFDX(1)**2*DEXP(-AE*Y(1))
1+ 3150.D0*SK*D*AE**5*MFDX(2)**4*DEXP(-2.D0*AE*Y(1))
1- 26040.D0*SK*D*AE**6*MFDX(2)**3*DEXP(-2.D0*AE*Y(1))*MFDX(1)**2
1- 1680.D0*SK*D*AE**5*(1.D0
1- DEXP(-AE*Y(1)))*MFDX(2)**2*MFDX(1)*DEXP(-AE*Y(1))*MFDX(3)
1- 210.D0*SK*D*AE**5*(1.D0
1- DEXP(-AE*Y(1)))*MFDX(2)**4*DEXP(-AE*Y(1))
1+ 510.D0*SK*D*AE**9*MFDX(1)**8*DEXP(-2.D0*AE*Y(1))
1- 2.D0*SK*D*AE**9*(1.D0
1- DEXP(-AE*Y(1)))*MFDX(1)**8*DEXP(-AE*Y(1))
1- 2.D0*SK*D*AE**2*MFDX(8)*DEXP(-2.D0*AE*Y(1))
1- 7112.D0*SK*D*AE**8*MFDX(1)**6*DEXP(-2.D0*AE*Y(1))*MFDX(2)
1- 112.D0*SK*D*AE**7*(1.D0
1- DEXP(-AE*Y(1)))*MFDX(3)*MFDX(1)**5*DEXP(-AE*Y(1))
1- 420.D0*SK*D*AE**7*(1.D0
1- DEXP(-AE*Y(1)))*MFDX(2)**2*MFDX(1)**4*DEXP(-AE*Y(1))
1+ 26460.D0*SK*D*AE**7*MFDX(1)**4*DEXP(-2.D0*AE*Y(1))*MFDX(2)**2
1+ 7056.D0*SK*D*AE**7*MFDX(1)**5*DEXP(-2.D0*AE*Y(1))*MFDX(3)
  MFDX(10)=MFDX(10)
1+ 1120.D0*SK*D*AE**6*(1.D0
1- DEXP(-AE*Y(1)))*MFDX(3)*MFDX(1)**3*DEXP(-AE*Y(1))*MFDX(2)
1- 3920.D0*SK*D*AE**4*MFDX(3)**2*DEXP(-2.D0*AE*Y(1))*MFDX(2)
1- 2940.D0*SK*D*AE**4*MFDX(4)*DEXP(-2.D0*AE*Y(1))*MFDX(2)**2
1+ 168.D0*SK*D*AE**3*MFDX(6)*DEXP(-2.D0*AE*Y(1))*MFDX(2)
1+ 336.D0*SK*D*AE**3*MFDX(5)*DEXP(-2.D0*AE*Y(1))*MFDX(3)
1+ 210.D0*SK*D*AE**3*MFDX(4)**2*DEXP(-2.D0*AE*Y(1))
1+ 56.D0*SK*D*AE**8*(1.D0
1- DEXP(-AE*Y(1)))*MFDX(1)**6*DEXP(-AE*Y(1))*MFDX(2)
1+ 2.D0*SK*D*AE**2*(1.D0 - DEXP(-AE*Y(1)))*MFDX(8)*DEXP(-AE*Y(1))
1+ 48.D0*SK*D*AE**3*MFDX(1)*DEXP(-2.D0*AE*Y(1))*MFDX(7)
1+ 336.D0*SK*D*AE**4*(1.D0
1- DEXP(-AE*Y(1)))*MFDX(5)*MFDX(2)*MFDX(1)*DEXP(-AE*Y(1))
1+ 420.D0*SK*D*AE**4*(1.D0
1- DEXP(-AE*Y(1)))*MFDX(4)*MFDX(2)**2*DEXP(-AE*Y(1))
1- 112.D0*SK*D*AE**3*(1.D0
```

```
1- DEXP(-AE*Y(1)))*MFDX(5)*MFDX(3)*DEXP(-AE*Y(1))
  MFDX(10)=MFDX(10)
1- 70.D0*SK*D*AE**3*(1.D0
1- DEXP(-AE*Y(1)))*MFDX(4)**2*DEXP(-AE*Y(1))
1- 3920.D0*SK*D*AE**4*MFDX(1)*DEXP(-2.D0*AE*Y(1))*MFDX(4)*MFDX(3)
1- 56.D0*SK*D*AE**3*(1.D0
1- DEXP(-AE*Y(1)))*MFDX(6)*MFDX(2)*DEXP(-AE*Y(1))
1- 2352*SK*D*AE**4*MFDX(1)*DEXP(-2.D0*AE*Y(1))*MFDX(5)*MFDX(2)
1+ 56.D0*SK*D*AE**4*(1.D0
1- DEXP(-AE*Y(1)))*MFDX(6)*MFDX(1)**2*DEXP(-AE*Y(1))
1- 16.D0*SK*D*AE**3*(1.D0
1- DEXP(-AE*Y(1)))*MFDX(7)*MFDX(1)*DEXP(-AE*Y(1))
1- 392.D0*SK*D*AE**4*MFDX(1)**2*DEXP(-2.D0*AE*Y(1))*MFDX(6)
1+ 1680.D0*SK*D*AE**5*MFDX(1)**3*DEXP(-2.D0*AE*Y(1))*MFDX(5)
1- 34720.D0*SK*D*AE**6*MFDX(1)**3*
1DEXP(-2.D0*AE*Y(1))*MFDX(3)*MFDX(2)
1- 112.D0*SK*D*AE**5*(1.D0
1- DEXP(-AE*Y(1)))*MFDX(5)*MFDX(1)**3*DEXP(-AE*Y(1))
  MFDX(10) = MFDX(10)
1- 840.D0*SK*D*AE**5*(1.D0
1- DEXP(-AE*Y(1)))*MFDX(4)*MFDX(1)**2*DEXP(-AE*Y(1))*MFDX(2)
1- 4340.D0*SK*D*AE**6*MFDX(1)**4*DEXP(-2.D0*AE*Y(1))*MFDX(4)
1+ 140.D0*SK*D*AE**6*(1.D0
1- DEXP(-AE*Y(1)))*MFDX(4)*MFDX(1)**4*DEXP(-AE*Y(1))
1- 560.D0*SK*D*AE**5*(1.D0
1- DEXP(-AE*Y(1)))*MFDX(3)**2*MFDX(1)**2*DEXP(-AE*Y(1))
1+ 25200.D0*SK*D*AE**5*MFDX(1)*DEXP(-2.D0*AE*Y(1))*
1MFDX(3)*MFDX(2)**2
1+ 12600.D0*SK*D*AE**5*MFDX(1)**2*DEXP(-2.D0*AE*Y(1))*
1MFDX(4)*MFDX(2)
1+ 560.D0*SK*D*AE**4*(1.D0
1- DEXP(-AE*Y(1)))*MFDX(3)*MFDX(1)*DEXP(-AE*Y(1))*MFDX(4)
1+ 560.D0*SK*D*AE**4*(1.D0
1- DEXP(-AE*Y(1)))*MFDX(3)**2*MFDX(2)*DEXP(-AE*Y(1))
1+ 8400.D0*SK*D*AE**5*MFDX(1)**2*DEXP(-2.D0*AE*Y(1))*MFDX(3)**2
1- C*MFDX(9) + F*DSIN(X)
  MFDX(11) = 560.D0*SK*D*AE**4*(1.D0
1- DEXP(-AE*Y(1)))*MFDX(3)**3*DEXP(-AE*Y(1)) - C*MFDX(10)
1+ 252.D0*SK*D*AE**6*(1.D0
1- DEXP(-AE*Y(1)))*MFDX(5)*MFDX(1)**4*DEXP(-AE*Y(1))
1- 2520.D0*SK*D*AE**5*(1.D0
1- DEXP(-AE*Y(1)))*MFDX(4)*MFDX(1)**2*DEXP(-AE*Y(1))*MFDX(3)
1- 7812.D0*SK*D*AE**6*MFDX(1)**4*DEXP(-2.D0*AE*Y(1))*MFDX(5)
1- 78120.D0*SK*D*AE**6*MFDX(1)**3*DEXP(-2.D0*AE*Y(1))*
1MFDX(4)*MFDX(2)
1- 52080.D0*SK*D*AE**6*MFDX(1)**3*DEXP(-2.D0*AE*Y(1))*MFDX(3)**2
1+ 630.D0*SK*D*AE**4*(1.D0
1- DEXP(-AE*Y(1)))*MFDX(4)**2*MFDX(1)*DEXP(-AE*Y(1))
1+ 37800.D0*SK*D*AE**5*MFDX(1)**2*DEXP(-2.D0*AE*Y(1))*
1MFDX(4)*MFDX(3)
1- 72.D0*SK*D*AE**3*(1.D0
1- DEXP(-AE*Y(1)))*MFDX(7)*MFDX(2)*DEXP(-AE*Y(1))
1+72.D0*SK*D*AE**4*(1.D0
1- DEXP(-AE*Y(1)))*MFDX(7)*MFDX(1)**2*DEXP(-AE*Y(1))
1+ 2520.D0*SK*D*AE**5*MFDX(1)**3*DEXP(-2.D0*AE*Y(1))*MFDX(6)
  MFDX(11) = MFDX(11)
1- 168.D0*SK*D*AE**5*(1.D0
1- DEXP(-AE*Y(1)))*MFDX(6)*MFDX(1)**3*DEXP(-AE*Y(1))
1+ 2.D0*SK*D*AE**2*(1.D0 - DEXP(-AE*Y(1)))*MFDX(9)*DEXP(-AE*Y(1))
1-18.D0*SK*D*AE**3*(1.D0
1- DEXP(-AE*Y(1)))*MFDX(8)*MFDX(1)*DEXP(-AE*Y(1))
1- 504.D0*SK*D*AE**4*MFDX(1)**2*DEXP(-2.D0*AE*Y(1))*MFDX(7)
1+ 504.D0*SK*D*AE**4*(1.D0
1- DEXP(-AE*Y(1)))*MFDX(6)*MFDX(2)*MFDX(1)*DEXP(-AE*Y(1))
1+ 1008.D0*SK*D*AE**4*(1.D0
1- DEXP(-AE*Y(1)))*MFDX(5)*MFDX(3)*MFDX(1)*DEXP(-AE*Y(1))
1+ 756.D0*SK*D*AE**4*(1.D0
1- DEXP(-AE*Y(1)))*MFDX(5)*MFDX(2)**2*DEXP(-AE*Y(1))
1+ 22680.D0*SK*D*AE**5*MFDX(1)**2*DEXP(-2.D0*AE*Y(1))*
1MFDX(5)*MFDX(2)
1-1512.D0*SK*D*AE**5*(1.D0
1- DEXP(-AE*Y(1)))*MFDX(5)*MFDX(2)*MFDX(1)**2*DEXP(-AE*Y(1))
1+ 2520.D0*SK*D*AE**4*(1.D0
```

```
1- DEXP(-AE*Y(1)))*MFDX(4)*MFDX(2)*DEXP(-AE*Y(1))*MFDX(3)
  MFDX(11) = MFDX(11)
1- 168.D0*SK*D*AE**3*(1.D0
1- DEXP(-AE*Y(1)))*MFDX(6)*MFDX(3)*DEXP(-AE*Y(1))
1- 252.D0*SK*D*AE**3*(1.D0
1- DEXP(-AE*Y(1)))*MFDX(5)*MFDX(4)*DEXP(-AE*Y(1))
1- 17640.D0*SK*D*AE**4*MFDX(3)*DEXP(-2.D0*AE*Y(1))*MFDX(2)*MFDX(4)
1- 3920.D0*SK*D*AE**4*MFDX(3)**3*DEXP(-2.D0*AE*Y(1))
1+ 75600.D0*SK*D*AE**5*MFDX(3)**2*DEXP(-2.D0*AE*Y(1))*
1MFDX(2)*MFDX(1)
1- 5292.D0*SK*D*AE**4*MFDX(5)*DEXP(-2.D0*AE*Y(1))*MFDX(2)**2
1+ 56700.D0*SK*D*AE**5*MFDX(4)*DEXP(-2.D0*AE*Y(1))*
1MFDX(2)**2*MFDX(1)
1+ 216.D0*SK*D*AE**3*MFDX(7)*DEXP(-2.D0*AE*Y(1))*MFDX(2)
1+ 504.D0*SK*D*AE**3*MFDX(6)*DEXP(-2.D0*AE*Y(1))*MFDX(3)
1- 3528.D0*SK*D*AE**4*MFDX(6)*DEXP(-2.D0*AE*Y(1))*MFDX(2)*MFDX(1)
1+ 756.D0*SK*D*AE**3*MFDX(5)*DEXP(-2.D0*AE*Y(1))*MFDX(4)
1- 7056.D0*SK*D*AE**4*MFDX(5)*DEXP(-2.D0*AE*Y(1))*MFDX(3)*MFDX(1)
1- 4410.D0*SK*D*AE**4*MFDX(4)**2*DEXP(-2.D0*AE*Y(1))*MFDX(1)
  MFDX(11) =MFDX(11)
1+ 756.D0*SK*D*AE**8*(1.D0
1- DEXP(-AE*Y(1)))*MFDX(2)**2*MFDX(1)**5*DEXP(-AE*Y(1))
1+ 158760.D0*SK*D*AE**7*MFDX(1)**4*DEXP(-2.D0*AE*Y(1))*
1MFDX(2)*MFDX(3)
1+ 15876.D0*SK*D*AE**7*MFDX(1)**5*DEXP(-2.D0*AE*Y(1))*MFDX(4)
1+ 2520.D0*SK*D*AE**6*(1.D0
1- DEXP(-AE*Y(1)))*MFDX(4)*MFDX(1)**3*DEXP(-AE*Y(1))*MFDX(2)
1+ 1680.D0*SK*D*AE**6*(1.D0
1- DEXP(-AE*Y(1)))*MFDX(3)**2*MFDX(1)**3*DEXP(-AE*Y(1))
1+ 18360.D0*SK*D*AE**9*MFDX(1)**7*DEXP(-2.D0*AE*Y(1))*MFDX(2)
1- 1022.D0*SK*D*AE**10*MFDX(1)**9*DEXP(-2.D0*AE*Y(1))
1-72.D0*SK*D*AE**9*(1.D0
1- DEXP(-AE*Y(1)))*MFDX(1)**7*DEXP(-AE*Y(1))*MFDX(2)
1+ 2.D0*SK*D*AE**10*(1.D0
1- DEXP(-AE*Y(1)))*MFDX(1)**9*DEXP(-AE*Y(1))
1- 2.D0*SK*D*AE**2*MFDX(9)*DEXP(-2.D0*AE*Y(1))
1+ 54.D0*SK*D*AE**3*MFDX(8)*DEXP(-2.D0*AE*Y(1))*MFDX(1)
1- 96012.D0*SK*D*AE**8*MFDX(1)**5*DEXP(-2.D0*AE*Y(1))*MFDX(2)**2
1- 21336.D0*SK*D*AE**8*MFDX(1)**6*DEXP(-2.D0*AE*Y(1))*MFDX(3)
  MFDX(11) = MFDX(11)
1- 252.D0*SK*D*AE**7*(1.D0
1- DEXP(-AE*Y(1)))*MFDX(4)*MFDX(1)**5*DEXP(-AE*Y(1))
1-2520.D0*SK*D*AE**7*(1.D0
1- DEXP(-AE*Y(1)))*MFDX(3)*MFDX(1)**4*DEXP(-AE*Y(1))*MFDX(2)
1+ 168.D0*SK*D*AE**8*(1.D0
1- DEXP(-AE*Y(1)))*MFDX(3)*MFDX(1)**6*DEXP(-AE*Y(1))
1+ 7560.D0*SK*D*AE**6*(1.D0
1- DEXP(-AE*Y(1)))*MFDX(2)**2*MFDX(1)**2*DEXP(-AE*Y(1))*MFDX(3)
1+ 1890.D0*SK*D*AE**6*(1.D0
1- DEXP(-AE*Y(1)))*MFDX(2)**4*MFDX(1)*DEXP(-AE*Y(1))
1+ 158760.D0*SK*D*AE**7*MFDX(1)**3*DEXP(-2.D0*AE*Y(1))*
1MFDX(2)**3
  MFDX(11) = MFDX(11)
1- 2520.D0*SK*D*AE**7*(1.D0
1- DEXP(-AE*Y(1)))*MFDX(2)**3*MFDX(1)**3*DEXP(-AE*Y(1))
1+ 37800.D0*SK*D*AE**5*MFDX(2)**3*DEXP(-2.D0*AE*Y(1))*MFDX(3)
1- 58590.D0*SK*D*AE**6*MFDX(2)**4*DEXP(-2.D0*AE*Y(1))*MFDX(1)
1- 234360.D0*SK*D*AE**6*MFDX(2)**2*DEXP(
1-2.D0*AE*Y(1))*MFDX(1)**2*MFDX(3)
1-5040.D0*SK*D*AE**5*(1.D0
1- DEXP(-AE*Y(1)))*MFDX(2)*MFDX(1)*DEXP(-AE*Y(1))*MFDX(3)**2
1- 2520.D0*SK*D*AE**5*(1.D0
1- DEXP(-AE*Y(1)))*MFDX(2)**3*DEXP(-AE*Y(1))*MFDX(3)
1-3780.D0*SK*D*AE**5*(1.D0
1- DEXP(-AE*Y(1)))*MFDX(2)**2*MFDX(1)*DEXP(-AE*Y(1))*MFDX(4)
1+ F*DCOS(X)
 RETURN
 END
```

D.2 Morse Oscillator Code With Forcing Frequency (& HF)

```
      INTEGER      K,NEQ,NPARM,IDO,IEND,IMETH,INORM,NOUT,KSTEP,KIIN,IIN
      PARAMETER      (NEQ=2, NPARM=50)
      DOUBLE PRECISION A(1,1),HINIT,PARM(NPARM),Y(NEQ),STEP,YINIT1,X0,
     1YPRIME(NEQ),X,SK,C,MFDX(11),TOL,XEND,H,AE,D,F,V,YINIT2,OM,Y1MAX,
     1Y1(4096),RM,SMU,MUL,FP,D1,D2,RE,VC,OM1,V1,V2,V3
      COMMON SK,C,AE,D,F,OM,RM,SMU,D1,D2,RE,OM1
      EXTERNAL         FCN,FCNJ,FCNP,DIVPAG,SSET
      READ(4,106) YINIT1,YINIT2,STEP,X0,SMU,C,KSTEP,TOL,AE,D,F,OM
C 106 FORMAT(6E11.3,I6,E8.0,4E11.3)
C     KSTEP   = 2*KSTEP
      IF (STEP.EQ.6.283D0) THEN
       STEP=8.D0*DATAN(1.0D0)
         WRITE(6,*) STEP
      END IF
C THE VALUES LISTED BELOW ARE HF PARMETERS THE CC CAPTIONS ARE REMOVED
      AE      = 1.1741D0
      D       = 0.22509D0
      F       = 1.067605D-03
      OM      = 1.791735D-02
      OM1     = 1.D0
C     OM1     = 1.791735D-02
C     STEP    = STEP*OM1
C     RM      = 1.694808D+3
      RM      = 1.D+0
C     SK      = 5.900372D-4
      SK      = 1.D+0
      SMU     = 5.731973D-4
C     SMU     = 1.000000D-0
C FOR LINEAR DIPOLE MOMENT, D2 IS SET TO ZERO
      D1      = 0.29769D-0
      D2      = 0.00000D0
C     D1      = 1.04941D0
C     D2      =-0.21551D0
      RE      = 1.73290D0
C     C       = C*SMU
      Y(1)    = YINIT1
C     Y(2)    = -DSQRT(2*D*YINIT2)
      Y(2)    = -DSQRT(2*D*YINIT2/SMU)
C     TOL     = 1.0D-6
      HINIT   = TOL
      IMETH   = 1
      INORM   = 2
      IDO     = 1
      CALL SSET (NPARM, 0.0, PARM, 1)
      PARM(1) = HINIT
      PARM(4) = 1.D+3*KSTEP
      PARM(10)= INORM
      PARM(12)= IMETH
      X       = X0
      XEND    = X0
      IIN     = 0
      KIIN    = KSTEP/10
      Y1MAX   = 0.D0
      DO 10 K=1,KSTEP
          XEND = XEND+STEP
      CALL DIVPAG (IDO,NEQ,FCN,FCNJ,AE,X,XEND,TOL,PARM,Y)
      CALL FCN (NEQ,X,Y,YPRIME)
      CALL FCNP (NEQ,X,Y,YPRIME,MFDX)
C      V  =  D*(1.D0-DEXP(-AE*Y(1)))**2
C I JUST USED THE SAME SYMBOL AS BEFORE BUT NOW THIS SHOULD BE
C THE TOTAL ENERGY.
       V  = (D*(1.D0-DEXP(-AE*Y(1)))**2  + Y(2)**2/2.D0*SMU)/D
       V1 =    (1.D0-DEXP(-AE*Y(1)))**2
       V2 =    (Y(2)**2/2.D0*SMU)/D
C  THE ENERGY CALCULATION BELOW IS A COMPENSATED ENERGY
       FP =  F*(D1 + 2.D0*D2*(Y(1) + RE))
C      FP =  0.D0
C      FP =  F*(1.04941D0 - 2.D0*.21551D0*(Y(1) + 1.7329D0))
C BELOW IS COMPENSATED ENERGY FOR USUAL TIME
       VC =  (D*(1.D0-DEXP(-AE*Y(1)))**2
```

```
     1 + (Y(2) + FP*DCOS(X*OM)/OM)**2*SMU/(2.D0))/D
       V3 = ((Y(2) + FP*DCOS(X*OM)/OM)**2*SMU/(2.D0))/D
C BELOW IS COMPENSATED ENERGY FOR SCALED TIME
C      VC =  (D*(1.D0-DEXP(-AE*Y(1)))**2
C    1 + (Y(2) + FP*DCOS(X*OM)/OM*OM1)**2*SMU/(2.D0))/D
C THIS IS OLD STUFF FOR FINDING MAXIMUM VALUE AND NORMALIZING
C      IF (DABS(Y(1)).GE.Y1MAX) THEN
C        Y1MAX = DABS(Y(1))
C       END IF
C       Y1(K)  = Y(1)
C  THE NEXT FOUR LINES ARE FOR THE OUTPUT OF DERIVATIVES
       WRITE(7,100) Y(1),Y(2)*SMU,YPRIME(2)*SMU,MFDX(3)*SMU,MFDX(4)*SMU,
      1 MFDX(5)*SMU,X
       WRITE(9,100) MFDX(6)*SMU,MFDX(7)*SMU,MFDX(8)*SMU,MFDX(9)*SMU,
      1 MFDX(10)*SMU,MFDX(11)*SMU,X
C      WRITE(5,101) V,Y(1)
       WRITE(8,101) VC,X
       WRITE(5,101) V,X
       WRITE(3,101) V1,X
       WRITE(2,101) V2,X
C      WRITE(8,101) V3,X
         IIN = IIN + 1
        IF (IIN.EQ.KIIN) THEN
          WRITE(6,*) K
          IIN = 0
        END IF
   10 CONTINUE
C      DO 20 K=1,KSTEP
C      WRITE(7,102) Y1(K)/Y1MAX*255.D0
C  20 CONTINUE
  100 FORMAT(7D14.6)
  101 FORMAT(1D16.8,1D14.6)
  102 FORMAT(1E14.6)
  106 FORMAT(6E11.3,I6,E8.0,4E11.3)
 1000 FORMAT(1D15.12)
C
       STOP
       END
       SUBROUTINE       FCN (NEQ,X,Y,YPRIME)
       INTEGER          NEQ
       DOUBLE PRECISION Y(NEQ),YPRIME(NEQ),X,SK,C,AE,D,F,OM,RM,SMU,
      1D1,D2,RE,OM1
       COMMON SK,C,AE,D,F,OM,RM,SMU,D1,D2,RE,OM1
       X = X
C      YPRIME(1) = Y(2)
C      YPRIME(1) = Y(2)/RM
C      YPRIME(1) = Y(2)*SK
       YPRIME(1) = Y(2)*SMU/OM1
       YPRIME(2) = (-C*Y(2)
      1- 2.D0*SK*D*AE*(1.D0 - DEXP(-AE*Y(1)))*DEXP(-AE*Y(1))
      1+ F*DSIN(X*OM)*(D1 + 2.D0*D2*(Y(1) + RE)))/OM1
C     1+ F*DSIN(X*OM)*(1.04941D0 - 2.D0*.21551D0*(Y(1) + 1.7329D0))
       RETURN
       END
C
       SUBROUTINE       FCNJ (NEQ,X,Y,DYPDY)
       INTEGER          NEQ
       DOUBLE PRECISION Y(NEQ),DYPDY(NEQ,NEQ),X
       RETURN
       END
C
       SUBROUTINE       FCNP (NEQ,X,Y,YPRIME,MFDX)
       INTEGER          NEQ
       DOUBLE PRECISION Y(NEQ),YPRIME(NEQ),X,SK,C,MFDX(11),AE,D,F,OM,RM,
      1SMU,D1,D2,RE
       COMMON SK,C,AE,D,F,OM,RM,SMU,D1,D2,RE
       X = X
C       F      =  D1*F
C      MFDX(1) = Y(2)
C      MFDX(1) = Y(2)/RM
       MFDX(1) = YPRIME(1)
       MFDX(2) = YPRIME(2)
       MFDX(3)  = - C*MFDX(2)
```

```
     1- 2.D0*SK*D*AE**2*MFDX(1)*DEXP(-2.D0*AE*Y(1))
     1+ 2.D0*SK*D*AE**2*(1.D0 - DEXP(-AE*Y(1)))*MFDX(1)*DEXP(-AE*Y(1))
C    1+ F*DCOS(X*OM)
C    1*(- 2.D0*.21551D0*MFDX(1))
     1+ F*(D1*DCOS(OM*X)*OM + 2.D0*D2*MFDX(1)*DSIN(OM*X)
     1+ 2.D0*D2*(Y(1) + RE)*DCOS(OM*X)*OM)
      MFDX(4)  = - C*MFDX(3)
     1- 2.D0*SK*D*AE**2*MFDX(2)*DEXP(-2.D0*AE*Y(1))
     1+ 6.D0*SK*D*AE**3*MFDX(1)**2*DEXP(-2.D0*AE*Y(1))
     1+ 2.D0*SK*D*AE**2*(1.D0 - DEXP(-AE*Y(1)))*MFDX(2)*DEXP(-AE*Y(1))
     1- 2.D0*SK*D*AE**3*(1.D0
     1- DEXP(-AE*Y(1)))*MFDX(1)**2*DEXP(-AE*Y(1))
C    1- F*DSIN(X*OM)
C    1*(- 2.D0*.21551D0*MFDX(2))
     1+ F*(-D1*DSIN(OM*X)*OM*OM + 2.D0*D2*MFDX(2)*DSIN(OM*X)
     1+ 4.D0*D2*MFDX(1)*DCOS(OM*X)*OM
     1- 2.D0*D2*(Y(1) + RE)*DSIN(OM*X)*OM*OM)
      MFDX(5)  = - C*MFDX(4)
     1- 2.D0*SK*D*AE**2*MFDX(3)*DEXP(-2.D0*AE*Y(1))
     1+ 18.D0*SK*D*AE**3*MFDX(2)*DEXP(-2.D0*AE*Y(1))*MFDX(1)
     1- 14.D0*SK*D*AE**4*MFDX(1)**3*DEXP(-2.D0*AE*Y(1))
     1+ 2.D0*SK*D*AE**2*(1.D0 - DEXP(-AE*Y(1)))*MFDX(3)*DEXP(-AE*Y(1))
     1- 6.D0*SK*D*AE**3*(1.D0
     1- DEXP(-AE*Y(1)))*MFDX(2)*MFDX(1)*DEXP(-AE*Y(1))
     1+ 2.D0*SK*D*AE**4*(1.D0
     1- DEXP(-AE*Y(1)))*MFDX(1)**3*DEXP(-AE*Y(1))
C    1- F*DCOS(X*OM)
C    1*(- 2.D0*.21551D0*MFDX(3))
     1+ F*(-D1*DCOS(OM*X)*OM*OM*OM + 2.D0*D2*MFDX(3)*DSIN(OM*X)
     1+ 6.D0*D2*MFDX(2)*DCOS(OM*X)*OM
     1- 6.D0*D2*MFDX(1)*DSIN(OM*X)*OM*OM
     1- 2.D0*D2*(Y(1) + RE)*DCOS(OM*X)*OM*OM*OM)
       MFDX(6)= - C*MFDX(5)
     1 - 2.D0*SK*D*AE**2*MFDX(4)*DEXP(-2.D0*AE*Y(1))
     1+ 24.D0*SK*D*AE**3*MFDX(3)*DEXP(-2.D0*AE*Y(1))*MFDX(1)
     1- 84.D0*SK*D*AE**4*MFDX(2)*DEXP(-2.D0*AE*Y(1))*MFDX(1)**2
     1+ 18.D0*SK*D*AE**3*MFDX(2)**2*DEXP(-2.D0*AE*Y(1))
     1+ 30.D0*SK*D*AE**5*MFDX(1)**4*DEXP(-2.D0*AE*Y(1))
     1+ 2.D0*SK*D*AE**2*(1.D0 - DEXP(-AE*Y(1)))*MFDX(4)*DEXP(-AE*Y(1))
     1- 8.D0*SK*D*AE**3*(1.D0
     1- DEXP(-AE*Y(1)))*MFDX(3)*MFDX(1)*DEXP(-AE*Y(1))
     1- 6.D0*SK*D*AE**3*(1.D0
     1- DEXP(-AE*Y(1)))*MFDX(2)**2*DEXP(-AE*Y(1))
     1+ 12.D0*SK*D*AE**4*(1.D0
     1- DEXP(-AE*Y(1)))*MFDX(2)*MFDX(1)**2*DEXP(-AE*Y(1))
     1- 2.D0*SK*D*AE**5*(1.D0
     1- DEXP(-AE*Y(1)))*MFDX(1)**4*DEXP(-AE*Y(1))
C    1+F*DSIN(X*OM)
     1+F*D1*DSIN(OM*X)*OM*OM*OM*OM
       MFDX(7)= 2.D0*SK*D*AE**2*(1.D0
     1- DEXP(-AE*Y(1)))*MFDX(5)*DEXP(-AE*Y(1))
     1- 10.D0*SK*D*AE**3*(1.D0
     1- DEXP(-AE*Y(1)))*MFDX(4)*MFDX(1)*DEXP(-AE*Y(1))
     1- 20.D0*SK*D*AE**3*(1.D0
     1- DEXP(-AE*Y(1)))*MFDX(3)*MFDX(2)*DEXP(-AE*Y(1))
     1+ 20.D0*SK*D*AE**4*(1.D0
     1- DEXP(-AE*Y(1)))*MFDX(3)*MFDX(1)**2*DEXP(-AE*Y(1))
     1+ 30.D0*SK*D*AE**4*(1.D0
     1- DEXP(-AE*Y(1)))*MFDX(2)**2*MFDX(1)*DEXP(-AE*Y(1))
     1- 20.D0*SK*D*AE**5*(1.D0
     1- DEXP(-AE*Y(1)))*MFDX(2)*MFDX(1)**3*DEXP(-AE*Y(1))
     1+ 2.D0*SK*D*AE**6*(1.D0
     1- DEXP(-AE*Y(1)))*MFDX(1)**5*DEXP(-AE*Y(1))
     1- 2.D0*SK*D*AE**2*MFDX(5)*DEXP(-2.D0*AE*Y(1))
     1+ 30.D0*SK*D*AE**3*MFDX(4)*DEXP(-2.D0*AE*Y(1))*MFDX(1)
     1+ 60.D0*SK*D*AE**3*MFDX(3)*DEXP(-2.D0*AE*Y(1))*MFDX(2)
     1- 140.D0*SK*D*AE**4*MFDX(3)*DEXP(-2.D0*AE*Y(1))*MFDX(1)**2
       MFDX(/) = MFDX(7)
     1- 210.D0*SK*D*AE**4*MFDX(2)**2*DEXP(-2.D0*AE*Y(1))*MFDX(1)
     1+ 300.D0*SK*D*AE**5*MFDX(2)*DEXP(-2.D0*AE*Y(1))*MFDX(1)**3
     1- 62.D0*SK*D*AE**6*MFDX(1)**5*DEXP(-2.D0*AE*Y(1))
C    1+ F*DCOS(X*OM) - C*MFDX(6)
     1+ F*DCOS(X*OM)*OM*OM*OM*OM*OM*D1
```

```
      MFDX(8) = - 210.D0*SK*D*AE**4*MFDX(2)**3*DEXP(-2.D0*AE*Y(1))
     1+ 30.D0*SK*D*AE**6*(1.D0
     1- DEXP(-AE*Y(1)))*MFDX(2)*MFDX(1)**4*DEXP(-AE*Y(1))
     1+ 126.D0*SK*D*AE**7*MFDX(1)**6*DEXP(-2.D0*AE*Y(1))
     1- 2.D0*SK*D*AE**7*(1.D0
     1- DEXP(-AE*Y(1)))*MFDX(1)**6*DEXP(-AE*Y(1))
     1- 2.D0*SK*D*AE**2*MFDX(6)*DEXP(-2.D0*AE*Y(1))
     1+ 90.D0*SK*D*AE**3*MFDX(4)*DEXP(-2.D0*AE*Y(1))*MFDX(2)
     1+ 60.D0*SK*D*AE**3*MFDX(3)**2*DEXP(-2.D0*AE*Y(1))
     1+ 2.D0*SK*D*AE**2*(1.D0 - DEXP(-AE*Y(1)))*MFDX(6)*DEXP(-AE*Y(1))
     1+ 36.D0*SK*D*AE**3*MFDX(1)*DEXP(-2.D0*AE*Y(1))*MFDX(5)
     1- 12.D0*SK*D*AE**3*(1.D0
     1- DEXP(-AE*Y(1)))*MFDX(5)*MFDX(1)*DEXP(-AE*Y(1))
     1- 30.D0*SK*D*AE**3*(1.D0
     1- DEXP(-AE*Y(1)))*MFDX(4)*MFDX(2)*DEXP(-AE*Y(1))
     1- 210.D0*SK*D*AE**4*MFDX(1)**2*DEXP(-2.D0*AE*Y(1))*MFDX(4)
      MFDX(8) =MFDX(8)
     1+ 30.D0*SK*D*AE**4*(1.D0
     1- DEXP(-AE*Y(1)))*MFDX(4)*MFDX(1)**2*DEXP(-AE*Y(1))
     1- 20.D0*SK*D*AE**3*(1.D0
     1- DEXP(-AE*Y(1)))*MFDX(3)**2*DEXP(-AE*Y(1))
     1- 840.D0*SK*D*AE**4*MFDX(1)*DEXP(-2.D0*AE*Y(1))*MFDX(3)*MFDX(2)
     1+ 120.D0*SK*D*AE**4*(1.D0
     1- DEXP(-AE*Y(1)))*MFDX(3)*MFDX(2)*MFDX(1)*DEXP(-AE*Y(1))
     1+ 600.D0*SK*D*AE**5*MFDX(1)**3*DEXP(-2.D0*AE*Y(1))*MFDX(3)
     1- 40.D0*SK*D*AE**5*(1.D0
     1- DEXP(-AE*Y(1)))*MFDX(3)*MFDX(1)**3*DEXP(-AE*Y(1))
     1+ 30.D0*SK*D*AE**4*(1.D0
     1- DEXP(-AE*Y(1)))*MFDX(2)**3*DEXP(-AE*Y(1))
     1+ 1350.D0*SK*D*AE**5*MFDX(1)**2*DEXP(-2.D0*AE*Y(1))*MFDX(2)**2
     1- 90.D0*SK*D*AE**5*(1.D0
     1- DEXP(-AE*Y(1)))*MFDX(2)**2*MFDX(1)**2*DEXP(-AE*Y(1))
     1- 930.D0*SK*D*AE**6*MFDX(1)**4*DEXP(-2.D0*AE*Y(1))*MFDX(2)
     1- C*MFDX(7)
C    1- F*DSIN(X*OM)
     1- F*DSIN(X*OM)*OM*OM*OM*OM*OM*OM*D1
      MFDX(9) = + 140.D0*SK*D*AE**4*(1.D0
     1- DEXP(-AE*Y(1)))*MFDX(3)**2*MFDX(1)*DEXP(-AE*Y(1))
     1+6300.D0*SK*D*AE**5*MFDX(1)**2*DEXP(-2.D0*AE*Y(1))*MFDX(3)*MFDX(2)
     1- C*MFDX(8)
     1- 70.D0*SK*D*AE**5*(1.D0
     1- DEXP(-AE*Y(1)))*MFDX(4)*MFDX(1)**3*DEXP(-AE*Y(1))
     1+ 1050.D0*SK*D*AE**5*MFDX(1)**3*DEXP(-2.D0*AE*Y(1))*MFDX(4)
     1+ 210.D0*SK*D*AE**4*(1.D0
     1- DEXP(-AE*Y(1)))*MFDX(4)*MFDX(2)*MFDX(1)*DEXP(-AE*Y(1))
     1- 70.D0*SK*D*AE**3*(1.D0
     1- DEXP(-AE*Y(1)))*MFDX(4)*MFDX(3)*DEXP(-AE*Y(1))
     1- 42.D0*SK*D*AE**3*(1.D0
     1- DEXP(-AE*Y(1)))*MFDX(5)*MFDX(2)*DEXP(-AE*Y(1))
     1+ 42.D0*SK*D*AE**4*(1.D0
     1- DEXP(-AE*Y(1)))*MFDX(5)*MFDX(1)**2*DEXP(-AE*Y(1))
     1- 14.D0*SK*D*AE**3*(1.D0
     1- DEXP(-AE*Y(1)))*MFDX(6)*MFDX(1)*DEXP(-AE*Y(1))
     1+ 2.D0*SK*D*AE**2*(1.D0 - DEXP(-AE*Y(1)))*MFDX(7)*DEXP(-AE*Y(1))
     1- 980.D0*SK*D*AE**4*MFDX(3)**2*DEXP(-2.D0*AE*Y(1))*MFDX(1)
      MFDX(9) =MFDX(9)
     1- 294.D0*SK*D*AE**4*MFDX(1)**2*DEXP(-2.D0*AE*Y(1))*MFDX(5)
     1- 1470.D0*SK*D*AE**4*MFDX(4)*DEXP(-2.D0*AE*Y(1))*MFDX(2)*MFDX(1)
     1+ 126.D0*SK*D*AE**3*MFDX(5)*DEXP(-2.D0*AE*Y(1))*MFDX(2)
     1+ 210.D0*SK*D*AE**3*MFDX(4)*DEXP(-2.D0*AE*Y(1))*MFDX(3)
     1+ 42.D0*SK*D*AE**3*MFDX(6)*DEXP(-2.D0*AE*Y(1))*MFDX(1)
     1+ 2.D0*SK*D*AE**8*(1.D0
     1- DEXP(-AE*Y(1)))*MFDX(1)**7*DEXP(-AE*Y(1))
     1- 2.D0*SK*D*AE**2*MFDX(7)*DEXP(-2.D0*AE*Y(1))
     1- 254.D0*SK*D*AE**8*MFDX(1)**7*DEXP(-2.D0*AE*Y(1))
     1- 42.D0*SK*D*AE**7*(1.D0
     1- DEXP(-AE*Y(1)))*MFDX(2)*MFDX(1)**5*DEXP(-AE*Y(1))
     1+ 2646.D0*SK*D*AE**7*MFDX(1)**5*DEXP(-2.D0*AE*Y(1))*MFDX(2)
     1+ 70.D0*SK*D*AE**6*(1.D0
     1- DEXP(-AE*Y(1)))*MFDX(3)*MFDX(1)**4*DEXP(-AE*Y(1))
     1+ 210.D0*SK*D*AE**6*(1.D0
     1- DEXP(-AE*Y(1)))*MFDX(2)**2*MFDX(1)**3*DEXP(-AE*Y(1))
     1- 1470.D0*SK*D*AE**4*MFDX(2)**2*DEXP(-2.D0*AE*Y(1))*MFDX(3)
```

```
     1+ 3150.D0*SK*D*AE**5*MFDX(2)**3*DEXP(-2.D0*AE*Y(1))*MFDX(1)
       MFDX(9) = MFDX(9)
     1- 6510.D0*SK*D*AE**6*MFDX(1)**3*DEXP(-2.D0*AE*Y(1))*MFDX(2)**2
     1- 210.D0*SK*D*AE**5*(1.D0
     1- DEXP(-AE*Y(1)))*MFDX(2)**3*MFDX(1)*DEXP(-AE*Y(1))
     1- 420.D0*SK*D*AE**5*(1.D0
     1- DEXP(-AE*Y(1)))*MFDX(3)*MFDX(2)*MFDX(1)**2*DEXP(-AE*Y(1))
C    1- F*DCOS(X*OM)
     1- 2170.D0*SK*D*AE**6*MFDX(1)**4*DEXP(-2.D0*AE*Y(1))*MFDX(3)
     1+ 210.D0*SK*D*AE**4*(1.D0
     1- DEXP(-AE*Y(1)))*MFDX(3)*MFDX(2)**2*DEXP(-AE*Y(1))
     1- F*DCOS(X*OM)*OM*OM*OM*OM*OM*OM*OM*D1
       MFDX(10) = 840.D0*SK*D*AE**6*(1.D0
     1- DEXP(-AE*Y(1)))*MFDX(2)**3*MFDX(1)**2*DEXP(-AE*Y(1))
     1+ 3150.D0*SK*D*AE**5*MFDX(2)**4*DEXP(-2.D0*AE*Y(1))
     1- 26040.D0*SK*D*AE**6*MFDX(2)**3*DEXP(-2.D0*AE*Y(1))*MFDX(1)**2
     1- 1680.D0*SK*D*AE**5*(1.D0
     1- DEXP(-AE*Y(1)))*MFDX(2)**2*MFDX(1)*DEXP(-AE*Y(1))*MFDX(3)
     1- 210.D0*SK*D*AE**5*(1.D0
     1- DEXP(-AE*Y(1)))*MFDX(2)**4*DEXP(-AE*Y(1))
     1+ 510.D0*SK*D*AE**9*MFDX(1)**8*DEXP(-2.D0*AE*Y(1))
     1- 2.D0*SK*D*AE**9*(1.D0
     1- DEXP(-AE*Y(1)))*MFDX(1)**8*DEXP(-AE*Y(1))
     1- 2.D0*SK*D*AE**2*MFDX(8)*DEXP(-2.D0*AE*Y(1))
     1- 7112.D0*SK*D*AE**8*MFDX(1)**6*DEXP(-2.D0*AE*Y(1))*MFDX(2)
     1- 112.D0*SK*D*AE**7*(1.D0
     1- DEXP(-AE*Y(1)))*MFDX(3)*MFDX(1)**5*DEXP(-AE*Y(1))
     1- 420.D0*SK*D*AE**7*(1.D0
     1- DEXP(-AE*Y(1)))*MFDX(2)**2*MFDX(1)**4*DEXP(-AE*Y(1))
     1+ 26460.D0*SK*D*AE**7*MFDX(1)**4*DEXP(-2.D0*AE*Y(1))*MFDX(2)**2
     1+ 7056.D0*SK*D*AE**7*MFDX(1)**5*DEXP(-2.D0*AE*Y(1))*MFDX(3)
       MFDX(10)=MFDX(10)
     1+ 1120.D0*SK*D*AE**6*(1.D0
     1- DEXP(-AE*Y(1)))*MFDX(3)*MFDX(1)**3*DEXP(-AE*Y(1))*MFDX(2)
     1- 3920.D0*SK*D*AE**4*MFDX(3)**2*DEXP(-2.D0*AE*Y(1))*MFDX(2)
     1- 2940.D0*SK*D*AE**4*MFDX(4)*DEXP(-2.D0*AE*Y(1))*MFDX(2)**2
     1+ 168.D0*SK*D*AE**3*MFDX(6)*DEXP(-2.D0*AE*Y(1))*MFDX(2)
     1+ 336.D0*SK*D*AE**3*MFDX(5)*DEXP(-2.D0*AE*Y(1))*MFDX(3)
     1+ 210.D0*SK*D*AE**3*MFDX(4)**2*DEXP(-2.D0*AE*Y(1))
     1+ 56.D0*SK*D*AE**8*(1.D0
     1- DEXP(-AE*Y(1)))*MFDX(1)**6*DEXP(-AE*Y(1))*MFDX(2)
     1+ 2.D0*SK*D*AE**2*(1.D0 - DEXP(-AE*Y(1)))*MFDX(8)*DEXP(-AE*Y(1))
     1+ 48.D0*SK*D*AE**3*MFDX(1)*DEXP(-2.D0*AE*Y(1))*MFDX(7)
     1+ 336.D0*SK*D*AE**4*(1.D0
     1- DEXP(-AE*Y(1)))*MFDX(5)*MFDX(2)*MFDX(1)*DEXP(-AE*Y(1))
     1+ 420.D0*SK*D*AE**4*(1.D0
     1- DEXP(-AE*Y(1)))*MFDX(4)*MFDX(2)**2*DEXP(-AE*Y(1))
     1- 112.D0*SK*D*AE**3*(1.D0
     1- DEXP(-AE*Y(1)))*MFDX(5)*MFDX(3)*DEXP(-AE*Y(1))
       MFDX(10)=MFDX(10)
     1- 70.D0*SK*D*AE**3*(1.D0
     1- DEXP(-AE*Y(1)))*MFDX(4)**2*DEXP(-AE*Y(1))
     1- 3920.D0*SK*D*AE**4*MFDX(1)*DEXP(-2.D0*AE*Y(1))*MFDX(4)*MFDX(3)
     1- 56.D0*SK*D*AE**3*(1.D0
     1- DEXP(-AE*Y(1)))*MFDX(6)*MFDX(2)*DEXP(-AE*Y(1))
     1- 2352*SK*D*AE**4*MFDX(1)*DEXP(-2.D0*AE*Y(1))*MFDX(5)*MFDX(2)
     1+ 56.D0*SK*D*AE**4*(1.D0
     1- DEXP(-AE*Y(1)))*MFDX(6)*MFDX(1)**2*DEXP(-AE*Y(1))
     1- 16.D0*SK*D*AE**3*(1.D0
     1- DEXP(-AE*Y(1)))*MFDX(7)*MFDX(1)*DEXP(-AE*Y(1))
     1- 392.D0*SK*D*AE**4*MFDX(1)**2*DEXP(-2.D0*AE*Y(1))*MFDX(6)
     1+ 1680.D0*SK*D*AE**5*MFDX(1)**3*DEXP(-2.D0*AE*Y(1))*MFDX(5)
     1- 34720.D0*SK*D*AE**6*MFDX(1)**3*
     1DEXP(-2.D0*AE*Y(1))*MFDX(3)*MFDX(2)
     1- 112.D0*SK*D*AE**5*(1.D0
     1- DEXP(-AE*Y(1)))*MFDX(5)*MFDX(1)**3*DEXP(-AE*Y(1))
       MFDX(10) = MFDX(10)
     1- 840.D0*SK*D*AE**5*(1.D0
     1- DEXP(-AE*Y(1)))*MFDX(4)*MFDX(1)**2*DEXP(-AE*Y(1))*MFDX(2)
     1- 4340.D0*SK*D*AE**6*MFDX(1)**4*DEXP(-2.D0*AE*Y(1))*MFDX(4)
     1+ 140.D0*SK*D*AE**6*(1.D0
     1- DEXP(-AE*Y(1)))*MFDX(4)*MFDX(1)**4*DEXP(-AE*Y(1))
     1- 560.D0*SK*D*AE**5*(1.D0
```

```
     1- DEXP(-AE*Y(1)))*MFDX(3)**2*MFDX(1)**2*DEXP(-AE*Y(1))
     1+ 25200.D0*SK*D*AE**5*MFDX(1)*DEXP(-2.D0*AE*Y(1))*
     1MFDX(3)*MFDX(2)**2
     1+ 12600.D0*SK*D*AE**5*MFDX(1)**2*DEXP(-2.D0*AE*Y(1))*
     1MFDX(4)*MFDX(2)
     1+ 560.D0*SK*D*AE**4*(1.D0
     1- DEXP(-AE*Y(1)))*MFDX(3)*MFDX(1)*DEXP(-AE*Y(1))*MFDX(4)
     1+ 560.D0*SK*D*AE**4*(1.D0
     1- DEXP(-AE*Y(1)))*MFDX(3)**2*MFDX(2)*DEXP(-AE*Y(1))
     1+ 8400.D0*SK*D*AE**5*MFDX(1)**2*DEXP(-2.D0*AE*Y(1))*MFDX(3)**2
     1- C*MFDX(9)
C    1+ F*DSIN(X*OM)
     1+ F*DSIN(X*OM)*OM*OM*OM*OM*OM*OM*OM*OM*D1
       MFDX(11) = 560.D0*SK*D*AE**4*(1.D0
     1- DEXP(-AE*Y(1)))*MFDX(3)**3*DEXP(-AE*Y(1)) - C*MFDX(10)
     1+ 252.D0*SK*D*AE**6*(1.D0
     1- DEXP(-AE*Y(1)))*MFDX(5)*MFDX(1)**4*DEXP(-AE*Y(1))
     1- 2520.D0*SK*D*AE**5*(1.D0
     1- DEXP(-AE*Y(1)))*MFDX(4)*MFDX(1)**2*DEXP(-AE*Y(1))*MFDX(3)
     1- 7812.D0*SK*D*AE**6*MFDX(1)**4*DEXP(-2.D0*AE*Y(1))*MFDX(5)
     1- 78120.D0*SK*D*AE**6*MFDX(1)**3*DEXP(-2.D0*AE*Y(1))*
     1MFDX(4)*MFDX(2)
     1- 52080.D0*SK*D*AE**6*MFDX(1)**3*DEXP(-2.D0*AE*Y(1))*MFDX(3)**2
     1+ 630.D0*SK*D*AE**4*(1.D0
     1- DEXP(-AE*Y(1)))*MFDX(4)**2*MFDX(1)*DEXP(-AE*Y(1))
     1+ 37800.D0*SK*D*AE**5*MFDX(1)**2*DEXP(-2.D0*AE*Y(1))*
     1MFDX(4)*MFDX(3)
     1- 72.D0*SK*D*AE**3*(1.D0
     1- DEXP(-AE*Y(1)))*MFDX(7)*MFDX(2)*DEXP(-AE*Y(1))
     1+72.D0*SK*D*AE**4*(1.D0
     1- DEXP(-AE*Y(1)))*MFDX(7)*MFDX(1)**2*DEXP(-AE*Y(1))
     1+ 2520.D0*SK*D*AE**5*MFDX(1)**3*DEXP(-2.D0*AE*Y(1))*MFDX(6)
       MFDX(11) = MFDX(11)
     1- 168.D0*SK*D*AE**5*(1.D0
     1- DEXP(-AE*Y(1)))*MFDX(6)*MFDX(1)**3*DEXP(-AE*Y(1))
     1+ 2.D0*SK*D*AE**2*(1.D0 - DEXP(-AE*Y(1)))*MFDX(9)*DEXP(-AE*Y(1))
     1-18.D0*SK*D*AE**3*(1.D0
     1- DEXP(-AE*Y(1)))*MFDX(8)*MFDX(1)*DEXP(-AE*Y(1))
     1- 504.D0*SK*D*AE**4*MFDX(1)**2*DEXP(-2.D0*AE*Y(1))*MFDX(7)
     1+ 504.D0*SK*D*AE**4*(1.D0
     1- DEXP(-AE*Y(1)))*MFDX(6)*MFDX(2)*MFDX(1)*DEXP(-AE*Y(1))
     1+ 1008.D0*SK*D*AE**4*(1.D0
     1- DEXP(-AE*Y(1)))*MFDX(5)*MFDX(3)*MFDX(1)*DEXP(-AE*Y(1))
     1+ 756.D0*SK*D*AE**4*(1.D0
     1- DEXP(-AE*Y(1)))*MFDX(5)*MFDX(2)**2*DEXP(-AE*Y(1))
     1+ 22680.D0*SK*D*AE**5*MFDX(1)**2*DEXP(-2.D0*AE*Y(1))*
     1MFDX(5)*MFDX(2)
     1-1512.D0*SK*D*AE**5*(1.D0
     1- DEXP(-AE*Y(1)))*MFDX(5)*MFDX(2)*MFDX(1)**2*DEXP(-AE*Y(1))
     1+ 2520.D0*SK*D*AE**4*(1.D0
     1- DEXP(-AE*Y(1)))*MFDX(4)*MFDX(2)*DEXP(-AE*Y(1))*MFDX(3)
       MFDX(11) = MFDX(11)
     1- 168.D0*SK*D*AE**3*(1.D0
     1- DEXP(-AE*Y(1)))*MFDX(6)*MFDX(3)*DEXP(-AE*Y(1))
     1- 252.D0*SK*D*AE**3*(1.D0
     1- DEXP(-AE*Y(1)))*MFDX(5)*MFDX(4)*DEXP(-AE*Y(1))
     1- 17640.D0*SK*D*AE**4*MFDX(3)*DEXP(-2.D0*AE*Y(1))*MFDX(2)*MFDX(4)
     1- 3920.D0*SK*D*AE**4*MFDX(3)**3*DEXP(-2.D0*AE*Y(1))
     1+ 75600.D0*SK*D*AE**5*MFDX(3)**2*DEXP(-2.D0*AE*Y(1))*
     1MFDX(2)*MFDX(1)
     1- 5292.D0*SK*D*AE**4*MFDX(5)*DEXP(-2.D0*AE*Y(1))*MFDX(2)**2
     1+ 56700.D0*SK*D*AE**5*MFDX(4)*DEXP(-2.D0*AE*Y(1))*
     1MFDX(2)**2*MFDX(1)
     1+ 216.D0*SK*D*AE**3*MFDX(7)*DEXP(-2.D0*AE*Y(1))*MFDX(2)
     1+ 504.D0*SK*D*AE**3*MFDX(6)*DEXP(-2.D0*AE*Y(1))*MFDX(3)
     1- 3528.D0*SK*D*AE**4*MFDX(6)*DEXP(-2.D0*AE*Y(1))*MFDX(2)*MFDX(1)
     1+ 756.D0*SK*D*AE**3*MFDX(5)*DEXP(-2.D0*AE*Y(1))*MFDX(4)
     1- 7056.D0*SK*D*AE**4*MFDX(5)*DEXP(-2.D0*AE*Y(1))*MFDX(3)*MFDX(1)
     1- 4410.D0*SK*D*AE**4*MFDX(4)**2*DEXP(-2.D0*AE*Y(1))*MFDX(1)
       MFDX(11) =MFDX(11)
     1+ 756.D0*SK*D*AE**8*(1.D0
     1- DEXP(-AE*Y(1)))*MFDX(2)**2*MFDX(1)**5*DEXP(-AE*Y(1))
     1+ 158760.D0*SK*D*AE**7*MFDX(1)**4*DEXP(-2.D0*AE*Y(1))*
```

```
     1MFDX(2)*MFDX(3)
     1+ 15876.D0*SK*D*AE**7*MFDX(1)**5*DEXP(-2.D0*AE*Y(1))*MFDX(4)
     1+ 2520.D0*SK*D*AE**6*(1.D0
     1- DEXP(-AE*Y(1)))*MFDX(4)*MFDX(1)**3*DEXP(-AE*Y(1))*MFDX(2)
     1+ 1680.D0*SK*D*AE**6*(1.D0
     1- DEXP(-AE*Y(1)))*MFDX(3)**2*MFDX(1)**3*DEXP(-AE*Y(1))
     1+ 18360.D0*SK*D*AE**9*MFDX(1)**7*DEXP(-2.D0*AE*Y(1))*MFDX(2)
     1- 1022.D0*SK*D*AE**10*MFDX(1)**9*DEXP(-2.D0*AE*Y(1))
     1-72.D0*SK*D*AE**9*(1.D0
     1- DEXP(-AE*Y(1)))*MFDX(1)**7*DEXP(-AE*Y(1))*MFDX(2)
     1+ 2.D0*SK*D*AE**10*(1.D0
     1- DEXP(-AE*Y(1)))*MFDX(1)**9*DEXP(-AE*Y(1))
     1- 2.D0*SK*D*AE**2*MFDX(9)*DEXP(-2.D0*AE*Y(1))
     1+ 54.D0*SK*D*AE**3*MFDX(8)*DEXP(-2.D0*AE*Y(1))*MFDX(1)
     1- 96012.D0*SK*D*AE**8*MFDX(1)**5*DEXP(-2.D0*AE*Y(1))*MFDX(2)**2
     1- 21336.D0*SK*D*AE**8*MFDX(1)**6*DEXP(-2.D0*AE*Y(1))*MFDX(3)
       MFDX(11) = MFDX(11)
     1- 252.D0*SK*D*AE**7*(1.D0
     1- DEXP(-AE*Y(1)))*MFDX(4)*MFDX(1)**5*DEXP(-AE*Y(1))
     1-2520.D0*SK*D*AE**7*(1.D0
     1- DEXP(-AE*Y(1)))*MFDX(3)*MFDX(1)**4*DEXP(-AE*Y(1))*MFDX(2)
     1+ 168.D0*SK*D*AE**8*(1.D0
     1- DEXP(-AE*Y(1)))*MFDX(3)*MFDX(1)**6*DEXP(-AE*Y(1))
     1+ 7560.D0*SK*D*AE**6*(1.D0
     1- DEXP(-AE*Y(1)))*MFDX(2)**2*MFDX(1)**2*DEXP(-AE*Y(1))*MFDX(3)
     1+ 1890.D0*SK*D*AE**6*(1.D0
     1- DEXP(-AE*Y(1)))*MFDX(2)**4*MFDX(1)*DEXP(-AE*Y(1))
     1+ 158760.D0*SK*D*AE**7*MFDX(1)**3*DEXP(-2.D0*AE*Y(1))*
     1MFDX(2)**3
       MFDX(11) = MFDX(11)
     1- 2520.D0*SK*D*AE**7*(1.D0
     1- DEXP(-AE*Y(1)))*MFDX(2)**3*MFDX(1)**3*DEXP(-AE*Y(1))
     1+ 37800.D0*SK*D*AE**5*MFDX(2)**3*DEXP(-2.D0*AE*Y(1))*MFDX(3)
     1- 58590.D0*SK*D*AE**6*MFDX(2)**4*DEXP(-2.D0*AE*Y(1))*MFDX(1)
     1- 234360.D0*SK*D*AE**6*MFDX(2)**2*DEXP(
     1-2.D0*AE*Y(1))*MFDX(1)**2*MFDX(3)
     1-5040.D0*SK*D*AE**5*(1.D0
     1- DEXP(-AE*Y(1)))*MFDX(2)*MFDX(1)*DEXP(-AE*Y(1))*MFDX(3)**2
     1- 2520.D0*SK*D*AE**5*(1.D0
     1- DEXP(-AE*Y(1)))*MFDX(2)**3*DEXP(-AE*Y(1))*MFDX(3)
     1-3780.D0*SK*D*AE**5*(1.D0
     1- DEXP(-AE*Y(1)))*MFDX(2)**2*MFDX(1)*DEXP(-AE*Y(1))*MFDX(4)
C    1+ F*DCOS(X*OM)
     1+ F*DCOS(X*OM)*OM*OM*OM*OM*OM*OM*OM*OM*OM*OM*D1
      RETURN
      END
```

D.3 Morse Oscillator Code for Lyapunov Calculation

```
      INTEGER        NEQ,NPARM,IDO,IEND,IMETH,INORM,NOUT,KSTEP,KIIN,IIN
      PARAMETER      (NEQ=4, NPARM=50)
      DOUBLE PRECISION A(1,1),HINIT,PARM(NPARM),Y(NEQ),PERTB,YINIT1,
     1YPRIME(NEQ),X,SK,C,MFDX(5),MFDXP(5),TOL,XEND,H,AE,D,F,V,YINIT2,
     1D0,D1,D2,D3,D4,D5,P0,P1,P2,P3,P4,P5,X0,DP0,P0A
      COMMON SK,C,AE,D,F
      EXTERNAL       FCN,FCNJ,FCNP,DIVPAG,SSET
      READ(4,106) YINIT1,YINIT2,STEP,X0,SK,C,KSTEP,TOL,AE,D,F,PERTB
C 106 FORMAT(6E11.3,I6,E8.0,4E11.3)
C     KSTEP   = 2*KSTEP
      Y(1)    = YINIT1
      Y(2)    = -DSQRT(2*1/SK*YINIT2)
      Y(3)    = YINIT1 + PERTB
      Y(4)    = -DSQRT(2*1/SK*YINIT2) - PERTB
C     TOL     = 1.0D-6
      HINIT   = TOL
      IMETH   = 1
      INORM   = 2
      IDO     = 1
      CALL SSET (NPARM, 0.0, PARM, 1)
      PARM(1) = HINIT
      PARM(4) = 1.D+3*KSTEP
      PARM(10)= INORM
      PARM(12)= IMETH
      X       = X0
      XEND    = X0
      IIN     = 0
      KIIN    = KSTEP/10
      DO 10 K=1,KSTEP
          XEND = XEND+STEP
      CALL DIVPAG (IDO,NEQ,FCN,FCNJ,AE,X,XEND,TOL,PARM,Y)
      CALL FCN (NEQ,X,Y,YPRIME)
C     CALL FCNP (NEQ,X,Y,YPRIME,MFDX,MFDXP)
        IIN = IIN + 1
        D0  =  Y(1)  -  Y(3)
        D1  =  Y(2)  -  Y(4)
C       D2  = MFDX(2)  - MFDXP(2)
C       D3  = MFDX(3)  - MFDXP(3)
C       D4  = MFDX(4)  - MFDXP(4)
C       D5  = MFDX(5)  - MFDXP(5)
C       P0A = DSQRT(D0*D0   +  D1*D1)
        P0  = DLOG10(DSQRT(D0*D0   +  D1*D1))
C       DP0 = ((D0*D0   +  D1*D1)**(-0.5D0)*(0.5D0)*
C     1(2.D0*D0*D1 + 2.D0*D1*D2))*(1/DLOG(1.0D1))*(1/P0A)
C       P1  = DLOG10(DSQRT(D1*D1   +  D2*D2))
C       P2  = DLOG10(DSQRT(D2*D2   +  D3*D3))
C       P3  = DLOG10(DSQRT(D3*D3   +  D4*D4))
C       P4  = DLOG10(DSQRT(D4*D4   +  D5*D5))
C       P5  = DLOG10(DSQRT(D5*D5   +  D6*D6))
C     WRITE(7,100) P0,P1,P2,P3,P4,P5,X
      WRITE(7,101) P0,X
      WRITE(8,102) Y(1),Y(2),Y(3),Y(4)
C     WRITE(7,102) P0,DP0,X
       IF (IIN.EQ.KIIN) THEN
         WRITE(6,*) K
         IIN = 0
       END IF
  100 FORMAT(7D14.5)
  101 FORMAT(2D14.5)
  102 FORMAT(4D14.5)
  106 FORMAT(6E11.3,I6,E8.0,4E11.3)
   10 CONTINUE
C
      STOP
      END
      SUBROUTINE       FCN (NEQ,X,Y,YPRIME)
      INTEGER          NEQ
      DOUBLE PRECISION Y(NEQ),YPRIME(NEQ),X,SK,C,AE,D,F
      COMMON SK,C,AE,D,F
      X = X
```

```
      YPRIME(1) = Y(2)
      YPRIME(2) = -C*Y(2)
     1- 2.D0*SK*D*AE*(1.D0 - DEXP(-AE*Y(1)))*DEXP(-AE*Y(1))
     1+ F*DSIN(X)
      YPRIME(3) = Y(4)
      YPRIME(4) = -C*Y(4)
     1- 2.D0*SK*D*AE*(1.D0 - DEXP(-AE*Y(3)))*DEXP(-AE*Y(3))
     1+ F*DSIN(X)
      RETURN
      END
C
      SUBROUTINE       FCNJ (NEQ,X,Y,DYPDY)
      INTEGER          NEQ
      DOUBLE PRECISION Y(NEQ),DYPDY(NEQ,NEQ),X
      RETURN
      END
C
      SUBROUTINE       FCNP (NEQ,X,Y,YPRIME,MFDX,MFDXP)
      INTEGER          NEQ
      DOUBLE PRECISION Y(NEQ),YPRIME(NEQ),X,SK,C,MFDX(5),MFDXP(5),AE,D,F
      COMMON SK,C,AE,D,F
      X = X
      MFDX(1) = Y(2)
      MFDX(2) = YPRIME(2)
      MFDX(3)  = - C*MFDX(2)
     1- 2.D0*SK*D*AE**2*MFDX(1)*DEXP(-2.D0*AE*Y(1))
     1+ 2.D0*SK*D*AE**2*(1.D0
     1- DEXP(-AE*Y(1)))*MFDX(1)*DEXP(-AE*Y(1))
     1+ F*DCOS(X)
      MFDX(4)  = - C*MFDX(3)
     1- 2.D0*SK*D*AE**2*MFDX(2)*DEXP(-2.D0*AE*Y(1))
     1+ 6.D0*SK*D*AE**3*MFDX(1)**2*DEXP(-2.D0*AE*Y(1))
     1+ 2.D0*SK*D*AE**2*(1.D0
     1- DEXP(-AE*Y(1)))*MFDX(2)*DEXP(-AE*Y(1))
     1- 2.D0*SK*D*AE**3*(1.D0
     1- DEXP(-AE*Y(1)))*MFDX(1)**2*DEXP(-AE*Y(1))
     1- F*DSIN(X)
      MFDX(5)  = - C*MFDX(4)
     1- 2.D0*SK*D*AE**2*MFDX(3)*DEXP(-2.D0*AE*Y(1))
     1+ 18.D0*SK*D*AE**3*MFDX(2)*DEXP(-2.D0*AE*Y(1))*MFDX(1)
     1- 14.D0*SK*D*AE**4*MFDX(1)**3*DEXP(-2.D0*AE*Y(1))
     1+ 2.D0*SK*D*AE**2*(1.D0
     1- DEXP(-AE*Y(1)))*MFDX(3)*DEXP(-AE*Y(1))
     1- 6.D0*SK*D*AE**3*(1.D0
     1- DEXP(-AE*Y(1)))*MFDX(2)*MFDX(1)*DEXP(-AE*Y(1))
     1+ 2.D0*SK*D*AE**4*(1.D0
     1- DEXP(-AE*Y(1)))*MFDX(1)**3*DEXP(-AE*Y(1))
     1- F*DCOS(X)
C
C
      MFDXP(1) = Y(4)
      MFDXP(2) = YPRIME(4)
      MFDXP(3)  = - C*MFDXP(2)
     1- 2.D0*SK*D*AE**2*MFDXP(1)*DEXP(-2.D0*AE*Y(3))
     1+ 2.D0*SK*D*AE**2*(1.D0
     1- DEXP(-AE*Y(3)))*MFDXP(1)*DEXP(-AE*Y(3))
     1+ F*DCOS(X)
      MFDXP(4)  = - C*MFDXP(3)
     1- 2.D0*SK*D*AE**2*MFDXP(2)*DEXP(-2.D0*AE*Y(3))
     1+ 6.D0*SK*D*AE**3*MFDXP(1)**2*DEXP(-2.D0*AE*Y(3))
     1+ 2.D0*SK*D*AE**2*(1.D0
     1- DEXP(-AE*Y(3)))*MFDXP(2)*DEXP(-AE*Y(3))
     1- 2.D0*SK*D*AE**3*(1.D0
     1- DEXP(-AE*Y(3)))*MFDXP(1)**2*DEXP(-AE*Y(3))
     1- F*DSIN(X)
      MFDXP(5)  = - C*MFDXP(4)
     1- 2.D0*SK*D*AE**2*MFDXP(3)*DEXP(-2.D0*AE*Y(3))
     1+ 18.D0*SK*D*AE**3*MFDXP(2)*DEXP(-2.D0*AE*Y(3))*MFDXP(1)
     1- 14.D0*SK*D*AE**4*MFDXP(1)**3*DEXP(-2.D0*AE*Y(3))
     1+ 2.D0*SK*D*AE**2*(1.D0
     1- DEXP(-AE*Y(3)))*MFDXP(3)*DEXP(-AE*Y(3))
     1- 6.D0*SK*D*AE**3*(1.D0
     1- DEXP(-AE*Y(3)))*MFDXP(2)*MFDXP(1)*DEXP(-AE*Y(3))
     1+ 2.D0*SK*D*AE**4*(1.D0
     1- DEXP(-AE*Y(3)))*MFDXP(1)**3*DEXP(-AE*Y(3))
     1- F*DCOS(X)
      RETURN
      END
```

D.4 Code For Calculation of Shock Parameters

```
C  CALCULATION OF SHOCK PARAMETERS FOR CCL3F + ARGON OR SF6 OR CCL3H
      IMPLICIT REAL*16 (A-H,O-Z)
      REAL*16 TE(2000),HMH(2000),Y(2000),X(2000),U0(2000),
     1DA(2000),PA(2000),TA(2000),AM(2000),PE(2000),T
C H1 IS FOR FREON-11 FOR 200 TO 600 AND H2 IS FOR ARGON
C     H1(T)=-19640.44559D0 + 54.78791D0*T + 0.03840D0*T**2
C H1 IS FOR FREON-11 FOR 200 TO 600
C     H1(T)=-16882.05629D0 + 30.82887D0*T + 0.10267D0*T**2-0.00005*T**3
C THE NEXT LINE IS H1(T) FOR CCL3H   FOR 200 TO 600
C     H1(T)=-15999.93755D0 + 42.52108D0*T +0.03819D0*T**2
C THE NEXT LINE IS H1(T) FOR CCL3H   FOR 200 TO 800
C     H1(T)=-17156.54321D0 + 49.11661D0*T +0.02966D0*T**2
C THE NEXT LINE IS H1(T) FOR CCL3H   FOR 200 TO 800
C     H1(T)=-14518.61748D0 + 29.65252D0*T +0.07277D0*T**2 -0.00003*T**3
C THE NEXT LINE IS H1(T) FOR CCL3H   FOR 200 TO 900   LOWEST STD DEV.
C     H1(T)=-14815.22069D0 + 31.98536D0*T +0.06726D0*T**2 -0.00003*T**3
C THE NEXT LINE IS H1(T) FOR SF6 FROM 200K TO 600K
C     H1(T)=-21332.69168D0 + 48.28439D0*T +0.08063D0*T**2
C THE NEXT LINE IS H1(T) FOR SF6 FROM 200K TO 600K   LOWEST STD DEV.
      H1(T)=-15305.83460D0 - 4.06808D0*T +0.22107D0*T**2-0.00012*T**3
C THE NEXT TWO LINES ARE H2(T) FOR DIFFERENT FITS TO ARGON
C     H2(T)=-6196.862586D0 + 20.788296D0*T -0.000006D0*T**2
C     H2(T)=-6195.940883D0 + 20.783256D0*T
C THE NEXT LINE IS H2(T) ARGON KEEPING IN  MIND THAT CP IS 2.5R FOR AR.
      H2(T)=  8.314510D0*2.5D0*(T - 298.15D0)
      N=2000
      X0=1.0000D0
      T0=295.15D0
      P0=1.880D+02*X0
CCC         [WM1]=[CCLF4]=KG/MOL
C     NEXT LINE IS WM(KG/MOL) FOR CCL3F
C      WM1=0.137368D0
C     NEXT LINE IS WM(KG/MOL) FOR SF6
      WM1=0.146050D0
C     NEXT LINE IS WM(KG/MOL) FOR CCL3H
C      WM1=0.119378D0
      WM2=0.039948D0
      WM=X0*WM1+(1.0D0-X0)*WM2
      R=8.314D0
      T=300.0D0
      DO 10 I=1,N
      T=   T    +  0.02D0
C     T=   T    +  0.04D0*DBLE(I-1)
C     T=275.0D0 +  1.0D0*DBLE(I)
      TE(I)=T
      HMH(I)=   X0*(H1(T)-H1(T0))
      HMH(I)=HMH(I)+(1.0D0-X0)*(H2(T)-H2(T0))
      Y(I)=HMH(I)/8.314D0
      X(I)=2.0D0*Y(I)-TE(I)+T0
      X(I)=(SQRT(X(I)*X(I)+4.0D0*TE(I)*T0)-X(I))/(2.0D0*T0)
      U0(I)=SQRT(2.0D0*HMH(I)/(WM*(1.0D0-X(I)*X(I))))
      PE(I)=1.0D0+WM*U0(I)*U0(I)*(1.0D0-X(I))/(R*T0)
 10   CONTINUE
      RA=5.0D0/3.0D0
      AA=SQRT(RA*8.314D0*T0/WM)
      DO 20 I=1,N
      AM(I)=U0(I)/AA
      DA(I)=(RA+1.0D0)*AM(I)**2/((RA-1.0D0)*AM(I)**2+2.0D0)
      PA(I)=(2.0D0*RA*AM(I)**2-RA+1.0D0)/(RA+1.0D0)
      TA(I)=PA(I)/DA(I)
 20   CONTINUE
      WRITE(8,75)
      WRITE(8,76)
      WRITE(8,77)
      WRITE(8,78)
      WRITE(8,79)X0,WM,T0,P0
      WRITE(8,70)
      WRITE(8,*)
      DO 40 I=1,N
      WRITE(8,60)TE(I),U0(I),DA(I),PA(I),TA(I),
     11.0D0/X(I),PE(I),TE(I)/T0
 40   CONTINUE
C60   FORMAT(2G11.6,6G10.5)
 60   FORMAT(8G10.5)
 70   FORMAT(5HTE(K),4X,7HU0(M/S),5X,5HDA/D0,5X,5HPA/P0,5X,5HTA/T0,
     15X,5HDE/D0,5X,5HPE/P0,5X,5HTE/T0)
 75   FORMAT(12X,48HSHOCK PARAMETERS FOR VIBRATIONALLY RELAXED CCL3F)
 76   FORMAT(17X,50HENTHALPIES OF ARGON, CCL3F, SF6 & CCL3H FROM JANAF)
 77   FORMAT(17X,45HJ.PHYS.CHEM.REF.DATA,VOL.14,SUPPL.1,1985,P173)
 78   FORMAT(17X,41HJ.PHYS.CHEM.REF.DATA,VOL.11,NO.1,1982,P97/)
 79   FORMAT(1X,23HINITIAL CONDITIONS: X0=,F6.4,3X,3HWM=,F8.6,3X,
     13HT0=,F6.2,3X,3HP0=,F7.3,//)
      STOP
      END
```

References

1. P. Berge, Y. Pomeau and C. Vidal, "Order Within Chaos" (Wiley & Sons, New York, 1984).

2. J.M.T. Thompson and H.B. Stewart, "Nonlinear Dynamics and Chaos" (Wiley & Sons, New York, 1986).

3. R. L. Devaney, "An Introduction to Chaotic Dynamical Systems" (The Benjamin/Cummings Publishing Co. Inc., Don Mills, Ontario, 1986) and "Chaos Fractals, and Dynamics" (Addison-Wesley Don Mills, Ontario, 1990).

4. D. R. Hartree, Proceed. Cambr. Phil. Soc., **24**, 89 (1928) and "The Calculation of Atomic Structures", p5 (Wiley & Sons, New York, 1957).

5. P.M. Morse Phys. Rev., **34**, 57 (1929).

6. J. M. Combes, A. Grossmann, and Ph. Tchamitchian (Eds.), *Wavelets* (Springer-Verlag, New York, 1989).

7. R.B. Shirts, J. Phys., Chem., **91**, 2258 (1987).

8. R.B. Walker and R.K. Preston, J. Chem. Phys., **67**, 2017 (1977).

9. D. ter Haar, Phys. Rev., **70**, 222 (1946).

10. Herzberg, G. "Spectra of Diatomic Molecules", p 101 (Van Nostrand Reinhold Company, New York, 1950).

11. C.N. Banwell, "Fundamentals of Spectroscopy" (3^{rd} Edition, McGraw-Hill, London, England, 1983).

12. J.M. Hollas, "High Resoluton Spectroscopy" (Butterworths & Co. Ltd., Toronto, 1982).

13. D.N.S. Permann, "Gas Phase FT-IR Spectroscopy of Thiophosgene and Phosgene" (M. Sc., University of Saskatchewan, 1989).

14. E.R. Cohen and B.N. Taylor, Phys. Today, August, BG9 (1991).

15. J.N. Murrell, S. Carter, S.C. Farantos and A.J.C. Varandas, "Molecular Potential Energy Functions" (Wiley & Sons, Chichester, 1984).

16. W.H. Miller and C.W. McCurdy, J. Chem. Phys., **69** , 5163 (1978); C.W. McCurdy, H.D. Meyer, and W.H. Miller, J. Chem. Phys., **70**, 3177 (1979); S.K. Gray and W.H. Miller, Chem. Phys. Lett., **93** , 341 (1982); D. P. Ali and W.H. Miller, Chem. Phys. Lett., **103**, 470 (1984); W.H. Miller and K.A. White, J. Chem. Phys., **84**, 5069 (1986).

17. T. Crilly, "Fractals and Chaos", p193 (Springer-Verlag, New York, 1991).

18. S. Vohra, M. Spano, M. Shlesinger, L. Pecora, and W. Ditto, (Eds.), "Proceedings of the 1^{st} Experimental Chaos Conference" (World Scientific, New Jersey, 1992).

19. P. Gray, Proc. R. Soc. Lond. **415A**, 1 (1988).

20. D.W. Noid, S.K. Gray, and S.A. Rice, J. Chem. Phys. **84**, 2649 (1986).

21. K.J. Laidler, "Chemical Kinetics" (3rd Edition, Harper & Row, New York, 1987).

22. E.N. Lorenz, J. Atmos. Sci. **20**, 130 (1963).

23. P. Gray, J.F. Griffiths, S.M. Hasko, and P.-G. Lignola, Proc. R. Soc. Lond. **374A**, 313 (1981).

24. G.B. Cook, P. Gray, D.G. Knapp, and S.K. Scott, J. Phys. Chem. **93**, 2749 (1989).

25. P. Gray, and S.K. Scott, Phil. Trans. R. Soc. Lond. **332A**, 69 (1990).

26. P. Gray, and S.R. Kay, J. Phys. Chem. **94**, 3304 (1990).

27. B. Peng, S.K. Scott, and K. Showalter, J. Phys. Chem. **94**, 5243 (1990).

28. S.K. Scott, B. Peng, A.S. Tomlin, and K. Showalter, J. Chem. Phys. **94**, 1134 (1991) and references therein.

29. See a third year differential equations textbook such as G.F. Simmons, "Differential Equations with Applications and Historical Notes" (McGraw-Hill, Toronto, 1972).

30. R.L. Burden, and J.D. Faires, "Numerical Analysis" (Fourth Edition, PWS-Kent Publishing, Boston, 1989).

31. C.W. Gear, "Numerical Initial Value Problems in Ordinary Differential Equations", (Prentice-Hall, Englewood Cliffs, New Jersey, 1971); L.F. Shampine and M.H. Gordon, "Computer Solution of Ordinary Differential Equations", (W.H. Freeman, San Francisco, 1975).

32. L.F. Shampine and C.W. Gear, SIAM Rev. **21**, 1 (1979).

33. C.W. Gear, SIAM Rev. **23**, 10 (1981). Also an e-mail communication from C.W. Gear to H. Teitelbaum.

34. K.L.C. Hunt, P.M. Hunt and J. Ross, Annu. Rev. Phys. Chem., **41**, 409 (1990).

35. N. Samardzija, L.D. Greller, and E. Wasserman, J. Chem. Phys., **90**, 2296 (1986).

36. F.C. Moon, "Chaotic Vibrations" (Wiley & Sons, New York, 1987).

37. Ch. Linenau, J.C. Williamson and A.H. Zewail, Chem. Phys. Lett. **213**, 289 (1993).

38. D. Permann and I. Hamilton, Am. J. Phys. **60**, 442 (1992).

39. N.H. Packard, J.D. Farmer, and R.S. Shaw, Phys. Rev. Lett. **45**, 712 (1980).

40. Th. M. Kreul, A. Freund, and F.W. Schneider, J. Chem. Phys. **93**, 416 (1990).

41. see a first year calculus text such as E. W. Swokowski, "Calculus with Analytic Geometry" (2^{nd} Edition, Prindle, Weber, & Schmidt, Boston Mass., 1979).

42. J. Guckenheimer and P. Holmes, "Nonlinear Oscillations, Dynamical Systems, and Bifurcations of Vector Fields" (Springer-Verlag, New York, 1983).

43. A.J. Lichtenberg and M.A. Lieberman, "Regular and Stochastic Motion" - (Springer-Verlag, New York, 1983).

44. K. M. Christoffel and J. M. Bowman, J. Phys. Chem. **85**, 2159 (1981).

45. S. C. Leasure, K. F. Melfield, and R. E. Wyatt, J. Chem. Phys. **74**, 6197 (1981).

46. M. J. Davis and R. E. Wyatt, Chem. Phys. Lett. **86**, 235 (1982).

47. P. S. Dardi and S. K. Gray, J. Chem. Phys. **80**, 4738 (1984).

48. S. K. Gray, Chemical Physics **83**, 125 (1984).

49. G. C. Lie and J.M. Yuan, J. Chem. Phys. **84**, 5486 (1986).

50. Y. Gu and J.M. Yuan, Phys. Rev. A **36**, 3788 (1987).

51. M. E. Goggin and P. W. Milonni, Phys. Rev. A **37**, 796 (1988).

52. D. Permann and I. Hamilton, J. Chem. Phys. **95**, 8188 (1991).

53. J. G. Leopold and I. C. Percival, Phys. Rev. Lett. **41**, 944 (1978).

54. Y. Meyer, *Ondelettes* (Hermann, Paris, 1990).

55. I. Daubechies, Commun. Pure Appl. Math. **41**, 909 (1988).

56. I. Daubechies, IEEE Trans. Information Theory **36**, 961 (1990).

57. S. G. Mallat, Technical Report No 412, Courant Institute of Mathematics, New York University, New York (1988).

58. S. G. Mallat, IEEE Trans. Pattern Analysis and Machine Intelligence **11**, 674 (1989).

59. G. Strang, SIAM Rev. **31**, 614 (1989).

60. P. Goupillaud, A. Grossmann and J. Morlet, Geoexploration **23**, 85 (1984/85).

61. I. Daubechies, *Ten Lectures on Wavelets* (SIAM, Philadelphia, 1992).

62. C. K. Chui, *An Introduction to Wavelets* (Academic Press, Boston, 1992).

63. M. Vetterli,p17 *Wavelets and Their Applications*, ed. M.B. Ruskai (Jones and Bartlett, Boston, 1992).

64. D. Pcrmann and I. Hamilton, Phys. Rev. Lett. **69**, 2607 (1992).

65. D. Pcrmann and I. Hamilton, J. Chem. Phys. **95**, 8188 (1992).

66. M. Cartwright, *Fourier Methods* (Ellis Horwood, Chichester, 1990).

67. E. O. Brigham, *The Fast Fourier Transform and its Applications* (Prentice-Hall, New Jersey, 1988).

68. A. J. Lichtenberg and M. A. Lieberman, *Regular and Stochastic Motion* (Springer-Verlag, New York, 1983).

69. Z. Cheng, Ph.D. Thesis, University of Ottawa, 1993.

70. Z. Cheng, I. P. Hamilton, and H. Teitelbaum, J. Phys. Chem., **95**, 4931 (1991).

71. N. Delprat, B. Escudié, P. Guillemain, R. Kronland-Martinet, P. Tchamitchian, B. Torrésani, IEEE Trans. Info. Theory **38**, 644 (1992).

72. R. R. Coifman and M. V. Wickerhauser, IEEE Trans. Info. Theory **38**, 713 (1992).

73. S. Mallat and W. L. Hwang, IEEE Trans. Info. Theory **38**, 617 (1992).

74. J. H. Kiefer, and R. W. Lutz, J. Chem. Phys., **44** 668 (1966).

75. J. Dove and H. Teitelbaum, Chem. Phys., **6** 431 (1974).

76. Z. Baalbaki, and H. Teitelbaum, Chem. Phys., **104** 83 (1986).

77. H. Teitelbaum, Ph.D. Thesis, University of Toronto, 1974.

78. M. W. Chase, Jr., C. A. Davies, J. R. Downey, Jr., D. J. Frurip, R. A. McDonald, and A. N. Syverud, eds., J. Phys. and Chem. Ref. Data **14**, 1985 Supplement No. 1, JANAF Thermochemical Tables (3^{rd} Edition, Published by the American Chemical Society and the American Institute of Physics for the National Bureau of Standards, 1986).

79. Z. Cheng, and H. Teitelbaum, to be published

80. C. Carruthers, K. Francoeur, and H. Teitelbaum in *Shock Tubes and Waves*, Proc. 16^{th} Internat. Symp. on Shock Tubes and Waves, H. Grönig, ed., 327 (VCH Publishers, Weinhem, 1988).

81. Froment-Mallat wavelet code is available from the anonymous ftp site cs.nyu.edu in subdirectory pub/wave/megawave. Other wavelet code is available from *Numerical Recipes in C* or *Numerical Recipes in Fortran*, Published by Cambridge University Press, Cambridge, UK, 1992. There are also example books and disks of code available from University of Cambridge Press.

82. Z. Su, Ph.D. Thesis, University of Ottawa, in progress.

83. A. V. Voronel, in *Phase Transitions and Critical Phenomena*, **5b**, C. Domb and M. S. Green , eds., 343 (Academic Press, New York, 1976).